



ON THE MEASUREMENT AND PREDICTION OF GRAPHENE PRODUCTION FOR ENABLING SUSTAINABLE PHOTOCATALYTIC PROCESSES

By

DIEGO TOMOHISA PÉREZ-ÁLVAREZ

A thesis submitted to
the University of Birmingham
for the degree of
DOCTOR OF PHILOSOPHY

Department of Mechanical Engineering
College of Engineering and Physical Sciences
University of Birmingham
September 2024

UNIVERSITY OF
BIRMINGHAM

University of Birmingham Research Archive

e-theses repository

This unpublished thesis/dissertation is copyright of the author and/or third parties. The intellectual property rights of the author or third parties in respect of this work are as defined by The Copyright Designs and Patents Act 1988 or as modified by any successor legislation.

Any use made of information contained in this thesis/dissertation must be in accordance with that legislation and must be properly acknowledged. Further distribution or reproduction in any format is prohibited without the permission of the copyright holder.

ABSTRACT

Two-Dimensional Materials (2DMs, such as MoS_2 , hBN, gC_3N_4 , graphene) have emerged over the last 20 years with diverse applications in construction, electronics, and energy storage, due to their unique electronic, chemical, optical and mechanical properties. One such application of 2DMs is for sustainable, passive water treatment using photocatalysis. Here, they have shown great promise over traditional catalysts (e.g., TiO_2) in treating heavily polluted groundwater using only sunlight as the driving mechanism. Reviewing these advanced visible light active photocatalysts (Chapter 1), show they are often composites of several different materials. In many of these photocatalytic systems, graphene has been demonstrated as an essential component for photocatalytic composites, due to its high conductivity and non-volatility. However, key challenges associated with synthesis of 2DMs remain salient. These include the cost and performance of synthesis techniques, limited knowledge of the mechanisms that drive production, and lack of predictive models that describe large scale manufacture.

One group of 2DMs synthesis techniques with demonstrable ability to upscale is Liquid Phase Exfoliation (LPE) using mechanical force. These techniques function by dispersing a layered material¹ in a fluid, and exposing the mixture to an intense mechanical force. Over time, the intense force destroys the layered material into a spectrum of differently sized particles, ranging from macroscopic agglomerates to few-layered material including nanosheets. LPE is also material agnostic, with the ability to synthesise numerous semi-

¹Often called the ‘precursor’ material, a prominent example is graphite for graphene.

conducting and conducting 2DMs that can form the building blocks of photocatalysts and their heterostructures. In Chapter 2, a simple exfoliation system consisting of a modified kitchen blender is presented alongside evaluation of the system for producing graphene, which formed the basis for *OpenLPE*, an open hardware and software platform that can be used by the research community. In Chapter 3, this testbed is used to investigate methods of *in situ* characterisation of few-layered material concentration and morphology, a process which for nanomaterials is otherwise long and exhaustive requiring many steps to ensure proper separation of nanomaterials. Here, UV-Visible spectroscopic measurements are used to enable quick discrimination between materials, highlighting challenges associated with the use of spectroscopic techniques in highly aerated fluid flows.

As exfoliating methods become more widespread, there are no mathematical models available to industry that describe nanomaterial production at scale. Such models would allow for accurate experimentation and evaluation of potential liquid-phase processes with fewer expensive iterations. To address this, Chapter 4 presents a statistical model of graphite breakup using the population balance approach, demonstrating a prediction of graphite breakage and yield of any size fraction. Further, we examine the applicability of positron emission particle tracking for evaluating the internal flow fields of exfoliating systems, with the intention that these measurements can be taken to physically interpret the system. Collectively, these results and models provide insights on the breakage mechanisms and fluid dynamics that underpin mechanochemical exfoliation processes for 2DMs, and provide direction for the eventual intensification and optimisation at any manufacturing scale.

DEDICATION

Dedicado a mi familia, con mucho cariño, por aguantarme estos largos años.

ACKNOWLEDGMENTS

Firstly and foremost, I extend my deepest gratitude to my supervisor, Prof. Jason Stafford, for his dutiful nurturing, wise counsel and unbounded patience. Nothing here would have been possible without you. You truly are the best around. Further, I thank my second supervisor, Prof. Philip Davies, for his dutiful review, guiding purpose and opportunities abroad.

To the scientists at the Egyptian National Research Council, Yasser Mohamed, Hos-sam El Nazer and Elzahraa Elgohary, for the help broadening my understanding of photo-catalytic processes and for being such gracious hosts, shukran.

To Keith Paton, Andrew Pollard, and Sofia Marchesini at the National Physical Laboratory, and to Diogo Fernandes and Jenny Burt at Malvern Panalytical. My deepest thanks for your full hearted support of my experiments by use of your equipment, for hosting me, and taking the time away from your busy schedules to conduct experiments. I thank Jack Sykes, Kit Windows-Yule and Tzany Kokalova at the school of Medical Physics for their guidance in the exploration of Positron Emission Particle Tracking for shear exfoliating process. Further, I deeply thank Dawid Hampel for his boundless support, determination and for finding the time among adverse conditions to help run the equipment.

To my friends and colleagues at the School of Engineering, especially to Jacob, Norman, Angharad, Martin, Maninder and Rhys. Thank you for helping me realise the joy of engineering is in the process of it.

Finally, to Katie, for being my rock. Love you bug!

ALTERNATE FORMAT THESIS

This thesis is composed of manuscripts that were accepted for publication, are under review, or that will be submitted to a scientific journal. Diego Tomohisa Pérez-Álvarez is the first author and predominant contributor of all the research presented in this thesis. Additional contributors are stated clearly at the start of each chapter.

- [1] Diego T. Pérez-Álvarez et al. “Challenges surrounding nanosheets and their application to solar-driven photocatalytic water treatment”. In: *Mater. Adv.* 3.10 (2022), pp. 4103–4131. DOI: [10.1039/D2MA00276K](https://doi.org/10.1039/D2MA00276K)
- [2] Diego T. Pérez-Álvarez, Philip Davies, and Jason Stafford. “Foam flows in turbulent liquid exfoliation of layered materials and implications for graphene production and inline characterisation”. In: *Chem. Eng. Res. Des.* 177 (Jan. 2022), pp. 245–254. ISSN: 0263-8762. DOI: [10.1016/j.cherd.2021.10.041](https://doi.org/10.1016/j.cherd.2021.10.041)
- [3] Diego T. Pérez-Álvarez, Jacob Brown, and Jason Stafford. “Modification of kitchen blenders into controllable laboratory mixers for mechanochemical synthesis of atomically thin materials”. In: *HardwareX* 16 (Dec. 2023), e00471. ISSN: 2468-0672. DOI: [10.1016/j.ohx.2023.e00471](https://doi.org/10.1016/j.ohx.2023.e00471)
- [4] Diego T. Perez-Alvarez et al. “Predicting graphene production with population balance modelling”. In: *Carbon* 231 (Jan. 2025), p. 119687. ISSN: 0008-6223. DOI: [10.1016/j.carbon.2024.119687](https://doi.org/10.1016/j.carbon.2024.119687)

Contents

	Page
Acronyms	xxiii
1 Introduction and Literature Review	3
1.1 Foreword	4
1.2 Motivation	6
1.3 Introduction	11
1.4 2D Photocatalysts	16
1.5 Synthesis & Morphology	25
1.5.1 Mechanical Exfoliation in Liquids	27
1.5.2 Thermal Exfoliation	33
1.5.3 Intercalation	36
1.5.4 Composites	38
1.6 Treatment and Reuse	43
1.6.1 Immobilised	44
1.6.2 Suspended	46
1.6.3 A Combined Approach	48
1.6.4 Photocatalytic Reaction Chambers (PRCs)	48
1.7 Recommendations for Photocatalysis Research	50
1.8 Conclusions	53

2	Equipment and Validation	59
2.1	Foreword	60
2.2	Introduction	62
2.3	Hardware description	65
2.4	Modifications	67
2.4.1	On/off cycling	67
2.4.2	Phase angle control	68
2.4.3	Speed sensor	71
2.4.4	PID control	72
2.4.5	Cooling jacket	73
2.4.6	In-line monitoring	76
2.5	Operation	79
2.5.1	Preparing samples	79
2.5.2	Vessel considerations	80
2.5.3	Blender operation	82
2.5.4	Recycling	83
2.5.5	Post Processing	85
2.6	Validation and Characterization	86
2.6.1	UV-vis-NIR Spectroscopy	86
2.6.2	Microscopy	87
2.7	Conclusion	89
3	Exploring Inline Characterisation	91
3.1	Foreword	92
3.2	Introduction	95
3.3	Methods	99
3.3.1	Experimental arrangement	99

3.3.2	Material synthesis and <i>ex situ</i> characterisation	101
3.3.3	<i>In situ</i> materials characterisation	102
3.3.4	Flow characterisation	104
3.4	Results and discussion	106
3.4.1	Liquid exfoliation of graphene	106
3.4.2	Variation in surfactant concentration	109
3.4.3	Kitchen blender hydrodynamics	110
3.4.4	Inline production monitoring	114
3.5	Conclusions	120
4	Breakage Analysis and Modeling	122
4.1	Foreword	123
4.2	Introduction	125
4.3	Methods	130
4.3.1	Liquid Phase Exfoliation	130
4.3.2	Materials	130
4.3.3	Laser Diffraction	133
4.3.4	Hydro Insight Imaging	135
4.3.5	UV-Visible-near-Infrared Spectroscopy	138
4.3.6	Nuclear Magnetic Resonance	138
4.3.7	Raman Spectroscopy	139
4.3.8	Optical Microscopy	140
4.3.9	Scanning Electron Microscopy	140
4.3.10	Positron Emission Particle Tracking	140
4.3.11	The Population Balance	144
4.4	Results and Discussion	151
4.5	Conclusion	165

5	Conclusions	167
A	Appendix: Derivation of the Population Balance Model	173
B	Appendix: Dimensional Analysis	178
B.1	Introduction	180
B.2	Analysis	182
B.2.1	Shear mixers	183
B.2.2	Sonicated probes	187
B.2.3	Microfluidisation	188
B.3	Results and Discussion	190
B.4	Conclusion	195
C	Appendix: Arduino Snippets	196
C.1	Simple Triac Control	196
C.2	Measuring Rotational Speed	197
C.3	PID Control	198
	References	200

List of Figures

1.1	Countries of the world, plotted against their strain on freshwater resources [12] and average daily incident light [33]. Bubbles are sized by population, and coloured by economic area denoted by the world bank. Selected countries are all experiencing withdrawals above 40% (high water stress), and have a population >5 million, though data is not available for all countries. Note that withdrawals exceed 100% in a number of countries, which indicates that the local freshwater is being sourced unsustainably (e.g. from aquifers) or heavy use of desalination.	9
1.2	A schematic diagram for a heterogenous photocatalytic process over a 2D photocatalyst surface, detailing some of the many reactions that can occur to pollutants through the use of photogenerated charge carriers. (A) and (D) represent the surface adsorbed acceptor and donor species respectively [34]. .	10
1.3	Intensity of sunlight (red) in juxtaposition to the photocatalytic activation (normalised) of TiO_2 [69] and a 2D nanocomposite constructed using graphitic carbon nitride (g- C_3N_4) [72]. A total of 46% of the solar energy falls within the visible light range [73].	15

1.4	Two-Dimensional Materials (2DMs) which have been a focus for photocatalysis research include g-C ₃ N ₄ , transition metal dichalcogenides such as MoS ₂ , insulators such as h-BN for composites, and other graphene-related materials (Gr, rGO and GO). Apart from graphene, which has a zero band gap, these materials can be exfoliated from their bulk materials to engineer nanosheets with a direct band gap. In the case of rGO and GO, modifications to the band gap are made possible by removing/adding functional groups. TiO ₂ has been included for reference, illustrating the advantages of narrow band gap nanosheets that can target visible wavelengths for solar-driven photocatalysis. For g-C ₃ N ₄ , a triazine structure is shown inset.	19
1.5	Search hits for “ <i>photocatalysis</i> ” and “ <i>2D</i> ” or “ <i>nanosheet</i> ”, filtered or unfiltered for synthesis synonyms (synthesis, construction, preparation). This shows the exponential rise in popularity of 2D Photocatalysts (PCs) (n.b. log scale), particularly in their synthesis. Search terms were applied to the Title and abstract of publications (when creating this figure, 2020 and 2021 figures were yet to stabilise as publications were still under review for release). Data accessed through the Web of Knowledge and the EUs’ Espacenet.	20
1.6	Schematic representation of the different exfoliation techniques discussed in this review: Liquid-Phase mechanical, thermal, chemical and electro-chemical exfoliation.	27

1.7	Circular barplot of all the synthesis techniques discussed in this section, ranked according to the process parameters of Scalability (S), Yield (Y), Morphology (M), Defects (D) and Cost (C), subplot b). Subplot a) isolates shear mixing, a technique which suffers almost exclusively from its poor yield (typ. $\sim 1 - 10$ wt%). Subplot c) isolates bottom-up methods, in this case Chemical Vapour Deposition (CVD) has been used as an example. CVD can be used to grow different materials on substrates, and is currently the most widespread technique for fabricating pristine monolayered graphene on copper substrates [154].	28
1.8	Sonication-based synthesis typically involves either probe or bath techniques. Exfoliation of layered materials into nanosheets is achieved through the rapid growth and collapse of cavitation bubbles in the liquid dispersion.	30
1.9	Microfluidisation of nanosheets from layered materials. The synthesis mechanisms depend on the hydrodynamic regime and chamber configuration. Production of nanosheets can be achieved through a) Laminar or viscous shear exfoliation, b) Turbulent shear exfoliation and/or c) localised flow impingement.	32
1.10	Synthesis of nanosheets using high shear mixing. Exfoliation and precursor particle break-up predominantly occur in the rotor (red) and stator region of these devices where collisions and the largest shear stresses in the batch volume exist.	33
1.11	Synthesis of nanosheets using thermal exfoliation can be achieved through a variation of thermal treatment approaches. a) Intercalation of H_2SO_4 between layers leads to the formation of gas bubbles during the heating and thermal decomposition step, leading to the separation of nanosheets. b) Thermal decomposition in air leads to layer-by-layer oxidation and layer splitting processes with gaseous products released. Fragmentation of nanosheets, together with the formation of pores and defects, also occur using these approaches.	34

1.12	TEM images of bulk g-C ₃ N ₄ (a), alongside porous g-C ₃ N ₄ exfoliated at 450°C (b), 500°C (c), 550°C (d). The heat decomposes certain areas of the nanosheets, leaving the resultant sheets ranging from slightly exfoliated and porous to fully exfoliated and with large holes. Reproduced with permission from Ref. [170]. Copyright 2015 Elsevier B.V.	35
1.13	Synthesis of nanosheets using electrochemical exfoliation. Intercalation of radicals and anions between layers leads to the formation of gas bubbles and separation of nanosheets. Oxidation of nanosheets can occur depending on the applied voltage, electrode configuration and other experimental conditions.	37
1.14	Synthesis of graphene oxide nanosheets. Chemical exfoliation is typically achieved using a modified Hummer's method. Graphite is oxidised to form graphite oxide, followed by dispersion and separation of Graphene Oxide (GO) nanosheets in water.	39
1.15	Schematic representation of the solvo- or hydrothermal synthesis process for producing nanosheets and nanocomposites.	40
1.16	An example of a hydrothermal route to composite synthesis, with corresponding SEM images (A) and photocatalytic activity. B) shows a schematic representation of the route, where rGO coated TiO ₂ Nanoparticles (NPs) were created through a combination of electrostatic interactions and in-solution mixing, followed by simultaneous hydrothermal reduction of the GO into rGO and crystallisation of the initially amorphous TiO ₂ NPs (Graphene-TiO ₂ NPs). These NPs were compared to separately crystallised TiO ₂ followed by the same electrostatic-assembly and hydrothermal reduction (two-step hydrothermal), and bare anatase NPs, in terms of their photocatalytic (C) and photoelectric activity (D). The scale bars shown in (A) represent 200 nm. Figure adapted from Lee et al. [68]. Reproduced with permission from Ref. [68].	41

1.17	One of the first pilot plants for photocatalysis, employing a slurry reactor (in a static concentrator array) installed at latitude 40° (Arganda del Rey, Madrid, Spain). Costing estimates in Table 1.1 for plant scale PCs are taken from this plant’s operation[63]. Reproduced with permission from Malato et al. [69]. .	49
1.18	The selection process for evaluating a Photocatalytic System (PCS). A systems approach can consist of creating and evaluating a singular ‘system’, or the creation of many modular ‘subsystems’ which can work together to create a usable ‘system’.	51
1.19	Summary of future research focus areas according to Technology Readiness Level (TRL). Topics within TRL 1-4 align with the photocatalytic systems approach presented in Figure 1.18. TRL 5 is highlighted as the prescribed TRL for laboratory research on solar photocatalytic water treatment to successfully transition to the pilot-scale demonstration stage in realistic environments. . .	56
2.1	Some examples of modified blenders tested in lab. i) is a Kenwood modified in accordance with Sections 2.4.3, 2.4.4 and 2.4.2 (with option B from Table 2.2) and includes a screen for a digital readout. ii) is an AMZchef with variable speed (Section 2.4.2, uses option C from Table 2.2) and is typically used with the programmable extension lead in Section 2.4.1. iii) is a modified Kenwood with option D from Table 2.2, and has an added servo to facilitate the <i>on/off</i> cycling. Software and build guides can be found on our Open Science Framework (OSF) page.	65
2.2	Arduino-controlled <i>on/off</i> extension lead. This automated relay switch controlled many of the appliances listed in this work, and can be combined with other sensors for dynamic, closed-loop control.	68

2.3	Visual guide to wiring a dimmer module (either arduino or potentiometer control) into a commercial blender, in this case the Kenwood BLP31.D0WG. The safety switch is left inline with the motor in A), to add an extra layer of security in the unlikely event the vessel detaches from the blender. B) shows the wiring diagram for arduino controlled and potentiometer controlled dimming modules.	70
2.4	Sensor modifications in A), the photo-interrupt module was brought up and away from the fan, with a small 3D printed interrupting ring fit into the fan itself. B) shows the speed of the first 15 minutes <i>on</i> of a run, with a constant <code>dim_time</code> (in orange, measured with an optical tachometer), and a Proportional Integral Differential (PID) control circuit (in purple, measured with an on-board sensor). Inset in B) is a histogram of speeds (log scale). For the "Constant" (orange) case, the speed was carefully measured as stable with the tachometer before the equipment was power cycled and the measurements taken. Note the much lower sampling rate (1 per minute) and the steady state error between the constant and PID cases.	71
2.5	Batch temperature during the synthesis of few-layer graphene in water-sodium cholate using (a) "bullet" style and (b) "jug" style process vessels. All other synthesis parameters were kept the same across both cases including $C_i = 20$ g/L, $C_{sc} = 4.3$ g/L, $V = 200$ mL and $\omega = 20,000$ rpm.	74

2.6	The cooling system utilises the phase change of ice (latent heat of fusion) to remove heat (Q''_{pc}) from the Liquid Phase Exfoliation (LPE) process. The cooling jacket is constructed using 3D-printed polyethylene terephthalate glycol-modified (PETG) parts and two large ethylene propylene diene monomer (EPDM) pipe connectors. A thermocouple board is connected to a Raspberry Pi 3B+ to record and plot temperatures from type K thermocouples in real-time. The addition of precursors and product sampling is possible using the vessel spout. When the synthesis process is completed, the product is emptied from this vessel spout also.	75
2.7	The temperatures of the (a) batch and (b) coolant during the synthesis of few-layer graphene in water-sodium cholate using a "bullet" style process vessel with integrated cooling system. The synthesis parameters were kept the same as for the cases without cooling in Fig. 2.5 including $C_i = 20$ g/L, $C_{sc} = 4.3$ g/L, $V = 200$ mL and $\omega = 20,000$ rpm.	76
2.8	The probe mounted in position above the impeller in part a) with a small inset schematic detailing its function. b) compares manual measurements taken exsitu to measurements taken with the probe for a similar 15 min run. c) shows the optical noise generated in between the probe and the mirror. . .	77
2.9	Failures of sealed vessels in a) and b), most occur at weak points in the vessels construction, likely due to thermal cycling weakening the material, and high pressure and temperature causing material failure. c) Shows a labeled selection of vessels we have tested with, leakage around the lower seal was common with the Kenwood vessels, but we found this could be mitigated by increasing the pretension on the lower seal (initially achieved this with PTFE tape, then moved on to a small 3D printed shim).	81

2.10	Graphene concentration is plotted against time in (b) within a window of uncertainty ($1.2\sigma_{max}$), and against speed in (c) with speed (± 1000 rpm) and concentration error bars (σ_{max}). We find production exponents of $t^{0.77}$ and $N^{1.46}$ for $C_s = 4.3$ mg/mL of Sodium Cholate (NaC) at a process volume of 200 mL and an average layer cutoff of $\langle N \rangle = 5$ (centrifuged for 45 minutes at 380 Relative Centrifugal Field (RCF), initial graphite concentration of $C_i = 20$ mg/mL). Optical extinction measurements were used to determine concentration (through the Lambert-Beer law) using a PerkinElmer Lambda 365 UV-Visible-near-Infrared (UV-vis-NIR) Spectrophotometer, and a measured extinction coefficient of $1521 \text{ L g}^{-1} \text{ m}^{-1}$ at $\lambda = 660 \text{ nm}$. The procedure for measuring the extinction coefficient is described in detail elsewhere [245].	84
2.11	Three different UV-vis-NIR extinction spectra of materials (Y is offset, arbitrary units) created with our mixer, graphene (Gr), MoS_2 and hBN, along with the salient points for establishing the thickness, concentration and/or length [240, 250, 251].	86
2.12	Atomic Force Microscopy (AFM) of graphene nanoplatelets $\langle L \rangle \approx 200 \text{ nm}$ exfoliated in IPA and water (50:50 mix by mass) note that Sodium Cholate (NaC) can obscure Atomic Force Microscopy (AFM) as it adheres to the surface of the nanoplatelets causing the probe tip to stick and drag.	88
3.1	Shear exfoliation in aqueous-surfactant dispersions can generate foam flows. (a) Liquid dispersions of few-layer graphene produced by the batch exfoliation process. (b) Foamy fluid mixture during turbulent shear exfoliation in a kitchen blender. (c) Gravitational phase separation when the process stops. .	97

3.2	Implementation of inline UV-vis-NIR spectroscopy for production monitoring.	
	(a) The standard kitchen blender vessel. (b) The modified vessel with fibre optic probe insertion. (b) Internal view of the vessel showing the location of the probe for <i>in situ</i> spectroscopy.	98
3.3	Evolution of the liquid-gas behaviour upon impeller start-up. (a) $\omega t = 2100$. (b) $\omega t = 2160$. (c) $\omega t = 2210$. (d) $\omega t > 7330$. Images shown are for a liquid volume, $V = 800$ mL, $Re \approx 2.6 \times 10^6$, $Fr \approx 6.1 \times 10^3$, and $We \approx 2.5 \times 10^6$. .	100
3.4	Extinction spectrum of few-layer graphene.	102
3.5	(a) Absorbance spectrum of blue food dye. The peak visible is situated at $\lambda = 617$ nm. (b) Relationship between the concentration of blue food dye (C_d) and absorbance measured using <i>in situ</i> spectroscopy at $\lambda = 617$ nm and $V = 400$ mL.	103
3.6	Near-wall graphite particle image velocimetry. (a) Raw high-speed image captured during liquid exfoliation. (b) contrast-enhanced region of interest. (c) instantaneous displacement vector field as viewed from the camera perspective. Images shown are for $V = 200$ mL, $\omega = 10^4$ rpm, initial graphite concentration, $C_i = 20$ mg/mL and surfactant concentration, $C_i/C_{fl} = 8$. . .	105
3.7	Concentration of graphene for different impeller rotational speeds (ω) and fluid volumes (V). All concentration data were measured at a process time, $t = 15$ mins.	107
3.8	Concentration of graphene for different surfactant concentrations (C_{fl}), fluid volumes (V) and starting graphite concentrations (C_i). All graphene concentration data were measured at a process time, $t = 15$ mins, and a constant rotational speed, $\omega = 10000$ rpm.. . . .	108

3.9	Ensemble-averaged near-wall graphite particle streamlines. (a) $C_i/C_{fl} = 1$. (b) $C_i/C_{fl} = 2$. (c) Graphite particle hold-up regions for $C_i/C_{fl} = 1$. (d) $C_i/C_{fl} = 4$. (e) $C_i/C_{fl} = 8$. (f) $C_i/C_{fl} = 40$. Streamlines have been ignored in the regions with light reflections. All data shown for $V = 200$ mL, $C_i = 20$ g/L, $\omega = 10000$ rpm. An in-depth description of the imaging setup is provided in Section 3.3.4.	112
3.10	Effect of surfactant concentration on foam volume (V_f) and liquid drainage time (t_{dr}). Experiments were performed at $\omega = 10000$ rpm, $t = 30$ s and without graphite.	114
3.11	<i>In situ</i> spectroscopy measurements of extinction at $\lambda = 660$ nm before, during and after turbulent mixing of water, water-surfactant, and water-surfactant-graphite dispersions. Turbulent mixing occurred between $1 \leq t \leq 2$ minutes. Experiments were performed at $\omega = 10000$ rpm and $V = 200$ mL.	117
3.12	(a) Comparison between <i>in situ</i> extinction measurements at $\lambda = 660$ nm and graphene concentration with time. Experiments were performed at $\omega = 10000$ rpm, $V = 200$ mL, $C_i = 1$ mg/mL and $C_i/C_{fl} = 2$. (b) Reduction in average number of atomic layers (N_{FLG}) for a few-layer graphene dispersion undergoing turbulent exfoliation. <i>In situ</i> measurements of the extinction ratio (A_{550}/A_{\max}) corresponding to changes in few-layer graphene spectra with time. Experiments were performed at $\omega = 10000$ rpm, $V = 200$ mL, $C_g = 2.61 \times 10^{-3}$ mg/mL and $C_{fl} \approx 1$ mg/mL.	119

4.1	Graphene production and modelling approaches. (A) Impeller-driven blender used in this study, modified for process control [3]. (B) Progression of samples exfoliated from 10 s to 1800 s duration, showing gradual darkening of the graphite/graphene suspensions with time. (C) Optical microscopy of the bulk material at different exfoliation times. (D) Scanning Electron Microscopy (SEM) images showing the progression of breakage towards smaller particles (all samples analysed were highly polydisperse). (E) Surface plot illustrating the Population Balance Model (PBM) used herein. An initial distribution of particles (in red) is gradually progressed forwards in time under the influence of a shear exfoliating system. After a period of exfoliation, the original Particle Size Distribution (PSD) gradually transforms as particles are destroyed and birthed into smaller size fractions (in green). Height and colour of the surface indicate the amount of material at the point specified. Summing the mass values of the nano-sizes yields an indication of the amount of nanomaterial produced.	129
4.2	An estimate of the particle-fluid regimes within the exfoliation system. Graphite loading of 20 mg/mL is indicated by the orange line.	132
4.3	Hydro insight imaging, at different process times (10 s \rightarrow 1800 s). All images are taken at the same magnification, using the Hydro Insight low magnification lens (measureable size range - 10 μ m to 800 μ m).	135

4.4	Hydro Insight Imaging accessory module to the Mastersizer 3000 was used to collect statistics on various particle size metrics using the low magnification lens. In (A) and (B), the measured Equaivalent Circle Area (ECA) and Mean Radius Circle (MRC) diameters are plotted alongside the Laser Diffraction (LD) Mastersizer 3000 measurements. Error bars and banded areas represent the 10th percentile and 90th percentile, with the central lines and markers representing the 50th percentile. (C) Mean particle smoothness is plotted against exfoliation time and alongside values for a simple square and rectangle of aspect 1:3. (D) The entire distribution of circularity for different exfoliation times are plotted together.	137
4.5	Tracer observations given as a percentage of total observations in the mixer. Graphite tracer observations are given in (D), with all other subfigures using a glass tracer.	142
4.6	Magnitude of model coefficients B , E , A and S plotted against mixer speed. Coefficients are scaled for better visibility. Breakup occurred for speeds above 1500 rpm, thereby making it difficult to fit the model coefficients to the data for the lowest speed investigated. (A) The model fitted to all data, using an automated fitting routine which balances the error in the nanomaterial and bulk precursor distribution. (B) The model fitted only to the LD data, with S adjusted to fit to the nanomaterial measurements. This provides a worse fit overall, much worse than that presented in Figure 4.10.	146
4.7	All speeds from no exfoliation or breakup 1500 rpm to highly exfoliating and high breakup 18500 rpm. Speed is denoted in the subcaption.	149
4.8	Visual indication of how the error is calculated in the PBM. The total error in the distribution is designated as both the error in the bulk distribution and the error (Δ , inset) at the small-scale.	150

4.9	Graphite breakup and production of few-layer graphene with exfoliation time. (A) Breakup of graphite at 11500 rpm. The PBM prediction is plotted in the background, similar to the surface illustration in Figure 4.1, with colour indicating volume of material produced. Independently measured experimental PSDs are plotted as green markers denoting the 50 th percentile diameter mark, with errorbars stating the 10 th and 90 th percentile. The red line represents the numerically predicted 50 th percentile. (B) Few-layer graphene yield (UV-vis-NIR concentration measurements, circular points) with fits derived from different PBMs (trendlines). The predicted concentration is from the same model defined in (A).	152
4.10	Fitting the PBM by omitting all measurements except pairs of nanomaterial measurements, with (<i>With PSD</i>) and without (<i>No PSD</i>) inclusion of the PSD measurements as aid, for two possible coefficient starting points ($B = 4 \times 10^{-3}, E = 1, A = 4 \times 10^{-1}$ and $B = 2 \times 10^{-3}, E = 2, A = 2 \times 10^{-1}$). Histograms are constructed using the resultant coefficients. Red dashed line indicates the fully fitted solution ($4.0 \times 10^{-3}, 2.1, 4.9 \times 10^{-1}$), using all available measurements (i.e. $\Omega = 11500$ rpm condition in Figure 4.9). Final root-mean-squared error between the predicted nanomaterial trendlines are noted in the legend.	155
4.11	Graphite breakup for two different starting size distributions. Left, both PSDs are plotted on a continuous colour plot (colour indicating volume of material produced) breaking under the influence of the same fractional PBM in time. Red and Green dashed lines mark the times at which experimental LD samples were taken. Right, two different starting distributions are exposed to the same exfoliation conditions (surfactant concentration of 4.3 mg/mL and impeller speed of 11500 rpm; but different starting concentrations of 4 mg/mL for the larger particles, and 20 mg/mL for the smaller particles).	156

4.12	Evolution of the spectroscopic characteristics of separated few-layer graphene samples with process time. (A) Statistical distributions of peak intensities I_D/I_G . (B) Averaged Raman spectra normalised to the G peak. Measurements correspond to $\Omega = 11500$ rpm impeller condition.	158
4.13	Forecasting graphene production yields and particle surface area using the PBM. (a) The PBM is extrapolated to $t \rightarrow \infty$ to view the extents of production. The lowest speed was fitted only to the LD measurement even though there was very little to no breakup, as there was no measurable increase in nanomaterial concentration (represented as a dashed line). (b) NMR measurements are compared to the PBM predicted surface area ($\Omega = 11500$ rpm). Two predictions are used, based on x_v (volume based diameter), spherical surface area $\approx x_v^2$ and accounting for the rough surface area $\approx x_v^{2.3}$	159
4.14	Particle velocity within the liquid exfoliation system using a glass bead tracer. (A) Mean particle velocity with impeller speed. Errorbars indicate one standard deviation in particle velocity, and inset figure shows the non-dimensionalised particle speed, u^* , from Eq. 4.3. (B-F) Flow fields while operating at differing impeller speeds (reconstructed as an averaged axisymmetric slice).	161
4.15	Graphite particle hydrodynamics within the liquid exfoliation system. Particle-particle shear rate fields at the lowest rotor speed (1500 rpm) for (A) graphite and (B) glass. (C) Scaling of the 90th and 50th percentile particle-particle shear rate with impeller speed. (D) The percentage of time a particle spends under the influence of different minimum shear rates. Dashed line represents the point at which nanomaterial production is first observed.	163

4.16	Compartmental analysis of the mixer system. Part (A) gives a visual description of the two compartments. Compartment 1 is defined as $r < 34$; mm, $y < 40$; mm, with compartment 2 adjoining the rest of the mixer. In (B), t_r is determined for all speeds for a glass tracer, and plotted against a scaling of $t_r \sim \Omega^{-0.65}$	164
A.1	Numerical methods compared to the base analytical truth according to Ziff and McGrady [5]. Zero time is indicated in the dotted blue line, with subsequent times in different colours. Though the maximum error is less when using a number-based solution (2%), a fractional solution is more accurate at the lowest sizes.	176
A.2	Direct comparison between models tracking number and fraction at a cutoff value of $S = 1.6 \mu\text{m}$, against few-layer graphene yield measurements. All data fitted to 11500 rpm speed.	177
B.1	Yield against a non-dimensional argument. From top left to bottom right, the works of Pérez-Álvarez, Brown, and Stafford [3], Varrla et al. [6], Pérez-Álvarez, Davies, and Stafford [2], Paton et al. [7], Varrla et al. [8] and Arao et al. [9] are digitised from their original sources. Surfactant concentration is indicated with @ where pertinent.	191
B.2	Yield against the best fitting argument. From top left to bottom right, the works of Pérez-Álvarez, Brown, and Stafford [3], Varrla et al. [6], Pérez-Álvarez, Davies, and Stafford [2], Paton et al. [7], Varrla et al. [8] and Arao et al. [9] are digitised from their original sources, subject to information provided by their authors to recreate them here. Surfactant concentration is indicated with @ where pertinent.	192

- B.3 Dispersed graphene concentration in NMP as a function of mixing time. These dispersions were prepared with $V=1500$ mL, $N=4500$ rpm and $D=32$ mm for a range of values of C_i . B) Histogram of all measured values of τ with the mean value of 0.66 shown. Reprint, with permission from Paton et al. [7]. . . 194

List of Tables

1.1	Operating cost values from literature ($\text{€}/\text{m}^3$), with stated prices adjusted for inflation.	13
1.2	A range of nanosheet photocatalysts and composites, their production methods, and application in water treatment.	21
2.1	A comparison of current commercial blender offerings and some of this works' modified alternatives.	64
2.2	A comparison of current commercial triac modules from several sources, their prices, and a brief note on their suitability in general.	69
4.1	Summary of coefficients in the PBM and their respective effects on bulk and nanomaterial predictions. In most cases the coefficients have similar effects, making it difficult to distinguish their individual contributions when fitting. .	148
B.1	Table of empirically derived exponents for various shear mixer devices, from multiple sources. Orange text indicates that surfactant conditions were not constant across all fits. g is graphite/graphene, \downarrow indicates the data was replicated and fitted using Equation B.4. Highlighted rows indicate that not enough information is given to replicate the dataset.	186
B.2	Table of empirical exponents for sonication, from multiple sources. g indicates graphite/graphene. Arao and Kubouchi [10] do exceptional work, varying volume from the tens of milliliters to the tens of litres.	187

Acronyms

AOP Advanced Oxidation Process

AFM Atomic Force Microscopy

BOM Bill Of Materials

BFGS Broyden–Fletcher–Goldfarb–Shanno

CVD Chemical Vapour Deposition

CPC Compound Parabolic Concentrator

CFD Computational Fluid Dynamics

CB Conduction Band

COF Covalent Organic Framework

CMC Critical Miscelle Concentration

DLS Dynamic Light Scattering

EMI Electro-Magnetic Interference

EC Emerging Contaminant

EDS Energy Dispersive X-ray Spectroscopy

ECA Equaivalent Circle Area

FLG Few-Layer Graphene

FTO Fluorine-doped Tin Oxide

GNP Graphene Nano-Platelet

GO Graphene Oxide

ITO Indium Tin Oxide

ISR Interrupt Service Routine

IPA Isopropyl Alcohol

LD Laser Diffraction

LoR Line of Response

LCC Liquid Cascade Centrifugation

LPE Liquid Phase Exfoliation

MNPC Magnetically Seperable Photocatalyst

MRC Mean Radius Circle

MMM Mixed Matrix Membrane

NP Nanoparticle

NO_x Nitrogen Oxide

NHE Normal Hydrogen Electrode

NMR Nuclear Magnetic Resonance

OSF Open Science Framework

PSD Particle Size Distribution

PC Photocatalyst

PCC	Photocatalytic Coating
PMR	Photocatalytic Membrane Reactor
PRC	Photocatalytic Reaction Chamber
PCS	Photocatalytic System
PTFE	Polytetrafluoroethylene
PBE	Population Balance Equation
PBM	Population Balance Model
PEPT	Positron Emmision Particle Tracking
PID	Proportional Integral Differential
QD	Quantum Dot
rGO	Reduced Graphene Oxide
RCF	Relative Centrifugal Field
SODIS	SOlar water DISinfection
SEM	Scanning Electron Microscopy
SE	Shear Exfoliation
SCR	Silicon Controlled Rectifier
SR	Slurry Reactor
NaC	Sodium Cholate
TRL	Technology Readiness Level
TOC	Total Organic Carbon
TMD	Transitional Metal Dichalcogenide
2DM	Two-Dimensional Material
UV-vis-NIR	UV-Visible-near-Infrared
UV	Ultra-Violet
VB	Valence Band
VLA	Visible Light Active
WHO	World Health Organisation

Structure and Aim

A recurring point in the review presented in Chapter 1 was the need to reduce the barrier for entry for advanced nanosheet-based Photocatalysts (PCs). Larger scale production of these materials would reduce costs (see Section 1.3) for researchers and industry, allowing for a more streamlined approach to analysis and production of PCs. Therefore, helping to *reduce the cost of sustainable nanosheet production while fully characterising the product* will be the aim of this thesis (point 1. of the review conclusion, Section 1.8). One promising method of production identified in this review is Liquid Phase Exfoliation (LPE) in liquids, which has been proven to scale in production unlike other techniques, while maintaining good quality output and being generally applicable to any layered precursor material [7, 11]. Additionally, the ecological impact is greatly reduced in comparison to other methods by exfoliating in green dispersants, thereby addressing sustainability concerns associated with economies of scale.

Crucial to experimentation and continued development, LPE is entirely reproducible in laboratory with minimal, inexpensive equipment that mirrors industry. Chapter 2 discusses the construction of laboratory scale mixers from simple kitchen blenders, and documents the many options available for customisation along with any challenges encountered.

Furthermore, it provides experimental validation of Two-Dimensional Material (2DM) agnostic production of h-BN, graphene and MoS₂, through UV-Visible-near-Infrared (UV-vis-NIR) extinction measurements and Atomic Force Microscopy (AFM). All experiments are conducted in aqueous-surfactant based solutions, as they are a green alternative to more toxic dispersants, and are readily removed in standard wastewater processes (treated with activated carbon). Chapter 3 pivots towards attempting to characterise these materials in operando, with a UV-vis-NIR fibre optic probe fitted into the mixer chamber. Predominantly, this provides valuable insights for creating equipment that can measure material morphology and structure during processing. For example, aqueous-surfactant solutions can present with bubbly, foam-laden flows when exposed to the extreme conditions of LPE processes. These foamy flows are shown to hamper inline measurements, as they interact with light inside the mixer.

Chapter 4 examines the use of population balance modelling to forecast material production under specific operating conditions. In essence, by monitoring changes in the size of the entire population of graphite particles as they undergo breakup provides a basis to model material production of any size fraction, including nanomaterial. Conditions inside the opaque dispersant during exfoliation are also revealed through the use of particle tracking techniques, representing the first time the conditions inside a LPE process have been measured directly. These results reveal the multi-scale dynamics of LPE, and provide an opportunity to optimise and forecast LPE from lab to industrial scales.

1. Introduction and Literature Review

Title of publication	Challenges Surrounding Nanosheets and their Application to Solar-driven Photocatalytic Water Treatment
Paper Information	(2022) Materials Advances 3 (10), 4103-4131

Author Contributions and Affiliations	
Jacob Brown ^a	Review, edits.
Elzahraa A. Elgohary ^b	Review, Table 1.2.
Yasser M. A. Mohamed ^b	Review, Table 1.2.
Hossam A. El Nazer ^b	Review.
Philip Davies ^a	Review.
Jason Stafford ^a	Review, edits, Figures 1.4, 1.8, 1.9, 1.10, 1.13, 1.14.

^a School of Engineering, University of Birmingham, Edgbaston, Birmingham B15 2TT, UK.

^b Photochemistry Department, National Research Center, Dokki, Giza 12622, Egypt.

1.1 Foreword

As communities in arid climates face a water crises, few techniques can effectively clean the heavily polluted water resulting from rapid industrialisation. Photocatalysis, a promising emerging technology, has the potential to treat water using only sunlight. Yet, traditional, inefficient photocatalysts like TiO_2 render the process time-consuming and challenging. Recently, a surge of interest has focused on Visible Light Active (VLA) 2DMs such as MoS_2 and $\text{g-C}_3\text{N}_4$. Additionally, other 2DMs play essential supporting roles as charge carriers in larger composite heterostructures. Graphene fills this role, but this and other materials are unrealised in their potential due to the ineffective synthesis techniques currently available. This chapter introduces the fundamentals of 2DMs, focusing on the synthesis and performance of 2D photocatalysts for water treatment. It explores various top-down production techniques for these materials, addressing the challenges inherent in achieving consistent material quality and scalable production. These insights lay the groundwork for the following chapters, which delve into experimental approaches and models aimed at overcoming obstacles in the synthesis of 2DMs, making them more accessible for photocatalytic water treatment.

Chapter Aims and Objectives

This chapter aims to provide a backdrop for the thesis, introducing the concept of water treatment with advanced photocatalysts, and establishing the critical role that 2DMs, such as graphene (and their composites), play in this and wider applications. Furthermore, this chapter seeks to discuss the methods used for producing 2D photocatalysts by top-down approaches, the limitations of said techniques, alongside the more general challenges barring the adoption of these materials more widely. This aim can be summarised into the following objectives:

- Review scientific advancements in photocatalysis, focusing on the key role of 2DMs in improving photocatalytic efficiency.
- Analyse key synthesis techniques for 2DMs, particularly LPEs, and the technical limitations hindering large-scale production.
- Highlight the potential of photocatalytic water treatment, outlining the practical challenges that dissuade widespread adoption.

1.2 Motivation

Increasing populations, weather extremes and rapid industrialisation with poor regulation has led to a scarcity of clean water sources in many developing countries, rendering them unsuitable even for irrigation [12]. This is especially true in arid, drought-prone climates, where intermediate water sequestration systems like dams and rainwater catchment are less relevant. Egypt's freshwater consumption for example, is much greater than its freshwater production, and with the extra competition for water upstream of the Nile, the crisis here is only set to deepen in the short term [13, 14]. The World Health Organisation (WHO) estimates that although the number of people who have access to water has increased since the millennium, most are drinking from polluted sources, with an estimated three out of every ten people lacking access to clean water [15]. In this vein, it is paramount to develop cost-efficient methods of water treatment, especially for arid climates.

Traditional methods of water treatment often struggle with the diversity of contaminants in such highly polluted waters. Chlorination for example has always been problematic, as it ends up creating even more toxic by-products [16]; other chemical treatments have historically been avoided due to mass-scale unforeseen medical consequences [17]. Traditionally, coagulation or adsorption are used, but by their nature simply concentrate the contaminants which remain after processing [18]. Membrane filtration systems have consistently suffered from complicated issues stemming from the fouling of the membranes and inefficient removal of pollutants [19], leading to increased costs incurred by using progressively smaller meshes from ultra-filtration to reverse-osmosis.

In the context of a small community, SOLar water DISinfection (SODIS) has been touted by the WHO for its passive ability to clean water; where post filtering, it takes 6 hours under less than 50% cloud cover to produce clean drinking water. This process requires

low turbidity water, and kills pathogens owing to a combination of Ultra-Violet (UV) light induced DNA damage, thermal inactivation, and photo-oxidative destruction [20]. Some heavier pollutants such as dyes and metals require excessively long exposure for inactivation, and much more intense treatment for timely remediation.

Part of a set of Advanced Oxidation Processes (AOPs) which accelerate the natural breakdown of difficult to treat Emerging Contaminants (ECs) and other pollutants, photocatalysis uses light to catalyse reactions directly [21] and sterilise environments [22]. From producing ammonia through nitrogen fixation [23], water splitting [24] and reducing greenhouse gases into synthetic fuels [25, 26], photocatalysis has proved to be a successful avenue of research. Conventional renewables can also be used to power high energy light sources for photocatalysis, which can be tailored to suit the activation range of a particular photocatalyst, whilst simultaneously degrading pollutants by direct UV excitation and allowing treatment to continue at night [27]. The primary byproducts of photocatalytic water treatment are CO_2 and H_2O [28]. Notably, hydrogen, a sustainable fuel source, is another byproduct that can be produced in reasonable quantities if the catalyst is optimised [29, 30]. This is beneficial as hydrogen from pollutant degradation is more thermodynamically favourable than from photocatalytic water splitting [29], making use of would be waste products.

Photocatalytic systems offer benefits on many levels, as an inherently clean, low-cost and environmentally friendly solution to many of these problems [31]. The cutting edge of photocatalytic research focuses on novel, VLA PCs, which rely heavily on nanomaterial composites, especially those based on 2DM. Since their application to photocatalysis, it has been difficult to intensify the procedure, as a number of life cycle considerations remain unaddressed [32]:

- **Production** - Particularly towards 2D PCs. They are difficult and expensive to produce which currently make them impractical at scale.

- **Application** - It is not clear what is best practice in applying PCs at scale, especially 2D PCs.
- **Recovery and Reuse** - By virtue of their size, nanomaterials represent an intrinsic difficulty to separate photocatalyst from solute post treatment.

From rooftop to industrial scale setups, solar-driven photocatalysis has the potential to fundamentally change the way water treatment is realised. Figure 1.1 provides a visualisation of areas that would benefit the most from widespread adoption of such a technique. Many Middle-Eastern to northeast African countries are currently experiencing an extremely high strain on their freshwater resources, with Egypt in excess of 1000%. They also experience a high amount of solar radiation, making them a prime candidate for solar photocatalysis.

Clean drinking water is a global problem, which will only come to affect more people. New technologies are essential to keep pace with human and climate developments. The discovery of efficient and generalised methods of preparing, applying and reusing PCs would open the door to this new industry, providing cheap and accessible freshwater to many of the regions which need it the most.

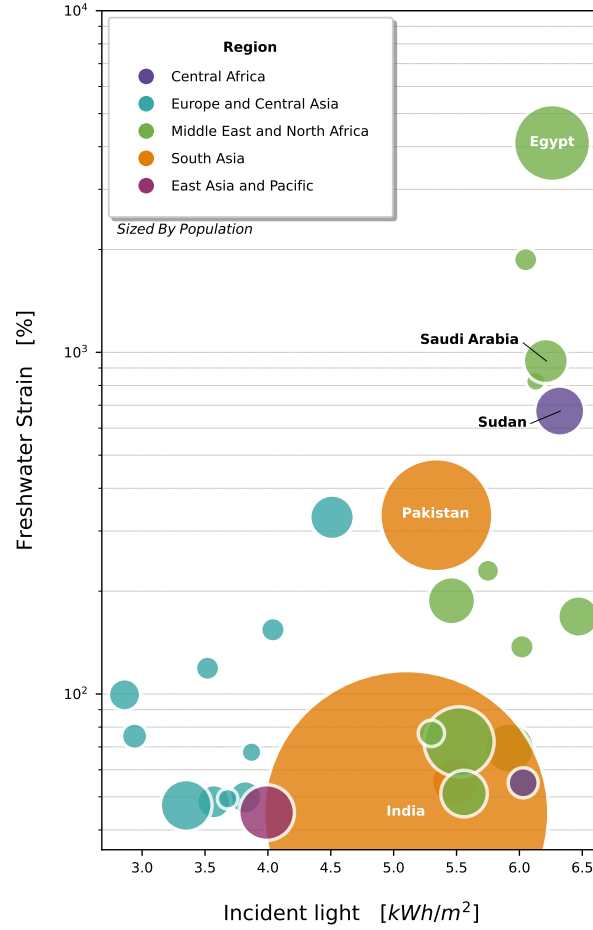


Figure 1.1: Countries of the world, plotted against their strain on freshwater resources [12] and average daily incident light [33]. Bubbles are sized by population, and coloured by economic area denoted by the world bank. Selected countries are all experiencing withdrawals above 40% (high water stress), and have a population >5 million, though data is not available for all countries. Note that withdrawals exceed 100% in a number of countries, which indicates that the local freshwater is being sourced unsustainably (e.g. from aquifers) or heavy use of desalination.

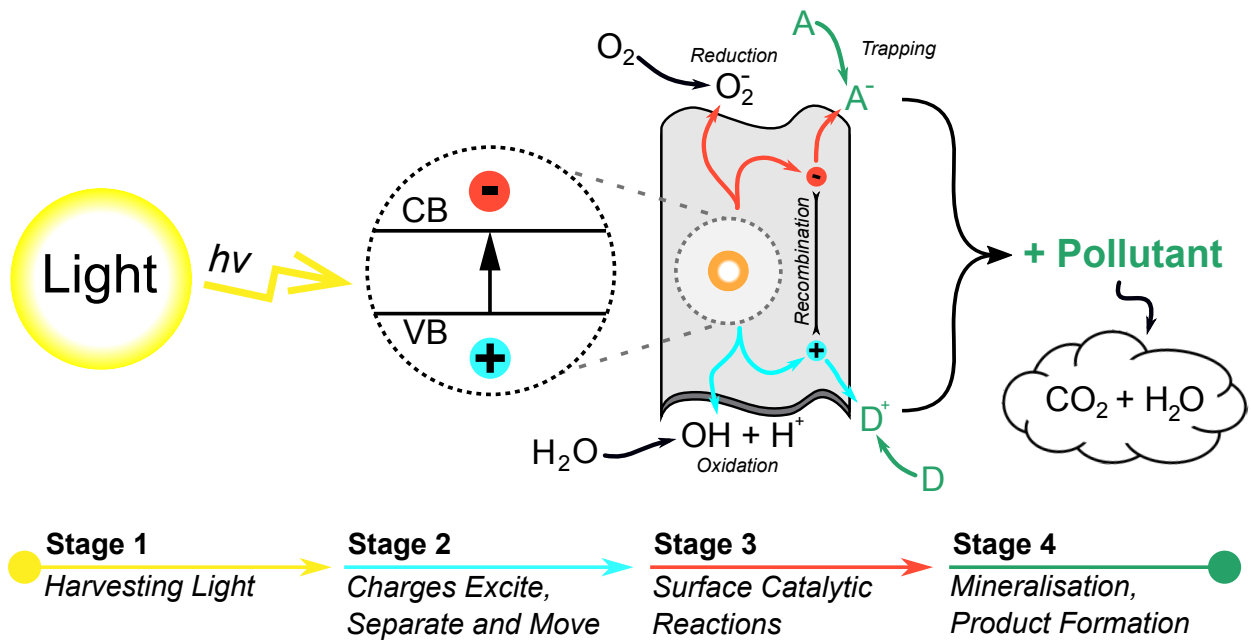


Figure 1.2: A schematic diagram for a heterogenous photocatalytic process over a 2D photocatalyst surface, detailing some of the many reactions that can occur to pollutants through the use of photogenerated charge carriers. (A) and (D) represent the surface adsorbed acceptor and donor species respectively [34].

1.3 Introduction

Since the discovery of the photocatalytic properties of TiO_2 in 1972 [35], photocatalytic materials have garnered attention due to their thermal stability, biocompatibility and sustainability [31]. In the wake of TiO_2 other metallic powders such as WO_3 , ZnO and Bi_2O_3 have all demonstrated the photocatalytic effect to varying degrees [36–39]. TiO_2 has gone on to moderate success as the only commercially available PC (sold under the name P25-degussa), though it has not broken into the water treatment sector due to its low efficiency and difficult recovery.

The general photocatalytic process for semi-conducting materials can be described as follows. An incident photon with energy greater than or equal to the PC’s band gap can excite electrons from the valence band to the conduction band creating an electron-hole pair [40, 41]. This electron-hole pair can interact with adsorbed compounds to directly degrade pollutants, or to generate redox species capable of degrading organic pollutants into CO_2 , water, and mineral acids [42–44]. It is generally agreed that the oxidative $\bullet\text{OH}$ degradation pathway is dominant [44]. The inability to use visible light in legacy bulk PCs stems from the large band gap required for excitation, but even when excited they are invariably inefficient, owing to the tendency of electron-holes to recombine at any point as they migrate to activation sites on the surface of the photocatalyst [45].

Novel developments in nanomaterials with tunable geometries have, however, opened new avenues of experimentation. What is striking about these materials is the diversity of structures they can take, from 0D nanospheres [46, 47] to 1D nanorods/nanotubes [48–51] and 2D nanosheets [52–55]. Regardless of morphology, nano-scale PCs outperform their bulk counterparts in all cases [56]. Of these structures, many behave completely differently in terms of photocatalysis, and 2D nanosheets in particular offer some unique advantages

arising from their structure.

1. They have a large surface area per amount of material, maximising the space available for photocatalytic reactions.
2. Their ultra-thin nature reduces the migration distance for electrons and holes to reach active sites, increasing the efficiency of photocatalytic reactions and reducing the possibility of electron-hole recombination.

Nowadays, there is a large body of research discussing the nanostructure of PCs, and it is clear that these materials offer a much better solution than their bulk counterparts. To give an example, TiO_2 nanosheets show an increase in activity when compared to their bulk phase counterparts, accompanied by a change in their band gap [21]. Li et al. [57] provides a comprehensive review into the design of these 2D based PCs, including many of the different construction strategies for tuning a PC's activity under different wavelengths of light. In the stride to boost catalytic performance, many researchers have taken to doping graphene and other 2DMs using a variety of material sources [58]. Graphene itself is also useful in many other styles of water treatment [59]. Even so, the literature tends to point towards a 2D atomic structure being the main component in the design of future PCs.

In essence, the lack of more widespread use of nanoscale PCs is due to the high synthesis and characterisation cost these materials entail. Take graphene as an example, where 100 g of commercial few-layer graphene costs within the region of € 200 (at the time of writing, 2022). This, coupled with the fact that only 20% of commercial sources consist of true mono to few layered graphene [60] hints at the great difficulty that the synthesis of 2DMs entails. Production intensification and international standards for graphene [61] offer a pathway to a wide range of commercial composites with reliable and remarkably enhanced photocatalytic activity, such is its prevalence within photocatalysis [62]. Importantly, 2D

semi-conductors that support solar-driven photocatalysis (e.g. MoS₂ nanosheets) currently have less commercial focus than graphene-based materials. This impacts on the availability and cost of high quality 2DMs for use in large-scale water treatment.

Table 1.1: Operating cost values from literature (€/m³), with stated prices adjusted for inflation.

Catalyst	Notes	Cost	Ref
TiO ₂ - P25 Slurry Reactor	Measured the destruction of pesticides EPTC, butiphos and γ -lindane beginning at concentrations of 500 μ g/L and ending at their maximum permissible level (0.1 μ g/L), and the four-log inactivation of E. faecalis bacteria. Tested using a 500m ² Compound Parabolic Concentrator (CPC) array with a calculated capacity of 42L/hm ² .	1.1	[63]
TiO ₂ - P25 Slurry Reactor	Measured the complete removal of Emerging Contaminants (ECs), includes a wide variety of compounds such as pharmaceuticals, personal care products, hormones, industrial additives and household chemicals, with most ECs not yet regulated.) and 20% reduction in Total Organic Carbon (TOC) levels. Tested with a 0.25 m ² CPC array at a maximum of 24L/min, in semi-batch operation.	TOC: 2.14 EC: 2.87	[64]
TiO ₂ coated rotating drum reactor	Illuminated by a combination of artificial UV lights and solar radiation. Specific enhancing conditions such as the acidic pH 4 and presence of H ₂ O ₂ at 250 mg/L noted. Measured the removal of 10mg/L Aniline solution in deionised water (100% after 10 minutes), and the removal of TOC (85% after 120 minutes).	0.72	[65]

Table 1.1, provides a summary of a number of different cost estimations for photocatalytic reactors, which demonstrates how much more expensive they are when compared to current methodologies costing near 0.39 €/m³ on average [66], (dependant on the original contamination of the groundwater source). These sources nearly all use the commercial P25-degussa [67], which is non-optimal. The use of more efficient nano-composite

PCs would dramatically improve efficiency; for example, Lee, You, and Park [68] presents a TiO_2 /Graphene heterostructure with a ninefold increase in methylene blue degradation over an hour trial period compared to P25-degussa. Lowering the cost of these materials requires high-throughput methods of synthesis, but this cannot come at the expense of quality, as nanosheet quality is intrinsically linked to its performance. Because of this, both aspects are looked at in parallel in Section 1.5.

Material synthesis is only part of the problem; in reality, the full life cycle of the photocatalyst must be examined, and as suggested before, the issues surrounding the application of these materials are as prevalent. Hence, there has been a push to evaluate the effectiveness of PCs at large scale, beginning with two small pilot plants in Morocco and Spain [69]. These examined a range of different techniques, but centered on employing Compound Parabolic Concentrators (CPCs) to maximise the incident light intensity [70]. Since the turn of the millennium, pilot plants such as these have begun to appear with greater frequency and complexity (complete with 1-2 axes solar tracking), mainly due to funding by the EU through projects such as SOLWATER and AQUACAT [71].

These pilot facilities have invariably used bulk PCs, as opposed to atomic scale materials, and therein circumvent one of the large issues surrounding nano-scale PCs; PC removal/recovery [74]. Separation of a nano-scale photocatalyst implies the post-process is as laborious as some of the aforementioned nano-filtration techniques, if standard methods are used. This suggests that the ideal photocatalytic material must have some thought for its reuse. This could either be intrinsic to the photocatalyst material itself, or through some external implementation. This opens up other methods of application, such as photoelectrocatalysis [75], where the photocatalyst is held within an anode, in contact with the water but not allowed to mix directly. This makes practical sense at a cost to efficiency [76], implying that the ideal implementation is one that looks at photocatalysis as an entire process when designing a PC, thereby ensuring that the material developed covers both efficient and

practical application [77, 78]. A holistic consideration of these trade offs is an essential part of selecting a suitable photocatalytic system.

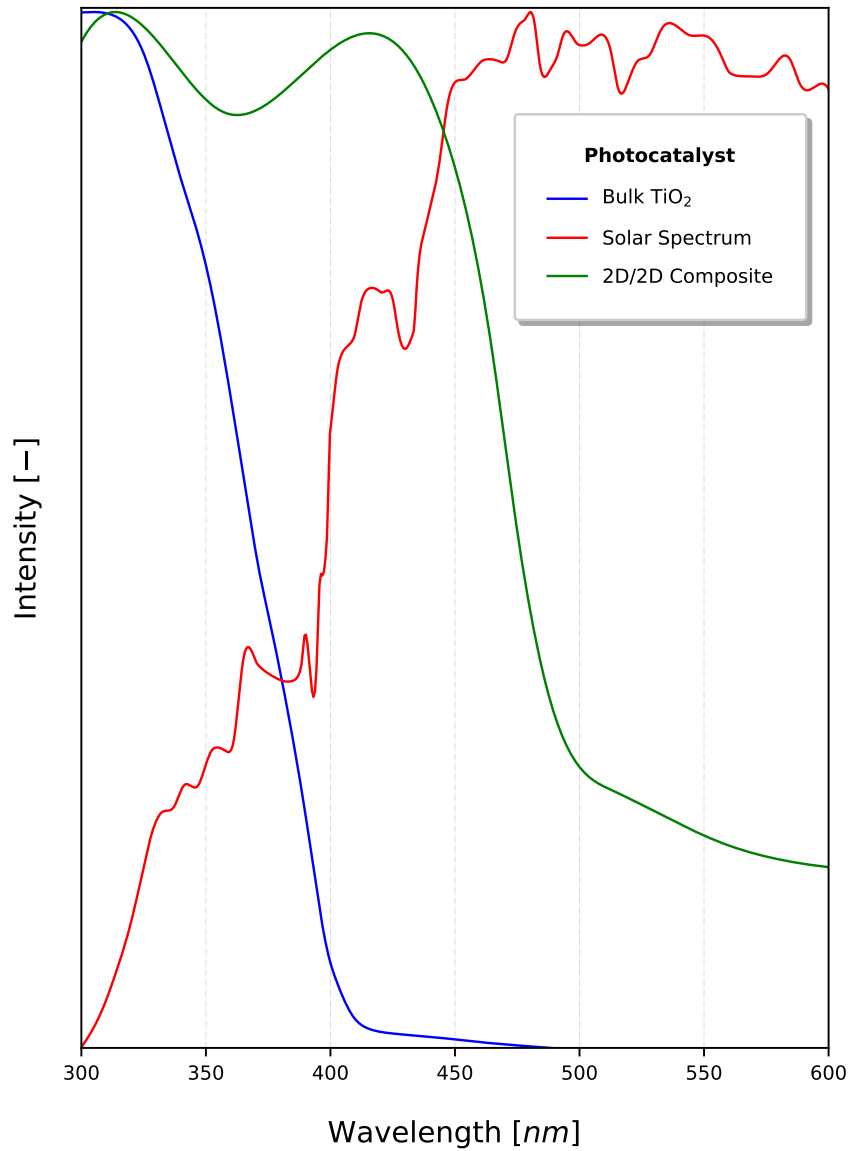


Figure 1.3: Intensity of sunlight (red) in juxtaposition to the photocatalytic activation (normalised) of TiO₂ [69] and a 2D nanocomposite constructed using graphitic carbon nitride (g-C₃N₄) [72]. A total of 46% of the solar energy falls within the visible light range [73].

1.4 2D Photocatalysts

2DMs are traditionally best known for their enhanced mechanical, optical and electrical properties [79, 80]. They have been rising steadily in popularity along with other low-dimensional materials due to their enhanced photocatalytic properties, which have been under investigation even before the discovery of graphene in 2004 [81, 82]. The benefits of nanostructure PCs stem primarily from the enhanced surface area available per amount of material. Though 0D & 1D PCs maximise these properties [83], 2DMs are able to effectively utilise incident sunlight because of their light-scattering properties (Figure 1.3), with the absorption and band gap being dependant on the depth of light penetrated [21, 84]. This also means that the number of atomic layers (or equivalently, the thickness) of these 2DMs is critical to the effective absorption of 2D PCs [85], as shown in Figure 1.4. In this thesis, few-layer material is used as the definition of ‘useful’ yield, following the guidance laid out by other authors [6, 7, 86]. Note that this definition of yield may not correspond to what is optimal for a specific PC, but serves as a point of reference to other works.

The rise in publications shown in Figure 1.5, describes the current prominence of nanosheets within research. Interestingly, most hits for unfiltered patents are false positives, and most simply are patenting a specific material and its method of production. This is slightly disingenuous, as generalised methodologies for the application of photocatalytic substances is prominent throughout patent searches, simply that few target the nano-scale PCs in particular. This principally demonstrates the lag between research and industrial uptake, but also tells of how important the synthesis route is to these PCs, as it effectively determines how the catalyst is to be used and reused.

The range of materials discovered so far only scratches the surface of a variety of naturally occurring materials held together by van der Waals forces [87–89], and with novel

developments in computational pre-screening of materials in terms of photocatalytic activity [90, 91], highly-active PCs can be found at an astonishing rate. The most active of which typically work in conjunction with other PCs in the form of composites [92, 93]. In fact, the search in Figure 1.5 found that one-third of all hits on articles/papers were directly examining functional composites of several different materials to improve photocatalytic activity.

Composites themselves vary dramatically in terms of structure and functionality. On an individual level, the dimensionality of a PC is clearly important (as discussed in Section 1.3), but compositing adds a level of inter-dependency between dissimilar materials which brings dimensionality to the fore [94]. At this point, interfacing between dissimilar materials can critically impact photocatalytic activity, for instance by altering the transfer rate of charge carriers between co-catalysts. 2DMs are again naturally suited to this, as they exhibit a large specific surface area, which gives reason for the rise in 2D/2D (one 2DM layered over another different 2DM) heterostructures [95–97].

As an example, most PCs can be doped with graphene [62] to enhance the separation of charge carriers from the parent PC, and in this regard graphene outperforms other carbon structures [98]. The same study reported the highest activity using 2D/2D titania-graphene nanosheet composites. This demonstrates a type II heterostructure, which due to their differing band gaps promote the movement of charge carriers between the titania and graphene. These types of heterostructures in particular have been rising in prominence because of this charge separating interaction [99, 100].

Though metal oxides have been extensively researched as one of the first consistently active photocatalytic materials, other categories have been found which demonstrate good photocatalytic activity. Transitional Metal Dichalcogenides (TMDs) being the most notable [21, 53, 101], as they exhibit similar or even better absorption of light, with MoS₂ nanosheets having suitable band-gap structure (1.35-1.8 eV [102]) for the absorption of visible light due

to quantum effects [103]. Even graphene, a zero band-gap material that is inactive by itself, can be functionalised by nitrogen doping (and other dopants) to work as a visible light photocatalyst [104, 105]. Functionalised graphene (GO, r-GO) makes up a small portion of a large number of non-metal based PCs. The most prominent non-metal is the polymeric g-C₃N₄ [106, 107], but there are other families of materials such as Covalent Organic Frameworks (COFs). Further materials and composites are presented in Table 1.2. Moreover, linking computational pre-screening techniques for photocatalytic activity [90, 91, 108] with large exploratory studies of layered materials held together by van der Waals forces [87, 89] provides the possibility to find new, exciting materials which have not been synthesized [109].

The morphology of these nanosheets is often as important as the type of photocatalyst itself. In bulk PCs, the crystalline structure affects photocatalytic performance, as demonstrated by the difference in activity between the different crystalline structures of TiO₂ [110, 111]. In 2DMs, oxidising graphene into GO or introducing defects along the edges or basal plane is known to affect the electron mobility of the sheets and indeed their photocatalytic activity [112–115]. Inclusions are commonly introduced during synthesis, and exemplify the importance of maintaining reliable production techniques which are also scalable. The search for scalable synthesis is what first gave rise to GO and its variants, accentuating the great difficulty in creating pristine nanosheets [60]. Thus the synthesis route plays a key role, impacting morphology, defect density, and ultimately, photocatalytic performance [116].

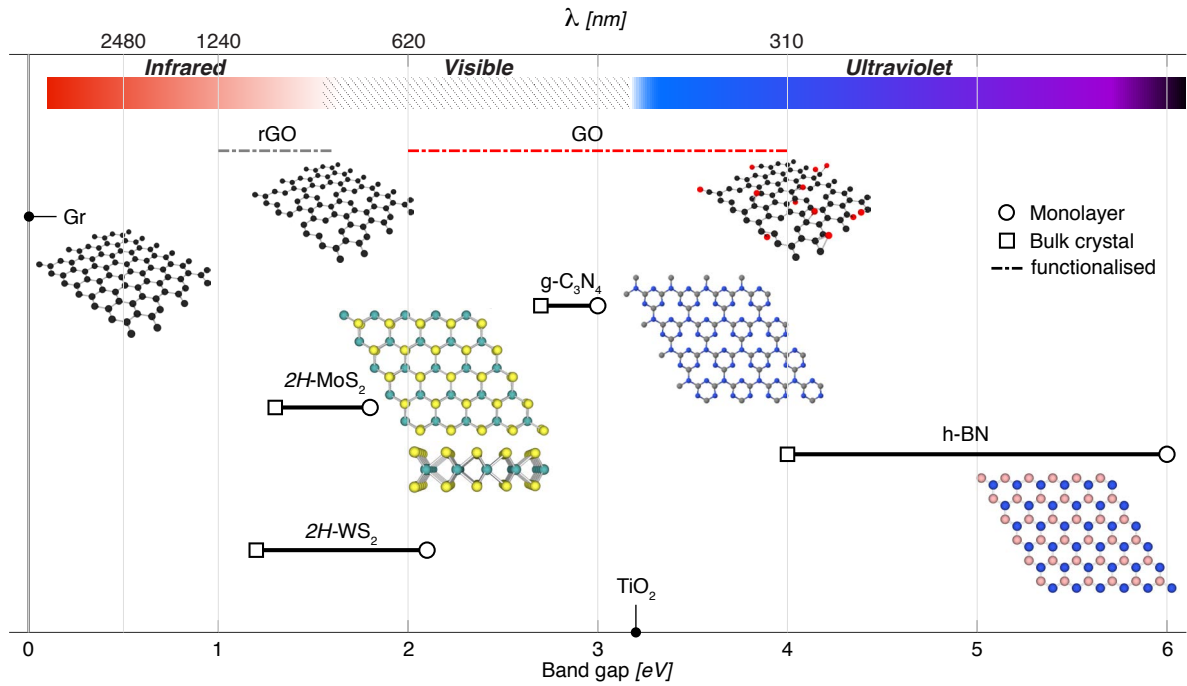


Figure 1.4: Two-Dimensional Materials (2DMs) which have been a focus for photocatalysis research include $g\text{-C}_3\text{N}_4$, transition metal dichalcogenides such as MoS_2 , insulators such as $h\text{-BN}$ for composites, and other graphene-related materials (Gr , $r\text{GO}$ and GO). Apart from graphene, which has a zero band gap, these materials can be exfoliated from their bulk materials to engineer nanosheets with a direct band gap. In the case of $r\text{GO}$ and GO , modifications to the band gap are made possible by removing/adding functional groups. TiO_2 has been included for reference, illustrating the advantages of narrow band gap nanosheets that can target visible wavelengths for solar-driven photocatalysis. For $g\text{-C}_3\text{N}_4$, a triazine structure is shown inset.

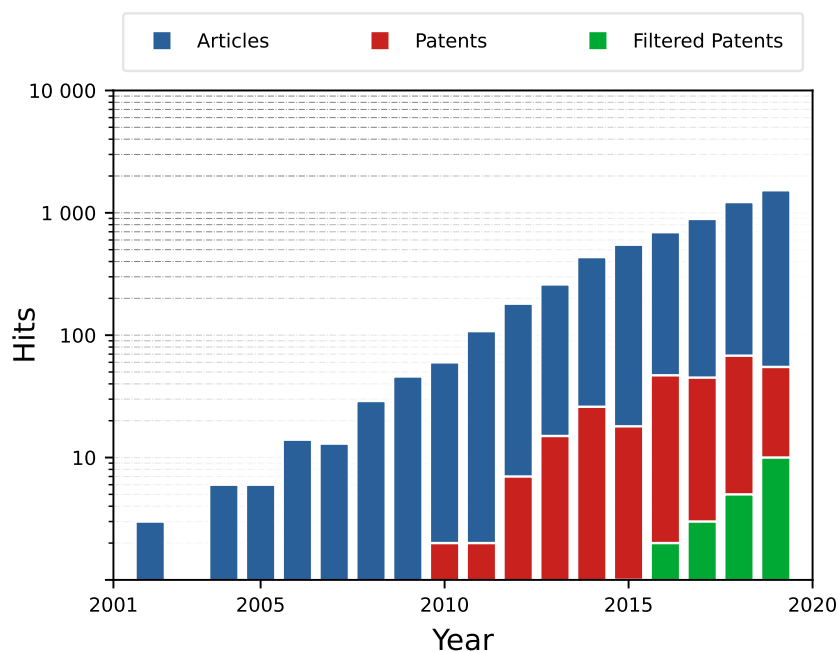


Figure 1.5: Search hits for “*photocatalysis*” and “*2D*” or “*nanosheet*”, filtered or unfiltered for synthesis synonyms (synthesis, construction, preparation). This shows the exponential rise in popularity of 2D PCs (n.b. log scale), particularly in their synthesis. Search terms were applied to the Title and abstract of publications (when creating this figure, 2020 and 2021 figures were yet to stabilise as publications were still under review for release). Data accessed through the Web of Knowledge and the EUs’ Espacenet.

Table 1.2: A range of nanosheet photocatalysts and composites, their production methods, and application in water treatment.

Photocatalyst	Water contaminant	Radiation source	Photocatalytic reaction results	Ref.
Hydrothermal method (HT)				
TiO ₂ -GO	Methylene Blue (MB) [‡]	Visible light, Solar simulator (100 mW/cm ²)	MB concentration fraction after 80 min: 0.20 for TiO ₂ NW-GO 0.56 for TiO ₂ NP-GO	[117]
rGO/Pd/TiO ₂	Rhodamine B (RhB) [‡]	UV light, 400 W mercury lamp	RhB degradation % after 40 min with 0.03 g catalyst and 10 ppm dye initial concentration: 79% for rGO/Pd/TiO ₂ -NPs 90% for rGO/Pd/TiO ₂ -NWs, after 5 cycles photocatalyst was stable with slight decrease in degradation %.	[118]
WO ₃ /rGO	Methylene Blue (MB) [‡]	Visible light, 300 W xenon lamp	83% dye degradation % within 70 min, 20 mg catalyst and 10 mg/L dye.	[119]
Boron-doped TiO ₂ /GO	Bisphenol A (BPA)	Visible light, 300 W xenon lamp	47.66% BPA degradation % after 4 h with GO amount equal to 2% of titania mass.	[120]
ZnO-TiO ₂ /rGO	Methylene Blue (MB) [‡]	UV light, TUV 11W	99.83% MB degradation after 120 min at pH 9 with 40 mg catalyst and 20 mg/L MB.	[121]
WO ₃ /rGO	Rhodamine B (RhB) [‡] Ciprofloxacin (CIP) antibiotic	Visible Light, 300 W metal halide lamp	96% RhB and 90% CIP degradation for WO ₃ /rGO-40 photocatalyst after 120 min with 20 µM pollutant, 20 mg/L catalyst.	[122]
g-C ₃ N ₄	Rhodamine B (RhB) [‡] Tetracycline (TC) antibiotic	Visible light, 300 W xenon lamp	100% RhB degradation rate after 15 min 100% TC degradation rate after 60 min with 20 mg catalyst and 20 mg/L pollutant.	[123]
Solvothermal method (ST)				
Ag/GO/TiO ₂	Paraoxon pesticide	Visible light, 570 W xenon lamp	nanocomposite with 6 wt% Ag and 1 wt% graphene content has the best photocatalytic activity and showed 100% TOC removal after 110 min with 31 mg/L pesticide and 0.2 g/L catalyst.	[124]
g-C ₃ N ₄ Fluorine doped/g-C ₃ N ₄ (F-CNS)	Rhodamine B (RhB) [‡]	Visible light, 500 W xenon lamp	Degradation rate of RhB by F-CNS was 1.6 times that of CNS after 2 h with 30 mg of catalyst, 10 mg/L dye.	[125]

MoS ₂ /CdS	Methylene (MO) ^{‡§}	Orange	Visible light, 350 W xenon lamp	100% MO degradation rate by MoS ₂ /CdS 1-220 (1:1 molar ratio prepared at 220 °C) within 60 min with 30 mg/L dye and 60 mg catalyst.	[126]
MnFe ₂ O ₄ /graphene sand composite (GSC)	Methylene Blue (MB) [‡]		Sunlight irradiation**	100% MB degradation rate after 180 min with 10 mg/L of MB and 0.25 g/L catalyst at pH 7.65 in presence of 5 mL of H ₂ O ₂	[127]
ZnO/GO	Neutral Red (NR) [‡] Crystal Violet (CV) [‡] Congo Red (CR) [‡] Methyl Orange (MO) [‡]		UV-light, 40 W	Dye degradation % with 400 mg/L cata- lyst and 10 ppm dye was: 100% NR after 20 min, 97% CV after 80 min, 68% CR after 150 min, 66% MO after 150 min.	[128, 129]

Self-assembly method

GO/CdS	<i>Escherichia coli</i> (<i>E. coli</i>) <i>Bacillus subtilis</i> (<i>B. subtilis</i>) Acid Orange 7 (AO7) Rhodamine B (RhB) [‡] photoreduction of Cr ⁶⁺		Visible light, solar light simulator (100 mW/cm ²)	100% of both <i>E. coli</i> and <i>B. subtilis</i> were inactivated within 25 min with 5 mg cat- alyst. 80% AO7 and 90% RhB were degraded within 60 min by 20 mg catalyst and 20 mg/L dye. 70% Cr ⁶⁺ was photoreduced after 120 min and 15 mg catalyst.	[130]
γ-Fe ₂ O ₃ /GO	Methylene Blue (MB) [‡]		UV irradiation, 250 W high pressure Hg lamp	100% MB degradation after 80 min with 10 mg of catalyst and 50 mg/L dye.	[131]
SnO ₂ /rGO	Methylene Blue (MB) [‡]		Sunlight Irradiation**, Tiruchirappalli city, August	100% MB disappearance by SnO ₂ : rGO (1:3 ratio) at less than 3 minutes with 20 mg of catalyst and 5ppm MB. Rapid dis- appearance is noted to be due to the effec- tive adsorption properties of SnO ₂ : rGO (1:3).	[132]

Co-precipitation method

Fe ₃ O ₄ /graphene/ sulfur-doped g-C ₃ N ₄ (Fe ₃ O ₄ /GE/SCN)	Ranitidine drug N- nitrosodimethylamine (NDMA)		Visible light, 300 W xenon lamp	100% ranitidine removal and 57.3% re- duction in NDMA formation potential by 20%-Fe ₃ O ₄ /GE/SCN composite after 60 min with 1 g/L catalyst and 2 mg/L pol- lutant initial concentration at pH 7.0	[133]
--	---	--	------------------------------------	---	-------

Chemical vapor deposition (CVD) technique

Graphene	Rhodamine B (RhB) [‡] Janus Green (JG) [‡]	Sunlight irradiation**	Graphene nanosheets (GNS) synthesized from black carbon collected from diesel engine. 98.65% RhB and 96.34% JG degraded by GNS after 120 minutes with 0.90 g /L catalyst and 10 mM dye at pH=6.	[134]
Ag/ReS ₂	<i>Escherichia coli</i> (<i>E. coli</i>)	Visible light [†]	Complete inactivation of <i>E. coli</i> within 30 min by Ag(3)/ReS ₂ with 1.72 mg/L catalyst and 104 CFU/mL <i>E. coli</i> . After 5 consecutive cycles the photocatalytic disinfection performance for the photocatalyst is not reduced.	[135]
Graphene/anatase-TiO ₂ (G/a-TiO ₂)	Methyl Orange (MO) [‡]	UV light, 250 W high-pressure mercury lamp	88% MO degradation rate by bilayer G-60/a-TiO ₂ composite after 40 min with 10 mg catalyst and 12.5 mg/L dye	[136]
Sonication-photo-biosynthesis combined method				
Ag/Au/rGO	Red sea water sample*	Visible light, halogen lamp	An ultra-pure water is obtained with zero micro-organisms (HPC), salts, TDS, and Total hardness at pH=7 after 5 h irradiation with 10 mg catalyst, 100mL red seawater and 120°C. Photocatalyst was stable for 3 cycles.	[137]
Water/oil microemulsion method				
Ag/AgBr/rGO-Si	p-nitrophenol (PNP)	Visible light, 75W halogen lamp	With 1 wt% catalyst and 1 mmol PNP: 95% photoreduction of PNP to p-aminophenol after 20 min. 93% photoreduction of PNP to paracetamol after 8 min with 1 mmol acetic anhydride. 92% photoreduction reached after 3 cycles.	[138]
Ultra-sonication exfoliation method				
Ag-FeCo ₂ O ₄ /rGO	Rhodamine B (RhB) [‡] Benzimidazole	Solar light**	86% RhB degradation rate after 120 min. 54.46% benzimidazole degradation rate after 140 min.	[139]

g-C ₃ N ₄	Rhodamine B (RhB) [‡]	Direct sunlight**, solar radiation on that particular day was 843 ± 2 W/m ² , and temperature was 26°C.	59% RhB degradation rate after 60 min with 5 mg catalyst and 5 mg/L	[116]
High shear mechanical exfoliation method				
MXene (Ti ₃ C ₂)	Methylene Blue (MB) [‡]	Visible light, 300 W [†]	98% MB degradation rate by MXene-Blender (MX-B) nanosheets within 60 min, 2 ppm dye and 1 mg catalyst.	[140]
Electrochemical exfoliation method - followed by hydrothermal treatment				
TiO ₂	Methylene Blue (MB) [‡]	UV, 8 W, Characteristic wavelength = 254 nm	87% MB degradation rate after 20 min with 0.2 g/L catalyst and 5 ppm dye.	[141]
Thermal exfoliation (thermal etching) method				
g-C ₃ N ₄	Rhodamine B (RhB) [‡]	Direct sunlight**, solar radiation on that particular day was 843 ± 2 W/m ² , and temperature was 26°C.	86% RhB degradation rate after 60 min with 5 mg catalyst and 5 mg/L 0.4% photocatalytic activity lost after 4 cycles	[116]

*Red sea water sample containing: 386 ppm Ca, 14,310 ppm Na, 742 ppm Mg, 210 ppm K, 22,219 ppm Cl, 146 ppm HCO₃, 3,115 ppm SO₄, 15 ppm NO₃, HPC >6,500 CFU/ml, 42,840 ppm TDS, 1,320 ppm Total hardness at pH=8.2

**Direct Sunlight irradiation is known to fluctuate with time, in some cases these sources do not specify time, date, or position

[†]Unspecified light source - spectra unknown

[‡]Organic dyes are known to have a sensitisation effect, potentially modifying the light adsorption spectra of a photocatalyst and affecting the apparent degradation [142–144]

[§][sic] Methyl Orange

1.5 Synthesis & Morphology

Each technique used to synthesise nanosheets comes with its own trade-offs. For synthesis, high yields must be balanced with suitable nanosheet quality and morphology, as this has a significant effect on material performance. Large scale production should be developed with this in mind. The benefits of atomically thin PCs are well known [21], but what is less understood is how the introduction of defects to the structure of PCs can increase the photo-activity of nanosheets [145]. Among these defects; pores, vacancies, pits and distortions can all act to impact the viability of the photocatalyst. Defects can be introduced directly through the initial synthesis route or by post-processing stages such as annealing [146–148]. Crucially, both pristine nanosheets and defective nanosheets are required, and many papers fail to fully characterise their findings in this sense [149]. This leaves a gap in research for examining the synthesis of nanosheets for photocatalysis in a practical sense. Synthesis of nanosheets can be divided into two areas:

Top-Down, where nanosheets are extracted through the exfoliation of a natural or synthetic layered material.

Bottom-up, where nanosheets are constructed from base molecules through chemical reactions.

Most methods of synthesis discussed in this section are top-down processes, as they are inherently scalable [7] and many are generally applicable to a wide variety of 2DMs (Table 1.2). Nanosheet synthesis through exfoliation of a precursor material is a primary top-down route, which can be achieved using a number of techniques illustrated in Figure 1.6. Facile synthesis of pristine nanosheets would ultimately lower the cost of manufacture for composite-PCs and allow researchers and practitioners to streamline the production of

their own advanced PCs. Take g-C₃N₄ as an example, with a straightforward synthesis route which can be realised through a number of different methods [150], has led to many papers discussing its excellent photocatalytic properties [151]; however, most use inherently unscalable production processes [11]. The use of appropriate techniques which can move synthesis of nanosheets away from the lab scale and into industry are essential in the long-term.

Importantly, there are many characteristics to consider with varying levels of importance depending on the end-use. Production rate, defects introduced to the nanosheets, power consumption, yield and morphology can be sensitive to the synthesis method and accompanying post-processing operations (e.g. centrifugation settings) [152]. Therefore, a direct comparison of different synthesis routes is non-trivial. To accommodate this, each process subsection has been ranked against each other in Figure 1.7 which separates the issue of production into five sub-topics, in the spirit of Raccichini et al. [153], scored out of a maximum of 3.

S *Scalability*, the quality of a process that can be scaled up, through larger process volumes and concentration.

Y *Yield*, the mass concentration of nanosheets with respect to the initial precursor concentration. Note that a process which is scalable can often be cost-effective even at a low yield through sheer volume.

M *Morphology*, encompasses the shape and thickness of the final product. Products with low number of atomic layers scores highly.

D *Defects*, takes into account the defects present in a material due to the method of production (e.g. basal plane vacancies). A low score indicates a defective nanosheet (which can be beneficial).

C *Cost*, a low cost efficient system (by starting capital and running costs) scores highly in this examination.

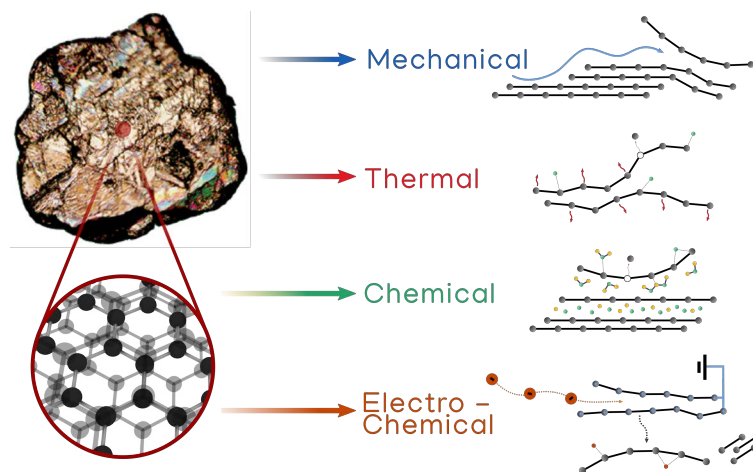


Figure 1.6: Schematic representation of the different exfoliation techniques discussed in this review: Liquid-Phase mechanical, thermal, chemical and electro-chemical exfoliation.

1.5.1 Mechanical Exfoliation in Liquids

Mechanical exfoliation is the process of taking a layered precursor material composed of 2D nanosheets held together by weak van der Waals forces, and breaking it down into its constituent nanosheets through the application of an external mechanical force. Many of the techniques described here involve liquid-phase dispersion routes to exfoliation, and are termed LPE methods. LPE has been seen as a rapid and scalable route to synthesis since soon after the discovery of graphene [155]. It typically requires additional post-processing steps to separate the synthesised nanosheets from the unexfoliated bulk material.

LPE processes disperse layered materials in an appropriate solvent, with the precursor predominantly in the form of microscale particles or flakes. The choice of solvent in suspensions is key, as the dispersion of the nanosheets must match the dispersion of the solvent in order for the solution to be stable and avoid re-aggregation of the sheets [156]. This can be

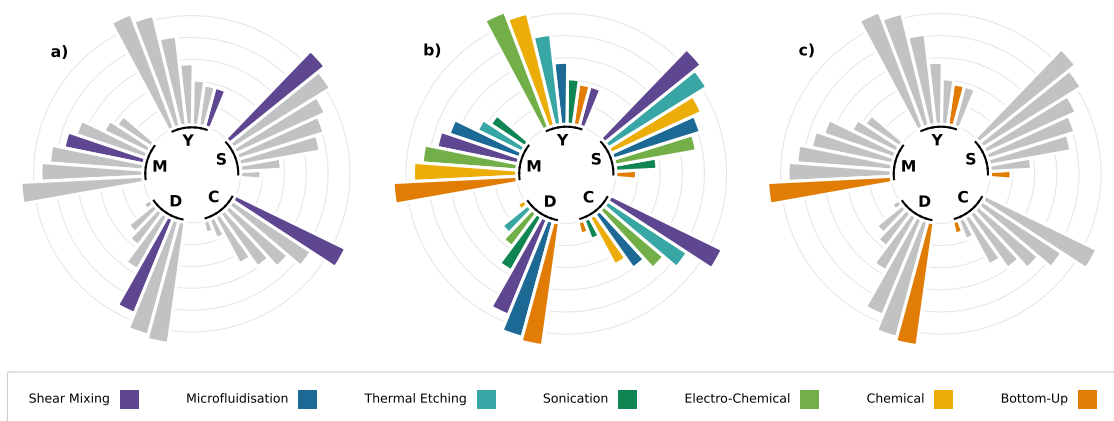


Figure 1.7: Circular barplot of all the synthesis techniques discussed in this section, ranked according to the process parameters of Scalability (S), Yield (Y), Morphology (M), Defects (D) and Cost (C), subplot b). Subplot a) isolates shear mixing, a technique which suffers almost exclusively from its poor yield (typ. $\sim 1 - 10$ wt%). Subplot c) isolates bottom-up methods, in this case Chemical Vapour Deposition (CVD) has been used as an example. CVD can be used to grow different materials on substrates, and is currently the most widespread technique for fabricating pristine monolayered graphene on copper substrates [154].

achieved through traditional solvents (e.g. N-Methyl-2-pyrrolidone, NMP), co-solvents, or the addition of surfactants in aqueous solutions that resist nanosheet restacking by steric or electrostatic repulsion [152]. Furthermore, an adequate choice of solvent can act to enhance exfoliation [157]. For example, the bio-compatible solvent cyrene has been shown to have the same dispersion characteristics as graphene, and methods using this combination are showing greatly improved exfoliation yields than previous attempts with other high-performance toxic solvents (e.g. NMP) [158].

Another aspect to these techniques is that they are generally applicable to all layered materials, and tend to produce defect-free nanosheets compared to other techniques, due to their being a mechanical route to exfoliation. Some defects can be introduced in the process; sonication produces localised regions of high shear rate through the rapid collapse

of microbubbles during cavitation, which although exfoliating, can also begin to produce holes in the nanosheet lattice. Shear mixing also produces high localised shear rates, at a lower magnitude, exfoliating nanosheets without basal plane defects. Microfluidisation can achieve some of the largest shear rates ($> 10^6 \text{ s}^{-1}$) to effectively overcome van der Waals forces but suffers from a high power consumption to instigate turbulent flows in microscale channels. Hence, there can be a number of trade-offs to consider when selecting synthesis strategies for photocatalytic materials that are producible on a large scale.

In this review, we focus on three techniques that are commonly used to produce nanosheets through liquid exfoliation. A variety of other non-oxidising techniques can be found documented elsewhere [152].

Sonication

Sonication has been the de-facto process for creating nanosheets in the lab since its demonstration in 2008 [155]. Its prominence is due to its simplicity, as it often uses readily available lab equipment; namely, bath sonicators and probe sonicators (Figure 1.8). This equipment is typically used to homogenise mixtures, but exposing a bulk precursor to these environments for extended periods of time induces exfoliation of its constituent nanosheets [159]. The exfoliation of the precursor is caused by ultrasonic waves emanated by the sonicator, the mechanics of which were not fully understood until recently [160]. As sonication is a predominantly physical route to exfoliation, it works with a wide variety of layered materials.

Sonication suffers from difficulties surrounding scalability, as the rate of production does not scale well with increasing volume [6]. A peak in nanosheet production has been observed depending on concentration and volume used [161–163], which is a difficulty for large scale production of nanosheets. Large sonicating probes are available industrially, but are prohibitively expensive, and can require the implementation of batch-type processes.

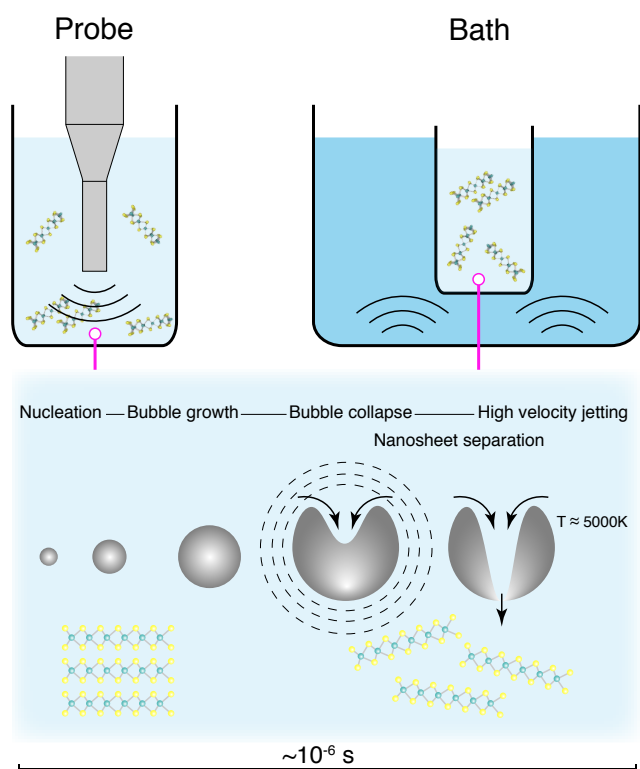


Figure 1.8: Sonication-based synthesis typically involves either probe or bath techniques. Exfoliation of layered materials into nanosheets is achieved through the rapid growth and collapse of cavitation bubbles in the liquid dispersion.

Sonication can also cause defects within the exfoliated nanosheets, such as holes within the basal plane, but it is not clear yet whether this is to do with extended exposure to a high shear environment [86, 164].

Microfluidisation

Microfluidisation for LPE is a relatively recent method, and was first demonstrated in 2017 [11, 165]. The process involves pumping a precursor/liquid mixture through a series of microfluidic channels, where the extreme shear forces within the channels (which include bends, tight turns, localised flow impingement and wall jets [166] that induce high shear

stresses) exfoliates the precursor (Figure 1.9). The equipment required for this type of method is relatively common, as similar machines are used in the pharmaceutical industry for homogenising mixtures. The key difference is that exfoliation requires a longer exposure to the shear within microfluidic devices, which in practical terms means more passes through the same reactor or a longer reactor.

The method has demonstrated complete conversion of graphite into micro/nano-platelets with thicknesses up to 70-200 nm [11]. However, the yield of few-layer graphene with average number of atomic layers less than 10 has been found to be typical of other high-performance shear exfoliation techniques at around 3% [165]. Other critical examinations of this methodology are required to address some of the practicalities for scale-up.

The microscale channels are often similar dimensions to the particle precursor ($\sim 10 - 100\mu\text{m}$), and can agglomerate within the small channels leading to clogging. Blockages in these systems can clearly be laborious to halt and clean. High shear stresses within the reactor result in viscous heating and large increases in temperature within the microfluidic device. Both high pumping power and cooling contribute to the total power required for operation when considering process efficiency. These items may be seen as minor or secondary issues in low volume laboratory or pilot synthesis. Extending the approach to high-throughput operation and varied starting materials, however, and batch failures, product variability, process down-time and energy use become important factors for material quality and cost.

Shear Mixing

Shear mixing concerns the set of LPE processes that focus on applying a shear force to the liquid-precursor mixture, above a critical shear rate for exfoliation, such as $\dot{\gamma} > 1 \times 10^4 \text{ s}^{-1}$ for graphene and $\dot{\gamma} > 3 \times 10^4 \text{ s}^{-1}$ for semi-conductors MoS_2 and WS_2 [7, 167]. This kind of setup

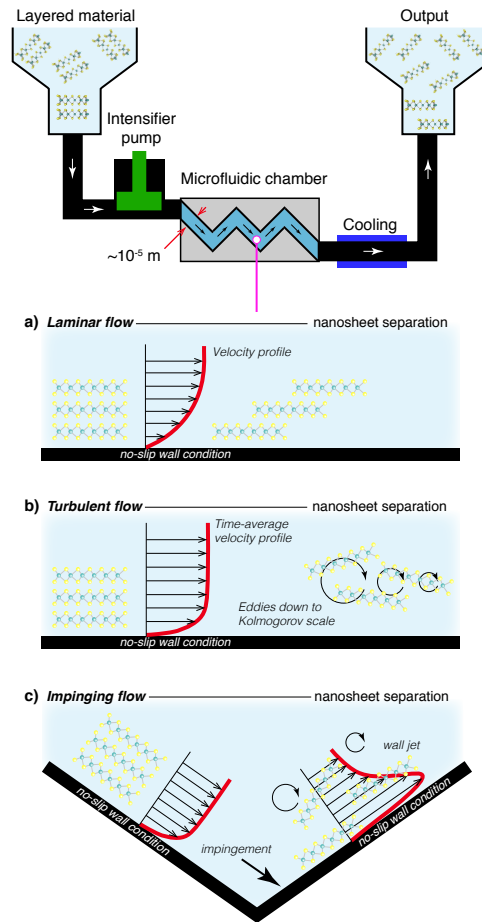


Figure 1.9: Microfluidisation of nanosheets from layered materials. The synthesis mechanisms depend on the hydrodynamic regime and chamber configuration. Production of nanosheets can be achieved through a) Laminar or viscous shear exfoliation, b) Turbulent shear exfoliation and/or c) localised flow impingement.

is inherently scalable and much of the technology is already widely used in large scale batch mixers, or even in small scale kitchen blenders [6]. These systems are however not optimised for nanosheet synthesis, and a purpose built system could reduce energy consumption and ensure a more homogeneous distribution of shearing forces within the mixture. Current high shear mixing designs focus on localised shear using batch homogenisers [7], such as the rotor-stator arrangement illustrated in Figure 1.10. This requires further process optimisation, either through targeted computational fluid dynamics studies [168] or through repeated

design iterations. Nonetheless, the groundwork is there for a successful process which would work on multiple materials and have minimal impact on quality or defects.

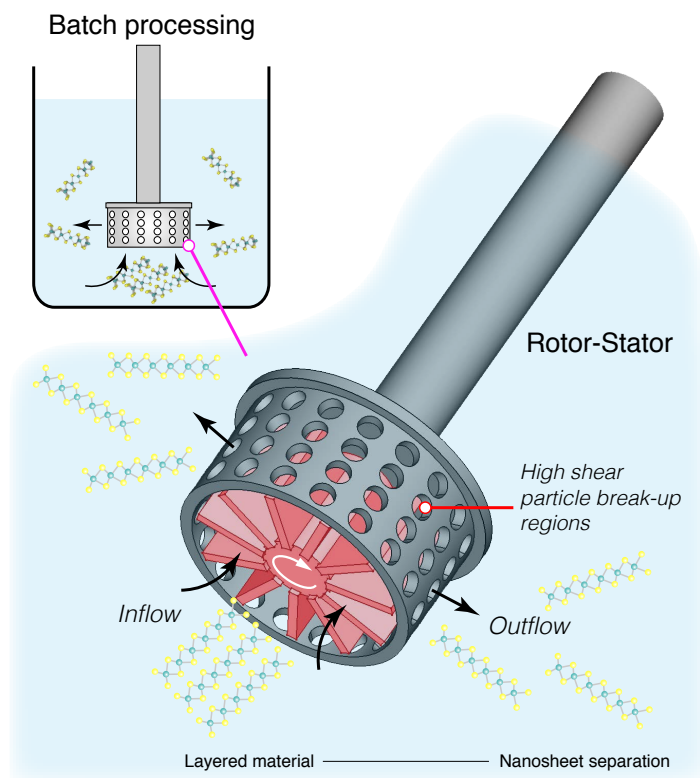


Figure 1.10: Synthesis of nanosheets using high shear mixing. Exfoliation and precursor particle break-up predominantly occur in the rotor (red) and stator region of these devices where collisions and the largest shear stresses in the batch volume exist.

1.5.2 Thermal Exfoliation

Thermal exfoliation consists of exposing a precursor, or a suspended precursor mixture to high temperatures (≈ 500 °C depending on the material). The variations on this method are illustrated in Figure 1.11 for the synthesis of g-C₃N₄ nanosheets. The first example exposes a bulk material containing an intercalant to high temperatures which lead to the decomposition of layers in the lattice through the release of gases. This also promotes the formation of pores in the basal plane that can increase surface area for photocatalysis

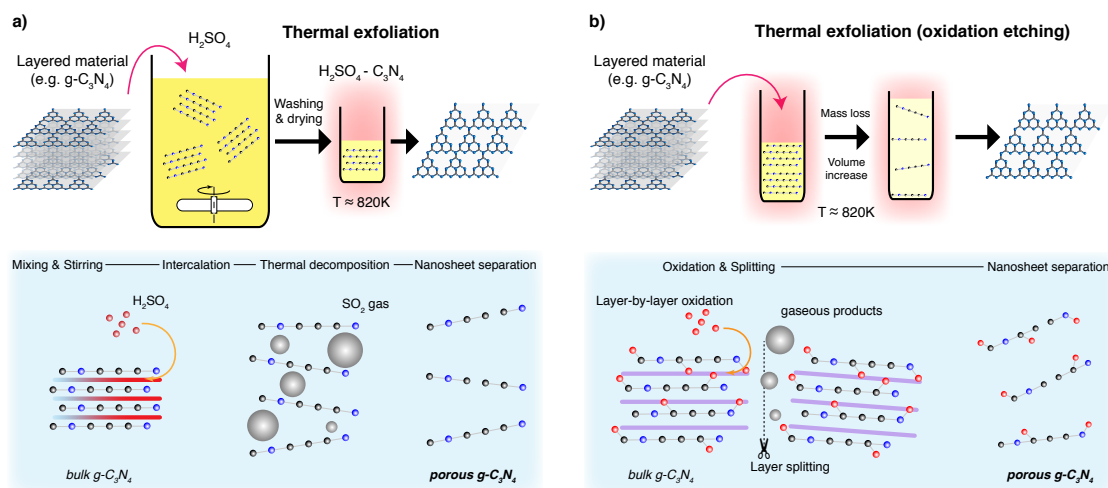


Figure 1.11: Synthesis of nanosheets using thermal exfoliation can be achieved through a variation of thermal treatment approaches. a) Intercalation of H₂SO₄ between layers leads to the formation of gas bubbles during the heating and thermal decomposition step, leading to the separation of nanosheets. b) Thermal decomposition in air leads to layer-by-layer oxidation and layer splitting processes with gaseous products released. Fragmentation of nanosheets, together with the formation of pores and defects, also occur using these approaches.

[169]. The second example exposes a bulk material to high temperatures in air, driving layer-by-layer oxidation, together with layer splitting and large volumes of gaseous product release [170]. This exfoliates and thins layered precursors, as well as leading to particle fragmentation and pore formation. For both synthesis routes, the precursor is usually dry, and can be exposed to an inert environment in some cases to avoid doping the nanosheets with oxygen. When applied to 2DMs, the process shown in Figure 1.11b is sometimes labeled thermal etching, which is indicative of a much more targeted application of heat; though this is rarely the case in practical use and is more aptly termed thermal annealing.

This basic methodology is widely known to create defective nanosheets with vacancies (see Figure 1.12), inclusions and even large holes [171]. Depending on the purpose, this type

of synthesis can have beneficial effects on the performance of the photocatalyst [116]. This approach is most prominently used in conjunction with $\text{g-C}_3\text{N}_4$, where it has been proven as a highly effective photocatalyst [172]. In contrast, thermal annealing of graphite produces highly defective graphene, which does not perform well as a charge carrier, but can be used as a photocatalyst in its own right.

A system like this is inherently scalable, and may provide a reasonable yield, though the quality and defectiveness of the nanosheets produced is not always adequate. Although these defects are easy to introduce, it is significantly challenging to remedy with post-processing. Therein, this method of synthesis is applicable to a few specific cases, and should be treated as a purpose-dependant method of synthesis.

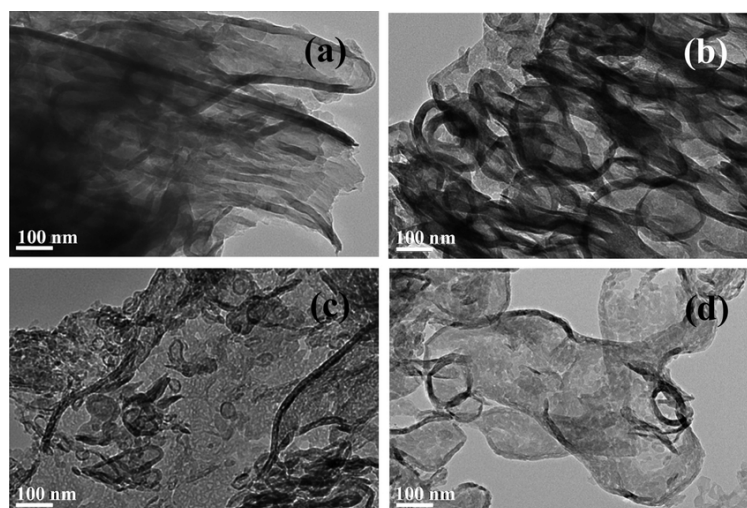


Figure 1.12: TEM images of bulk $\text{g-C}_3\text{N}_4$ (a), alongside porous $\text{g-C}_3\text{N}_4$ exfoliated at 450°C (b), 500°C (c), 550°C (d). The heat decomposes certain areas of the nanosheets, leaving the resultant sheets ranging from slightly exfoliated and porous to fully exfoliated and with large holes. Reproduced with permission from Ref. [170]. Copyright 2015 Elsevier B.V.

1.5.3 Intercalation

Non-mechanical routes to exfoliation typically involve chemically intercalating foreign molecules or atoms in between the layers of the crystal to exfoliate the precursor directly, or to assist mechanical exfoliation. These routes often oxidise, to an even higher degree than that of thermal exfoliation. Non-oxidising routes to exfoliation can be preferred to oxidising routes, as the introduction of new defects is much easier than the removal of pre-existing defects. Intercalation is oxidising, as it is unavoidable that some of the intercalated ions adhere to the nanosheets after exfoliation. Intercalation alone can also leave small parts of the precursor material untouched, and therefore it is usually complimented in the literature with some form of mechanical exfoliation to assist the decomposition of these leftover unexfoliated materials.

Electrochemical exfoliation

Many layered materials are conductive or semi-conductive, and this property permits some 2D nanosheets to be synthesized through electrochemical interactions (Figure 1.13). In practice, these methods resemble electrolytic reactions, with the cathode being replaced with a raw precursor ore (such as graphite); when a voltage is applied across the electrodes, charged ions permeate the precursor and break it apart. For highly conductive materials such as graphene, this method has been proven to be a facile method to create GO [173]. Certain photocatalytic nanosheets can also be fabricated in a similar way [174], though conductance does limit the range of materials which can be synthesised. This method of synthesis has rarely been explored for manufacturing 2D-PCs, but not because of the conductive threshold. Typically, there exists more proven routes to synthesis (such as sonication or thermal annealing) and therefore the potential of electrochemical processes has not yet been fully explored, even though a variety of PCs such as MoS_2 , WS_2 and $\text{g-C}_3\text{N}_4$ have been synthe-

sised [175]. The production rate is favourable in comparison to other methods, and the level of oxidation can be tailored, in some instances, by adjusting the applied voltage difference between electrodes.

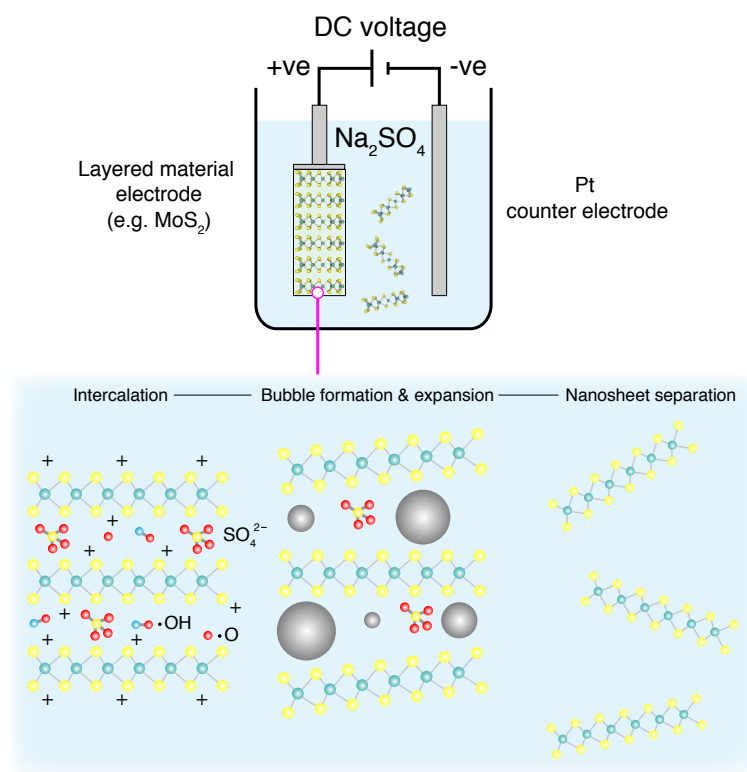


Figure 1.13: Synthesis of nanosheets using electrochemical exfoliation. Intercalation of radicals and anions between layers leads to the formation of gas bubbles and separation of nanosheets. Oxidation of nanosheets can occur depending on the applied voltage, electrode configuration and other experimental conditions.

As highlighted, defective PCs can be advantageous, therein, this technique does seem to offer a scalable route to production for many suitable photocatalytic materials. However, many of these bulk materials range in conductivity, indicating that some of the potential difference applied to the electrodes will be spent overcoming the internal resistance of such a system. This can be mitigated by the use of a conducting additive such as Li⁺, but this complicates the process [174]. Furthermore, the product is not strictly composed of mono-

or few-layers, but can contain stacked unexfoliated precursor particles which break off and subsequently cannot be exfoliated further due to their distance to the electrodes.

Chemical exfoliation

Chemical exfoliation requires enough time for a chemical solution to intercalate between layers before applying a chemical reactant to break apart the van der Waals forces, separating the layers (Figure 1.14). A number of PCs, including g-C₃N₄, can be manufactured by exposure to concentrated sulfuric acid and a subsequent exothermic reaction with water [176]. This kind of process is far more toxic and laborious than other more simple methods (often taking at least 4-5 hours), and ends up producing much more defective nanosheets, improving the photocatalytic properties of synthesised g-C₃N₄ further than those produced by thermal exfoliation [177].

When tailored to graphite, this methodology is known as the modified Hummer's method, and produces highly functionalised GO [178]. The sheets produced are morphologically well-formed large mono- and few-layers, with some pores induced through the exothermic reaction. These sheets require intensive post-processing to form Reduced Graphene Oxide (rGO) nanosheets with a reduced defect quantity. By themselves, functionalised GO sheets can perform as PCs, but do not perform well as charge carriers [179].

1.5.4 Composites

Photocatalytic composites account for approximately one third of the total published research online (when comparing 'synthesis photocat' to 'synthesis photocat composite' on the Web of Knowledge). Of which, half mention the use of TiO₂ while a quarter include graphene (does not include heterostructure synonyms). Both of these materials are excellent

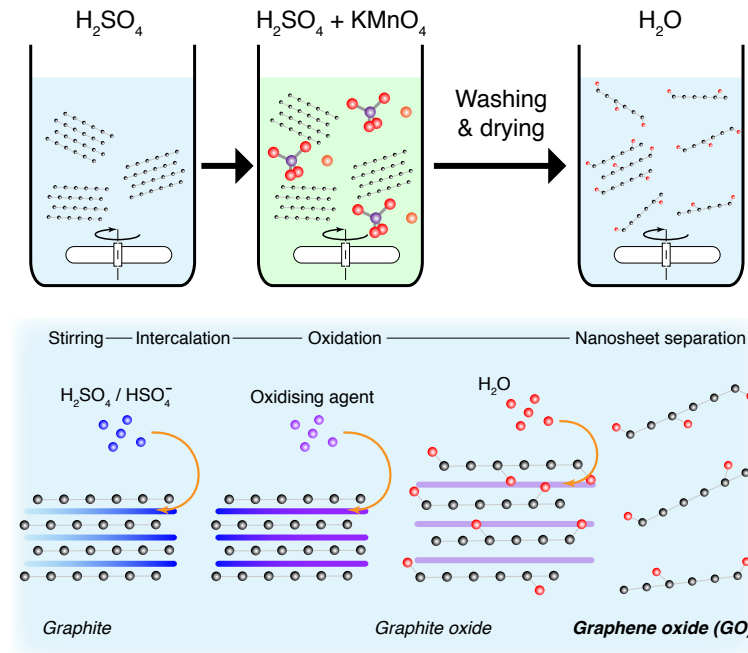


Figure 1.14: Synthesis of graphene oxide nanosheets. Chemical exfoliation is typically achieved using a modified Hummer's method. Graphite is oxidised to form graphite oxide, followed by dispersion and separation of GO nanosheets in water.

supporting materials for VLA PCs, but do not perform well on their own.

Combining charge carriers and dedicated PCs as a composite material provides a route for electron-hole pairs to separate efficiently and react with the surrounding water. Prefabricated nanosheets mixed in solution are essential to all of these methods. In that regard, the methods discussed here are approaches that can further the viability of composites in photocatalysis and enable the intrinsic advantages of nanosheet PCs to be fully exploited.

Hydro/Solvothermal synthesis

In terms of synthesising composite-PCs, just over half of the total studies into synthesising composite photocatalysts included the terms "hydrothermal" or "solvothermal". The preva-

lence of hydro/solvothermal synthesis is due to its simplicity and the variety of composites that can be produced (see Table 1.2). It typically only requires the mixing of disparate materials in solution, then under the application of an external force (heat and pressure), the constituents can be brought close enough to bind or react together (Figure 1.15). Hydrothermal and solvothermal differ only in the reaction medium be it aqueous (hydro-) or solvent (solvo-) based. The conditions required for the process are typically only achievable in an autoclave, though not all hydro/solvothermal processes require extreme temperatures and pressures. Hydro/Solvothermal synthesis can also be used to tune the nanostructure of various nanomaterials and increase their photocatalytic activity [57].

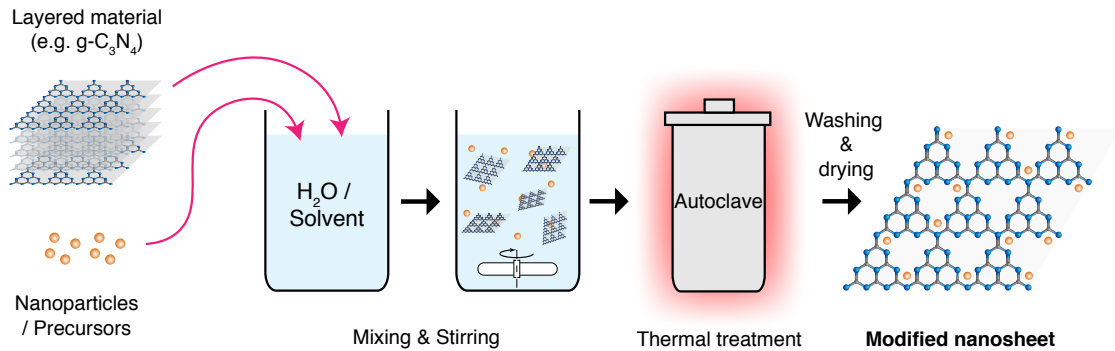


Figure 1.15: Schematic representation of the solvo- or hydrothermal synthesis process for producing nanosheets and nanocomposites.

Hydro/Solvothermal synthesis has been used with great success to apply nanomaterial coatings to nanosheets. Graphene is one of the most prominent materials here, with many inorganic nanocrystals being successfully deposited on its surface, irrespective of its oxidised state. These materials include Metal Oxides, Nitrides and Chalcogenides, among others [180]. These composites can take a variety of shapes and forms as shown in the example in Figure 1.16 for rGO coated TiO₂ nanoparticles [68].

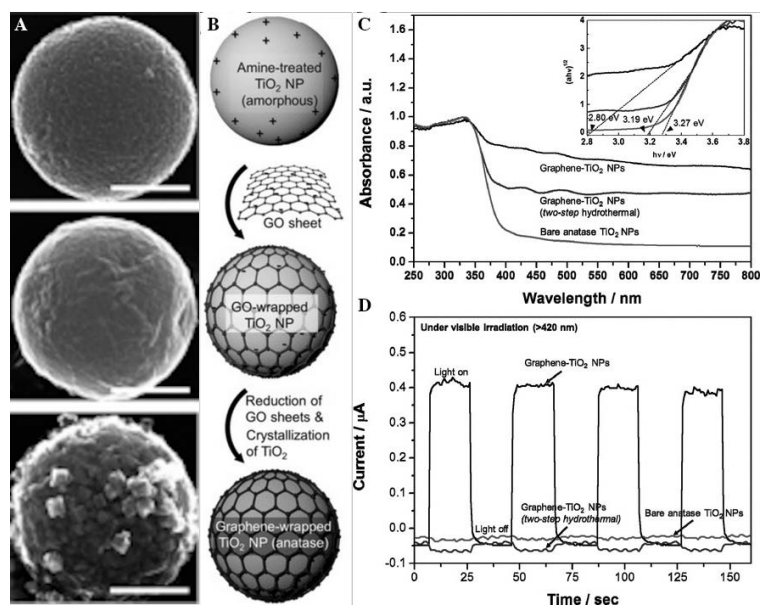


Figure 1.16: An example of a hydrothermal route to composite synthesis, with corresponding SEM images (A) and photocatalytic activity. B) shows a schematic representation of the route, where rGO coated TiO_2 Nanoparticles (NPs) were created through a combination of electrostatic interactions and in-solution mixing, followed by simultaneous hydrothermal reduction of the GO into rGO and crystallisation of the initially amorphous TiO_2 NPs (Graphene- TiO_2 NPs). These NPs were compared to separately crystallised TiO_2 followed by the same electrostatic-assembly and hydrothermal reduction (two-step hydrothermal), and bare anatase NPs, in terms of their photocatalytic (C) and photoelectric activity (D). The scale bars shown in (A) represent 200 nm. Figure adapted from Lee et al. [68]. Reproduced with permission from Ref. [68].

Templated Growth/Assembly

2D nanomaterials can also be used as templates on which a variety of exotic structures can be formed. Porous $\text{g-C}_3\text{N}_4$ nanosheets created through thermal exfoliation can be coated in a secondary co-catalyst or charge carrier nanomaterial to greatly improve its photocatalytic activity. These nanostructures provide abundant surface area and improved light scattering,

with improved mass transfer of pollutants through the structure.

The most commonly templated nanomaterial is again graphene, however these processes are more sensitive to oxidised graphene, meaning that epitaxial growth of nanostructures has only been demonstrated on pristine graphene sheets, manufactured out of solution [151]. Therefore, full epitaxial growth of 2D/2D heterostructures is currently reserved for the lab scale and unsuitable for the large scale synthesis required for photocatalysis. A variety of 2D nanosheets have since been grown on in-solution graphene, including the main classes of photocatalysts discussed here [181]. These nanostructures often have much better adhesion to the templated material, demonstrating a greatly enhanced photocatalytic activity. Templated assembly (self-assembly) defines the materials to be fully formed before combination. These assembly techniques (much like hydro/solvothermal methods) often require some external energy or take advantage of the electrostatic interactions between materials [179].

Other synthesis routes

Though other routes to synthesis have been explored for composites which deposit atomically thin layers of material (e.g. CVD) [182], their suitability for the wide range of photocatalytic water treatment applications is limited. Composite synthesis for photocatalysis should be as scalable an approach as possible, due to the amount of material required for industrialised water treatment. Additionally, the variety of approaches, from immobilised to mobilised, tends to favour the use of general solution processing methods. Thus, simple one-pot methods and self-assembling techniques will mainly be preferred due to their robust and scalable nature.

1.6 Treatment and Reuse

Practicality can drastically affect the way PCs are implemented in large scale treatment operations. The groundwork of such systems is composed of three stages:

- The *treatment* stage, or the application of a photocatalyst to water purification.
- The *separation* or filtration of the photocatalyst from the water.
- The *reuse* and reapplication of the photocatalyst after treatment.

These factors can be highly interwoven depending on approach. Each individual photocatalyst then brings its own pros and cons. Some obvious ones include material activity, ease of synthesis and processing. Other features such as the PCs tendency to aggregate to other particles, or the average size of the photocatalyst, are less obvious. 2DMs are inherently difficult to separate from treated water, as any technique utilising the photocatalyst in suspension must then apply suitable filtration to remove the catalyst from the water. This adds resistance to the flow, and additional treatment stages and complexities, ultimately increasing the running costs to the point where it is unsustainable [183]. Therefore, the larger the photocatalyst, the more trivial the separation and reuse; but any decrease in the surface area of the photocatalyst in contact with the water has a detrimental effect on the photocatalytic activity, and *vice versa*. This interdependence marks most trade-offs and choices for the application of PCs in water treatment. Treatment methods are hence split into two groups depending on how the photocatalyst is allowed to contact the water, e.g. whether it has been *immobilised* on a substrate or whether it is *suspended* within the fluid (or allowed to mix liberally) [184].

1.6.1 Immobilised

Immobilised PC are at first glance the more practical in terms of large scale implementation, with systems trading efficacy (due to reduced active sites in contact with the fluid) for simplified operating procedures, negating the requirement for a recovery stage. In terms of cost scaling, these methods increase in efficiency when scaled [185].

Limited active site availability has been discussed earlier in this review with methods such as heteroatom doping to increase the number of active sites on a 2D photocatalyst introduced. It is also important when considering immobilised photocatalysts that the exposure of active sites be considered. Many immobilisation techniques such as dip coating, immobilisation within a carrier medium, inclusion in a membrane precursor dope, can act to block active sites. Methods to increase the active sites on the basal plane of a material are still of importance, especially when particles are aligned parallel to the deposition surface. When considering immobilised photocatalysts at the 2DM scale, a number of configurations may be possible, owing to the rich variety of ways 2D sheets can be organised onto a plane¹. Depending on the orientation of the sheets, a greater number of the active sites on the catalyst are exposed, or obscured.

Photocatalytic Coatings (PCCs)

PCCs have gained significant attention as a means of air-quality enhancement by abatement of Nitrogen Oxide (NO_x) in urban environments, though there is debate over their effectiveness (sources vary wildly, but it is likely < 2% reduction) [186]. The coatings used vary in the use of suspension medium, porosity, and roughness that the actual effectiveness of the

¹I admire the analogy of playing cards on a table, which can be left to randomly stack on top of each other, spaced evenly in a grid, or balanced on the thin edge (if physics allowed).

PC is obscured. What does stay consistent is the choice of commercial P25-degussa, a now lower performing photocatalyst in a rapidly evolving field. In the sphere of water treatment, PCCs represent a significant section of the research area, with preliminary studies showing that such techniques are realistic and somewhat effective [187–189]. The efficacy of this technique is highly dependant on reactor design, as maximising the mass transfer at the boundary layer is essential for the proper functioning [190, 191], the mathematics of which are described in a comment by Turchi and Ollis [192]. Therein, internal coated structures or extending contact surfaces are essential for maximising the potential mass transfer over the photocatalyst. A benefit of these systems is that they are suitable for continuous and semi-batch processes.

Issues with PCCs stem from their highly reactive nature, which in turn make them sensitive to environmental conditions in terms of mass loss and colour change [193]. Though PCCs remain active and can slightly increase in activity throughout their life as the coating is degraded exposing new active sites [194], the effect of PCCs leaching nanomaterial into water supplies at a large scale would impact water quality downstream and have unknown health effects [195]. At industrial scale, PCCs become difficult to implement as the space required for effective throughput scales poorly compared to suspended methods.

As well as the previously discussed PCCs which immobilise the PC in a carrier medium, such as a paint, PCs can also be coated directly onto a surface. Bayat et al. [196] immobilised MoS₂ nanosheets on Fluorine-doped Tin Oxide (FTO) slides for hydrogen evolution reaction. Using FTO negated the need for a binder material, reducing the potential for mass loss and coating degradation. This approach has the same scalability concerns as previously mentioned and is not applicable in urban spaces such as for remediation of NO_x.

Photocatalytic Membrane Reactors (PMRs)

PMRs in this case refer to those which immobilise PC with a membrane in order to increase the mass transfer over the immobilised photocatalyst. PMRs have been applied at medium to large scales throughout the past decade, with early tests determining that increasing the efficiency of such systems would be essential to their long-term adoption [197]. This could be realised by improving the quality of the photocatalyst; Increasing the surface area exposed to water, by changing the reactor shape/design; and/or improving the suspension medium/mesh. Indeed, these early tests saw a 50% improvement simply by switching the suspension medium.

Zheng et al. [198] provides an exhaustive list of the myriad of factors which can influence their performance, and notes that they have been used with success to treat sewage, pharmaceutical waste and micro pollutants, among others. PMRs can also be readily deployed in many ways as a continuous, semi-batch or batch process. One of the main challenges to this technique is the fouling of the membranes, which can be abated to some extent via good reactor design [199], though efficiency dictates that reactors are designed such that the flow passes through and not along the photocatalytic membrane for optimal performance (aptly named "flow-through" membranes) [200]. Hence, PMRs behave like enhanced PCCs, yet are on the whole more difficult to construct and bring about issues with membrane fouling.

1.6.2 Suspended

Suspending PCs in water provides the highest quantity of active sites to be exposed at all times. The downsides of this method include turbidity in the liquid, caused by pollutants or PCs, and the requirement for an additional processing step to remove PCs from the effluent.

Suspended applications usually require batch processes which can be less advantageous than continuous flow processes.

Magnetically Seperable Photocatalysts (MNPCs)

Magnetically Seperable Photocatalysts (MNPCs) have been experimented with for some time [201, 202], and typically involve the aggregation of a photocatalytically active material onto a larger magnetic particle. This allows for quick separation of the MNPCs while maintaining good contact area with the water. Improved material recovery alone will lower costs, and allow for more exotic constituents (such as noble metals) in a photocatalytic composite for even greater efficiency; however, increasing the life-span also introduces concerns about the photo-stability and photo-corrosion properties of the specific MNPCs [203]. The design of such systems have been proposed [204], and have very recently been applied at scale [205]. These early tests have again confirmed the efficacy of MNPCs, and show that with a small boost in efficiency they would be as effective as traditional toxic techniques utilising H_2O_2 .

There are still some unanswered questions to their function, with competing separator design (magnet orientation, location, attempts to make the process continuous-flow are complex etc.) being one of the smaller concerns [206]. Moreover, the stability of MNPCs is still in question. Although nanosheets themselves offer better chemical and photo-stability than their microscopic counterparts, this is often not well characterised within previous literature reviewing MNPCs. Simply put, many are touted as ‘stable’ over repeated cycles, but with no supporting evidence as to whether this is the case [207]. Macro-ZnO for example, is usually prone to photocorrosion, but is generally stable at the nano-scale. Nonetheless, photostability remains a concern across the board, and as VLA photocatalysis has been demonstrated with MNPCs utilising a wide range of materials [206, 208], this system remains a promising technique.

1.6.3 A Combined Approach

As previously discussed, PCs can either be immobilised onto a solid or porous substrate, immobilised onto a substructure which is then placed in suspension, or simply used in suspension. Substructure immobilisation provides a middle ground, facilitating mixing, recovery and aiding the PC's retention. Some ways in which this approach can be applied are by: immobilising a PC on ceramic beads [209, 210], permeable hydrogel beads [211–213], large inert carriers [208] or cilia-like constructions which are fixed on one end and allowed to move freely [214], or forced to move using an external magnetic field [215]. Most of these systems which immobilise the PC onto a larger suspended particle will require further post processing similarly to a slurry style reactor, however this processing is simplified by the increased size of the PC and thus a coarser filter can be used for separation.

Zeolite has been experimented with for some time as a micro-scale TiO_2 carrier that when agitated within flow, releases TiO_2 which is then free for reactions, but also crucially reabsorbs TiO_2 when left to settle, allowing the TiO_2 to be recovered [216]. These systems may require post-process filtering stages or are challenging to synthesize, but eliminate the need for fine meshes or membranes, which reduces their cost. Leeching is also a problem with these systems, as certain carriers degrade over time (such as the UV degradation of hydrogels [212]), leading to possible contamination of the freshwater output. Unfortunately, these methods, though better than static PCCs, still reduce the number of active sites and are therein less effective than suspended PCs [217].

1.6.4 Photocatalytic Reaction Chambers (PRCs)

Photocatalytic Reaction Chambers (PRCs) in practice vary in design depending on the light source, necessary recovery processes, immobilisation method, and the PC used. A non-

exhaustive list of possible designs could be:

- A sunlight irradiated PRC, using a stirred vessel with internal walls coated in a PCC.
- A lamp driven, actively mixed PRC, which employs a MNPC. MNPCs would typically be used in batch processes, this could imply a high capital cost but would maximise the effectiveness of the photocatalyst.
- A UV-tube lamp surrounded by glass beads with PC immobilised on their surface.
- A sunlight irradiated membrane with PC incorporated into the membrane. Mirrors could be used to concentrate sunlight onto the membrane surface. This could form a continuous flow, modular system.
- A sunlight irradiated tank utilising PC doped hydrogel beads which float and can be skimmed from the surface of the treated water.

Implementation thus dictates the design of the reactor, and its effectiveness [218].



Figure 1.17: One of the first pilot plants for photocatalysis, employing a slurry reactor (in a static concentrator array) installed at latitude 40° (Arganda del Rey, Madrid, Spain). Costing estimates in Table 1.1 for plant scale PCs are taken from this plant's operation[63]. Reproduced with permission from Malato et al. [69].

Suspended PC reactors are much more active than immobilised systems, providing a near threefold improvement in degradation rate over contemporary PCCs [219]. Suspended reactors, often dubbed photocatalytic Slurry Reactor (SR) are the most efficient method of applying PCs, yet operate on the assumption that the PC recovery process occurs elsewhere in the system, effectively separating the challenge of recovery and application. The numerical modelling of such photocatalytic systems can be extremely challenging [220] due to the combined effect of particle-fluid modelling (multi-phase flows) with combined radiation and chemical reaction modelling. Hence, full models examining steady-state PRC operation are largely in their infancy [221].

Moving away from SR, there are a wide variety of PRCs designed to be implemented with PCCs and PMRs. Thin-film PRCs have been examined thoroughly, especially for use with immobilised [222] and suspended [223, 224] PCs. These systems have largely fallen out of favour due to the generally low throughput and inherent drawbacks to immobilised photocatalysts [219]. Moreover, scaling these processes would require increasing footprint area, potentially making this system unfeasible for industry.

1.7 Recommendations for Photocatalysis Research

Throughout this review, the authors have come to several conclusions over what is best practice in the manufacture of photocatalytic composites. Foremost of these is a holistic view for PCs; Treatment, synthesis and recoverability should all be considered in unity when establishing the utility of a PC. This type of PC design is thus termed a Photocatalytic Systems (PCSs) approach (See Figure 1.18). A PCSs view is key for both material synthesis and design, as well as certain recovery techniques, such as MNPCs and PMRs.

Environmental stability is one such factor which is consistently omitted from most

papers, even though longevity and stability have a sizeable bearing on whether the system will be realistically worthwhile. TiO_2 is widely available simply because of this fact, appearing in a large proportion of the literature [21]. As P-25 is still in production, it proves low-cost and simple photocatalysts have their place in the market, but not yet widespread in industry. Putting effort into making a full product, from nanomaterial to device scales, can thus offset a number of hurdles for industrial adoption down the line.

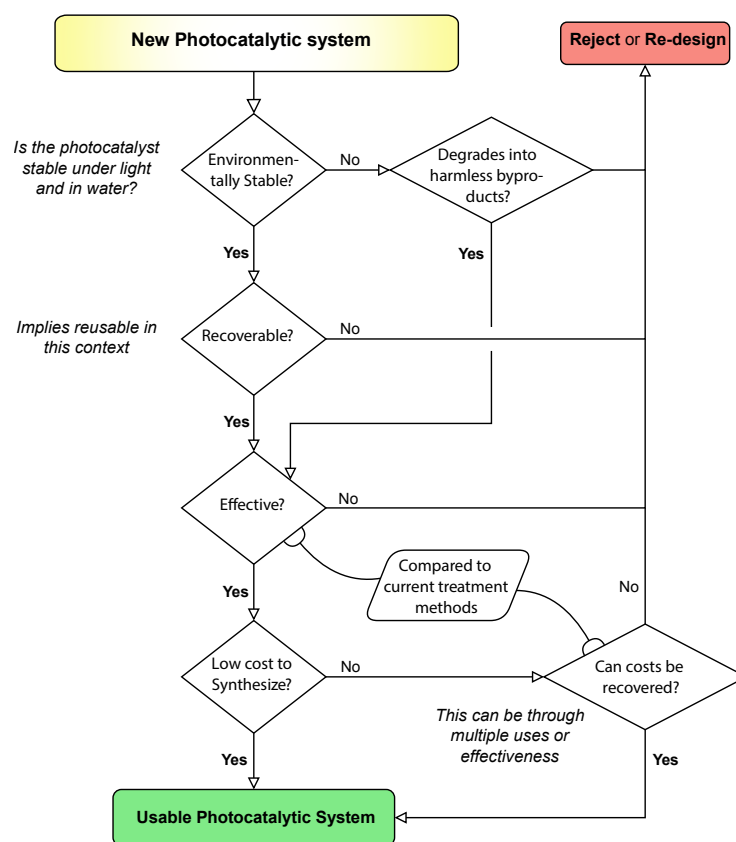


Figure 1.18: The selection process for evaluating a PCS. A systems approach can consist of creating and evaluating a singular ‘system’, or the creation of many modular ‘subsystems’ which can work together to create a usable ‘system’.

A particular concern is an apparent lack of standardisation in solar-driven photocatalytic materials research. This inhibits reproducibility, prevents direct comparisons between materials systems, and ultimately delays the translation of research for large-scale water

treatment. Table 1.2 highlights a sample of publications on photocatalytic materials or systems. In many cases, different model pollutants are used, with many known to have sensitisation effects [144]. There is large variability too in light sources, with a lack of detail in several instances. Additionally, each has different conventions for interpreting and displaying data, and differing time scales for pollutant removal. A common claim in much of the literature is a seemingly enormous % removal of pollutant which upon closer inspection appears to be simply a large % removal via adsorption and then a subsequent, smaller than claimed, photocatalytic degradation of pollutant.

1.8 Conclusions

Nanoscale photocatalyst materials are quintessentially one of many applications within water treatment (incl. nano-adsorbents and membrane nanotechnology, disinfection, sensing) where nanosheets are poised to play a major role in the coming years [183]. Two dimensional PCs in particular are gaining attention due to their increased quantum efficiency, surface area, facile construction of composites and crucially, their visible light active performance. Though the benefits of using 2DMs are well understood, scalable and sustainable routes to synthesis for many of the base 2DMs are lacking. These are required for manufacturing high performing photocatalytic composites at large scales. Most published research and patent-protected developments focus on the final PC, while those that focus on material synthesis struggle to balance high yields with defect-engineered nanosheet production. In most cases, a lack of standardisation for industry to adhere to has resulted in insufficient material quality that stymies progress in many fields using 2DMs, including sustainable photocatalysis. This highlights the critical need for material quality control and assurance methods to support with developments in international standardisation.

For applications in photocatalysis, scaling up production of nanomaterials is key for industrialised water treatment. Top-down methods have provided the primary synthesis for 2D semiconductors, charge carrier materials, and nanocomposites used in photocatalytic pollution remediation research. However, no single synthesis technique can address the breadth of photocatalytic materials possible. This highlights the importance for a variety of synthesis routes to be designed with considerations for sustainable and resource-efficient large-scale production and post-processing.

VLA-PCs are often constructed from a variety of different nanomaterials as composites, and though they are pioneering at the lab scale, they do not account for any systematic

recovery of the composite essential for pilot plants. Development of new materials and composites which can maintain performance and permit easy removal and re-use is key. Even trading a some efficiency for easy separation is a worthwhile trade-off, as the costs incurred separating nanoparticles from water sources are steep. Further materials research is necessary to achieve this balance, though a systems approach to these problems can guide research in the future. Modular approaches to PCs simply do not account for the entire life cycle of the photocatalyst, opting for a narrow view without addressing the factors preventing the adoption of nanosheet PCs.

Throughout this review, the authors have noted a marked difficulty in the comparison between different photocatalytic systems (Table 1.2, Section 1.7). There are no well-defined metrics which allow for direct comparisons between photocatalytic systems such as PCCs, PMRs, PRCs etc. There have been rapid research developments focused on engineering VLA-PCs to achieve high pollution remediation efficiencies. This has grown the library of suitable 2D nanosheets and nanocomposite materials. However, this performance objective has been favoured over basic concerns of manufacture, stability and application, under the assumption that these issues can be addressed later. Due to the intertwined nature of synthesis, photocatalytic performance, application and recovery, more holistic approaches are necessary to engineer 2D photocatalysts for large-scale use. In summary, the main points barring the adoption of nanosheet PCs and others into water treatment are:

1. *Reduce the cost of nanosheet production while fully characterising the product* - Specific nanosheets required for VLA photocatalysts are prohibitively expensive. Lowering costs through production scaling will improve industrial accessibility for nanosheet-derived photocatalysts. This must be combined with accurate descriptions of the average nanosheet size including their length, width and number of layers along with their associated distributions and the typical lattice structure including any

systematic defects present in the final material.

2. ***Approach the design of nanosheet PCs at a systems level*** - Nanosheet PCs are consistently designed without foresight towards their life-cycle. In order for them to be seen as a usable alternative to TiO_2 , nanosheet PCs must be easy to synthesise and separate from inception, with PRCs being designed around their unique properties.
3. ***Clearly state the stability of PC over multiple cycles*** - Most research discussing novel PCs (not exclusive to nanosheet-PC) decline to provide any information on the stability of the PC in question, instead assuming inherent stability due to them being nano-sized. At a minimum, PCs should demonstrate sufficient stability so as to be cost effective with TiO_2 -derived compounds. Standardisation across the research community would support this.
4. ***Create simple, transferable metrics for comparing photocatalytic systems*** - Many PC systems define throughput under differing conditions and metrics. This complicates comparisons between systems, and leaves a gap to derive standardised tests [225] and metrics for photocatalytic water treatment that can then be stated clearly when proposing new photocatalysts.

Nevertheless, solving these issues do not preclude the deployment of industrial water treatment. TiO_2 -derived PCs have historically been much less effective in operation and slightly more expensive to set up when compared to other contemporary light absorption based AOPs (UV/ O_3 , UV/ H_2O_2)[226]. A shift to visible light absorbing, nanosheet-based PCs would close this gap; so long as material manufacture and recovery concerns are addressed.

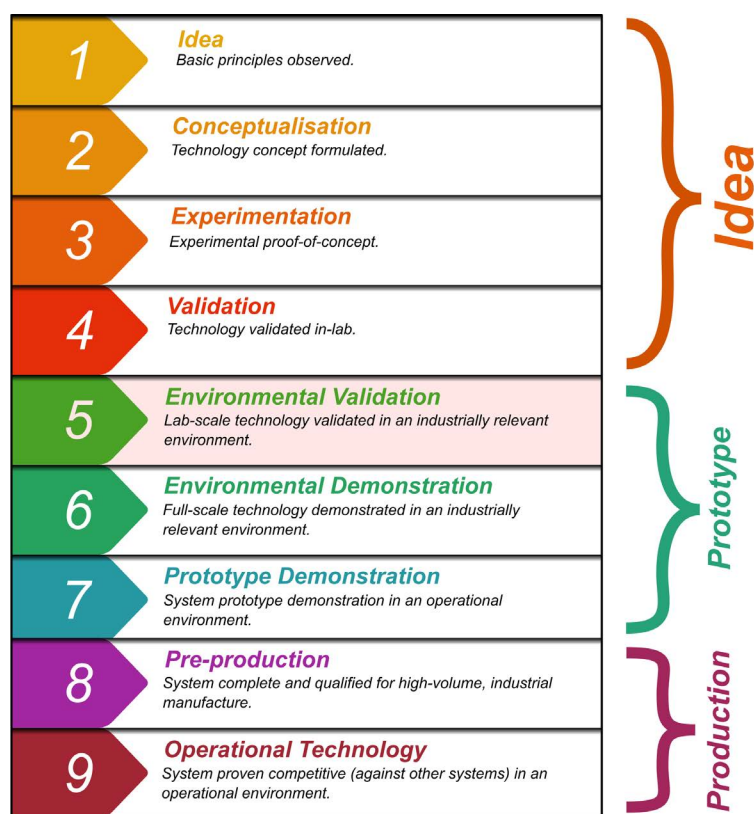


Figure 1.19: Summary of future research focus areas according to Technology Readiness Level (TRL). Topics within TRL 1-4 align with the photocatalytic systems approach presented in Figure 1.18. TRL 5 is highlighted as the prescribed TRL for laboratory research on solar photocatalytic water treatment to successfully transition to the pilot-scale demonstration stage in realistic environments.

Future Research Focus for Photocatalysis

Cost and real-world effectiveness are the primary reasons for the lack of competitive solar-driven photocatalytic systems today. To address these challenges, a number of key research focus areas and their corresponding Technology Readiness Level (TRL) are summarised in Figure 1.19. Topics within TRL 1-5 should be considered holistically and with a systems thinking approach described previously (Figure 1.18). Discovery and development of new photocatalytic materials and composites which are stable, maximise catalytic activity, and

that can be produced on a large scale from abundant precursor sources will improve the cost and sustainability of nanosheet-based solutions. Similarly, scalable synthesis approaches with the ability to engineer material properties for targeted application-specific water treatments will be advantageous.

On top of this, nanomaterial separation post-treatment remains a lasting issue, with some promising leads (MNPCs, membrane technology). Despite the recent work, significant effort is required to address this challenge and create a suite of viable solutions for material recovery and reuse. Nanotechnology advancements, either at the material discovery/synthesis level and/or the larger water treatment system level, are required to create efficient treatment and re-use processes that minimise operational and whole-life costs. A push towards greener treatment methods will be favourable for solar-driven photocatalysis, and with the correct incentives it can be made competitive with other AOPs.

Currently, the TRL for industrial scale photocatalytic water treatment systems is 5, as though some large scale demonstration plants have been made, most research is still focused on the small scale, seeking to push the boundaries of photocatalytic efficiency. Fundamental research efforts should continue, supported by the development of new standards for assessing photocatalytic performance using nanomaterials. This would ensure repeatability and robust performance comparisons between different materials and devices.

The step between lab-scale validation and pilot-scale demonstration (TRL 5 to TRL 6) is non-trivial, however, a systems approach can ultimately lower the risk of a photocatalytic water treatment technology failing to progress beyond TRL 6. Pilot-scale demonstrations are often smaller than the full-scale prototype (TRL 7-9). Proving out the technology at this smaller pilot-scale may also open up other opportunities. Intensifying the passive nature of solar photocatalytic technology lends itself well to small, off-grid water purification strategies. Attempting to force photocatalysis to work at large scales is currently challenging, due

primarily to how inexpensive other methods are in comparison, but also to a lesser extent the large footprint needed for a high-throughput system [227], and the decreased effect they have against complex mixtures of organic pollutants in real wastewater [228]. Therefore, tailoring small scale photocatalytic reactors as air or water purifiers, could be another way to advance the commercialisation of fundamental research from TRL 1-5, allowing businesses to develop the viability of the technology and further strengthening the systems approach to designing nanomaterials for sustainable, solar-driven photocatalytic water treatment.

2. Equipment and Validation

Title of publication	Modification of kitchen blenders into controllable laboratory mixers for mechanochemical synthesis of atomically thin materials
Paper Information	(2023) HardwareX, 16, e00471
Additional Contributors	
Jacob Brown ^a	Review, edits.
Jason Stafford ^a	Review, edits, Contributed Section 2.4.5.
^a School of Engineering, University of Birmingham, Edgbaston, Birmingham B15 2TT, UK.	

2.1 Foreword

A large number of advanced photocatalysts use graphene as a functional component (see Sections 1.4, 1.5.4). To study how production can be scaled for photocatalysis, LPE serves as a simple technique to replicate in lab, and crucial to photocatalysis, LPE can scale to industrial volumes [7]. For applications concerning graphene more widely, it maintains the material quality essential to maintaining graphene’s exceptional optical, mechanical and electrical properties, with the product created through LPE being generally useful for templates, coatings and other structures. A further advantage to LPE methods is that these techniques are entirely material agnostic, and applicable to a wide variety of layered precursor materials far beyond simple graphene.

In this chapter, kitchen blenders are used to deliver shear-driven exfoliation, with a wide range of inexpensive hardware solutions developed that can allow researchers to synthesise 2DMs using a controllable, scalable (scale-out) and sustainable process. Extensive modifications of the blenders were necessary as the onboard electronics lack the experimental controls (temperature, speed, characterisation) for rigorous scientific research and precision synthesis. As the third study produced chronologically, this work built on the incremental developments made on the equipment over the course of three years, focusing on cataloguing the technical considerations, including the many lessons learned over that time. Specific build notes with detailed instructions, cost breakdown and associated files are provided in the Open Science Framework (OSF) repository, [OpenLPE](#) associated with this work.

Chapter Aims and Objectives

The aim of this chapter is to create and validate a readily modifiable laboratory system for the production of graphene through LPE. The adapted equipment, derived from readily available commercial blenders must be a cost-effective platform for graphene synthesis and delivered in a way that is digestible for readers seeking to pursue their own research with the equipment. This aim can be summarised into the following objectives:

- Develop a modified kitchen blender system tailored to enhance laboratory experiments for the exfoliation of graphene. This includes hardware modifications for precise process control, especially speed control, required to keep consistent conditions inside the blender.
- Characterise the performance of the modified blender system and validate the production of different 2DMs using it.
- Deliver the information in a readily accessible format to inspire and support researchers seeking to conduct their own experiments.

2.2 Introduction

Owing to their remarkable optical, mechanical and electrical properties over bulk counterparts [229], nanosheets have shown immense promise in numerous applications from photocatalysis, energy storage and generation to wearable healthcare technologies [230]. Although these exciting materials have the potential to transform future technologies, they are challenging to synthesize using sustainable routes that avoid harsh chemicals and toxic solvents. It is also expensive to purchase research-grade materials for scientific investigations (1 g of “Graphene” at the time of writing [2023] retails for [£800](#)). To compound this issue, graphene, being the most commercially mature and readily available 2DM, represents the lowest price currently available. The majority of the many other 2DMs (e.g., semi-conductors and insulators) are not as easy to source. Off-the-shelf materials also require a complete characterisation to confirm their quality is acceptable, primarily due to the prevalence of poor quality products that have been found in the market [231]. This added cost and uncertainty for purchased nanomaterials can price out many researchers, stifling innovation, and negatively impact the translation of ideas into real-world technologies.


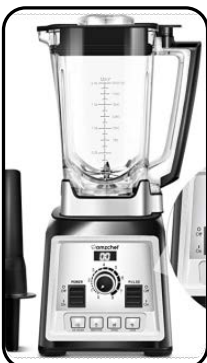



One of the most democratising steps in nanosheet production in the past decade has been the use of standard household kitchen blenders to effectively produce a variety of different 2DMs such as Graphene, MoS₂, h-BN, WS₂ and others [7, 8, 232, 233] through the mechanism of LPE [88]. The low-cost and widespread availability make this equipment attractive for laboratory investigations. Importantly, impeller-driven mixing and blending processes have been scaled-up for many industrial chemical engineering applications over several decades. Therefore, this simple shear-exfoliation system can support translation pathways for laboratory research, facilitating widespread industrial uses for 2DMs compared to today’s more common laboratory synthesis methods that are inefficient at large-scales (e.g., ultrasonication). A significant limitation, however, is that kitchen blenders are not

designed for nanomaterial synthesis and lack the necessary experimental controls for scientific research. The quality of a 2DM has a significant impact on its material properties, emphasising the importance of precise synthesis control and characterisation when it comes to research. Modifications are mandatory due to this, and by the fact that increasing the level of automation increases the reliability and repeatability of the synthesis process¹. This work describes how to accommodate this and maintain a low-cost for this scientific instrument. At a minimum, the most modest modifications begin at controlling the power cycling of the blender (see Section 2.4.1) and end at the precise control over the speed of the blender (Section 2.4.4) and process temperature (Section 2.4.5). Similar commercial blenders are open-loop and do not support power cycling as a rule.

Nowadays, there are numerous examples of open-source equipment which use some form of 2DMs in solution (such as conductive inks) to create functional devices [111, 234, 235]; but simultaneously, there are few such open-source projects for the production of 2DMs. The only recent example the authors could find of an open-source framework for scalable production of 2DMs is AutoCVD [236]. This bottom-up approach uses Chemical Vapour Deposition (CVD) to grow 2DMs on copper substrates. Although this method produces large-area 2DM thin-film deposits which can be useful in sensing and electronics, it is not suitable for producing large quantities of 2DM as required for functional inks and photocatalytic composites (typically $\sim 1 - 100$ g/L). LPE is a top-down approach that has been proven using sonicating probes [10], ultrasonic baths [155], jets [237], industrial homogenisers [165] and more [216], though on the whole, these systems are either prohibitively expensive or offer little advantage to the standard kitchen blender when comparing 2DM concentrations and production rates. Table 2.1 juxtaposes some modified blenders from this work to the nearest commercial equivalent lab blender (Waring LB20ES). Though the commercial blender has greater chemical resistance due to its use of a stainless steel vessel, the modified

¹It also reduces human input, as the equipment is often run for several hours at a time.

Table 2.1: A comparison of current commercial blender offerings and some of this works' modified alternatives.

	Commercial			Modified	
					
Brand S/N	Kenwood BLP31.D0WG	AMZ Chef NY-8088MJD	Waring LB20ES	AMZ Chef Pot-Blender v2	Kenwood PID-Blender
Cost	£ 50	£ 150	£ 1200	£ 170	£ 100
Power	350 W	2 kW	400 W	2 kW	400 W
Chemical	Low	Medium	High	Medium	Low
Speed	11 or 19 krpm ± 1000 rpm	Only runs on Propriety cycles	1 - 20 krpm ± 1000 rpm	1 - 25 krpm ± 1000 rpm	0.5 - 19 krpm ± 500 rpm
Control	Open-Loop		Open-Loop	Open-Loop	Closed-Loop

alternatives are both cheaper and of similar or higher power. All setup information can be found in more detail on the OSF page [OpenLPE](#). Furthermore, we give insights into the pre-processing, analysis, characterisation and process intensification which will aid researchers in manufacturing their own 2DMs reliably in-house.

2.3 Hardware description

In its simplest form, the equipment is a standard kitchen blender modified to conduct an *on/off* cycling procedure to ensure the batch and high-power internal motor do not overheat. All blenders examined utilise similar single phase AC motors, making the power electronics straightforward to regulate. The cost of the base blender tends to parallel the increasing complexity in power regulation, power output, and the chemical resistance of the vessel. Synthesis occurs by exerting mechanical force on the precursor/solvent mixture, which leads to particle break-up and produces shear rates that are dependent on the rotational speed of the impeller ($\dot{\gamma} \sim \omega^{3/2}$ [2]). Adding speed control ensures the conditions within the blender are precisely set, allowing for more selective and repeatable synthesis.

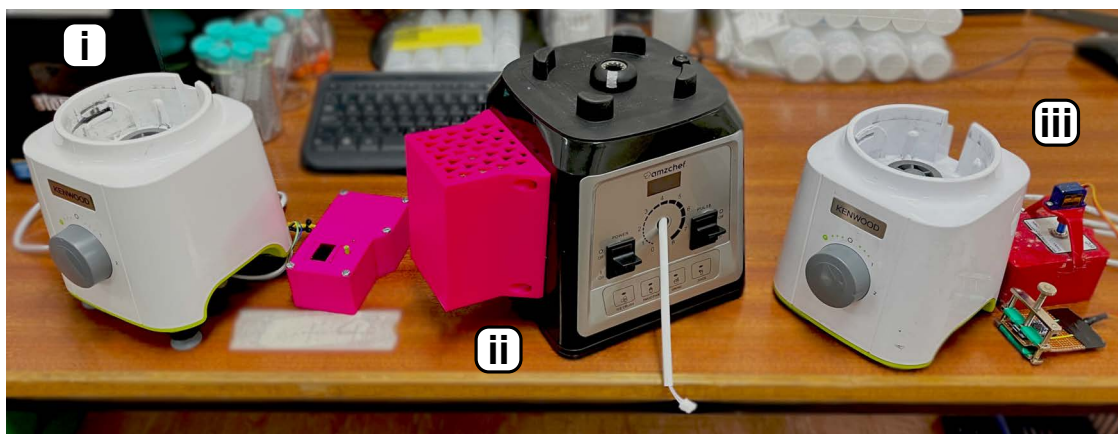


Figure 2.1: Some examples of modified blenders tested in lab. i) is a Kenwood modified in accordance with Sections 2.4.3, 2.4.4 and 2.4.2 (with option B from Table 2.2) and includes a screen for a digital readout. ii) is an AMZchef with variable speed (Section 2.4.2, uses option C from Table 2.2) and is typically used with the programmable extension lead in Section 2.4.1. iii) is a modified Kenwood with option D from Table 2.2, and has an added servo to facilitate the *on/off* cycling. Software and build guides can be found on our Open Science Framework (OSF) page.

The ease of use of this type of system, coupled with the synthesis information and characterisation of production given here, allows anyone to reliably control the synthesis of 2DMs for their own research application. The only other systems that come close in terms of simplicity include the original scotch-tape method [238], and the modified Hummer's method [239]. LPE offers a few distinct advantages here:

- One can choose to use green solvents (depending on vessel compatibility), thereby making the process non-toxic and environmentally friendly.
- It is a straightforward approach that requires minimal set up.
- 2DMs manufactured using LPE maintain good quality as the process does not introduce additional nanosheet defects (e.g., oxidation, basal plane defects).
- It is the most cost effective system currently available. We estimate that the equivalent of 1 g of Few-Layer Graphene (FLG) can be produced (average number of atomic layers $\langle N \rangle < 10$) in a water-surfactant solution in one hour of processing for less than £200 (including capital costs).

Graphene and related materials have already been shown to have an enormous impact within many application areas [230]; hence, it is important to share the build process and documentation, as well as pitfalls and lessons learned, to thereby increase accessibility and innovation around these novel nanomaterials.

2.4 Modifications

The systems described in this article are all inherently modular, with the blenders themselves being entirely interchangeable with any other commercial blender due to the standardised use of mains supply AC motors. Each sub-system is described individually, giving a brief overview of their function and application, including build notes. More details about the individual sub-systems and how they are applied can be found on the OSF page.

2.4.1 On/off cycling

On/off cycling or switching is essential to avoid overheating and maintain device reliability.

Commercial blenders have restrictions in their duration of continuous operation. This is to prevent overheating of the motor and thermally-induced failures of the mixing vessel components. To run a material synthesis for the typical process times used in LPE (e.g., $\sim 10 - 100$ mins), an automated method to perform *on/off* cycling without user intervention significantly reduces manual efforts. This requires only three adjustments to the Arduino code "relay-switch.ino" before beginning a material synthesis. The process *on* time interval (ms) is set by adjusting `on=60000`; process *off* time interval (ms) is set by adjusting `off=120000`; and the total process *on* time (ms) required of the synthesis operation is set by adjusting the maximum time to be `t<1800000`. In this example, the blender operates for 1 min *on*, 2 mins *off* for a total *on* time of 30 mins. After the total *on* time is reached, the relay reverts to a normally-open condition and the blender remains *off*.

Note that for certain blenders, such as the AMZChef in Table 2.1, *on/off* cycling as described here is difficult due to interference from the onboard electronics. If this is the case, consider the installation with a triac module (see Section 2.4.4). Simpler blenders such as

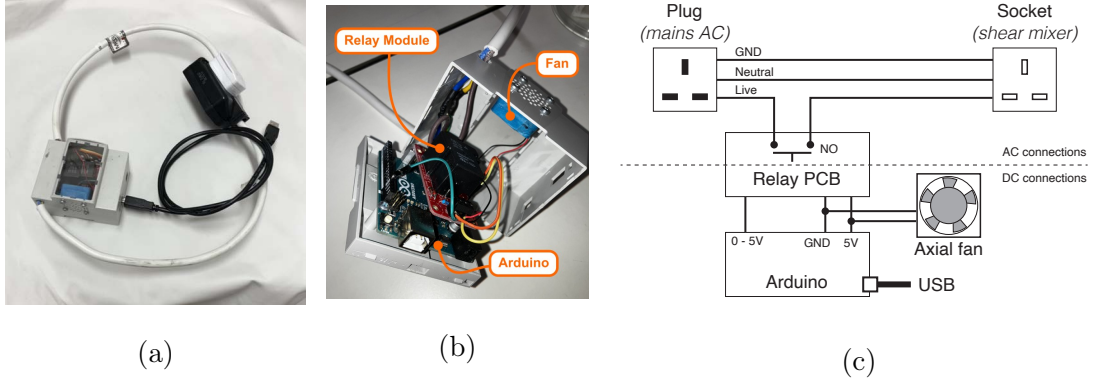


Figure 2.2: Arduino-controlled *on/off* extension lead. This automated relay switch controlled many of the appliances listed in this work, and can be combined with other sensors for dynamic, closed-loop control.


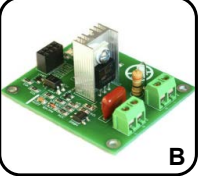
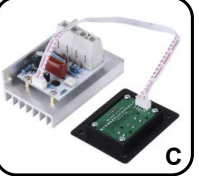

this Kenwood model have no in-built software to detect shut-off, so this basic addition is typically all one needs. To avoid failures during experiments, we found it was essential to follow the manufacturer’s recommendations and alternate running 1 minute *on* together with an *off* time that ensures sufficient cooling of the product batch and internal motor. To avoid tampering with any on-board electronics, this modification is made completely separate to the blender, as a programmable extension lead.

2.4.2 Phase angle control

Phase angle control allows for accurate power delivery to the blender rotor. This in turn allows for a more exact operating condition, and is a necessary step depending on the blender chosen. Phase angle control modules with microcontroller interfaces supersede Section 2.4.1, as on-off cycling can be directly implemented within the arduino code.

Phase angle control in brief is a way of regulating the duty cycle of an AC signal. Dimming in this context is inherited from the primary use of these circuits as dimmer

Table 2.2: A comparison of current commercial triac modules from several sources, their prices, and a brief note on their suitability in general.

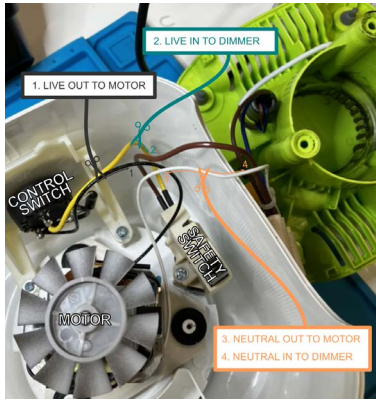
	Arduino Compatible			Fixed
				
Brand	RoboDyn	Krida	Walfront	Untd. Automation
Cost	£ 16	£ 12	£ 17	£ 64
Notes	Small form factor & well documented, arduino compatible header files available.	Well isolated and good arduino compatibility.	Potential arduino Compatability, screen module for manual control. High power.	No compatability, RFI suppressed and easy installation. Reliable and well documented. High power.

switches. The function of these triac dimming circuits² (Triode for Alternating Current) is simple in principle, as they act as a diode in the direction of a voltage applied to the gate and simply latch open until the voltage inverts, where it reverts to closed. This simple technology is available as a standalone box with a potentiometer (e.g., [6]) or with an isolated zero-cross interface (see Table 2.2) suitable for use with an arduino or similar microcontroller (Section 2.4.4). The wiring is identical for both cases:

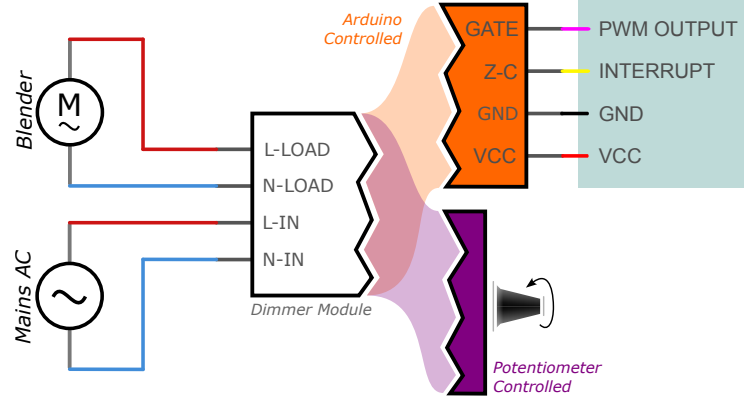
As blenders are mostly powered by brushed AC motors, the wiring of the triac module is directly in series with the motor, regulating the live signal from mains voltage. Hence, wiring is simply a matter of connecting the input of the blender to the output of the the triac module, then to mains voltage. It is important to ensure that the triac circuit selected pertains a similar power rating as the blender to be used, but note that the power dissipated through the triac is typically quite low.

Zero-cross detection is the typical interface for most of the commercially available

²Sometimes called a thyristor or Silicon Controlled Rectifier (SCR)



(a)



(b)

Figure 2.3: Visual guide to wiring a dimmer module (either arduino or potentiometer control) into a commercial blender, in this case the Kenwood BLP31.D0WG. The safety switch is left inline with the motor in A), to add an extra layer of security in the unlikely event the vessel detaches from the blender. B) shows the wiring diagram for arduino controlled and potentiometer controlled dimming modules.

phase angle control circuits, and the majority consist of three inputs (power, gate and ground) and one output (zero-cross). To give a small overview of how these boards function, the zero-cross signal pulses high when the AC voltage into the board changes potential (through an in-built zero-cross detection circuit), while the gate input controls a switch which determines whether the signal to the gate pin of the triac is on or off. These circuits are often optically-isolated, but even with this isolation, Electro-Magnetic Interference (EMI) can still be an issue and some shielding may be required, especially if the control board is close to the phase angle control circuitry.

The final control method used (See Appendix C) provides good stability in the rotor speed, and at most can vary between $\pm 1'000$ RPM. It especially fails under differing loading conditions, i.e. different vessels and liquids, requiring new measurements in order to set the speed accurately each time.

2.4.3 Speed sensor

Adding a speed sensor facilitates precise impeller speed measurements.

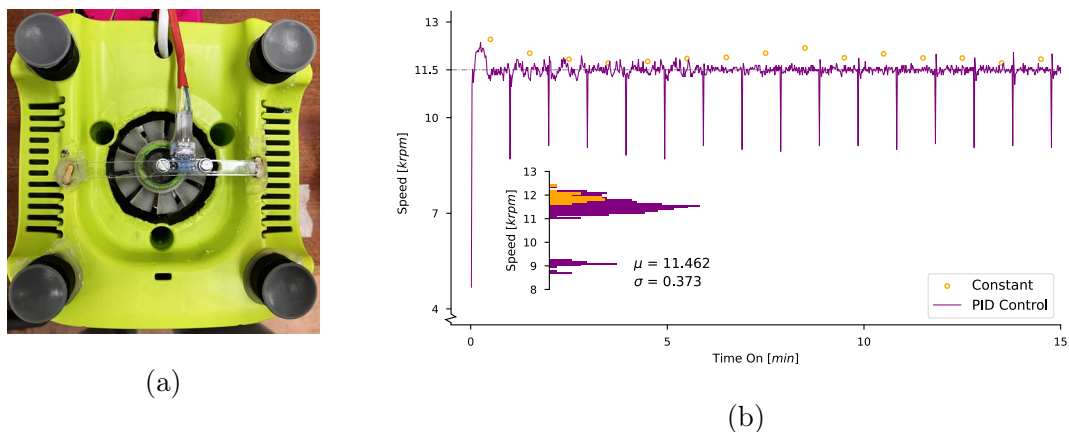


Figure 2.4: Sensor modifications in A), the photo-interrupt module was brought up and away from the fan, with a small 3D printed interrupting ring fit into the fan itself. B) shows the speed of the first 15 minutes *on* of a run, with a constant `dim_time` (in orange, measured with an optical tachometer), and a Proportional Integral Differential (PID) control circuit (in purple, measured with an on-board sensor). Inset in B) is a histogram of speeds (**log scale**). For the "Constant" (orange) case, the speed was carefully measured as stable with the tachometer before the equipment was power cycled and the measurements taken. Note the much lower sampling rate (1 per minute) and the steady state error between the constant and PID cases.

Potentiometer-controlled dimmers (option D, Table 2.2) can accurately maintain the speed to a reasonable range (± 1000 rpm between experiments), but there can be significant variability especially at low speeds. Figure 2.4b shows a snapshot of the first 15 minutes of a synthesis run, and we can see that after having found a set point for 11.5 krpm with a tachometer, a constant setpoint (set in code as `dim_time`, see Appendix C) shows a steady state error from the set point. More expensive blenders such as the AMZchef (in Table 2.1)

have in-built zero-cross and speed sensing circuitry, making it useful for these requirements. Lower cost models, such as the Kenwood described here, do not have an integrated speed sensor and require modification. Modifying the Kenwood involved removing part of the housing to get access to the cooling fan at the bottom of the machine to then attach an interrupting ring³, for a precise reading directly from the motor shaft. It also involved printing extensions for the blenders' rubber feet, and a bar to mount the photo-interruptor across the gap in the housing. These modifications can be seen in Figure 2.4a.

Speed measurements can be calculated as a counts per time or time per counts basis. Both have their own advantages; time per counts is accurate at low speeds and can fail at higher speeds where the time between counts is very low, counts per time has a set resolution depending on the number of sections in the photo-interrupting strip. For the blender, the simpler and more easily implemented is the counts per time basis, which with 1 s between readings and single gap in the interrupting strip gives a resolution of 60 rpm, resulting in a good balance of accuracy at most speeds (see Appendix C).

2.4.4 PID control

Speed sensing (2.4.3) coupled with phase angle control (2.4.2) allows for closed-loop speed control, to maintain a precise speed.

Though the AMZchef has many of the features needed natively; it unfortunately controls speed through a basic relay-switching type circuit, where power is regulated by switching slower relay circuits to control power delivery. This method again works to regulate the duty cycle of the AC signal, but instead of regulating every half wave, the cycle is every tens or twenty periods, which does not allow for the precise speed control required for

³If printing in PLA note that this material is transparent to infra-red, so the interrupting ring should have something opaque to ensure the beam is interrupted.

scientific research. For this reason, we decided on closed loop control by integrating a speed sensor into the blender. This is achieved through implementation of a PID controller, as it is simple to implement and easy to tune (see Appendix C for further details). The inset of Figure 2.4b is the speed represented as a histogram, where the variation from the set point is shown.

2.4.5 Cooling jacket

Adding a cooling jacket around the vessel can help control the temperature of the batch during synthesis and ensure the blender components maintain reliable operating temperatures.

Higher product yields can be achieved by exposing the precursor and solvent mixture to higher strain rates more frequently or for longer residence times [2, 168]. For the high shear blender, this can be achieved by reducing the vessel size. Active temperature control becomes a requirement when moving from large volume "jug" vessels ($\approx 1 - 2\text{L}$) to smaller volume "bullet" vessels ($\approx 0.1 - 1\text{L}$, see Fig. 2.9). It may also be necessary for controlling mechanochemical synthesis when chemical reactions that are sensitive to temperature are present. Heat is generated in the LPE process through viscous heat generation as the fluid experiences turbulent shear stresses. This is illustrated in the schematic in Fig. 2.6, where \dot{Q} is the volumetric heat generation and Q''_{nc} is the natural cooling to the environment. The practical issue when moving to small vessel geometries is the reduction in heat transfer to the ambient surroundings. The batch temperature ($T_{product}$) can increase to/above the point where there is a risk of thermomechanical failures to the vessel and/or rotor coupling between the impeller and motor. Temperature rises can occur rapidly ($\approx 12^\circ\text{C}/\text{min}$), as shown in Fig. 2.5 which plots the batch temperature during the exfoliation of graphite into FLG using the two different styles of vessels. After just three minutes (*on time*), the temperature increases by 36°C when operating with a "bullet" style vessel. The corresponding increase when using

the “jug” style vessel was only 12°C. One way to address this is to set the OFF time to a sufficiently long duration, however, the thermal capacitance of these systems can require an excessive OFF time that can be impractical. Indeed, we found that *off* time intervals of up to 75 mins were necessary to avoid the batch exceeding 50°C when leaving the system to cool naturally in ambient air (see Figure 2.5b). In contrast, the synthesis of FLG using the “jug” vessel required OFF time intervals typically of 1-3 mins.

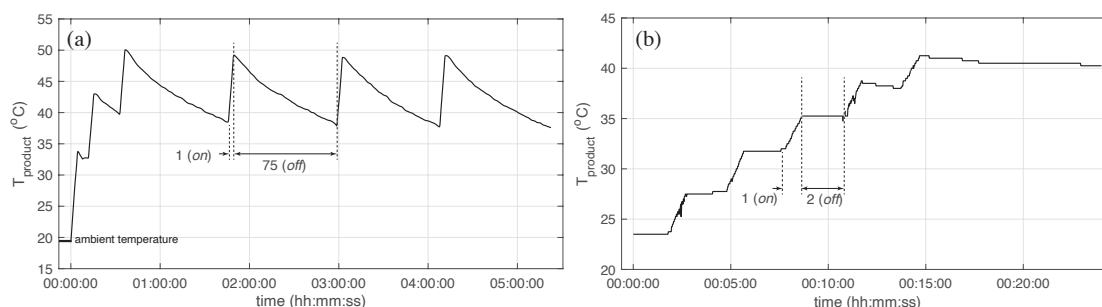


Figure 2.5: Batch temperature during the synthesis of few-layer graphene in water-sodium cholate using (a) “bullet” style and (b) “jug” style process vessels. All other synthesis parameters were kept the same across both cases including $C_i = 20$ g/L, $C_{sc} = 4.3$ g/L, $V = 200$ mL and $\omega = 20,000$ rpm.

An alternative approach that limits the OFF time interval and maintains process temperature control is to introduce active cooling. This build involved two main components: (i) a cooling jacket that efficiently transfers heat from the process and (ii) temperature acquisition to enable process monitoring and control. To avoid the requirement for expensive chillers that may not be accessible to every lab, we designed the cooling system to function using ice cubes/chilled water as a coolant (note the system can also be operated with a chiller if this is available). Illustrations of the cooling assembly and its breakdown, including the type K thermocouple data logger are shown in Figure 2.6.

This system can cool the LPE process to sub-ambient temperatures and/or maintain

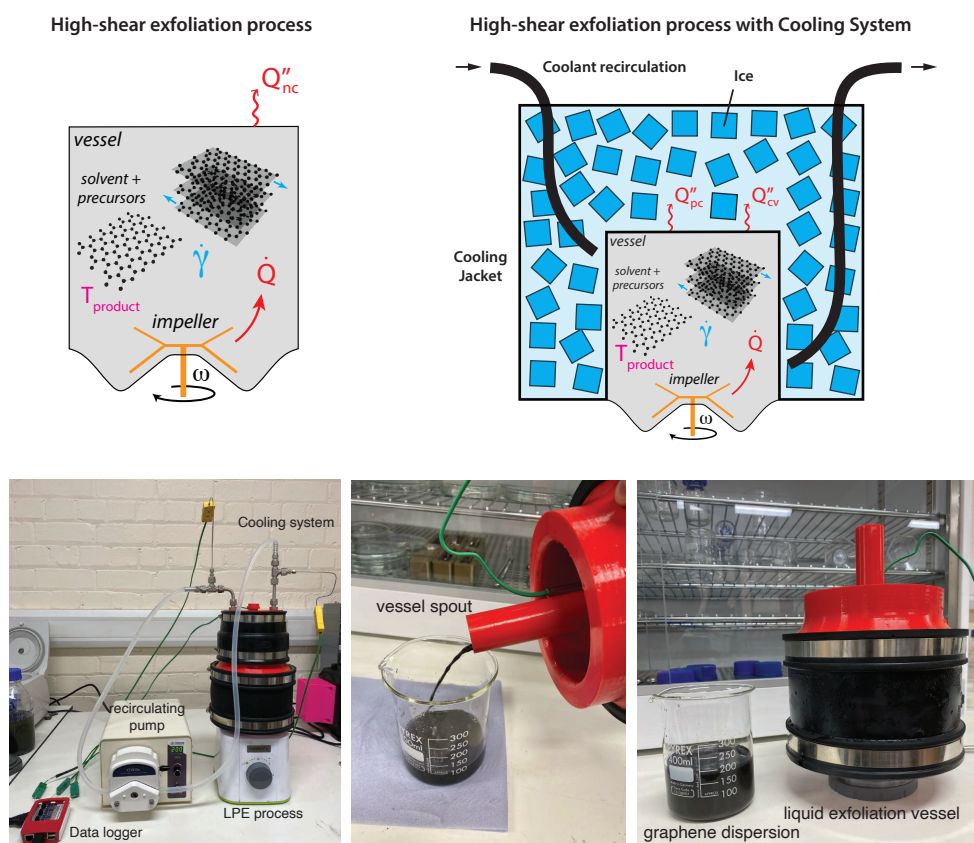


Figure 2.6: The cooling system utilises the phase change of ice (latent heat of fusion) to remove heat (Q''_{pc}) from the Liquid Phase Exfoliation (LPE) process. The cooling jacket is constructed using 3D-printed polyethylene terephthalate glycol-modified (PETG) parts and two large ethylene propylene diene monomer (EPDM) pipe connectors. A thermocouple board is connected to a Raspberry Pi 3B+ to record and plot temperatures from type K thermocouples in real-time. The addition of precursors and product sampling is possible using the vessel spout. When the synthesis process is completed, the product is emptied from this vessel spout also.

batch temperature below a target limit. To demonstrate this, Figure 2.7 presents the batch temperature during a 15 min synthesis of FLG in an aqueous-surfactant solution where the OFF time was dynamically adjusted to target an average product temperature of $30 \pm 5^\circ\text{C}$. The inlet and outlet temperatures of the coolant demonstrate the change in cooling modes

(latent and sensible heat). For 1.5 hours (10 mins *on*), the coolant temperature increases by $\approx 2^\circ\text{C}$ and much of the heat generated by the shear exfoliation process goes into melting the ice cubes. Then, as most of the ice melts, the coolant temperature increases $> 15^\circ\text{C}$ and the heat is removed by convection. In this operating region, longer OFF times are necessary to maintain the target product temperature. It is recommended that users size their cooling system and ice packing levels to meet their required process times and impeller power input.

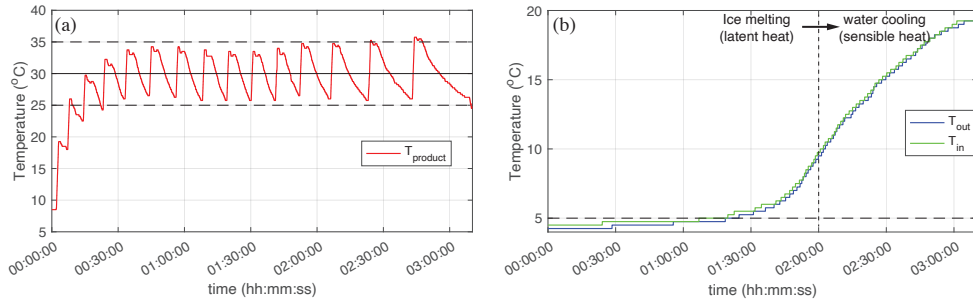


Figure 2.7: The temperatures of the (a) batch and (b) coolant during the synthesis of few-layer graphene in water-sodium cholate using a “bullet” style process vessel with integrated cooling system. The synthesis parameters were kept the same as for the cases without cooling in Fig. 2.5 including $C_i = 20$ g/L, $C_{sc} = 4.3$ g/L, $V = 200$ mL and $\omega = 20,000$ rpm.

2.4.6 In-line monitoring

In-line monitoring can be used to assess 2DM production in parallel to other ex situ characterisation methods. An examination of this technique is given in Chapter 3

A significant challenge from lab to industrial scales of graphene and other 2DM production is the lack of high-throughput materials characterisation tools. Rapid optimisation of LPE processes and batch-to-batch material quality assurance is restricted as a consequence. To address this, our group conducted in-line monitoring of few-layer graphene production within these blenders using an optical spectroscopy method that has been documented in

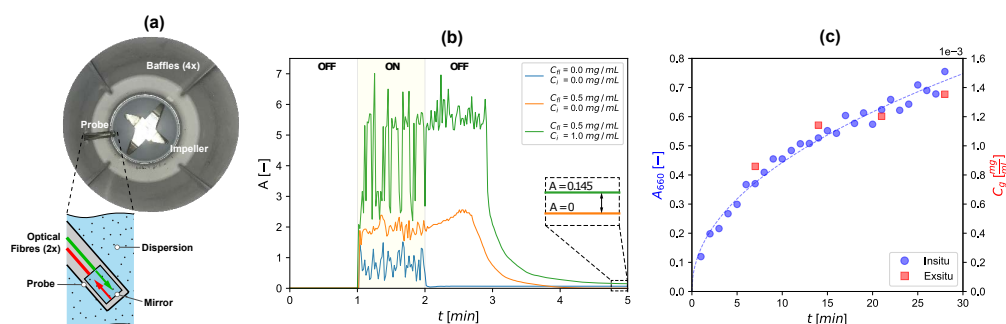


Figure 2.8: The probe mounted in position above the impeller in part a) with a small inset schematic detailing its function. b) compares manual measurements taken *ex situ* to measurements taken with the probe for a similar 15 min run. c) shows the optical noise generated in between the probe and the mirror.

previous work [2] (see Chapter 3). This method integrates UV-vis-NIR spectroscopy by suspending a fibre-optic probe within the liquid being agitated in the mixer. To conduct our measurements, a hole was cut into the side of the vessel and a probe holder was 3D-printed and bonded to the side wall. This allowed the fibre-optic probe to be placed inside the vessel just above the impeller blades. To remove external lighting effects, the vessel was finished by painting the outside surface to make it opaque.

The LPE process contains a heterogeneous mixture of solvent, precursor particles and exfoliated materials. Indirect measurements of changes in concentration are obtained through an initial correlation of extinction with *ex situ* measurements of product concentration. This is performed at a suitable wavelength where changes in nanosheet morphology (thickness and length) have a negligible influence on the extinction coefficient [240]. This in-line approach can be integrated to any blender system with a few important considerations:

- **Material sensitivity:** This transmission spectroscopy method using an external fibre-optic probe is applicable for materials where the extinction coefficient (ε) is dominated by absorbance (α), where $\varepsilon(\lambda) = \alpha(\lambda) + \rho(\lambda)$. Graphene is one example, however,

other 2DMs (e.g., h-BN) can have large scattering contributions (ρ).

- Process dynamics: During impeller rotation, there is a significant amount of signal noise created by light scattering off the bubbles and large solid particles in the system. To address this, we developed a protocol to take measurements during a period when the equipment is off so that the bubbles coalesce, large particles sediment, and any foam can drain out (for aqueous-surfactant dispersions).
- Optical characteristics of the system: The vessel must be made completely opaque so that no other light interferes with the optical measurements.

2.5 Operation

2.5.1 Preparing samples

LPE is a top-down approach to synthesis, hence an appropriate precursor must be selected to obtain the target two-dimensional material, i.e. flake graphite for graphene, bulk MoS₂ for MoS₂ nanosheets, bulk h-BN for h-BN nanosheets. Once a precursor has been selected, a solvent or dispersion-assisted liquid has to be chosen. For solvents, the suitability for exfoliation and stable 2DM dispersions is typically based on matching the Hansen solubility parameters with the nanomaterial desired [241]. Unfortunately, many commonly used solvents for LPE can be toxic [242], have high boiling points, and tend to be incompatible with the blender vessel materials (e.g., NMP). Alternative 'green' solvents, such as co-solvents of water/Isopropyl Alcohol (IPA) and water/ethanol [169], have been shown to produce stable dispersions, have lower boiling points than traditional solvents, and are compatible with certain kitchen blender materials.

Liquid dispersants based on aqueous-surfactant solutions (e.g., water/NaC) or macromolecules can produce high concentration 2DM dispersions through either electrostatic or steric repulsion mechanisms. These solutions have good compatibility with most, if not all kitchen blenders. One disadvantage is the high shear mixing process leads to aeration and the formation of stable foams which increase the temperature and pressure inside the vessel. On the application side, surfactants can also be difficult to wash off the nanosheets, and can persist after evaporating the excess liquid, altering the material properties.

A good choice of solvent or dispersion-assisted liquid can have a drastic impact on the concentration of nanomaterial produced. The list of potential liquid dispersants has grown considerably over the last decade, with many examples in the scientific literature covering a

variety of different mediums, including off-the-shelf items from single malt whiskey [243] to black tea [244].

Quantities are more nuanced, though most have found that the concentration of nanomaterial (C) produced scales linearly with the concentration of bulk precursor, C_i [7]. This relationship ($C \propto C_i$) breaks down at the extremes of precursor concentrations or when the liquid is sufficiently saturated [168]. Changes in surfactant concentration typically produce one maxima, though there are some outlier cases for lower purity graphite precursors [245]. Generally, only small amounts of surfactant are required for stabilising 2DMs, with anything above 10 mM dropping off sharply, the maxima usually lying somewhere in this range [246]. Choice of surfactant here seems to have little effect, hence a green surfactant would be ideal for this purpose. Additionally, though LPE may have been demonstrated in a specific scenario, it may not work in the mixer; one example we have come across is water/urea co-solvent which has been demonstrated in cooled sonicated baths [247]. We recommend either aqueous-surfactant solutions, or green co-solvents such as aqueous IPA or Ethanol (depending on your vessel, see 2.5.2).

2.5.2 Vessel considerations

When selecting a vessel there are a number of considerations that should be made:

1. The solvent compatibility with the vessel material (see Section 2.5.1).
2. To avoid reliability issues, the vessel must not exceed temperatures $> 60^\circ\text{C}$, i.e. by active cooling. This is particularly important for foaming solutions (aqueous-surfactants) that increase pressure build-up inside the vessel.
3. The blender creates vibrations and acoustic noise when operating, so the location must be suitable.

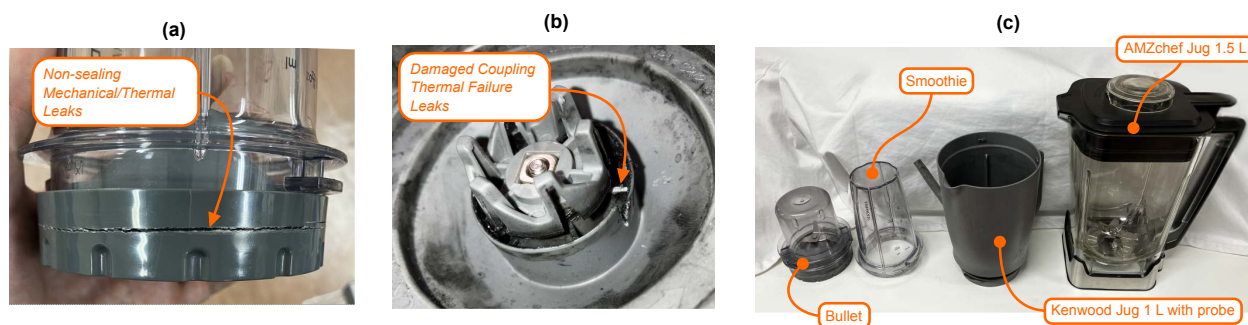


Figure 2.9: Failures of sealed vessels in a) and b), most occur at weak points in the vessels construction, likely due to thermal cycling weakening the material, and high pressure and temperature causing material failure. c) Shows a labeled selection of vessels we have tested with, leakage around the lower seal was common with the Kenwood vessels, but we found this could be mitigated by increasing the pretension on the lower seal (initially achieved this with PTFE tape, then moved on to a small 3D printed shim).

4. No foreign objects are around the blender during operation.
5. All avenues of liquid release are checked and properly inhibited.

In a sealed vessel, fluid temperature and subsequently vessel pressure will increase which may cause failure of the vessel material, or any sealing surfaces, resulting in leaks or catastrophic equipment failure. Thermal cycling through extended operation of this style of vessel may also weaken the materials, which combined with the high pressure could increase the risk of failure (Figure 2.9); hence the recommendation in Point 2. If the solvent compatibility is unknown, a simple patch test on a region of the vessel can be carried out. Alternatively, if feasible, a small amount of the material could be cut from the vessel housing and left in the chosen solvent overnight. A visual check is then performed to determine whether the material has been dissolved or damaged by the solvent⁴.

⁴Our testing has shown that the AMZchef is resistant to ethanol mixtures. The Kenwood vessels used in this work were not resistant to ethanol or Cyrene, but are resistant to water/IPA mixtures.

2.5.3 Blender operation

The blender must be operated in intervals to prevent excessive heating of the motor and the liquid dispersion in the absence of a cooling jacket. Manufacturers often recommended running for a minute *on* per minute *off*, though there is less of an issue with the more powerful blenders such as the AMZChef, where couplings and motor are of higher quality, these can be run at moderate→high loads without the risk of immediate failure. Example Arduino sketches for providing automated control are available on the OSF page. Some solvent choices may increase the risk of coupling failure, for example when the blender is operated using surfactant solutions, aeration creates a foam which increases the fluid resistance, thereby putting more strain on the blender components. Organic solvents, such as ethanol, do not suffer from this issue. Intensifying 2DM production for a particular solvent or liquid dispersant predominantly depends on increasing the process time t , rotor speed N , impeller diameter d_i and/or reducing the volume V [2, 7, 8]. The precise scaling of these factors is approximately in line with the energy inputted (E) to the mixture per unit volume of liquid, irrespective of the method of liquid exfoliation [7]. Power ($E = P t$) for stirred batch reactors is well known to scale as follows [248]:

$$P \sim \rho N^3 d_i^5 \quad (2.1)$$

Equation 2.1 suggests that increasing the rotor diameter and rotational speed are the most important factors for increasing production. Through our extensive testing, we have collated a sizeable amount of data on running the Kenwood blender with an optimum amount of NaC ($C_s = 4.3$ g/L). This is presented in Figure 2.10b and 2.10a. Note too, that at shear rates under a critical value ($\dot{\gamma}_c \approx 1000$ s⁻¹ for graphene), the mechanical forces inside the blender vessel are too low to overcome the interstitial van der Waals forces of the

layered precursor [7]. Another compounding issue is the instability in rotor speed at low power values, where the variance in rotor speed (usually ± 1000 rpm) can reach as high as ± 2000 (for open-loop blenders) as the rotor repeatedly stalls and picks up speed. For these reasons, we recommend running at speeds above ≈ 4000 rpm.

The highest yields were observed when using the smaller, bullet-style vessel at moderate speeds (≈ 10 krpm), where most of the power is dissipated into the fluid (2% mass yield of 5 layer average graphene after 30 minutes on, using the Kenwood with a water/NaC dispersant). This yield and production rate is favourable compared to existing and more expensive laboratory methods (e.g., ultrasonication). Separation and characterisation of the material after processing is explained in more detail within Section 2.6.

LPE produces nanosheets in the range of 40 nm to 200 nm, but nanosheet length can depend on the solvent chosen. Varrla et al. showed with surfactant mixtures, that the largest, thinnest nanosheets are produced at the Critical Miscelle Concentration (CMC) [8]. They also showed that increasing the rotor speed does slightly increase the length of sheets produced, with other factors having a negligible effect. More recently, surfactant concentrations of ≈ 10 mM were shown to be a critical point for concentration, length and thickness, irrespective of the surfactant choice or CMC [246]. LPE tends to produce nanosheets within large size distributions, though it is possible to reprocess any separated supernatant to reduce the average layer count [2, 245].

2.5.4 Recycling

Once processing has completed, and all nanomaterial has been removed from the batch, the precursor sediment can be recycled using a fresh batch of solvent/liquid dispersant. We have found that recycling this sediment using a second exfoliation run and fresh aqueous-surfactant

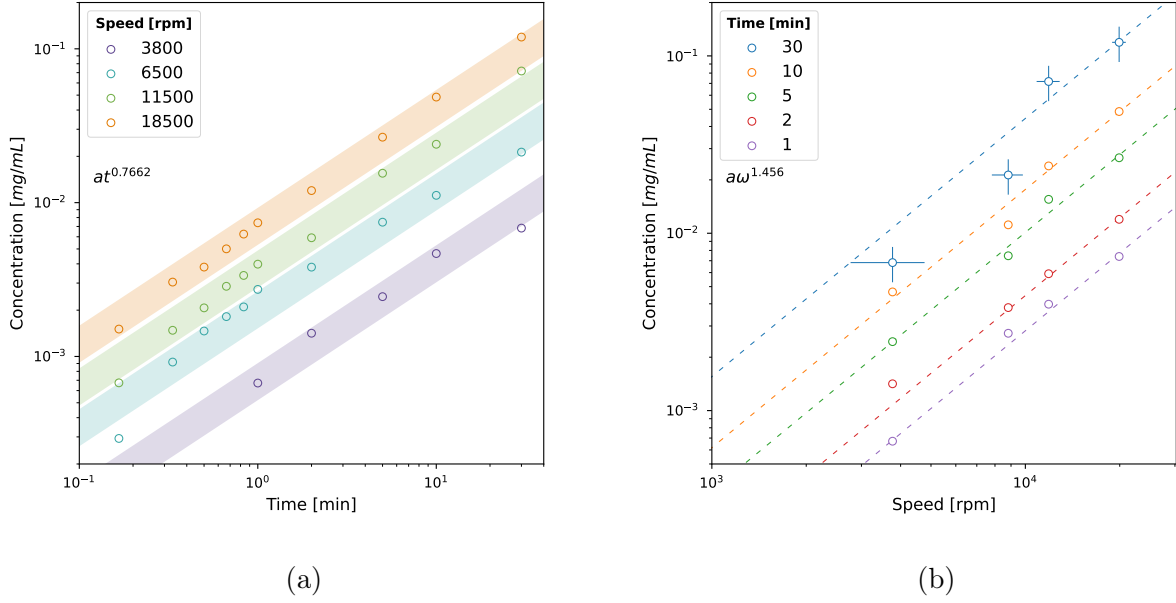


Figure 2.10: Graphene concentration is plotted against time in (b) within a window of uncertainty ($1.2\sigma_{max}$), and against speed in (c) with speed (± 1000 rpm) and concentration error bars (σ_{max}). We find production exponents of $t^{0.77}$ and $N^{1.46}$ for $C_s = 4.3$ mg/mL of Sodium Cholate (NaC) at a process volume of 200 mL and an average layer cutoff of $\langle N \rangle = 5$ (centrifuged for 45 minutes at 380 Relative Centrifugal Field (RCF), initial graphite concentration of $C_i = 20$ mg/mL). Optical extinction measurements were used to determine concentration (through the Lambert-Beer law) using a PerkinElmer Lambda 365 UV-vis-NIR Spectrophotometer, and a measured extinction coefficient of $1521 \text{ L g}^{-1} \text{ m}^{-1}$ at $\lambda = 660$ nm. The procedure for measuring the extinction coefficient is described in detail elsewhere [245].

solution can produce $\approx 70\%$ of the initial 2DM output [245]. One can also conduct LPE in recovered solvents, or upcycling other layered precursor sources as Stafford and Kendrick showed in their recent paper on end-of-life Li-ion battery anode materials [245].

2.5.5 Post Processing

Whilst post processing is not specifically related to the hardware in discussion, in this paper it is nonetheless an important step in the synthesis of nanomaterial dispersions. The most common method for post processing is to centrifuge liquid exfoliated dispersions to sediment out large, unexfoliated material. There are also other methods available to separate out size fractions such as Liquid Cascade Centrifugation (LCC) [249] in which nanosheets of specific sizes can be isolated using multiple centrifugation steps. It is also possible to obtain powders of the synthesised 2DM dispersion by evaporating the liquid after separating the 2DM from the bulk precursor. When using surfactant-assisted methods, the surfactant adheres to the 2DM making it difficult to wash off completely. Co-solvents such as ethanol or IPA are better suited for synthesising powders for this reason, as they boil off at low temperatures, leaving the remaining nanomaterial. Using the dispersions directly from the LPE process remains the easiest way to implement the 2DM in applications. However, this depends on the application and the mass fraction of few-layer nanosheets in dispersion that are required to obtain suitable properties.

2.6 Validation and Characterization

2.6.1 UV-vis-NIR Spectroscopy

The hardware described has been used effectively to synthesise few-layer graphene, h-BN and MoS₂ dispersions in both surfactant solutions (aqueous-sodium cholate), and organic co-solvents (aqueous-ethanol). These can be easily isolated from residual bulk material by centrifugation, allowing for UV-vis-NIR measurements of material concentration.

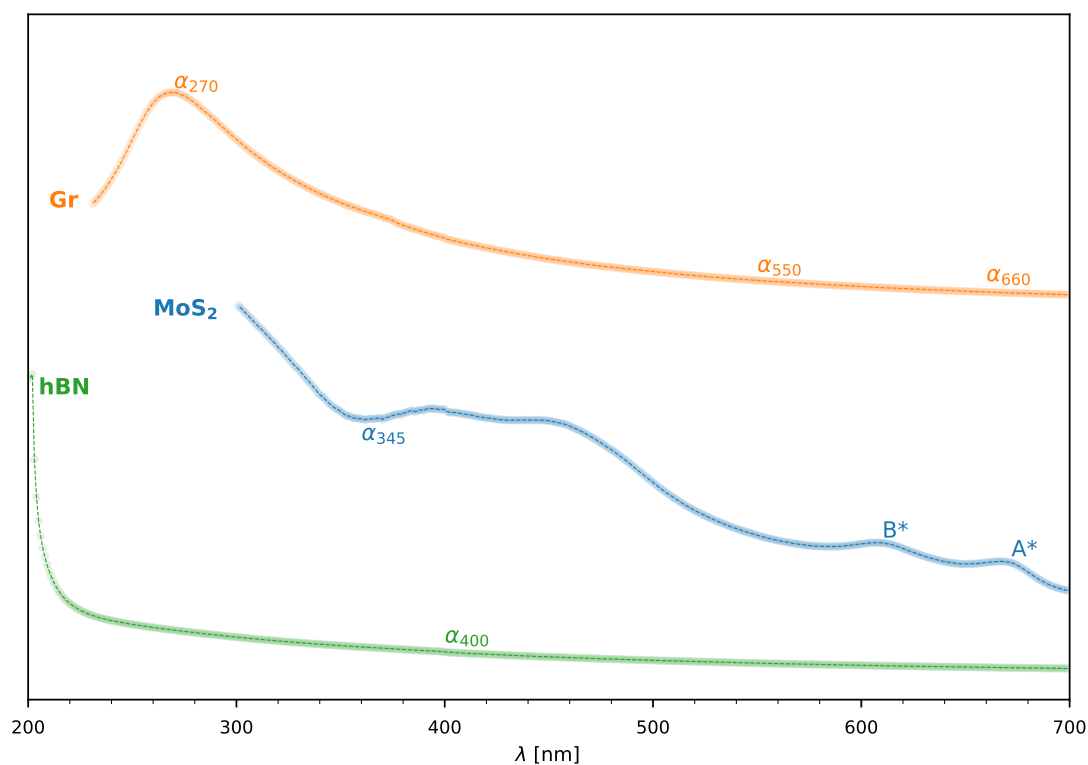


Figure 2.11: Three different UV-vis-NIR extinction spectra of materials (Y is offset, arbitrary units) created with our mixer, graphene (Gr), MoS₂ and hBN, along with the salient points for establishing the thickness, concentration and/or length [240, 250, 251].

Optical extinction can be easily measured at any point along the UV-vis-NIR spectra,

but the value at certain points along the response curve is affected by the morphology of the nanosheets. For instance, the spectra for Gr shows a distinct absorbance peak near 270 nm (Figure 2.11), indicative of the electronic conjugation of graphene. The height of this peak relative to the absorbance at longer visible wavelengths has been shown to increase with decreasing layer numbers [240]. In the longer wavelength region (600–800 nm), extinction is not affected by nanosheet morphology rather acting solely in relation to the concentration of nanomaterial within the sample. If the material in question is functionalised, these changes are visible in the characteristic UV-vis-NIR response (e.g. the absorbance peak for graphene oxide is blue shifted slightly to 230 nm, unlike that of pristine graphene). Therefore, UV-vis-NIR spectroscopy allows for an inexpensive and rapid indication of the morphology of the nanosheets.

2.6.2 Microscopy

Graphene production is validated using AFM, where there is agreement with existing literature [6, 8], and with spectroscopic layer number estimations $\langle N \rangle$ [240]. Single layer height for graphene is also found to be between 1 and 2 nm which though larger than the theoretical value, aligns with those found by Backes et al. [252]. AFM samples prepared in Figure 2.12 were exfoliated in an IPA and deionised water solution (50:50 mix by mass), with 10 μL of solution drop cast onto a freshly cleaved and heated mica sheet ($0.5 \times 0.5 \text{ cm}^2$) which was then allowed to dry, following the procedural steps laid out by Backes et al. [252]. Measurements were taken using an Oxford Instruments Vero AFM using non-contact soft-tapping AFM probes.

We have found that surfactants obscure AFM measurements due to their adherence onto the surface of the FLG sheets and probe tips. Removing them is difficult, but can be achieved through a combination of diluting and washing the sample once prepared [252].

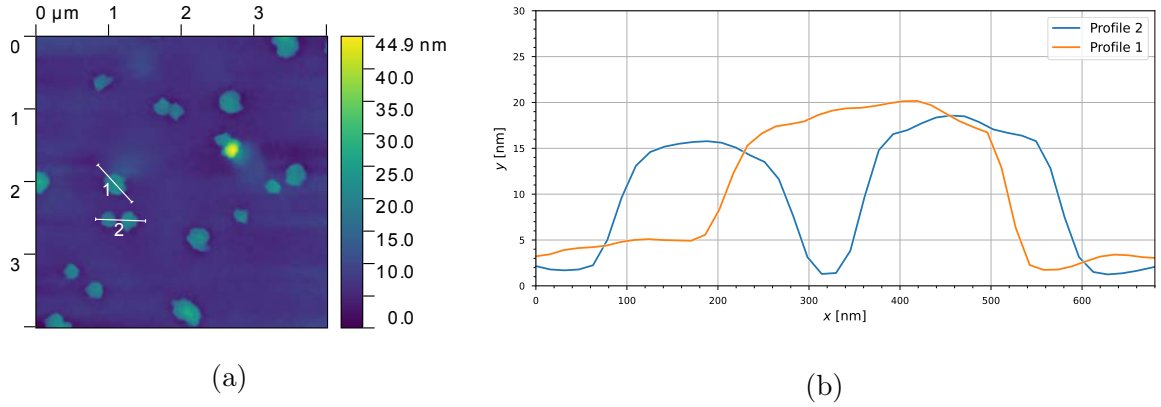


Figure 2.12: Atomic Force Microscopy (AFM) of graphene nanoplatelets $\langle L \rangle \approx 200$ nm exfoliated in IPA and water (50:50 mix by mass) note that Sodium Cholate (NaC) can obscure Atomic Force Microscopy (AFM) as it adheres to the surface of the nanoplatelets causing the probe tip to stick and drag.

This ‘post-washing’⁵ cleaning step created a reliably sharp image despite the surfactant and mitigated the probe tip sticking and dragging the sample.

⁵Post-washing involved cleaning the deposited sample with IPA solvent, to remove any residual surfactant.

2.7 Conclusion

This chapter presents low-cost, open-source LPE processes for producing atomically thin materials and demonstrates the synthesis of few-layer graphene, MoS₂ and h-BN nanosheets. [OpenLPE](#) is a mechanochemical process based off traditional household kitchen blenders that have been adapted to provide precise control over key shear-exfoliation parameters that influence nanosheet concentration and morphology. Automated control was developed and implemented to ensure repeatable synthesis conditions (fluid shear stresses, batch temperature) and hardware reliability. Detailed descriptions of the hardware and software for controlling impeller speed, synthesis duration, process temperatures and measuring inline spectroscopic characteristics have been provided. These have been outlined in a modular framework, with the aim of allowing researchers to decide which components to choose for their application, ensuring every stage of construction is repeatable and attainable. Each module has an accompanying repository containing codes, designs and build instructions to facilitate this.

Validation of the hardware for the synthesis of 2DMs was used to identify process restrictions and performances. The range of solvents that are compatible with blender vessels can be a limitation. However, this can also indirectly promote green synthesis strategies. The need to use aqueous-surfactant or other mild co-solvent methods inherently avoids the use of toxic solvents which have high boiling points (e.g. NMP). Glass vessels are available and would broaden the range of solvents if required. In this arrangement, an examination of the compatibility of the seals around the impeller would be necessary to prevent leaks.

The investigations on graphene synthesis revealed a minimum 20% increase in concentration when moving from jug to bullet type vessels. These smaller vessels were found to be advantageous for low volume batches (< 160 mL), achieving 1.4%wt yield in 15 min-

utes compared to $\approx 0.5\%$ wt for the larger jug type. Active cooling is required to operate the small vessel process reliably and we demonstrated this without using expensive ancillary heat pumps. Using MoS_2 as a model 2D material, the quality of the shear-exfoliated product compares favourably to contemporary synthesis approaches like ultrasonication. Furthermore, there are other advantages that are attractive for materials processing. This LPE system is capable of processing nanosheet dispersions from dilute to ~ 100 g/L concentrations. This robustness across low/high solids content and liquid viscosity make it an appropriate technique for broad laboratory research and suitable for numerous applications including functional inks, pastes and composites.

While the modifications to laboratory mixers presented in this chapter enable cost-effective production of 2DMs, challenges persist in ensuring consistent material quality. Chapter 3 will explore the development of inline characterisation techniques designed to address these challenges, evaluating material properties throughout the synthesis process.

3. Exploring Inline Characterisation

Title of publication	Foam flows in turbulent liquid exfoliation of layered materials and implications for graphene production and inline characterisation
Paper Information	(2022) Chem. Eng. Res. Des., 177, 245–254
Additional Contributors	
Philip Davies ^a	Review.
Jason Stafford ^a	Review, PIV analysis and imaging (Figures 3.3, 3.6 and 3.9), edits.
^a School of Engineering, University of Birmingham, Edgbaston, Birmingham B15 2TT, UK.	

3.1 Foreword

A significant challenge to the application of 2DMs for photocatalysis is the long and laborious process of material characterisation. As nanomaterials are highly sensitive to morphological changes and defects within the nanosheets (see Chapter 1), small changes in process execution can impact the properties of synthesised materials. Being able to track these changes quickly and efficiently is therefore essential for commercial success and to avoid failures in production. Inline characterisation has the potential to simplify the characterisation process of separation, dilution and measurement; integrate it into an existing system, and drastically reduce effort by taking measurements *in operando*. By utilising the mixer developed in Chapter 2, we examine the effectiveness of inline UV-vis-NIR spectroscopy to determine graphene production and atomic layer number changes in-process.

As the first study produced chronologically, the authors decided to follow in the footsteps of Varrla et al. [6] who first demonstrated low-cost graphene synthesis in blenders, using fairy liquid as the dispersing agent (surfactant) to prevent agglomeration of nanosheets through steric and electrostatic repulsion. Note that the use of fairy liquid is not recommended, in fact it is to be avoided in most scientific study, as there can be batch-to-batch variations and changes to the recipe over time¹. Chapter 4 advanced to follow the guidance of Griffin et al. [246], replacing fairy liquid with sodium cholate as it is repeatable and widely replicated in literature.

Owing to the lowered surface tension caused by these surfactants under highly turbulent LPE, these flows become heavily aerated (foamy), which obfuscates UV-vis-NIR measurements. Measurements on the motion of graphite particles indicate that surfactant con-

¹In Appendix B, the variation of these experiments are analysed, and they demonstrate the worst correlation with the dimensional arguments in comparison to all other works analysed.

centration can alter the rheology of the mixture under dynamic conditions and change the material flow patterns within the device. As a result, the surfactant concentration that maximised graphene concentration was found to be non-unique. This highlights that the design and selection of surfactants should consider both molecular scale repulsion effectiveness and macro-scale hydrodynamics of the liquid exfoliation process.

Chapter Aims and Objectives

The primary aim of this chapter is to develop and test a real-time, *in operando* measurement system that can monitor the synthesis of 2DMs, like graphene, during mixing. This system seeks to overcome the limitations of traditional, ex-situ methods that require stopping the process for lengthy amounts of time to measure and analyse samples. A secondary goal is to understand how this mixing process changes at with scale² and under the high-shear conditions used to produce these materials. This aim can be summarised into the following objectives:

- Implement a UV-vis-NIR spectrometer that can monitor the material's characteristics continuously during mixing, minimising the need to pause the process.
- Assess how well the inline measurement system performs, identifying any significant challenges or limitations it presents compared to traditional methods.
- Examine how foams form and behave during the high-shear mixing process. This involves studying the effects of foam on the measurements and exploring how material and mixing conditions contribute to foam and flow dynamics.

²Scaling of LPE processes is evaluated rigorously in Appendix B.

3.2 Introduction

The remarkable properties of graphene and related two dimensional 2DMs have shown enormous potential to create nanotechnologies that address pressing challenges across energy, sustainability and healthcare. Although graphene is the most well-known, the library of 2DMs is extensive, including insulators such as h-BN, semi-conductors from the TMD family (e.g. MoS₂), and numerous 2D oxides (e.g. MoO₃) [89, 253]. One of the main challenges restricting the translation of these promising materials beyond laboratory settings and into real world applications is large-scale production of high quality materials [230]. Insufficient nanomaterial production rates and quality control are key areas that require attention [89]. Addressing this will improve the economic viability and lower the risk for manufacturers who incorporate these materials into future technologies [152].

Liquid exfoliation has emerged as a prime candidate for large-scale production of 2DMs. This top-down method disperses a layered precursor material (e.g. graphite) in a suitable solvent and separates the layers in solution using either mechanical, chemical or electro-chemical forces to create nanomaterial dispersions (e.g. mono- and few-layer graphene) [152]. Mechanical methods that rely predominantly on shear-driven exfoliation are beneficial as they typically produce defect-free 2DMs without oxidation. Sonication [155], high-shear mixing [7], microfluidisation [165], Taylor-Couette and thin film reactors [168, 254] are a few of many examples that have been used successfully.

Among these, batch approaches such as high-shear mixing (such as that achievable through a kitchen blender, Chapter 2) and turbulent stirred tank reactors have been demonstrated as suitable platforms for shear exfoliation of graphene, h-BN, MoS₂ and WS₂ [6, 7, 167, 232]. These approaches have been studied experimentally and using computational fluid dynamics to provide insights on modes of material breakup [255], coherent flow structures

[256, 257], turbulent statistics [258] and mixing effectiveness [259].

Molecular simulations and micromechanical modelling of the controlled separation of graphene sheets have provided insights on the shear and peeling mechanisms at the nanoscale [260, 261]. Experiments by Paton et al. [7] and Bicca et al. [167] showed there is a minimum shear rate required to overcome van der Waals attractive forces and exfoliate layered materials. Stafford et al. [168] recently uncovered the general scaling relationship governing production for continuous flow, shear exfoliation systems. Combining high fidelity numerical simulations, fluid dynamic experiments and nanomaterial characterisation, it was found that graphene concentration depends on derived parameters of shear rate and particle residence time. Transmission and scanning electron microscopy on individual nanosheets showed signatures of slip and peel exfoliation mechanisms at the nanoscale. In shear exfoliation environments generated by turbulent Taylor-Couette flows, surface erosion of the precursor micro-scale particles was observed. More aggressive break-up of graphite precursor particles was shown for cavitation-driven exfoliation using sonication [262].

Solvent choice also influences nanomaterial concentration in liquid exfoliation processes [241]. Many high performance solvents are toxic and have high boiling points which has led to research on greener alternatives [152, 158]. Water can function as a suitable solvent for few-layer graphene dispersions when modified through co-solvent strategies [168] or with the addition of surfactants [263, 264]. In the latter approach, surface-active agents adsorb to nanosheets and prevent re-stacking through steric and electrostatic repulsion mechanisms. This has been found to enable high concentration formulations in water (>1 mg/mL)[6].

These previous studies suggest that the synthesis route from precursor to nanosheet can be sensitive to the approach. They also suggest that the predominant impact of adding surface-active agents in aqueous-surfactant dispersions of 2DMs is molecular scale repulsion at the nanosheet scale. In this study, we investigate batch exfoliation using a kitchen blender

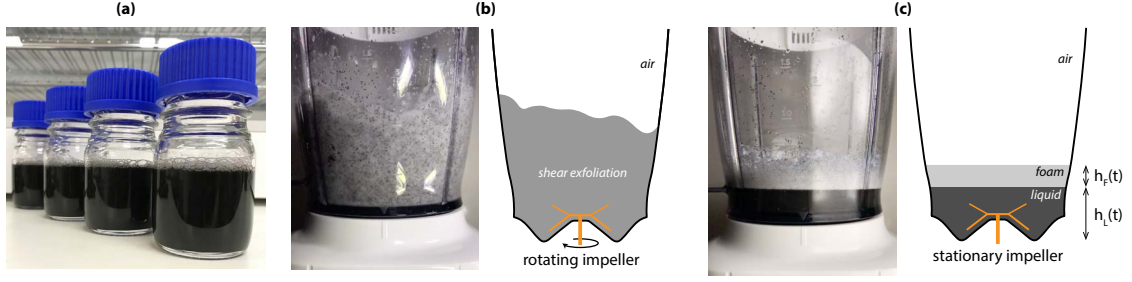


Figure 3.1: Shear exfoliation in aqueous-surfactant dispersions can generate foam flows. (a) Liquid dispersions of few-layer graphene produced by the batch exfoliation process. (b) Foamy fluid mixture during turbulent shear exfoliation in a kitchen blender. (c) Gravitational phase separation when the process stops.

to produce graphene in aqueous-surfactant dispersions and examine secondary foam formation effects that are currently neglected. This system is capable of exfoliating 2DMs [6, 232] and can serve as a template for studying contemporary stirred tank reactors that are used at larger scales for production and material blending operations. A reliance on slow and expensive *ex situ* materials characterisation tools also presents a bottleneck for realising large-scale high-throughput material quality control [168, 240]. Here, turbulent mixing and shear exfoliation have been investigated using inline spectroscopy to probe the process characteristics *in situ* and exfoliation performance on-the-fly.

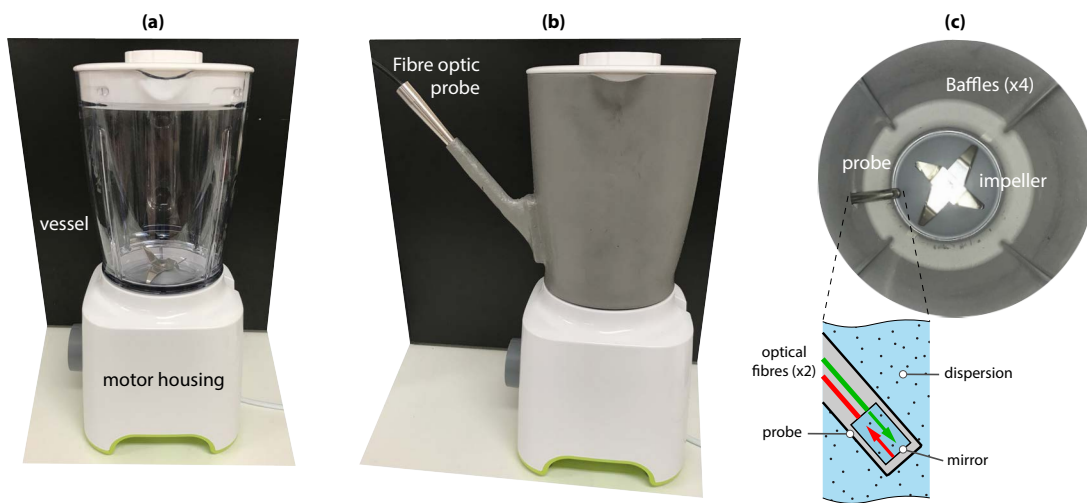


Figure 3.2: Implementation of inline UV-vis-NIR spectroscopy for production monitoring. (a) The standard kitchen blender vessel. (b) The modified vessel with fibre optic probe insertion. (c) Internal view of the vessel showing the location of the probe for *in situ* spectroscopy.

3.3 Methods

3.3.1 Experimental arrangement

Batch production of few-layer graphene using turbulent shear-assisted liquid exfoliation was performed using a 350W kitchen blender modified with a triac power regulator (United Automation QVR-TB-RFI, see Chapter 2, Figs. 3.1 and 3.2). This allowed variable speed control from $500 \pm 100 \text{ rpm} < \omega < 20000 \pm 1500 \text{ rpm}$ and the impeller speed was monitored during operation using an optical tachometer (Omega HHT13). In this speed range, the resulting non-dimensional numbers based on the properties of water were: Reynolds number, $Re = \rho\omega D^2/\mu \sim 10^5 - 10^6$, Froude number, $Fr = \omega^2 D/g \sim 10^1 - 10^4$, and Weber number, $We = \rho\omega^2 D^3/\sigma \sim 10^3 - 10^7$. This indicates that fluid mixing in a vessel containing water only is dominated by the applied inertial forces. The confirmation of this is shown in the flow observations presented in Figure 3.3 for an intermediate impeller speed and $Re \approx 2.6 \times 10^6$.

This model system parallels traditional stirred mixers which operate across a broad range of scales from lab to industry. The kitchen blender has a contour vessel shape and a 4-blade impeller design with two blades angled upwards and two facing downwards. This configuration promotes solids suspension [265]. The diameter of these upper and lower blades differs ($D_u = 48 \text{ mm}$; $D_l = 62 \text{ mm}$) and an average diameter of $D = 55 \text{ mm}$ has been used for the calculation of non-dimensional parameters. The vessel contains four baffles and is tapered with an average diameter $\approx 110 \text{ mm}$. These baffles are 5 mm in width and extend beyond the full height of all liquid volumes investigated ($200 \text{ mL} \leq V \leq 800 \text{ mL}$).

Graphite flakes (Sigma Aldrich, 332461) were dispersed in de-ionised water (5 MΩm) and a surfactant (Fairy Liquid). The surfactant is a household detergent that has been shown to be an effective stabilising agent for graphene in water [6]. This detergent contains

15-30% anionic surfactants and 5-15% non-ionic surfactants. During shear exfoliation the fluid is a mixture of unexfoliated graphite particles, exfoliated few-layer graphene, foam and liquid (Figure 3.1b). When the process is stopped, gravity separates out the foam and liquid phases into two distinct layers (Figure 3.1c). The height of these layers is time-dependent with liquid draining to the base of the vessel from the thin films and Plateau borders within the foam structure [266].

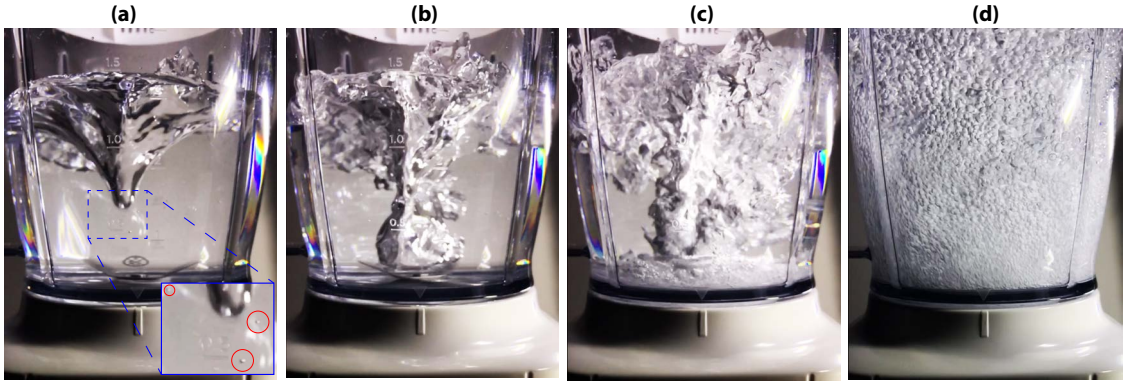


Figure 3.3: Evolution of the liquid-gas behaviour upon impeller start-up. (a) $\omega t = 2100$. (b) $\omega t = 2160$. (c) $\omega t = 2210$. (d) $\omega t > 7330$. Images shown are for a liquid volume, $V = 800$ mL, $Re \approx 2.6 \times 10^6$, $Fr \approx 6.1 \times 10^3$, and $We \approx 2.5 \times 10^6$.

The foam formation process can be explained in part by examining the evolution of the liquid-gas interface for the case of water without surfactant. Figure 3.3 shows snapshots during the early stages of impeller start-up and to the point where quasi-steady bubbly flow exists throughout. The vessel has a large diameter to baffle width ratio ≈ 22 that typically suppresses vortexing for fluids with high viscosity [248].

Water is a low viscosity liquid and a vortex forms in this system leading to a drop in liquid level in the core (Figure 3.3a). A small number of cavitation microbubbles were also observed at this Reynolds number $Re \approx 2.6 \times 10^6$. Vortexing pulls air into the path of the rapidly rotating impeller and when this interacts with the blades it produces large quantities of small gas bubbles that are forced outwards (Figure 3.3b, c). These propagate

throughout the vessel and the resulting bubbly flow pattern persists indefinitely (Figure 3.3d). Smaller bubbles near the base of the vessel in the impeller region rise and coalesce to form larger bubbles near the top. In the presence of surfactants, this aeration process leads to foam formation as surfactant molecules concentrate at liquid-gas interfaces preventing bubble coalescence and lowering surface tension.

3.3.2 Material synthesis and *ex situ* characterisation

Aqueous-surfactant mixtures of graphite particles were processed over time using a 1 minute *ON* followed by 1 minute *OFF* operating procedure. This was necessary as the manufacturer’s recommend a maximum 1 minute operating interval to avoid overheating the motor. Results have been presented using a processing time that corresponds to the impeller ON time (e.g. a 15 minute process time required operating the blender 1 min ON / 1 min OFF for 30 minutes). Few-layer graphene (FLG) were separated from the mixture by post-process centrifugation. At the end of each test, 15 mL samples were pipetted into centrifugation tubes from the vessel. Samples were centrifuged at 1500 rpm (214 RCF) for 45 mins and the top 5 mL supernatant containing few-layer graphene (FLG) was removed for analysis. Confirmation of FLG with average atomic layer number $N_{FLG} < 10$ was obtained by measuring the extinction spectra and applying spectroscopic metrics to calculate average layer number using the relationship $N_{FLG} = 25(A_{550}/A_{max}) - 4.2$ [240]. An example of a FLG extinction spectrum for $250 \text{ nm} < \lambda < 700 \text{ nm}$ is shown in Figure 3.4. Concentration (C_g) was measured by performing UV-vis-NIR spectroscopy on samples at a wavelength where absorbance is unaffected by nanomaterial size and thickness. This was quantified using extinction measurements at $\lambda = 660 \text{ nm}$, an extinction coefficient of $\varepsilon_{660} = 6600 \text{ mL mg}^{-1} \text{ m}^{-1}$ [6], and the Lambert-Beer relationship, $C_g = A_{660}/\varepsilon_{660}L$, where $L = 10 \text{ mm}$ was the optical path length of the quartz cuvette containing the sample.

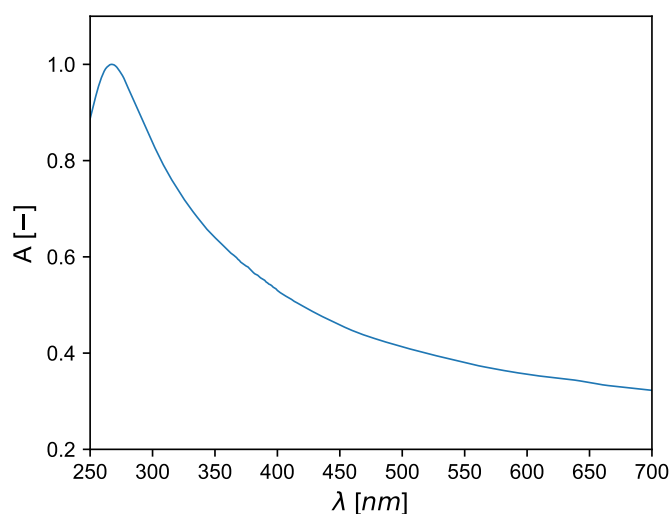


Figure 3.4: Extinction spectrum of few-layer graphene.

3.3.3 *In situ* materials characterisation

Investigations were performed to assess if inline spectroscopy could be implemented in turbulent batch exfoliation of aqueous-surfactant dispersions of 2DMs. The vessel was modified to allow insertion of a stainless steel probe into the process volume (Figure 3.2). This probe housed two fused silica optical fibres. One fibre transmitted light from the spectrophotometer source into the measurement region. This light travelled through the fluid medium, reflected off a mirror, and returned to the spectrophotometer through the second fibre. The probe was mounted at an obtuse angle and located near the base of the vessel to lower the risk of solids depositing on the mirror surface and to ensure the probe was submerged for all process volumes examined in this study. The vessel was painted opaque to block light from external sources in the laboratory and avoid interference with the fibre optic probe.

Initial trials were performed using a simpler solution without surfactant or graphite. Blue food dye (Spirulina, Glycerine, Water) was added to a vessel filled with 400 mL of

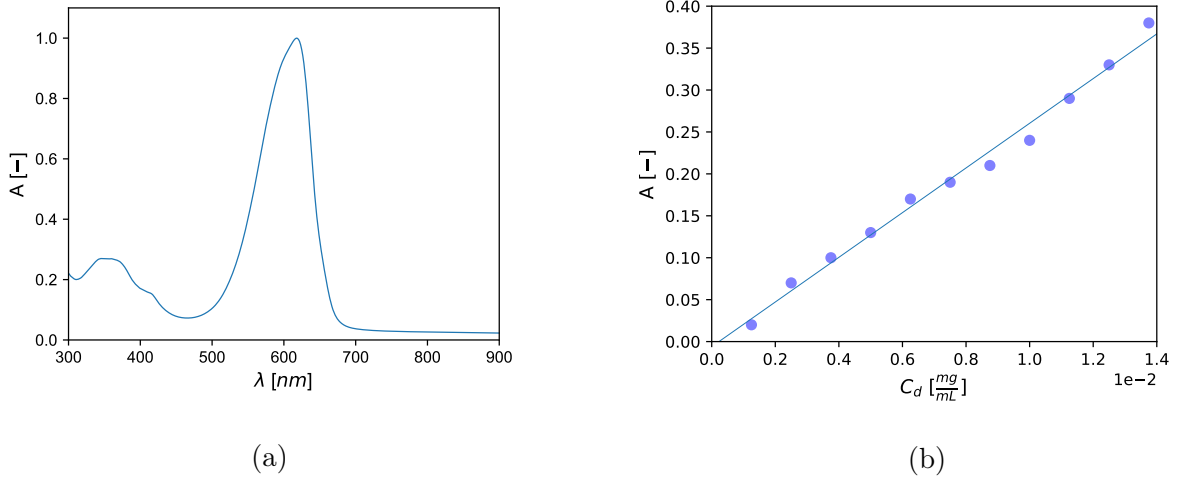


Figure 3.5: (a) Absorbance spectrum of blue food dye. The peak visible is situated at $\lambda = 617$ nm. (b) Relationship between the concentration of blue food dye (C_d) and absorbance measured using *in situ* spectroscopy at $\lambda = 617$ nm and $V = 400$ mL.

water. The blue dye was found to have an absorbance peak at $\lambda = 617$ nm using *ex situ* UV-vis-NIR spectroscopy (Figure 3.5a). This wavelength was subsequently chosen to measure changes in absorbance due to dye concentration changes. During mixing, the formation and transport of gas bubbles disturbs the optical measurements making it difficult to detect dye concentration changes. During the OFF period however, gas bubbles coalesced, absorbance readings stabilised and were solely dependent on the dye concentration in solution. Figure 3.5b shows these changes in dye concentration together with a linear fit that follows the anticipated Lambert-Beer relationship, $A = \epsilon CL$, where the slope is $\epsilon_{617} \approx 2600$ $\text{mL mg}^{-1} \text{ m}^{-1}$. These trials confirm that the inline measurement system is capable of detecting concentration changes when considerations are made for the additional gas phase that is present during operation. In the following results sections, the inline characterisation method has been extended to the batch exfoliation process where foam flows and graphitic materials exist.

3.3.4 Flow characterisation

The flow behaviour during turbulent exfoliation inside the kitchen blender has been investigated to explore connections between the hydrodynamics of the multiphase process and the nanomaterial produced. Images were acquired during shear exfoliation in aqueous-surfactant dispersions to examine the graphite material flows within the foam mixtures. An example of one of these images is shown in Figure 3.6a. Dark graphite particles with an average diameter $\approx 500 \mu\text{m}$ are visible within the bright foam structure (Figure 3.6b). This contrast was exploited to perform particle image velocimetry (PIV) and reveal the graphite flow behaviour in the near-wall region of the vessel (Figure 3.6c).

Images were achieved with a clear vessel illuminated with a $4 \times 2\text{W}$ LED light source. High speed images were acquired at 720p and 240 fps (taken using an Iphone 11, with a standard 12 MP sensor) for an intermediate impeller speed, $\omega = 10^4$ rpm. This was also used to investigate the impeller startup process and bubbly flows discussed previously (Figure 3.3).

Recordings began after the impeller start-up phase and for $\omega t > 10^4$, when the aqueous-surfactant dispersion was in a quasi-steady state. A total of 3000 image pairs were recorded and analysed to determine graphite particle displacements for each image pair (Figure 3.6c) [267]. Notably, these particle displacements were from the perspective of the camera viewpoint. The vessel has a circular cross-section that varies along its height and the captured particle motions are in three-dimensions. As a result, velocity magnitudes have not been resolved. For the purpose of this study, quantitative measurements on the particle flow direction were obtained and presented in the perspective view. Ensemble-averaged streamlines were calculated from the instantaneous graphite displacement fields in the near-wall region. The ensemble average was based on a sample size of 3000 to capture statistically

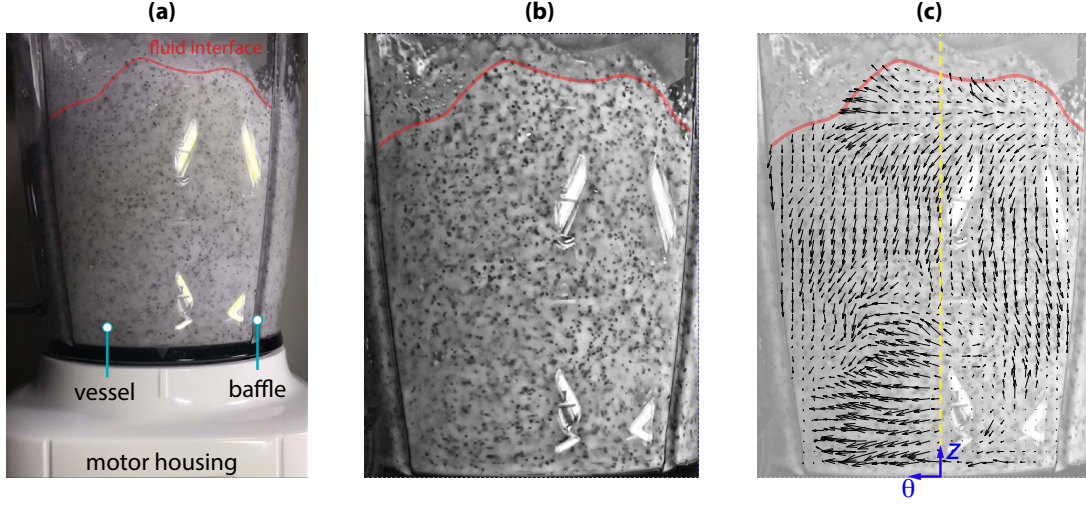


Figure 3.6: Near-wall graphite particle image velocimetry. (a) Raw high-speed image captured during liquid exfoliation. (b) contrast-enhanced region of interest. (c) instantaneous displacement vector field as viewed from the camera perspective. Images shown are for $V = 200$ mL, $\omega = 10^4$ rpm, initial graphite concentration, $C_i = 20$ mg/mL and surfactant concentration, $C_i/C_{fl} = 8$.

significant information in turbulent flows [268]. This ensured the measurements accurately represented the time-averaged graphite flow behaviour for the entire liquid exfoliation process.

3.4 Results and discussion

3.4.1 Liquid exfoliation of graphene

The concentration of graphene produced after 15 mins processing in the kitchen blender for different impeller speeds and fluid volumes is shown in Figure 3.7. At speeds higher than $\omega \approx 1500$ rpm, the concentration increases from $C_g \sim 10^{-3}$ mg/mL to $C_g \sim 10^{-2}$ mg/mL, with the smaller 200 mL volume process producing higher concentrations of few-layer graphene.

The kitchen blender is similar to a stirred tank reactor with a power input per unit volume that is related to the shear rate within the fluid, $P/V = \mu\dot{\gamma}^2$ [269]. The power input can be expressed through the non-dimensional power number, $Po = P/\rho\omega^3 D^5$, which is sensitive to flow regime. In the turbulent regime ($Re > 10^4$), $Po \approx \text{constant}$ for baffled vessels, or a slightly negative slope for unbaffled vessels [248]. Assuming a constant here for simplicity ($Po = C_1$), the average shear rate becomes:

$$\dot{\gamma} = \left(\frac{C_1 \rho \omega^3 D^5}{\mu V} \right)^{1/2} \quad (3.1)$$

For the blender parameters directly varied in this work, this relationship suggests the scaling, $\dot{\gamma} \sim \omega^{3/2} V^{-1/23}$. The increase in shear rate with decrease in volume explains the higher graphene concentration measured for the smaller volume in Figure 3.7.

A notable reduction in graphene concentration is observed in Figure 3.7 at rotational speeds, $\omega < 1000$ rpm, similar to the findings by Varrla et al. [6]. At lower impeller speeds of $\omega \sim 10^2$ rpm, the shear rate is $\dot{\gamma} \sim 10^1 - 10^2 \text{ s}^{-1}$, far below the critical criterion for

³For a more in depth look at the dimensionality of shear exfoliation processes, see Appendix B

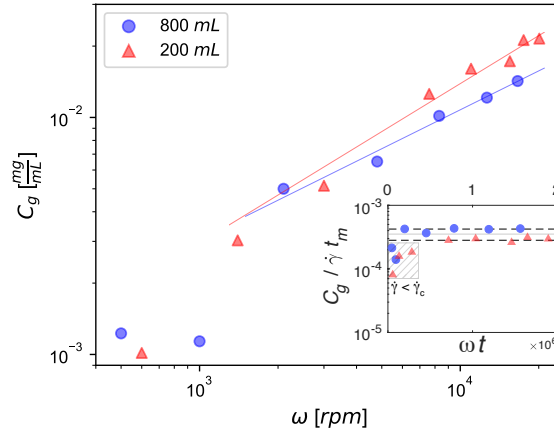


Figure 3.7: Concentration of graphene for different impeller rotational speeds (ω) and fluid volumes (V). All concentration data were measured at a process time, $t = 15$ mins.

overcoming the van der Waals attractive force that holds graphene layers together ($\dot{\gamma}_c \approx 10^4 \text{ s}^{-1}$) [7]. In the speed range $\omega \sim 10^3 - 10^4 \text{ rpm}$, the shear rate increases to $\dot{\gamma} \sim 10^3 - 10^5 \text{ s}^{-1}$ and graphene nanosheets are separated from the graphite precursor particles.

In addition to strain rate, precursor residence time (t_{res}) has been shown to play an equally important role in 2DM production by shear exfoliation in continuous flow laminar and turbulent flow regimes. Stafford et al. [168] showed for shear exfoliation using turbulent Taylor-Couette flows that $C_g \sim \dot{\gamma} t_{res}$ when operating above the critical shear rate for exfoliation. In the high Reynolds number flows examined here, the macro-scale mixing time is dominated by convective fluid motions due to the mean flow and turbulent diffusion [270]. The turbulent Peclet number, $Pe = Re \cdot Sc$, takes a constant value and the non-dimensional mixing time is constant irrespective of vessel volume, $t^* = \omega t_m$. Making the assumption that fast mixing times correspond with short graphite particle residence times in the high shear regions of the vessel, this characteristic exfoliation time scales as $t_m \sim t_{res} \sim \omega^{-1}$. Concentration has been rescaled with $\dot{\gamma} t_m$ on the inset plot in Figure 3.7 with the collapsed data showing a reasonable agreement ($\approx 20\%$) considering the simplified assumptions of

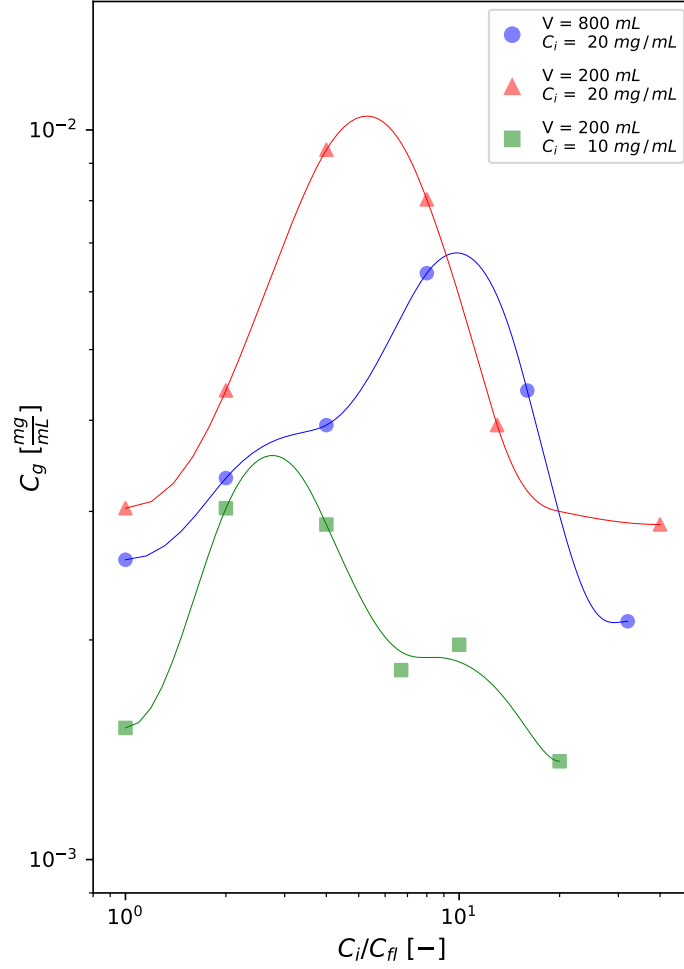


Figure 3.8: Concentration of graphene for different surfactant concentrations (C_{fl}), fluid volumes (V) and starting graphite concentrations (C_i). All graphene concentration data were measured at a process time, $t = 15$ mins, and a constant rotational speed, $\omega = 10000$ rpm..

isotropic turbulence and Newtonian fluid in eq. (3.1). A departure from this scaling relation occurs when $\dot{\gamma} < \dot{\gamma}_c$. This indicates that the important derived hydrodynamic parameters in turbulent batch exfoliation of 2DMs are also strain rate and mixing time.

3.4.2 Variation in surfactant concentration

The influence of surfactant concentration on graphene production is shown in Figure 3.8. For each process volume and initial starting graphite concentration examined, the concentration of graphene reaches a maximum value. The occurrence of a peak in graphene concentration agrees with previous studies on aqueous-surfactant dispersions using sonication with sodium dodecylbenzene sulfonate [263], sonication with sodium cholate [264], and turbulent shear exfoliation with detergent [6]. This optimum surfactant concentration was initially thought to be located close to the Critical Miscelle Concentration (CMC). However, it has been found to occur at much lower concentrations⁴.

For $V = 800$ mL and $C_i = 20$ mg/mL, the optimum concentration $C_i/C_{fl} \approx 10$ agrees closely with the work of Varrla et al. [6] who showed for the same initial graphite concentration and a lower process volume, $V = 500$ mL, that $C_i/C_{fl} \approx 8$. At a process volume $V = 200$ mL, a further departure from this value was observed and the optimum surfactant concentration decreased to $C_i/C_{fl} \approx 3 - 4$. This trend suggests that the liquid exfoliation process has an important role in addition to the molecular scale nanosheet-surfactant coverage mechanisms that have been the focus of previous studies. Here, the turbulent liquid exfoliation process is sensitive to volume and this impacts the final surfactant concentration that produces the highest graphene concentrations.

⁴Since Varrla et al. [6], it has been shown that the optimum surfactant concentration is in fact not dependant on the CMC or the choice of surfactant, but is impacted negatively at concentrations above 10 mM [246]. This is hypothesized to be due to preferential flocculation of larger nanosheets. This chapter follows the approach taken by Varrla et al., for comparable results.

3.4.3 Kitchen blender hydrodynamics

Although the shear rate is a function of the volume (eq. 3.1), this alone is insufficient to explain the shift in optimum surfactant choice in Figure 3.8. However, different volumes and surfactant concentrations were found to influence foam formation, structure, and stability. This, in turn, changed the fluid rheology under turbulent shear exfoliation conditions. Figure 3.9 shows the time-averaged near-wall graphite flow behaviour for the lowest volume and different surfactant concentrations investigated in this work. In the presence of surfactant, the aeration process described in Figure 3.3 leads to the formation of stable foams containing fine gas bubbles. The rotation of the impeller within the contoured base spreads the foam and graphite dispersion outwards from the centre of the vessel. This is where the highest particle velocities exist and is captured by the streamlines in the lower half of the vessel. The surfactant concentration varies the axial-circumferential components of velocity in this region $(\bar{u}_z, \bar{u}_\theta)$, altering the flow angle, α . This upward flow angle reduces from $\alpha = 60^\circ$ for the highest surfactant concentration $C_i/C_{fl} = 1$, to $\alpha = 17^\circ$ for the lowest $C_i/C_{fl} = 40$.

The increase in axial velocity component relative to the circumferential flow in the vessel is a consequence of changes to the foam rheology. As surfactant concentration is increased, the foam volume increases. Figure 3.10 shows the change in foam volume for different surfactant concentrations measured using ASTM standard procedures [271]. Between the lowest and highest surfactant concentrations in Figure 3.9, the foam volume increases tenfold. Larger foam viscosities are experienced and this effect increases the natural resistance to flow which supports self-baffling and dampening vortexing due to liquid swirl [248]. By dampening the vortexing within the vessel, the circumferential velocity component is reduced and the flow behaviour in this high shear region changes significantly.

In the upper half of the vessel, the graphite precursor that has been propelled outwards

and upwards by the impeller returns due to gravity along pathways that are also influenced by the surfactant concentration. The downward flow angle increases from $\beta = 16^\circ$ for the highest surfactant concentration $C_i/C_{fl} = 1$, to $\beta = 43^\circ$ for the lowest $C_i/C_{fl} = 40$. Smaller flow angles are observed at higher surfactant concentrations as the larger fluid viscosity reduces the axial component of velocity. The meeting of the upward and downward graphite particle flows produces different time-average flow patterns within the vessel. For $C_i/C_{fl} \leq 4$, saddle points (1) and nodes (2) were observed (Figure 3.9a-d). In locations where the axial velocity component approaches zero, preferential clustering of graphite particles occurred (Figure 3.9c). These particles have been restricted from motion in the circumferential direction due to the physical presence of the baffles. The combination of low axial velocity, high viscosity and viscoplasticity of the foams formed at high surfactant concentration also support this particle hold-up effect. The preferential clustering of graphite particles in this hold-up region is unfavourable for graphene production as the material is unlikely to be exposed to exfoliation conditions when kept away from the rapidly rotating impeller.

For $C_i/C_{fl} \geq 8$, liquid swirl becomes more dominant and the topology of the flow pattern changes. Singular points in the flow field of the measurement region are non-existent (Figure 3.9e, f). In addition to the expected change to the fluid stress fields, graphite hold-up was no longer apparent for foam flows at these surfactant concentrations. Based on these observations, it is hypothesised that foam rheology is the leading reason for the variation in optimum surfactant concentration. Although we do not have a measure of viscosity for the foams, we have directly measured what the change in rheology does to the graphite precursor material flows. The addition of surfactant has a coupled effect on turbulent shear exfoliation conditions inside the vessel. Different graphite flow behaviours have been observed which alter the turbulent shear mixing conditions at the macro-scale. Changes in mixture rheology also influence the stress fields through viscosity. The shear-rate dependent viscosity of foams can be described by a Bingham plastic model behaviour [266], $\mu(\dot{\gamma}, C_{fl}) = \tau_y/\dot{\gamma} + k|\dot{\gamma}|^{n-1}$.

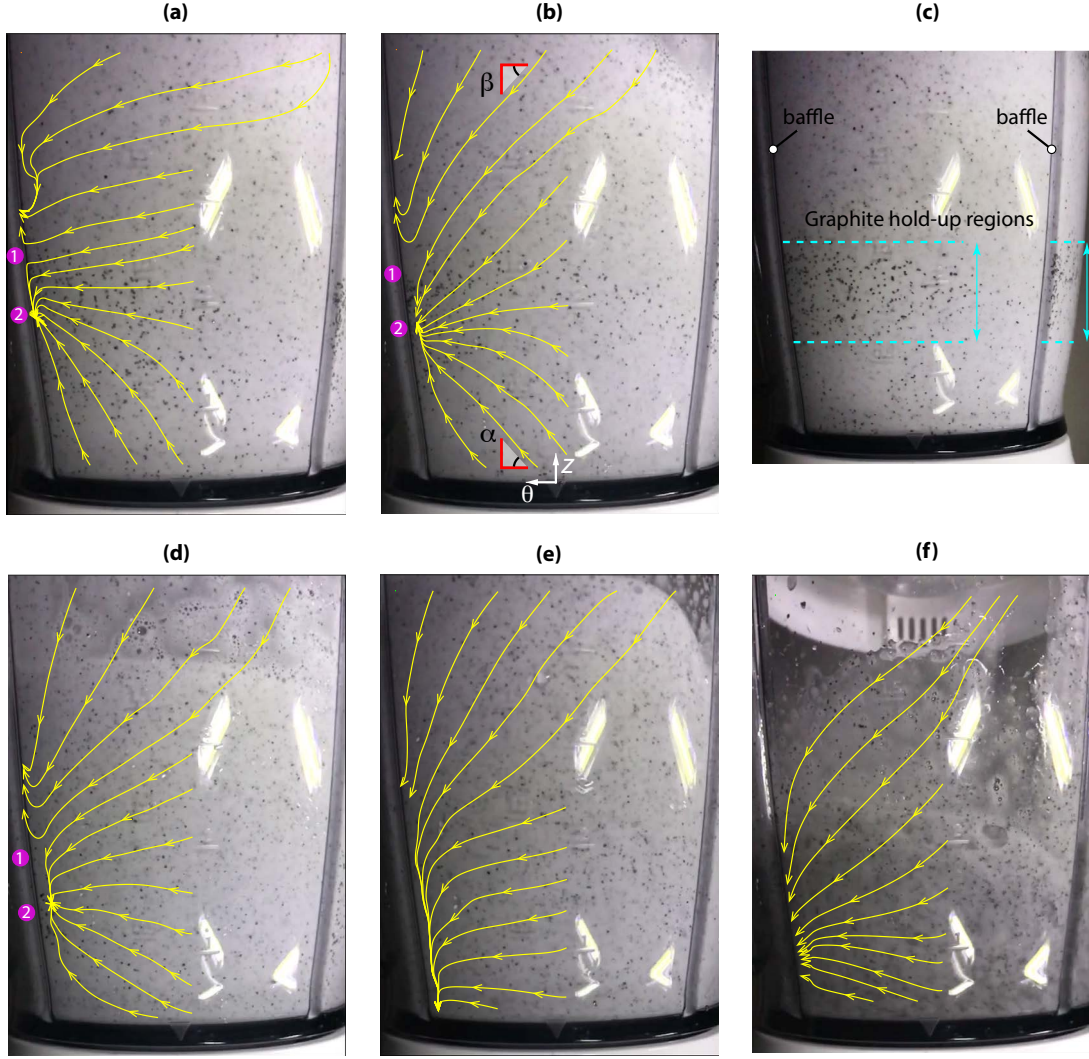


Figure 3.9: Ensemble-averaged near-wall graphite particle streamlines. (a) $C_i/C_{fl} = 1$. (b) $C_i/C_{fl} = 2$. (c) Graphite particle hold-up regions for $C_i/C_{fl} = 1$. (d) $C_i/C_{fl} = 4$. (e) $C_i/C_{fl} = 8$. (f) $C_i/C_{fl} = 40$. Streamlines have been ignored in the regions with light reflections. All data shown for $V = 200$ mL, $C_i = 20$ g/L, $\omega = 10000$ rpm. An in-depth description of the imaging setup is provided in Section 3.3.4.

Foam viscosity depends on both the shear rate and the surfactant concentration, the yield stress (τ_y), and the flow and consistency indices (k, n). Therefore, recalling $P/V = \mu\dot{\gamma}^2$ and $C_g \sim \dot{\gamma}t_m$, the concentration of graphene produced is not only sensitive to surfactant

repulsion mechanisms at the nanoscale but also the macro-scale hydrodynamics.

LPE processes, such as those demonstrated in the blender system presented in this thesis, have shown good scalability at small volumes (less than 10 litres [7, 10]). However, as the process is upscaled for industrial purposes, rheological changes at larger volumes can impact performance. In impeller-driven systems, including those based on high-shear mixing, macro-scale changes in the viscosity and flow behaviour of the suspension can alter the dynamics and amount of material exposed to regions of high shear. For example, as shear forces distribute unevenly in larger batches, the resulting flow can deviate from ideal mixing conditions. The rheological properties, including shear thinning or thickening behaviours, can compound the issue, disrupting the conditions across the mixer. This non-uniformity may reduce the efficiency of material exfoliation or increase energy consumption to maintain adequate shear forces throughout the entire volume. Overall, while LPE remains promising for small-scale production, providing a competent route to scale-out, its application to larger volumes in industrial shear mixers requires further understanding and potentially addressing of these complex flow behaviours to maintain process efficiency.

Figure 3.10 shows that larger foam volumes are generated with increasing surfactant concentration. This increases the foam viscosity as demonstrated by the observations of swirl and vortex suppression in the vessel. In Figure 3.8, there is a trend of decreasing optimum surfactant concentration with increasing process volume. Approximately twice the surfactant concentration is required to maximise graphene concentration in a 200 mL process volume compared to the 800 mL process volume. The reason for this trend is believed to be related to the differences in foam formation at small and large process volumes.

The amount of foam generated per unit volume of water (V_f/V) for processes with $V \geq 400$ mL is double that which is formed at $V = 200$ mL for the same surfactant concentration (Figure 3.10). In the smaller volume process, the impeller is located just

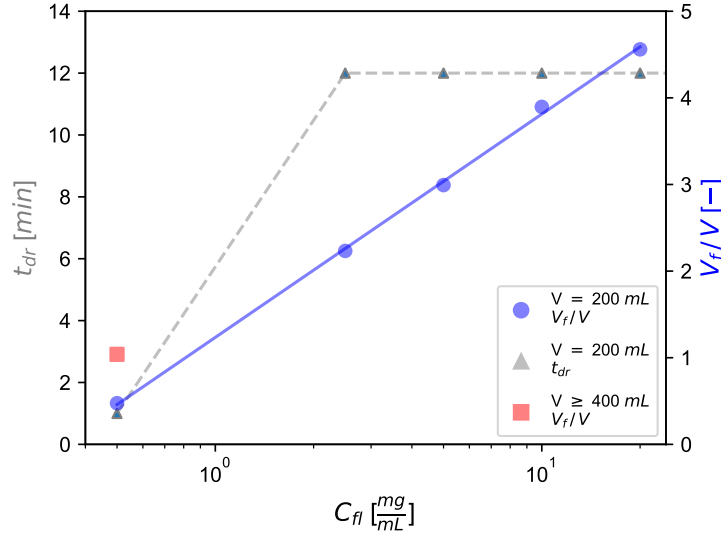


Figure 3.10: Effect of surfactant concentration on foam volume (V_f) and liquid drainage time (t_{dr}). Experiments were performed at $\omega = 10000$ rpm, $t = 30$ s and without graphite.

below the liquid interface on start-up. The aeration process is less effective at producing bubbly flows throughout than the larger process volumes (e.g. Figure 3.3). Less liquid-gas interface area per unit volume is available for the accumulation of surface-active agents. As a result, the larger volumes require $\approx 50\%$ less surfactant to generate the same foam levels as $V = 200$ mL during turbulent exfoliation. Although this adds another variable to consider for surfactant selection, it also presents an opportunity to design batch processes for low levels of surfactant usage. An advantage of this flexibility for graphene and other 2DMs is that it could reduce post-production washing and annealing requirements that are needed to remove residual surfactant from the product and recover material properties [263].

3.4.4 Inline production monitoring

The multi-phase flows in turbulent shear exfoliation of layered materials in aqueous-surfactant dispersions pose a challenge for inline material characterisation using UV-vis-NIR spec-

troscopy. In section 3.3.3, a provisional assessment and validation of the fibre optic probe system was carried out using water and blue dye. Bubbly flows within the vessel during turbulent mixing at $Re \approx 2.6 \times 10^6$ produced large fluctuations in the optical signal that required sampling to be performed during OFF times in the process. Using water, or water and blue dye, the gas bubbles coalesce within seconds of stopping the mixing process and sampling can begin almost immediately. This behaviour is shown in Figure 3.11.

The addition of surfactants, and the subsequent formation of foams, requires a change in the sampling interval time as bubble coalescence is suppressed. We found this to depend on the liquid drainage time (t_{dr}) which describes the time it takes for liquid to drain out of the foam structure when the process is stopped. In the current study, the t_{dr} was determined based on the liquid returning to 85% of the original fluid height in the vessel, $h_L(0)$ (Figure 3.1c). Figure 3.10 shows the liquid drainage time for different surfactant concentrations. For $C_{fl} > 1$ mg/mL, the drainage time went beyond 10 minutes. In order to limit the sampling interval time, therefore, inline spectroscopy was performed on dispersions containing $C_{fl} \leq 1$.

For water-surfactant mixtures, the foam covers the probe for $\approx 40 - 50$ s after the impeller is turned OFF (Figure 3.11). Without graphite ($C_i = 0$ mg/mL), the extinction measurements return to the baseline after 2 mins ($A = 0$). When graphite particles are added ($C_i = 1$ mg/mL) and exfoliation begins (ON), the average and fluctuations in extinction increase substantially as both graphitic material and gas bubbles flow across the sensor measurement zone. The addition of the layered precursor resulted in a slightly longer period of time for liquid drainage (≈ 60 s). This was followed by a stable decay in extinction, reaching a constant value within 3 minutes of stopping the exfoliation process. The difference in extinction between the baseline and this settled value shown in the inset plot in Figure 3.11 is a result of exfoliated graphitic material in dispersion.

Exfoliation was performed for $t = 30$ mins with inline characterisation to investi-

gate if the changes in extinction discussed above correlate with changes in concentration measured ex-situ of few-layer graphene. The protocol for performing liquid exfoliation was altered to 1 min (ON) followed by 3 mins (OFF) to permit *in situ* measurements within the heterogeneous dispersions. Agreement was found between the inline monitoring result and the graphene concentration measurements obtained from manual sampling and ex-situ characterisation as shown in Figure 3.12a. This suggests the inline characterisation approach and sampling procedures outlined in this work could provide a useful means to estimate production rate in batch exfoliation systems where multi-phase flows exist. These flows preclude real-time information on graphene content using this inline approach. By incorporating inline measurements, this approach offers significant benefits for process control, especially in batch exfoliation systems where multi-phase flows present challenges for real-time monitoring. Traditional methods of characterisation often suffer from delays due to the need for manual sampling and ex-situ analysis, limiting their ability to provide immediate feedback for process optimisation. In contrast, the inline approach enables continuous monitoring, and provides allowing for timely adjustments to the exfoliation process, which can help improve the overall yield and quality of the material. Additionally, it mitigates the variability that arises from sampling and manual handling, ensuring a more consistent production process. The capability to gather real-time information about the concentration of graphene in such complex systems suggests that inline characterisation could be a critical tool for scaling up exfoliation processes in industrial applications. The foam drainage time requirements for monitoring also increases the overall process time. However, the high sampling frequency shown here (1/60 Hz for ON process time) may not be necessary for industrial production systems. For example, four inline measurements required 12 min whereas four *ex situ* measurements took ≈ 120 min to prepare and analyse.

High-throughput batch quality control is another important area for process scale-up. The properties of graphene and other 2DMs are intrinsically linked with the nanosheet

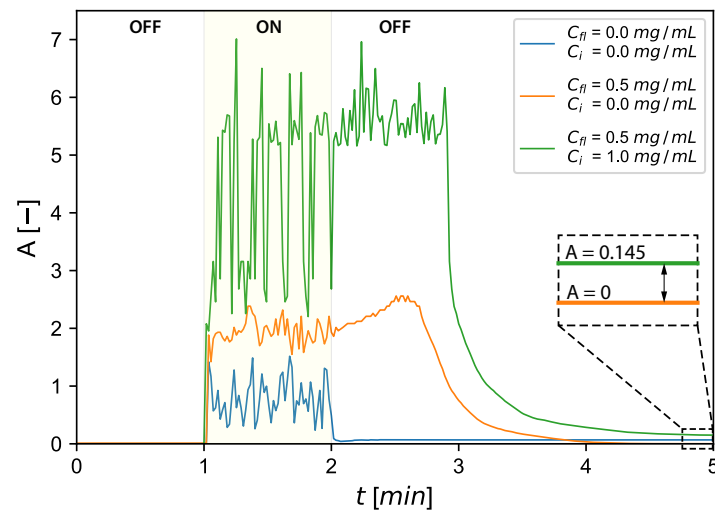


Figure 3.11: *In situ* spectroscopy measurements of extinction at $\lambda = 660$ nm before, during and after turbulent mixing of water, water-surfactant, and water-surfactant-graphite dispersions. Turbulent mixing occurred between $1 \leq t \leq 2$ minutes. Experiments were performed at $\omega = 10000$ rpm and $V = 200$ mL.

thickness or average number of atomic layers, N_{FLG} . To explore if inline spectroscopy could detect changes in layer number, a few-layer graphene dispersion that had been produced in the kitchen blender and centrifuged to remove graphitic material was re-introduced. The process was operated above the critical exfoliation criterion, $\dot{\gamma} > \dot{\gamma}_c$, with the aim of reducing N_{FLG} over time. The extinction spectra was measured before and after the process using *ex situ* UV-vis-NIR spectroscopy. Applying spectroscopic metrics from the work of [240], the average layer number was found to reduce by $\Delta N_{FLG} = -0.8$ over the 25 minute process time (Figure 3.12b). In parallel, *in situ* spectroscopy measurements were acquired following the same 1 min ON / 3 min OFF procedure previously described. Changes in the spectroscopic metric (A_{550}/A_{\max}) that correlate with a reduction in average layer number over time were also observed. Interestingly, this shows that there is a slower rate of change after $t = 10$ mins and highlights an advantage of performing *in situ* monitoring as exfoliation proceeds. Depending on the material application and quality control requirements, the batch exfoliation process could be optimised for tuning layer number while also minimising energy use by avoiding prolonged process times.

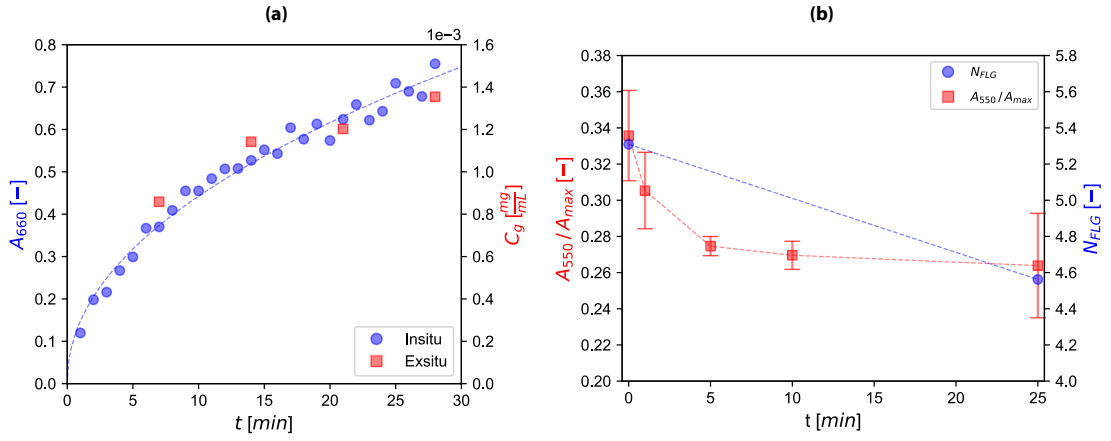


Figure 3.12: (a) Comparison between *in situ* extinction measurements at $\lambda = 660$ nm and graphene concentration with time. Experiments were performed at $\omega = 10000$ rpm, $V = 200$ mL, $C_i = 1$ mg/mL and $C_i/C_{fl} = 2$. (b) Reduction in average number of atomic layers (N_{FLG}) for a few-layer graphene dispersion undergoing turbulent exfoliation. *In situ* measurements of the extinction ratio (A_{550}/A_{max}) corresponding to changes in few-layer graphene spectra with time. Experiments were performed at $\omega = 10000$ rpm, $V = 200$ mL, $C_g = 2.61 \times 10^{-3}$ mg/mL and $C_{fl} \approx 1$ mg/mL.

3.5 Conclusions

Foams can form during turbulent liquid exfoliation of layered materials in aqueous-surfactant dispersions. In this chapter, the impact of foam flows on graphene production and inline spectroscopy has been explored using a kitchen blender to perform batch exfoliation. The optimal surfactant concentration for few-layer material production was found to vary with process volume and starting concentration of flake graphite precursor. Particle image velocimetry measurements on graphite precursor particles revealed that this can be attributed to the hydrodynamics of the batch exfoliation process and the mixture rheology. Foam volume and rheology changes with surfactant concentration and process volume, altering the macro-scale flow behaviour that is central to the production of graphene when using turbulent shear exfoliation.

The presence of stable foams, persistent gas bubbles and precursor particles also complicates analysis and inline 2DM characterisation during exfoliation in aqueous-surfactant dispersions. A measurement protocol has been developed for obtaining concentration and average layer number information during the exfoliation process. Combined with the insights on the hydrodynamics of batch exfoliation in aqueous-surfactants, the findings support the advancement of resource-efficient batch processes with embedded material quality control. Due to the variability of Fairy liquid as a surfactant, the results of this chapter are inherently more variable than the results of Chapters 2 and 4, which used NaC surfactant. This much more reliable choice is keeping with trends in the literature [246]. Additionally, another point of comparison is that the work in this chapter was conducted with a simple, static, phase-angle controlled blender, making the speed less reliable and prone to instabilities. Regardless, the findings are reasonable though they do demonstrate larger variability than those in later works (Chapters 2 and 4).

These findings highlight how foams, influenced by surfactant concentration, impact flow characteristics and measurement accuracy, especially during complex, high-shear mixing processes. In the following chapter, we will evaluate how these mixing conditions drive particle breakage, discovering the broader implications on material production efficiency.

4. Breakage Analysis and Modeling

Title of publication	Predicting graphene production with population balance modelling
Paper Information	(2025) Carbon, p. 119687.

Additional Contributors	
Sofia Marchesini ^a	Review, key support with NMR and Raman measurements.
Keith R. Paton ^d	Review, key support with Raman measurements.
Andrew J. Pollard ^d	Review, key support.
Jack Sykes ^{b,e}	Supported some PEPT data processing.
Dawid Hampel ^b	Key support, performed LoR acquisition during PEPT experiments.
Chris. Widows-Yule ^{b,e}	Review, supported PEPT measurements.
Tzany Kokalova Wheldon ^b	Review, supported PEPT measurements.
Jennifer Burt ^c	Supported laser diffraction measurements and hydro insight imaging.
Diogo Fernandes ^c	Supported laser diffraction measurements and hydro insight imaging.
Konstantinos Despotelis ^d	Conducted SEM of graphite particles.
Philip Davies ^a	Review.
Jason Stafford ^a	Review, edits.

^a School of Engineering, University of Birmingham, Edgbaston, Birmingham B15 2TT, UK.

^b School of Medical Physics, University of Birmingham, Edgbaston, Birmingham B15 2TT, UK.

^c Malvern Panalytical Ltd., Grovewood Road, Worcestershire, Malvern, WR14 1XZ, UK.

^d National Physical Laboratory, Hampton Road, Teddington, Middlesex, TW11 0LW, UK.

^e School of Chemical Engineering, University of Birmingham, Edgbaston, Birmingham B15 2TT, UK.

4.1 Foreword

Switching from characterisation, the ongoing production of 2DMs through top-down processes also hinges on the ability to understand and predict the processes that lead to material yield. In this chapter, by monitoring changes in the distribution of graphite particles as they undergo breakup in a top-down LPE process, we show that statistical PBMs are a feasible and effective technique for establishing yield and future production in liquid phase exfoliating processes of any material quantity of interest including nanomaterial. To achieve this distinction, a combination of laser diffraction and few-layer graphene concentration measurements are used to recover the material distribution and fit the PBM over all scales respectively. This fitted PBM can then be used to examine production over time, or coupled with Nuclear Magnetic Resonance (NMR) proton relaxation measurements to recover surface area scaling with particle size. Furthermore, to examine the dynamic process conditions inside the vessel, radioactively labeled large graphite flake and density matched glass beads functioned as tracer particles for Positron Emission Particle Tracking (PEPT), a Lagrangian technique allowing for ergodic measurements of averaged quantities inside the exfoliating system. Collectively, these results and models provide insights on the breakage mechanisms and fluid dynamics that underpin LPE, and provide direction for their intensification and optimisation.

Chapter Aims and Objectives

This chapter aims to understand, analyse and model how graphite breaks down into useful, few-layer, 2DM inside a kitchen blender. Gaining a high-level understanding of this process is crucial for improving the production of 2DMs and expanding their practical applications towards water treatment. This aim can be summarised into the following objectives:

- Assess the changes in particle size as graphite breaks into its smallest components, and identify any patterns in how these particles break apart over time.
- Create a model that can represent and follow the full range of particle sizes during the blending process, and under different impeller conditions.
- Establish the use of PEPT as a method for tracking graphite and recreating the fluid conditions during the blending process.
- Use PEPT to visualise how shear forces are distributed within the blender. If possible, combine this data with the model to provide new insights into the dynamics of the exfoliation process.

4.2 Introduction

Graphene and related 2DMs have garnered substantial attention since their extraordinary properties and mechanical isolation were demonstrated by Novoselov et al. [238]. Although these materials and their larger stacked counterparts (nanoplatelets) are making their way into diverse applications including construction [272], environmental remediation [273], and energy storage [274], the challenge of efficient and controlled large-scale synthesis persists. Key issues revolve around scaling production of 2DMs without introducing structural defects which would hinder their performance, maintaining material quality control of processes, and optimising process yields for energy and resource efficiency. Presently, manufacturing technologies are classified into two categories: top-down approaches disassemble a 3D precursor material (such as graphite for graphene), whereas bottom-up methods directly synthesise 2DMs from their atomic foundations. It has been shown that industry can produce material at scale using top-down processes, which involve applying an external force to break apart the layered material into smaller particles, and eventually nanomaterial. Numerous techniques exist to break these materials, encompassing chemical [275], electrochemical [276] or mechanical [7] methods. Above all, mechanical processes warrant consideration as they are generally applicable to all 2DMs, do not significantly alter the chemical structure of the nanomaterial, and can be inherently sustainable by avoiding harsh chemicals and oxidising agents. As exemplified by the original scotch tape method, a form of micro-mechanical cleavage employed by Novoselov et al. [238], force is directly applied to overcome the van der Waals forces. However, production becomes challenging at scale, as one cannot easily apply forces to all sheets at once without altering the nanomaterial structure. In practice, forces on nanoparticles and particle interactions can alter the size, structure and morphology of the exfoliated material [277]. This juncture represents a critical point in the pursuit of scalable, repeatable, and high-quality 2DM production systems.

Liquid Phase Exfoliation (LPE) via mechanical force is a low cost and scalable option [165]. This methodology disperses particles in a liquid, where under the exposure of a high shear environment, they break apart into smaller material fragments including nanosheets. The force necessary to produce such an environment can be achieved by a variety of different means, such as through cavitation [10], ultrasonication [155], and turbulence [7]. Intensive shear processes can produce reasonable yields ($\approx 10\%$ wt) of few-layer material at the cost of high energy input, material blockages and material quality [9, 11]; whereas in milder processes such as Taylor-Couette devices [168], these points are reversed (lower yield, low energy input, avoidance of blockages, and high-quality few-layer material).

Discovering new systems for LPE and scaling their performance from lab to industrial scales is difficult without a description of the underlying breakage processes. Therein, predicting the few-layer material yield achievable through some exfoliation technique ahead of empirical observations can be immensely useful before any financial commitment is made. Such methods to analyse production are still in their infancy. There have been attempts to describe LPE at the nanosheet scale, defining the atomic interactions at which it occurs [261, 277, 278]. Empirical models can be applied to estimate certain material parameters such as the critical shear rate [7] and material stability [241], with the advantage that it inherently captures the numerous parameters that affect synthesis performance (e.g., precursor quality, Hansen solubility parameters, solvent viscosity, surface tension, etc.). Beyond this, there are no attempts to describe production according to the fluid dynamics present in the process except by ascribing how production scales according to key hydrodynamic parameters of the system [7, 168].

The largest non-fluidic effects on the yield are attributed to the dispersing solvent, and careful choice of dispersant is essential [241, 246]. Barring this factor, synthesis is predicated by the internal dynamics of the system, where precursor particle breakages occur and directly lead to the production of nanomaterial. This breakage can take multiple different forms, but

is dependent on how the process imparts energy to the system. For instance, under cavitating fluid conditions, through high-power probe sonication or jet impingement, precursor particles are shattered and nanosheets can fragment [279]. In the case of 2DMs, this energy can lead to the development of edge defects through the formation of kink bands as sheets separate from the graphite precursor [160]. Less intensive methods, such as LPE in Taylor-Couette cells, produce small quantities of high-quality material through steady attrition of the precursor material [168].

The Population Balance Model (PBM) is a well-established statistical method for exploring the dynamics and relationships of populations applicable to numerous fields. As a system of equations, it defines the dynamics of a population in time and space under a given system and initial conditions. In the study of particle flows, it is a robust and well explored model often applied to evaluate production of aggregates and pharmaceuticals. As the defining trait of LPE is the destruction of precursor particles into their 2DM constituents, there is potential scope for applying PBMs to explore and predict the dynamics of this multi-scale synthesis system. The only prerequisite to applying this type of model is that enough information is collected on the particles in suspension across all scales of interest. An example of a PBM used in this work is given in Figure 4.1e. The PBM is fitted with only one internal dimension, the particle's volume based diameter x_v , and is observed changing in time. Once the PBM is fitted to the PSDs and the dynamics of breakage are known, determining production of any particular size of material over time can then be ascertained simply by integrating over the fraction of interest. Given there are industrial uses for nanoplatelets ($\gg 10$ atomic layers) and few-layer materials (≤ 10 atomic layers), this provides several practical advantages for process intensification, quality control, and end-user applications.

In this study, we present a PBM approach to predict the distribution of particles over time for liquid exfoliation of graphite into graphene related nanomaterial. We combine several material characterisation techniques that span from the precursor particle down to the

nanomaterial scale, exploring the synthesis space and validating the model. The results show that this pure PBM approach implicitly captures the breakup characteristics of turbulent shear exfoliation processes, offering a method to predict and optimise the mechanochemical synthesis of graphene and related materials. Furthermore, we reveal underlying details about this shear exfoliation process using Raman spectroscopy as well as Positron Emission Particle Tracking (PEPT) [280], the latter of which tracks the motion of graphite particles as they move through the system. Collectively, the observations in this work provide insights on the hydrodynamics of mechanochemical synthesis processes for layered materials, and a pathway for predicting material yield performance and important material outputs.

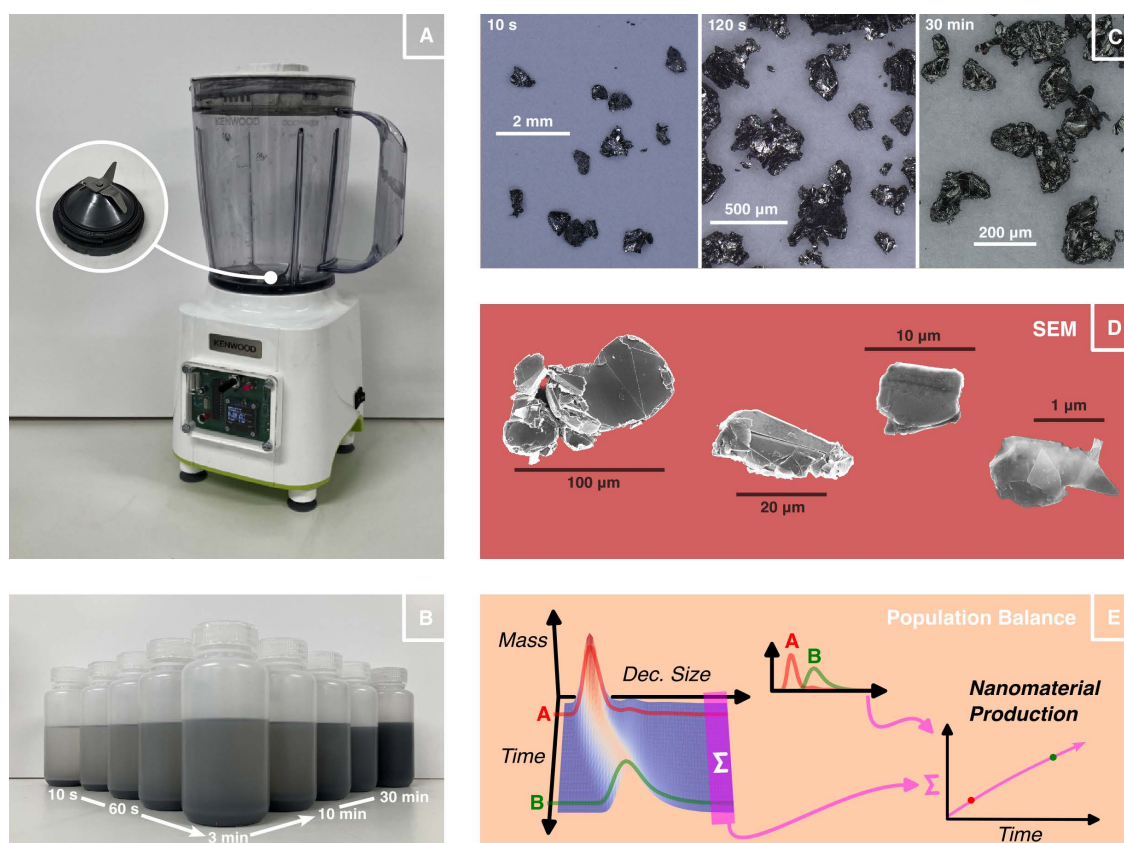


Figure 4.1: Graphene production and modelling approaches. (A) Impeller-driven blender used in this study, modified for process control [3]. (B) Progression of samples exfoliated from 10 s to 1800 s duration, showing gradual darkening of the graphite/graphene suspensions with time. (C) Optical microscopy of the bulk material at different exfoliation times. (D) Scanning Electron Microscopy (SEM) images showing the progression of breakage towards smaller particles (all samples analysed were highly polydisperse). (E) Surface plot illustrating the Population Balance Model (PBM) used herein. An initial distribution of particles (in red) is gradually progressed forwards in time under the influence of a shear exfoliating system. After a period of exfoliation, the original Particle Size Distribution (PSD) gradually transforms as particles are destroyed and birthed into smaller size fractions (in green). Height and colour of the surface indicate the amount of material at the point specified. Summing the mass values of the nano-sizes yields an indication of the amount of nanomaterial produced.

4.3 Methods

4.3.1 Liquid Phase Exfoliation

A modified kitchen blender (Kenwood BLP31.d0wg) was used to conduct all LPE experiments (see Figure 4.1a). The blender is fitted with a ‘jug’ vessel, with four blades on the impeller assembly set in opposition to each other, of radius ~ 30 mm. To avoid overheating the equipment, it is operated in set periods of 1 minute *on* to 1 minute *off*, where the reported time is the total time *on*. A fixed experimentation volume of 200 mL is maintained throughout. The mixer can reliably maintain stable speeds between $1000 \leq \Omega \leq 18500$ rpm. Modifications to the blender centre around maintaining a stable impeller speed, and an in-depth description of the system and its construction can be found elsewhere [3].

4.3.2 Materials

Graphite (Sigma Aldrich flake graphite, product code 332461), with a mesh size +100 ($> 149 \mu\text{m}$) was chosen as the precursor material and has been used extensively in the literature for LPE studies. Unless otherwise stated, the initial concentration of graphite was 20 mg/mL. An aqueous-surfactant mixture comprising of de-ionised water (200 mL) and NaC (Sigma Aldrich, product code C1254) was used as a solvent for all tests. The concentration was fixed at the CMC of 4.3 mg/mL. NaC is a well documented surfactant in the manufacture of 2DMs, and as a bile extract from natural sources has a low environmental impact (biodegradable), and is non-toxic at low concentrations [281, 282].

As this chapter investigates particle hydrodynamics and breakup mechanisms, particle-solvent and particle-particle interactions in turbulent flows were examined by comparing with

the one-way, two-way and four-way coupled regimes identified by Elghobashi [283]. Graphite dispersions considered in the literature span from low loading (dilute) to dense particulate flows. Most analyses in the literature takes place for dilute or moderately dense particle flow interactions, and typically demonstrate precursor material affecting nanomaterial production linearly, i.e. $C \propto C_i$. With a similar system to that used here [2], Varrla et al. [6] demonstrated that under high precursor loading (100 mg/mL) this relationship can break down, suggesting a change in regime where both dense flow and solvent effects may impact yield. Considering the general particle-laden turbulent flow regime map described by Elghobashi [283], typical particle flows in LPE systems were estimated to span from low loading (dilute) to denser dispersions where four way fluid-particle interactions exist (Figure 4.2). Most analyses of LPE in the literature takes place slightly below or where four-way particle interactions become important. Other effects in the aqueous-surfactant mixer system used in this study include liquid-gas flows (e.g., bubbles) and foam formation due to aeration and the presence of surfactants. Nonetheless, this simple analysis of the flow regime is sufficient to identify the need to consider particle interactions as potential participants in the break-up process, and include the correct graphite loading for PEPT measurements.

To avoid introducing inconsistencies in sampling, each test was conducted entirely independently, on a batch by batch basis. In the case of UV-vis-NIR concentration measurements (Section 4.3.5) and Raman spectroscopy (Section 4.3.5), exfoliated material underwent a short separation process before analysis (see *Supernatant Sampling*, below).

Raw Sampling

Raw sample indicates that the material used for the measurement was taken directly from an exfoliation process, immediately after the process time concluded. In all cases, independent samples and experiments were executed to ensure no sampling or volume discrepancies were

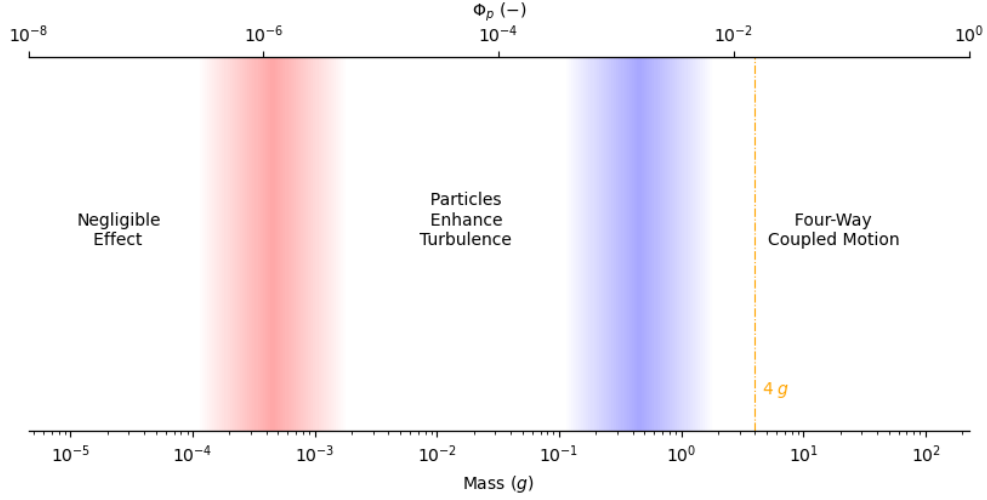


Figure 4.2: An estimate of the particle-fluid regimes within the exfoliation system. Graphite loading of 20 mg/mL is indicated by the orange line.

introduced over the measurement. After a period of storage, a light stir is required before measurements such as LD or NMR, to ensure a homogeneous sample.

Supernatant Sampling

Supernatant samples undergo centrifugation to separate the larger sediment and smaller nanomaterial. To achieve this:

- Samples were taken directly from a finished exfoliation run and placed into 6×15 mL centrifuge tubes.
- These six samples were centrifuged at 380 Relative Centrifugal Field (RCF) for 45 minutes.
- Without disturbing the settled sediment, the top 5 mL of each tube is recovered for a final mean thickness of ≈ 5 atomic layers.

These supernatant samples were used for UV-vis-NIR concentration measurements as well as for Raman spectral analysis. This method of separation does not precisely separate the bulk material from the few-layered material, with some bulk material being entrained during separation, evidenced by the graphitic behaviour in the early Raman measurements.

4.3.3 Laser Diffraction

A rapid and non-invasive technique, LD measures the angle and intensity of light scattered by particles. Graphitic materials for characterisation by LD were taken directly from their *raw* state to ensure homogenous sampling and measured using Malvern Panalytical Particle Size Analyser Mastersizer 2000 (Figure 4.9a). These measurements were used as inputs for the PBM, and were validated against other independent measurements taken using a Malvern Panalytical Particle Size Analyser Mastersizer 3000, with the additional Hydro Insight Dynamic Imaging accessory module. The Hydro Insight module permitted *inline* analysis of particle shape and size in tandem to LD measurements. These measurements facilitated prompt and accurate reconstruction of the bulk particle distribution by volume. Samples for LD were measured directly from their raw state (i.e. without separation) to reduce any sampling uncertainty caused by centrifugation and separation, and lightly stirred to ensure all particles flow through the size analyser flow cell. Mastersizer 2000 measurements were agitated through the system with a stirrer speed of 1500 rpm using the Hydro SM manual liquid sample dispersion unit. Mastersizer 3000 measurements were agitated through the system at a higher 2500 rpm using the Hydro MV automated liquid sample dispersion unit, though this change had a negligible impact on the result.

Central to tracking production via the PBMs is obtaining a good estimate of the PSD across all scales. This can be challenging for polydisperse cases: when using LD, as larger particles can obscure smaller particles, or the optical characteristics of the nanomaterial may

differ from the bulk material [284–286]. Hence, interpreting volume-based PSD information for non-spherical particles obtained through LD is not always straightforward. Effects due to changing particle shape are mitigated in part as the shape does not drastically change as the particles progress from large flake, to small grains to nano-platelets. The dominant method of determining PSDs from light scattering is Mie theory, which assumes spherical particles. Work on the validity of LD for such dispersions has been conducted by Rabchinskii et al. [285]. This showed that Mie theory breaks down in the case of polydisperse GO at low lateral flake sizes ($< 1 \mu\text{m}$), due to the edge-scattering effects of GO, with respect to the number of particles in solution. If instead of number, one factors according to particle volume, the relative error becomes much smaller (with x_v^3 , volume to number), and Rabchinskii et al. note that Mie theory is still able to capture the mean size with respect to number of particles with good accuracy. Further, they demonstrate that larger particles are not affected by this scattering, suggesting this approach is extendable to graphitic suspensions used in this study. Amaro-Gahete et al. [284] corroborate the results of Rabchinskii et al. [285], noting that PSDs obtained through LD are biased towards larger sizes. Amaro-Gahete et al. [284] also note that distributions produced by nanoparticle tracking analysis and asymmetric flow field fractionation are useful alternatives to LD for more precise particle sizing across the lower size ranges, though the maximum size measurement prevents a full picture of the distribution required for the analyses performed in this work. Though LD measurements can provide insights to describe how larger material breaks, it alone does not provide enough information to uncover information on the nanomaterial. This is predominantly due to the volume weighting, as for highly polydisperse samples such as these, larger particles will obscure smaller particles during measurement. Further, as LD can only infer size and surface area statistics, certain material behaviours such as aggregation or agglomeration would only be detectable using more advanced spectroscopic techniques such as SEM or Raman Spectroscopy. To overcome this limitation, and bridge the gap between the micro-scale and nanoscale graphitic materials, other characterisation approaches were required

(UV-vis-NIR spectroscopy, for example) to measure the contribution of the nanomaterial particles produced by the process.

4.3.4 Hydro Insight Imaging

Hydro Insight was used to perform direct measurements of material size and shape from high-speed images taken of the graphitic particles during LD measurements (Figure 4.3). These provided an additional level of certainty to the information given by LD and allowed for the acquisition of shape information. Figure 4.3 displays a selection of particle images taken at different process times, where the shift in particle size is readily apparent.

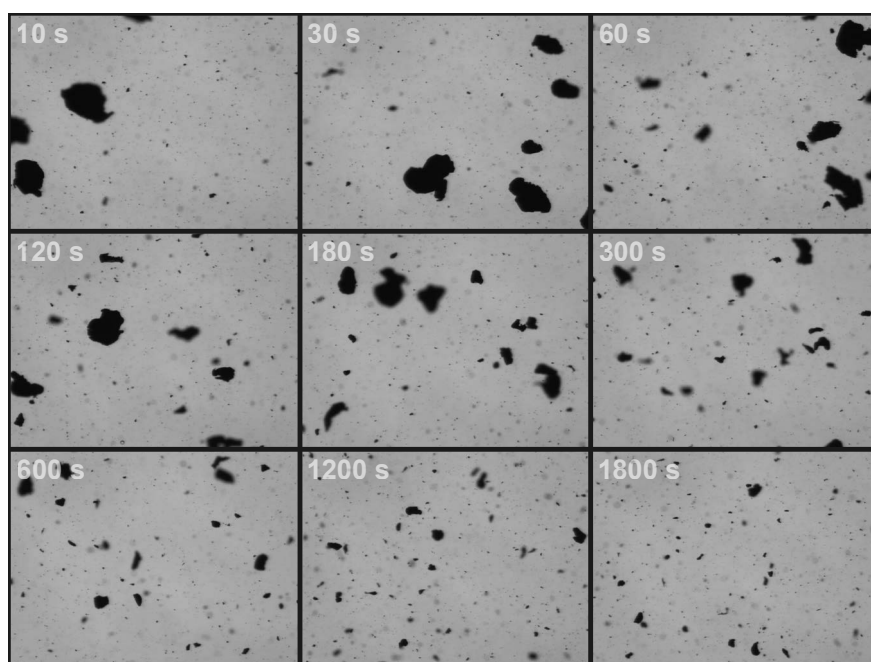


Figure 4.3: Hydro insight imaging, at different process times (10 s \rightarrow 1800 s). All images are taken at the same magnification, using the Hydro Insight low magnification lens (measurable size range - 10 μm to 800 μm).

For particle size, Hydro Insight mirrored the findings of the LD using the Hydro Insight low magnification lens, with a minimum measurable 10 μm size. After this point,

the LD captured the PSD of material smaller than $10\text{ }\mu\text{m}$, which served as a validation of the technique for these larger sizes. Analysing the images for particle shape, there seemed to be very little variation in particle shapes at different processing times, with the overall smoothness and circularity varying negligibly between the samples. Testing with higher magnification lens showed a similar trend and stability at the times measured (20 and 30 min) in the smaller material, limiting to a minimum measurable $1\text{ }\mu\text{m}$ size. This gives good confidence that over this short processing period of 30 min, there is no substantial difference between particle shapes in the larger material $> 1\text{ }\mu\text{m}$.

Figure 4.4 provides quantitative detail to support the comparison. Here, both Equivalent Circle Area (ECA) and Mean Radius Circle (MRC) diameters were selected to correlate the particles' volume-based diameter x_v . Diameter measurements based on the ECA are calculated using the total silhouetted area of the particle, which is then used to determine the equivalent diameter. The MRC diameter is established by taking the imaged particles' centroid and measuring the distance to the perimeter at set intervals (36) around an entire revolution, and taking a geometric average to return the final diameter. These measurements followed the size measured by LD closely, until size became a limiting factor in the image analysis with a minimum measurable particle size of $10\text{ }\mu\text{m}$. Overlaying LD (volume weighted) and Hydro Insight image analysis (weighted towards number of particles), a good agreement is observed. Smoothness and circularity behaved similarly, and the distributions of circularity in Figure 4.4 show a negligibly small shift in circularity towards longer processing times. Smoothness and circularity are defined with respect to the apparent particle area A , perimeter P , and bounding circle diameter d .

$$\text{Smoothness} = \frac{4\pi A}{P^2} \quad \text{Circularity} = \frac{4A}{\pi d^2}$$

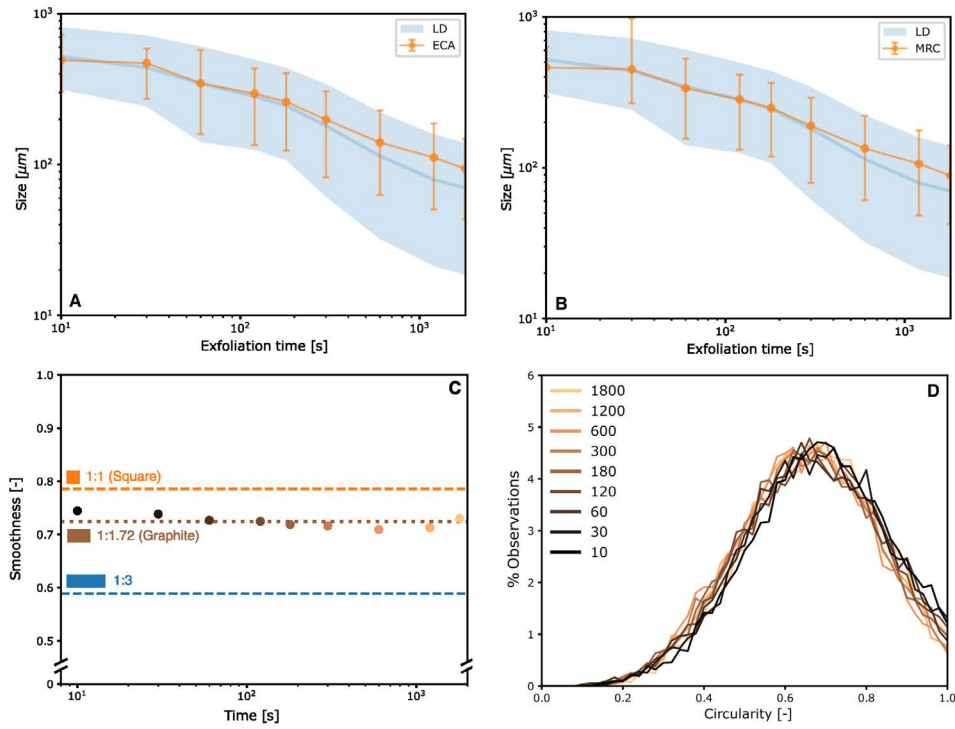


Figure 4.4: Hydro Insight Imaging accessory module to the Mastersizer 3000 was used to collect statistics on various particle size metrics using the low magnification lens. In (A) and (B), the measured Equaivalent Circle Area (ECA) and Mean Radius Circle (MRC) diameters are plotted alongside the LD Mastersizer 3000 measurements. Error bars and banded areas represent the 10th percentile and 90th percentile, with the central lines and markers representing the 50th percentile. (C) Mean particle smoothness is plotted against exfoliation time and alongside values for a simple square and rectangle of aspect 1:3. (D) The entire distribution of circularity for different exfoliation times are plotted together.

4.3.5 UV-Visible-near-Infrared Spectroscopy

Similar to chapters 3 and 2, the concentration of few-layer graphene was determined in dispersion using UV-vis-NIR spectroscopy (Perkin Elmer Lambda 365). For this, separated supernatant samples were used. In cases where the material concentration in the supernatant was too high to measure, the supernatant was diluted at a ratio of 1 : 2 (sample:solvent) to maintain extinction levels below ≈ 1 a.u. (as per the manufacturers recommendations). The concentration of graphene dispersions was then determined using the Lambert-Beer law and with a measured extinction coefficient of $\epsilon_{\lambda=660 \text{ nm}} = 1521 \text{ mg mL}^{-1} \text{ m}^{-1}$ [245]. The extinction coefficient was obtained by filtering the nanosheets through a 220 nm pore-size Polytetrafluoroethylene (PTFE) membrane, oven-drying to remove the solvent, and measuring the mass of the dried product. Average layer thickness was also estimated from the extinction spectra using the empirical correlations obtained previously for liquid-exfoliated few-layer graphene by Backes et al. [240]. Across all samples analysed, the average was found to be between 4 and 7 atomic layers.

4.3.6 Nuclear Magnetic Resonance

Nuclear Magnetic Resonance (NMR) proton relaxation measurements were performed using an approach outlined for graphene dispersions [287]. NMR as a technique, magnetically perturbs the solvent molecules in solution, and then measures how long it takes for the molecules to return to equilibrium, known as the relaxation time. In solution, solvent molecules take longer to reach equilibrium than molecules adsorbed onto particles. As particle breakages produce new surface area, total surface area in solution increases, thereby leading to a reduction in relaxation time. Spin-spin (T2) relaxation measurements were performed with an Acorn Area benchtop NMR from Xigo Nanotools operating at ~ 13 MHz. The exact

relation between the measured relaxation time T_2 , specific surface area \mathbf{A} , the relaxation rate R_{av} and solvent parameters is given in Equation 4.1 [287, 288].

$$\frac{1}{T_2} \equiv R_{av} = \psi \mathbf{A} K_{\mathbf{A}} + R_b \quad (4.1)$$

Where ψ is the volume fraction, $K_{\mathbf{A}}$ is the specific surface relaxivity constant and R_b is the relaxation rate of the solvent alone. To ensure representative aliquots of the system, *raw* samples were agitated for 5 mins in a light sonicating bath to break up any agglomerates formed over the storage period. Immediately afterwards, gentle agitation must be maintained during sampling to ensure a representative distribution is taken and introduced to the small 1.5 mL NMR tubes. Finally, the NMR proton relaxation measurement was taken, showing little variance between samples. This process is essential, as proper sampling keeps the sampled ψ representative of the entire batch. Though challenging, and highly dependant on the method of separation, following this procedure ensured repeatable readings. It was evident throughout that issues were predominantly caused by the largest particles, which would both create blockages during sampling and sediment quickly if not agitated, changing the sample concentration within the small NMR tubes, and impacting the overall measurement.

4.3.7 Raman Spectroscopy

Supernatant samples centrifuged at 380 RCF for 45 min were vacuum filtered through an alumina membrane with 20 nm pore size. Raman spectroscopy was undertaken with a Renishaw inVia Qontor Raman spectroscope, using a 532 nm laser employed with a 50 \times objective lens. A map with a 100 $\mu\text{m} \times 100 \mu\text{m}$ area (5 μm step size) was measured, for a total of 441 spectra per sample. The final averaged spectra were low pass filtered to reduce

the higher frequency noise in the data.

4.3.8 Optical Microscopy

Optical microscopy of bulk particles was conducted using a Keyence VHX 7000 optical microscope, using a white paper background. Particles were prepared at $\Omega = 11500$ rpm impeller condition at different processing times from the resulting sediment. This sediment was separated from natant and allowed to evaporate.

4.3.9 Scanning Electron Microscopy

SEM images were taken using a Zeiss Supra scanning electron microscope by measuring secondary electrons (in lens detector, 5 kV accelerating voltage). Samples were processed at the $\Omega = 11500$ rpm impeller condition, taken raw and at varying processing times (> 60 s, no morphological differences were visible in the samples). Samples were gently evaporated (40°C) until dried, and deposited onto a conductive, adhesive surface.

4.3.10 Positron Emission Particle Tracking

Typically, LPE within systems is difficult to observe directly due to the optically opaque conditions inside the process. This imposes a challenge dealt with in previous work by limiting measurements to low material loading and early-stage periods of the process [2, 168]. To complement the PBM analysis and measure the particle flow behaviour in this mechanochemical synthesis system, Positron Emission Particle Tracking (PEPT) was utilised. This approach was used to track a radioactive tracer in space with high temporal resolution (kHz). PEPT has previously been applied to evaluate a diverse range of fluid, particulate and multiphase

flows [280, 289, 290].

As the tracer undergoes radioactive decay, it releases a pair of high energy gamma-rays in opposite directions, denoted as a singular Line of Response (LoR). Taking a group of LoRs together can locate the tracer in the system [280]. To recover the positional trace from the LoRs, the Birmingham method was used [280] as implemented in the `peptml` library by Nicuşan and Windows-Yule [291]. In this work, two different radioactive tracers including glass beads (1 mm, quasi-spherical) and large graphite flakes (flake length between 1 to 2 mm) were considered. Graphite flakes were also the precursor materials for the graphene synthesis, providing an opportunity to directly observe the conditions inside the process. Glass beads serve as a close density match to the graphite flakes ($\sim 2200 \text{ kg/m}^3$), and demonstrated similar particle shear fields¹ within the blender. As the glass beads are significantly harder than graphite flakes, it allowed for examining velocity and shear fields under intense exfoliating conditions where graphite flakes would tend to break up very quickly, before a statistically significant number of samples could be taken.

Though the measurement of the liquid velocity was successful with both particles, the particles resided differently within the mixer. In Figures 4.5a and 4.5d, particle residence maps are presented for graphite and glass at the same speed, showing a significant difference between the two tracers. This is reflected by the change in frequency of tracer observations throughout the batch volume. Indeed, examining the trace showed large portions of operation where the bead remained stationary in the base of the mixer, only occasionally being thrown up into the general flow. Due to this lack of interaction, there was less data overall in the glass bead runs as opposed to the graphite runs. To better visualise the data captured in the majority of the mixer, these sections were removed for analysis with the remaining observations visible in Figure 4.5, showing the glass tracer tended to reside differently to the graphite tracer. The observational differences between these two tracers can be attributed to

¹Particle shear is differentiated here as these data are calculated from the particle velocity in the blender.

several characteristics, such as the differing size, shape, resultant weight and hydrodynamic drag. The limitations on observations of the glass tracer may also affect the data statistics, hence, the residency data presented in Figure 4.15 should be taken as an indication of the residency of the graphitic particle, and cannot be taken as the ground truth.

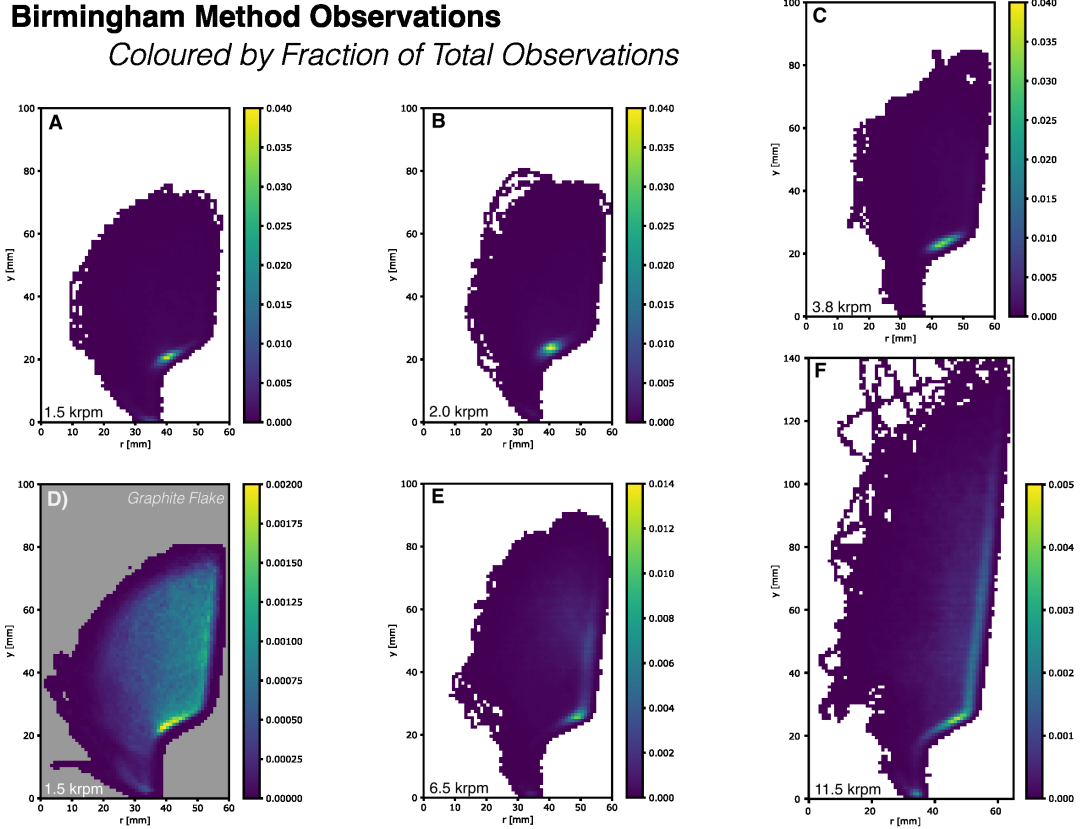


Figure 4.5: Tracer observations given as a percentage of total observations in the mixer. Graphite tracer observations are given in (D), with all other subfigures using a glass tracer.

A single particle (graphite or glass) was radioactively labelled using the University of Birmingham's cyclotron facility to produce a suitable positron-emitting radioisotope: Fluorine-18 in the case of glass and carbon-11 in the case of graphite. This tracer particle was then introduced into the LPE process and its position (x, y, z) in time determined from LoRs captured using either an ADAC Forte positron camera [292] or CTI/Siemens ECAT PET scanners that were recently developed for high data rate SuperPEPT measurements

[293]. Solvent, surfactant, and initial graphite concentration were maintained to match the same system conditions during graphene synthesis trials. This was also necessary given the importance of four-way particle coupling in this concentration regime (See Figure 4.2).

PEPT is a Lagrangian particle tracking approach. In this work, a single particle is tracked throughout the LPE process for a sufficient period of time to map out the flow behaviour across the entire batch volume (applying the assumption of an ergodic process). For visualisation purposes, and to examine particle quantities in more detail, it is useful to average these instances onto a grid; in this case, all particle quantities were averaged onto an axisymmetric grid with a 1×1 mm grid spacing. Using this grid, particle-particle shear rate was calculated following the approach of Dapelo, Alberini, and Bridgeman [294].

$$|\dot{\gamma}(r, y)| = \left| \frac{\partial u_r}{\partial y} + \frac{\partial u_y}{\partial r} \right| \quad (4.2)$$

Note that the particle-particle shear rate calculated above is not equivalent to the shear rate experienced between the graphite and the solvent. Rather, it is used analogously in this work for identifying the shear distribution within the liquid exfoliation process. Though pristine glass proved strong enough to withstand all mixer speeds, when irradiated by the cyclotron beam, particle fracture was observed randomly at all speeds, adding to the variability in the data acquired. Particle break-up, when significant, causes tracking to be lost as the LoRs become too scattered to reconstruct a trace. Irradiated glass beads would often also visibly distort in shape. Glass remained intact for longer at the higher speeds, and allowed for reconstruction of the velocity fields at speeds greater than 1500 rpm.

The flow fields and batch volumes were compared to investigate the synthesis behaviour for each LPE operating condition. By equating particle inertia to the inertial forces in the liquid, the speed of the particle (u) can be non-dimensionalised through Eq. (4.3),

allowing for direct comparisons between different mixer conditions.

$$u^* = \frac{\rho_g u d_p}{\rho_l \omega d_i^2} \quad (4.3)$$

where ρ_g is the density of the glass bead, ρ_l is the density of the solvent, ω and d_i are the impeller rotational speed and diameter, and d_p is the particle diameter.

4.3.11 The Population Balance

To model how the entire system of particles evolves with time, Population Balance Equations (PBEs) provide a system with which to monitor the process relative to a set of input conditions. Assuming the conditions are constant in time and are self-similar to the system, there are a system of equations which model how the PSD develops. In this work, simple particle breakage (by mass fraction f) is defined as:

$$\begin{aligned} \frac{\partial f(v, t)}{\partial t} &= \text{Birth} - \text{Death} \\ \frac{\partial f(v, t)}{\partial t} &= \int_f^\infty k(v') \Phi(v|v') .df' - k(v) f(v, t) \end{aligned} \quad (4.4)$$

As parent particles of volume v' break, several child particles are created with volume v . The breakage rate k is defined as a function of particle size (using the diameter of a sphere with the same volume, x_v) and determines the frequency with which that size is destroyed. Φ is the breakage kernel, and sets how the parent mass is distributed into the smaller mass fractions. The equation itself is a simple balance, equating the change in a particular size fraction f

to the fraction birthed into the size fraction minus the amount broken and distributed into different fractions. Validation of the solver and system of equations used against analytical solutions by Ziff and McGrady [5]. By noting the mode of breakup through empirical particle size measurements observed via LD, the form of the rate function k and the kernel Φ can be determined.

$$k = \left(\frac{x_v}{B}\right)^E \quad (4.5)$$

$$\Phi(v|v') = l_1 \left(\left(\frac{v}{v'} \right)^A \right) \quad (4.6)$$

Constant A captures the spread of the log-normal distribution produced in this case. One further restriction within these models is that both kernels are set to be zero where $v > v'$, as no particles can break from a smaller to a larger volume. With this numerical model of the general breakup, it is possible to sum volume fractions below a cutoff, S , to determine the amount of small-scale material produced. S took a value of $1.6 \mu\text{m}$ as it provided the best fit to the experimental data across all scales and speeds measured. Indeed, this value makes practical sense, as although the nanomaterial produced through shear exfoliation typically produces a smaller average length ($\approx 200 - 800 \text{ nm}$, e.g., [3, 6]), the one step centrifugation process implemented here does not precisely discriminate by size, and larger particles are retained which are up to $\approx 2 \mu\text{m}$ [7] (Raman spectroscopy also confirms the presence of graphitic contamination in the separated material, in Figure 4.12b).

A summary of the effect the individual model coefficients have on the fit, see Table 4.1. Initially, the distribution data acquired through LD measurements were subjected to an

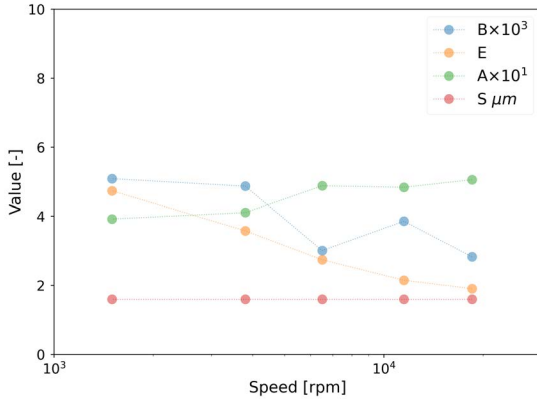
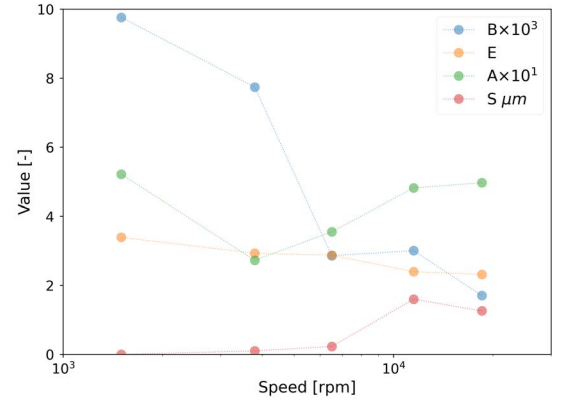
(a) Blended Fit, fixed S (b) LD fit only, adjusted S

Figure 4.6: Magnitude of model coefficients B , E , A and S plotted against mixer speed. Coefficients are scaled for better visibility. Breakup occurred for speeds above 1500 rpm, thereby making it difficult to fit the model coefficients to the data for the lowest speed investigated. (A) The model fitted to all data, using an automated fitting routine which balances the error in the nanomaterial and bulk precursor distribution. (B) The model fitted only to the LD data, with S adjusted to fit to the nanomaterial measurements. This provides a worse fit overall, much worse than that presented in Figure 4.10.

automated fitting routine to determine coefficients A , E and B (which minimised the error in the LD sizes only); after which, the concentration measurements were used to determine the optimum value of S . This technique minimized the error in the bulk particle distribution, but performed inadequately as a fit to the smaller sizes. To improve on this, it was found that a blended fitting approach, where all PSD and nanomaterial yield data are used in one step proved optimal, with the cutoff being fixed to $S = 1.6 \mu m$. The slight disconnect here is due to the model coefficients, as they produce very similar effects on the bulk distribution, but at the same time disproportionately impact the predicted yield, barely affecting the fit of the larger sizes while acutely affecting the production at smaller sizes. Small changes in A (see Table 4.1) can increase production by several orders of magnitude simply by pushing the lognormal tail towards the lower end of production. To better gauge production conditions, the model coefficients were extracted and plotted in Figure 4.6, to establish whether there was a link between these coefficients and the speed of impeller.

During fitting of the lowest speeds, it was found that $B \rightarrow \infty$ unless limited, and when limited to search below $B = 10$, the solutions in Figure 4.6 were found. The validity of the model towards lower speeds cannot be tested as nearly no breakage occurs, thereby allowing a large range of acceptable values for A , E and B . Hence it is more suitable to disregard this datum and instead make correlations from the four other speeds which are above the critical exfoliation criteria and where particle breakup occurs. To extrapolate future performance, the large dependence on local minima discussed can lead to variance in the value of the PBM coefficients, which over long timescales accumulate and lead to inaccurate estimates. In these cases, it is best to fit to a range of different conditions (herein, impeller speed), and examine the trend in the values. This overall model of the LPE system is more robust as the system coefficients are derived from a greater number of measurements (within error) of the original system.

Figure 4.7 shows all rotational speeds fitted by the PBM with the experimental mea-

Table 4.1: Summary of coefficients in the PBM and their respective effects on bulk and nano-material predictions. In most cases the coefficients have similar effects, making it difficult to distinguish their individual contributions when fitting.

Value	Eqn.	Effect on bulk material	Effect on nanomaterial
B	4.5	Scales rate, delays the onset of breakup (lower is earlier)	Changes shape and slightly effects amount of material produced
E	4.5	Rate of breakup (lower is quicker)	Changes trajectory and amount of material produced
A	4.6	The spread with which volume is distributed at breakup (lower indicates higher spread)	Changes shape and significantly effects amount of material produced
S	-	-	Cutoff, under which all volumes up to size S are summed to estimate quantity (yield) of material produced

surements superimposed. The conditions ranged from below the critical exfoliation point (< 2000 rpm) where no breakup was observed in the bulk particles, to highly exfoliating (> 11500 rpm) where breakup is clearly visible. Where no significant breakup is observed, there was no measurable concentration of nanomaterial under UV-vis-NIR. The value of the model coefficients at different speeds are presented in Figure 4.6. These unanimously follow a log-linear trend against impeller speed, showing that a full model of the shear mixer between these speeds solely using a PBM is possible by simple fitting. As opposed to only using the LD information to fit the model and subsequently fitting to the nanomaterial after the fact (in Figure 4.6b which provided a worse overall fit), the final fit was achieved by fixing the cutoff at $1.6 \mu\text{m}$ and performing an automated fitting routine to the LD and UV-vis-NIR data in one step. The routine focused on minimising the error in both areas equally:

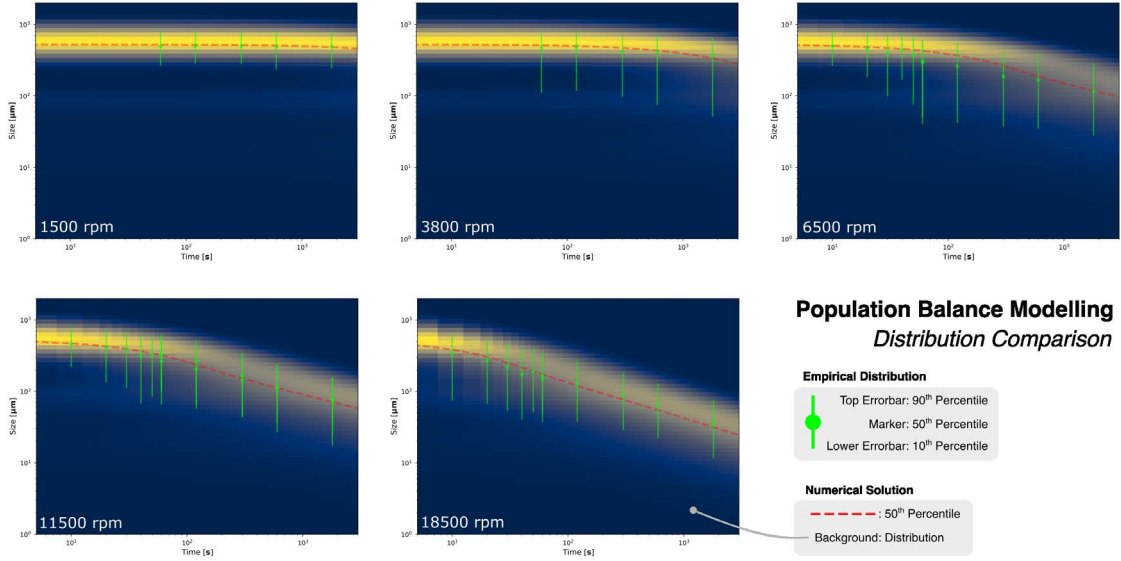


Figure 4.7: All speeds from no exfoliation or breakup 1500 rpm to highly exfoliating and high breakup 18500 rpm. Speed is denoted in the subcaption.

$$\epsilon = \frac{1}{N_n} \cdot \sum_{0 \rightarrow S}^{N_n} \left\| \frac{Y_i - \sigma_i}{Y_i} \right\| + \frac{1}{N_b} \cdot \sum_{S \rightarrow \infty}^{N_b} \left\| \frac{D_i - f_i}{D_i} \right\| \quad (4.7)$$

Where ϵ is apparent error and N denotes the number of measurements. The subscript b indicates bulk, where the individual distributions (D_i , measured) are compared to the predicted distribution (f_i). The subscript n stands for nanomaterial, where the summation compares the measured amount of nanomaterial (Y_i), to the predicted amount of nanomaterial (σ_i). The calculation is visualised in Figure 4.8. The final optimisation loop was conducted using SciPy's optimize routine using the Broyden–Fletcher–Goldfarb–Shanno (BFGS) algorithm. To initiate the BFGS algorithm, an estimate for the model coefficients is required. The value for these coefficients was slightly adjusted throughout the fitting to avoid local minima between the lowest and highest speeds.

The volume based approach taken with the LD measurements is replicated here in the PBM. Fitting the PBM is performed by finding the minimum error between the LD

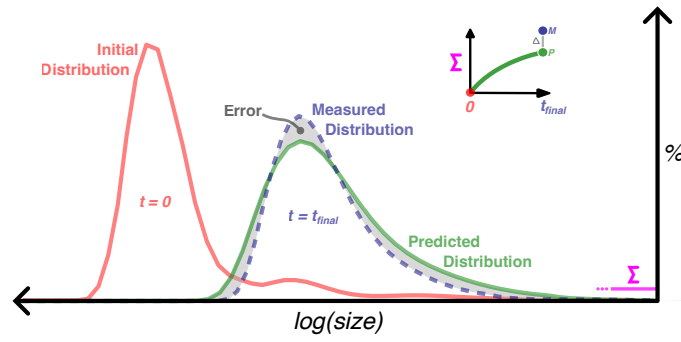


Figure 4.8: Visual indication of how the error is calculated in the PBM. The total error in the distribution is designated as both the error in the bulk distribution and the error (Δ , inset) at the small-scale.

measurements above the cutoff and the UV-vis-NIR measurements below the cutoff. For these reasons, this technique can be said to abstract detail from intermediate size ranges, as it fits to the majority of particles by volume and the region of interest.

4.4 Results and Discussion

To explore breakage, impeller rotational speed was varied from below the critical exfoliation point (approximately 1500 rpm [2]) where no breakage or nanomaterial production was observed, to highly exfoliating (18500 rpm). This allowed the PBM to be fitted to a variety of conditions in the mixer, Figure 4.9a demonstrates an example of the PBM fit to the LD-based PSD data for 11500 rpm, while Figure 4.9b demonstrates the fit to the graphene yield measurements taken from the supernatant dispersions for all impeller speeds when summing below the cutoff $S = 1.6 \mu\text{m}$. This same value of S was used to fit all concentration data, and was selected as it reduced error across all fits. Leaving S as a constant across all speeds came at no reduction in the fit, and demonstrates that a unified model for a breakage system would only require 3 coefficients from Eq. (4.5) and (4.6) to capture the dynamics of the bulk graphitic material and nanomaterials. The other coefficients A , E and B showed a distinct trend in their value in correlation to the impeller speed (see Figure 4.6). Almost no particle breakage or production was found at the lowest speed of 1500 rpm, hence this is not included in Figure 4.9.

The fit from bulk material to nanomaterial achievable through the PBM provides an argument for describing production simply as owing to breakage. While the breakage model predicts the magnitude of production well for this shear exfoliation system, it is important to highlight that in its current form, it is too simple to account for chemical effects (such as material agglomeration). Nonetheless, conceptually it is a framework that could be applied to different exfoliation processes by expanding the functions of the PBM. Note too that fitting solely to LD data alone, there is correlation but poor fit to the nanomaterial. This discrepancy means that though one could use this method to infer how production could scale from LD data, fitting from this alone omits key information. Issues fitting the PBM stem from the similar contribution between coefficients B , E and A , as they all affect the prediction

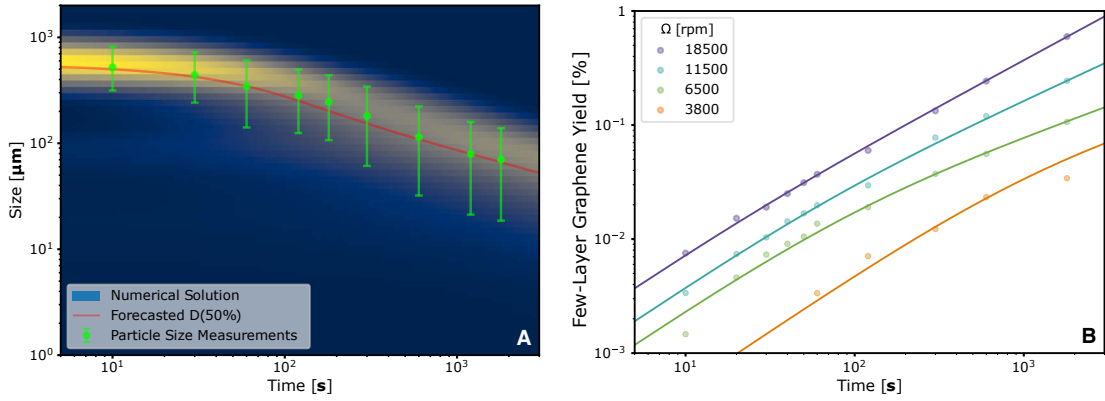


Figure 4.9: Graphite breakup and production of few-layer graphene with exfoliation time. (A) Breakup of graphite at 11500 rpm. The PBM prediction is plotted in the background, similar to the surface illustration in Figure 4.1, with colour indicating volume of material produced. Independently measured experimental PSDs are plotted as green markers denoting the 50th percentile diameter mark, with errorbars stating the 10th and 90th percentile. The red line represents the numerically predicted 50th percentile. (B) Few-layer graphene yield (UV-vis-NIR concentration measurements, circular points) with fits derived from different PBMs (trendlines). The predicted concentration is from the same model defined in (A).

of the smallest sizes in the distribution (i.e. the tail of the log-normal distribution). Ideally, the use of different measurement techniques that target different size ranges is essential to separate these contributions and fit the PBM. Where less breakage occurs, the PBM tends to provide a poor fit as it statistically predicts breakage occurs so long as enough time has passed. This could be because fewer particles break or that the breakage switches in mode (shattering to erosion, for example), requiring different PBM treatment.

With the suitability of this approach for predicting graphite breakup and graphene production demonstrated (Figure 4.9), the effect of the number and type of sample data on the accuracy of the prediction was investigated. The similarity in effect from the coefficients in the PBM leads to an optimisation space with several local minima, and consolidates the importance of a well selected initial point (x_0) to avoid perturbing the PBM during fitting. For this initial condition, PSD measurements provide an excellent technique to establish an estimate for the coefficient value (B, E, A)². Once an initial value for these coefficients is known, it is simple to solve for the PBM with a small number of few-layer material yield measurements. To study the stability of the solution, various PBM coefficients were estimated based on their best fit to a reduced selection of data, and presented in histograms in Figure 4.10, under the $\Omega = 11500$ rpm impeller condition. Figure 4.10 presents all possible combinations of two points from a selection of few-layer yield measurements (Figure 4.9b, $\Omega = 11500$ rpm), fitted with and without the addition of LD PSD measurements (Figure 4.9a). This test was repeated with two pre-established initial values (x_0), based on the PSD solution ($B = 4 \times 10^{-3}, E = 1, A = 4 \times 10^{-1}; B = 2 \times 10^{-3}, E = 2, A = 2 \times 10^{-1}$). One of these points ($4 \times 10^{-3}, 1, 4 \times 10^{-1}$) is expected to perform better, as the relative difference in the initial value is similar to that in the final result. The histograms show remarkable coherence towards specific minima and vary little in spite of the lack of information used to construct them, but they also show that a poor initial value can lead to inaccurate results, a

²Rough coefficient bounds can be manually estimated by examining where the solution is stable.

pitfall often encountered in optimisation related problems such as this. If the rough order of magnitude for the coefficients is known for the specific exfoliating condition, it is possible to fit the PBM with relatively few measurements. To summarise, PSD measurements across all scales are essential to obtain a good starting point for the PBM and to understand the mode of breakage. Nanomaterial measurements are essential for tracking production, but relatively few of these nanomaterial measurements are needed to enable an accurate estimation of the coefficients. Here, root-mean-squared errors of 0.01-0.016% are introduced when using only two concentration measurements with PSD measurements to construct the PBM for this impeller speed. This is a significant advantage, given the extensive time required to sample, post-process, and characterise nanomaterials from liquid exfoliation processes.

To assess the validity of the breakage model further, a representative quantity (4 mg/mL) of larger graphite flakes were sifted, enough so as to not affect the conditions inside the blender, but still provide an insight into how different initial distributions would behave under similar exfoliating conditions. A comparison of the PBM's performance to acquired LD-based PSD data is presented in Figure 4.11. In both cases, the distributions differ initially and coalesce to become near identical within the first minute of processing. It shows that for a specific exfoliating condition, assuming particle material properties are maintained when scaled, a single model can capture the underlying dynamics as a function of the particle size. This independence between the conditions in the vessel and particle size demonstrates that a PBM is robust for analysing and predicting these types of mechanochemical synthesis processes.

An interesting implication of Equation 4.6, is that for a parent particle size of unity, the shape of the kernel is defined by Equation 4.8:

$$P(v) = A \left(\frac{1}{v} \right)^{1-A} \Big|_{v < 1} \quad (4.8)$$

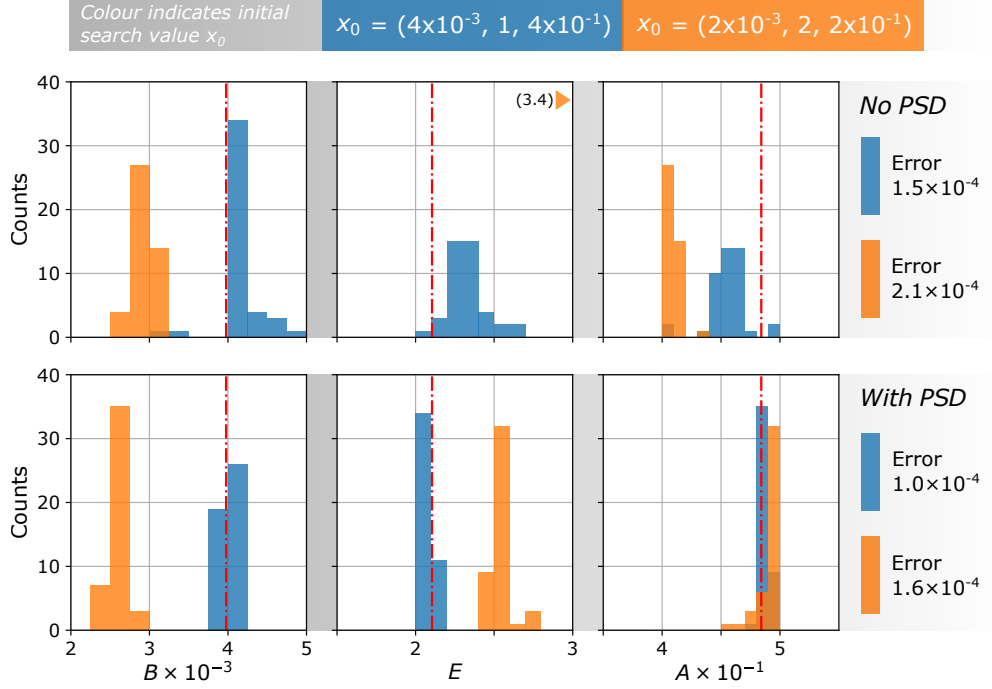


Figure 4.10: Fitting the PBM by omitting all measurements except pairs of nanomaterial measurements, with (*With PSD*) and without (*No PSD*) inclusion of the PSD measurements as aid, for two possible coefficient starting points ($B = 4 \times 10^{-3}, E = 1, A = 4 \times 10^{-1}$ and $B = 2 \times 10^{-3}, E = 2, A = 2 \times 10^{-1}$). Histograms are constructed using the resultant coefficients. Red dashed line indicates the fully fitted solution ($4.0 \times 10^{-3}, 2.1, 4.9 \times 10^{-1}$), using all available measurements (i.e. $\Omega = 11500$ rpm condition in Figure 4.9). Final root-mean-squared error between the predicted nanomaterial trendlines are noted in the legend.

As v approaches 0, $P(v)$ increases with $1/v$, effectively showing that this method of breakage has a high probability to break into small v , indicative of an attritive process [295]. When $A = 1$ there is equivalent breakage into all sizes, i.e. random breakage. The kernel function is process specific, and though a power-law fit certainly describes the process happening herein, it depends entirely on how the parent material is broken. This suggests that the PBM approach applies more broadly to other methods of LPE, and that similar

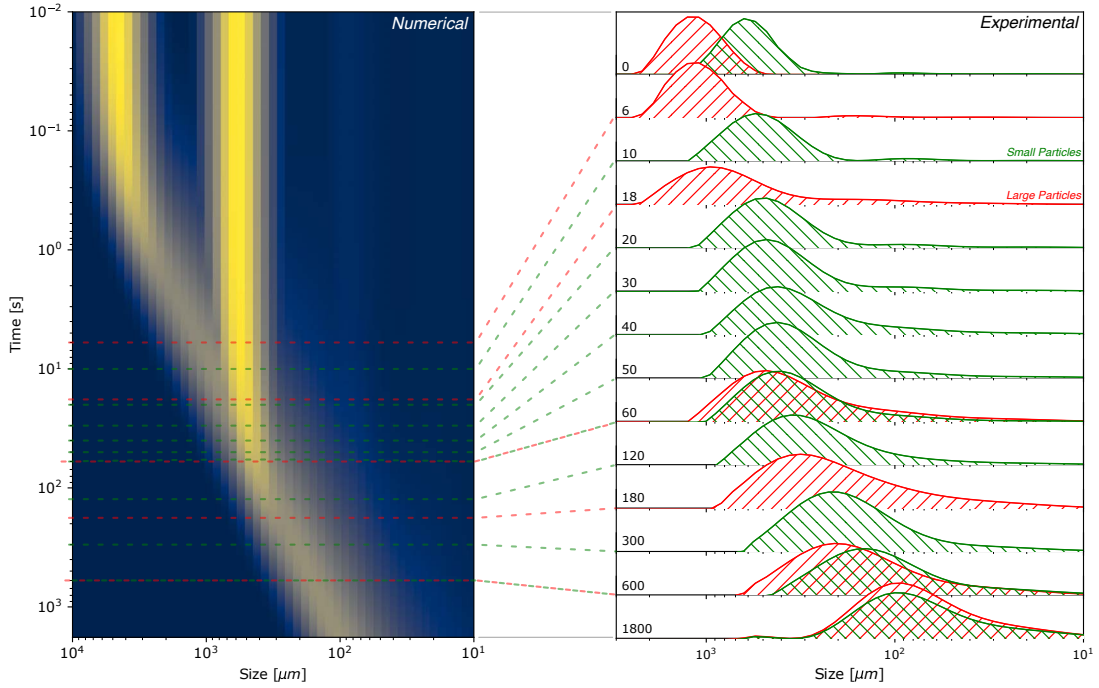


Figure 4.11: Graphite breakup for two different starting size distributions. Left, both PSDs are plotted on a continuous colour plot (colour indicating volume of material produced) breaking under the influence of the same fractional PBM in time. Red and Green dashed lines mark the times at which experimental LD samples were taken. Right, two different starting distributions are exposed to the same exfoliation conditions (surfactant concentration of 4.3 mg/mL and impeller speed of 11500 rpm; but different starting concentrations of 4 mg/mL for the larger particles, and 20 mg/mL for the smaller particles).

exfoliating techniques promote efficient production of 2DMs as the breakage kernel is skewed towards smaller sizes.

Measurements of Raman spectra normalised to the G-peak in Figure 4.12 uncovered changes in the product structure as liquid exfoliation proceeded. Raman spectral peaks, labeled G, D, D' and 2D, evolve in time to reveal the material conversion from bulk graphitic behaviour into few-layer graphene. The shape of the 2D peak from a stepped shape typical of bulk graphite at 10 s changed to resemble that of fewer layer graphite (2-5 atomic layers) by

180 s [296]. Figure 4.12 also shows a presence and subsequent growth in the D (1350 cm^{-1}) and D' (1620 cm^{-1}) bands, settling on a distinctive shape beyond 180 s. The growth of the D and D' bands are associated with an increase in nanomaterial defects. For shear exfoliation processes on this precursor material, these are known to be due to nanosheet edges rather than basal plane defects, suggesting that the separated material is becoming smaller and therefore has more edges [6, 7].

The histograms in Figure 4.12a confirm that for early synthesis times (0 – 120 s) the I_D/I_G ratio is skewed towards bulk graphite characteristics ($I_D/I_G \approx 0.2$). The measurement statistics for > 180 s illustrate a shift in the mode with more of the product displaying characteristics of few-layer graphene ($I_D/I_G \approx 0.5$). This trend with process time is in agreement with the PBM predictions which show a significant broadening of the PSD tail into smaller size fractions when the exfoliation time exceeds ≈ 120 s (Figure 4.11). The progression of Raman spectra in Figure 4.12b show the presence of graphite especially in samples taken early in the exfoliation run, suggesting that the one-step method of separation implemented here does not exactly discriminate the few-layered material.

Another benefit of PBMs is the ability for them to be used as a tool for predicting potential future production (up to $t \rightarrow \infty$) assuming that production is not limited by extraneous factors (Figure 4.13a). Some limiting examples are solubility or reaggregation, but there could also be a drop in breakage rate past a certain size. These factors would be challenging to correct for unless enough accurate preliminary measurements had been taken across a range of sizes. With current LD techniques this could prove difficult to measure depending on the material [285], as discussed earlier in Section 4.3.

The production curves in Figure 4.13a suggest that yield in the liquid exfoliation process takes a piecewise power-law form. This starts with a region of highest production, where large bulk particles break superlinearly to form a log-normal distribution; followed by

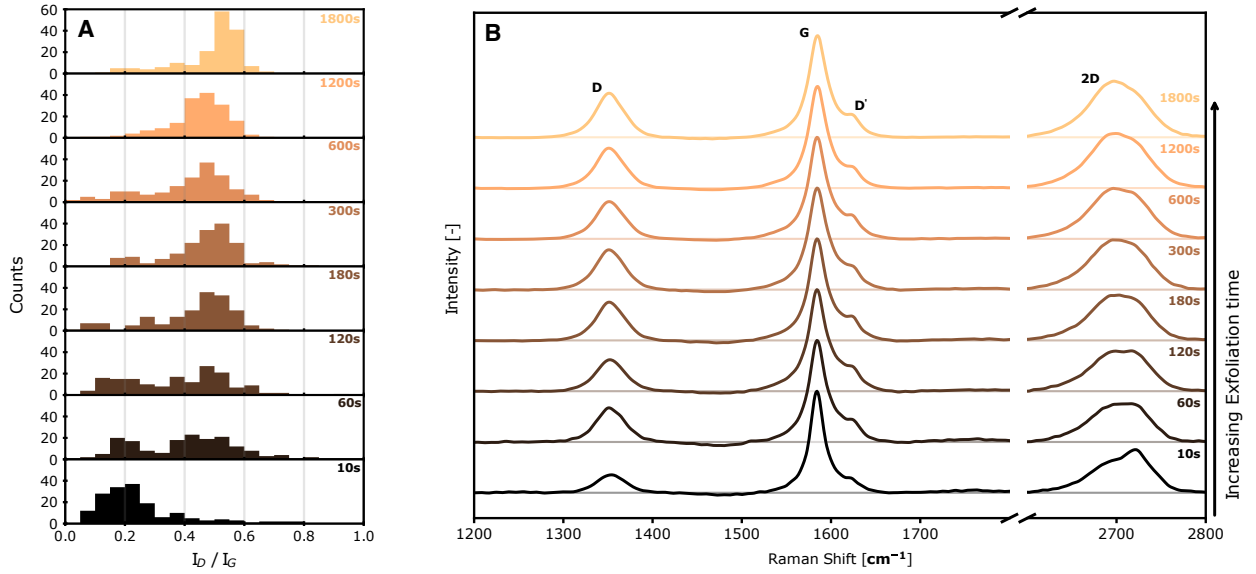


Figure 4.12: Evolution of the spectroscopic characteristics of separated few-layer graphene samples with process time. (A) Statistical distributions of peak intensities I_D/I_G . (B) Averaged Raman spectra normalised to the G peak. Measurements correspond to $\Omega = 11500$ rpm impeller condition.

breakup towards the smaller sizes with rate E . The extrapolation in Figure 4.13a shows the time taken to reach 90%wt yield between the top two speeds differs on the order of months. Of course, these extreme scenarios are not practical, however, it illustrates that through the use of the PBM approach, it would be possible to explore and optimise system-level process efficiencies and trade-offs (e.g., energy consumption, yield, production rate, operating costs). Furthermore, there are a variety of graphitic nanomaterials that have different applications based on their size. This includes graphite flakes with thicknesses of up to 200 nm [11], and few-layer materials with thicknesses typically below 3 nm. The PBM approach described in this study could also be used to predict the fractions (and yields) of these different synthesis products, representing an important step away from linear regression, and towards physically constrained and informed models.

In conjunction with NMR measurements, the PBM can be used as a predictor of

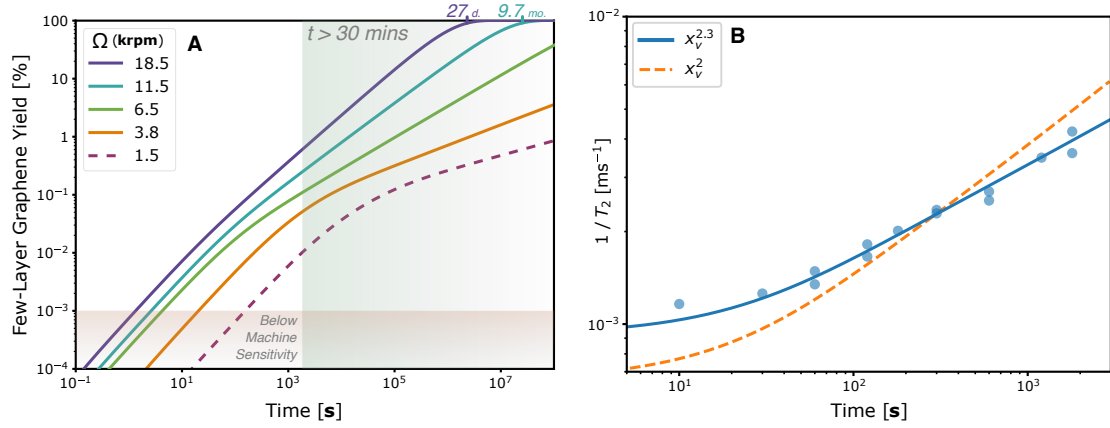


Figure 4.13: Forecasting graphene production yields and particle surface area using the PBM. (a) The PBM is extrapolated to $t \rightarrow \infty$ to view the extents of production. The lowest speed was fitted only to the LD measurement even though there was very little to no breakup, as there was no measurable increase in nanomaterial concentration (represented as a dashed line). (b) NMR measurements are compared to the PBM predicted surface area ($\Omega = 11500$ rpm). Two predictions are used, based on x_v (volume based diameter), spherical surface area $\approx x_v^2$ and accounting for the rough surface area $\approx x_v^{2.3}$.

the rate of surface area increase in the product. Examining Equation 4.1, if ψ , K_A and R_b remain constant, surface area represents the only parameter changing in Figure 4.13b. Comparing to the PBM, it is evident that simply using the (minimum) spherical surface area obtained with the diameter estimated from the volume of the particle (x_v) was not enough to provide an accurate fit, though suitable approximations can be made for a better fit. As graphite particles typically exhibit some surface roughness at all scales caused by inter-grain boundaries, a level of self-similarity between particles is visible, with very little change in the particle shape observed from optical measurements (see hydro-insight imaging in Section 4.3.4). In this case, as the shape does not change drastically between the large and small size fractions, the surface area should scale with x_v^D , where D is limited between $2 < D < 3$, with the lower limit indicating a perfectly smooth surface and the higher limit a surface which completely fills all available space. A value of $D = 2.3$ was found to closely fit the NMR measurements and agrees with empirical measurements taken by Persson [297], who found that most brittle fractures typically cause self-affine surfaces with $D \approx 2.2$.

The dynamics behind the graphite breakup process were investigated by obtaining particle velocity measurements *in operando* for the liquid exfoliation process. Figure 4.14 shows the particle flow behaviour within the vessel spanning a range of impeller speeds from $\Omega = 1500$ rpm to 11500 rpm. Here, a glass bead (density-matched with graphite) was tracked within the batch to map the flow behaviour. This was necessary to overcome particle tracking challenges associated with graphite tracer breakup at speeds > 1500 rpm.

A comparison of the flow regimes between graphite and glass at the lowest speed (1500 rpm) can be seen in Figure 4.15. Though both sets of particles behaved similarly in speed and particle-particle shear (the latter is pictured in Figures 4.15a-b), the residency maps in Figure 4.5 show the glass tracers tended to reside away from the bulk flow regions of interest. Though graphite also demonstrated an affinity to the same regions as the glass bead, it spent much more time in the fluid as a whole.

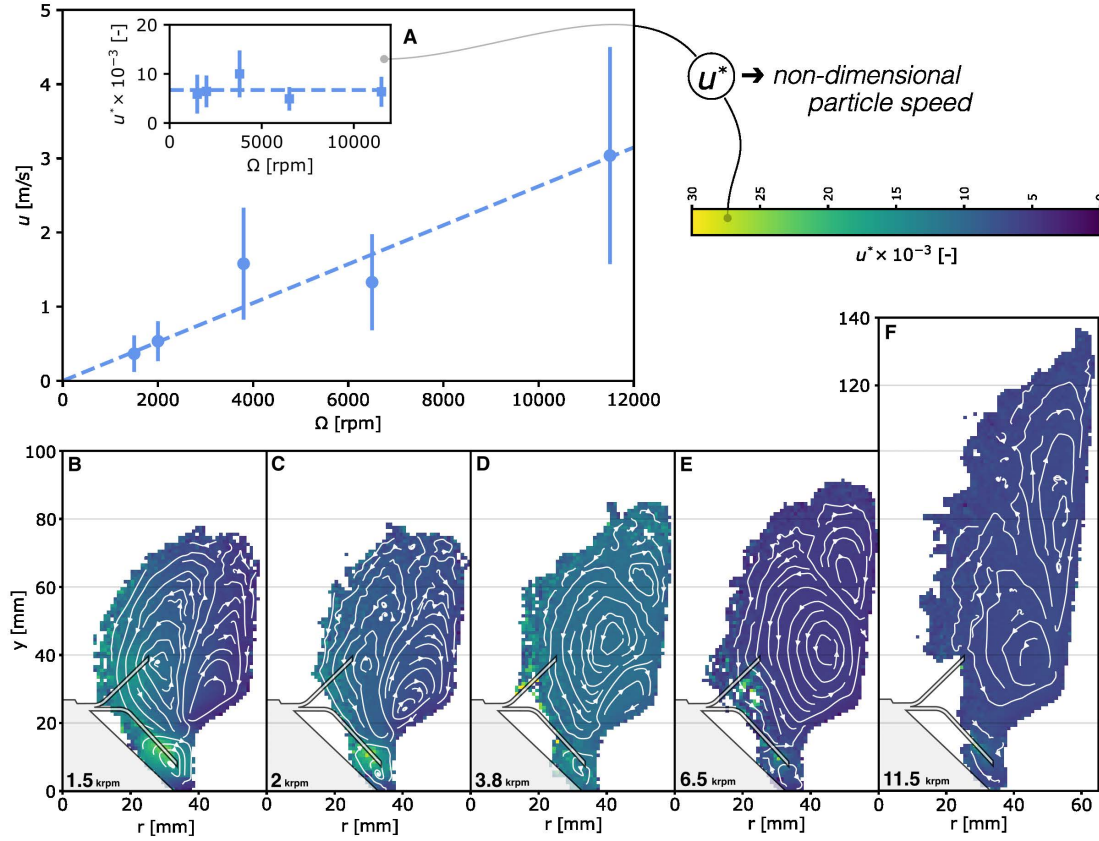


Figure 4.14: Particle velocity within the liquid exfoliation system using a glass bead tracer. (A) Mean particle velocity with impeller speed. Errorbars indicate one standard deviation in particle velocity, and inset figure shows the non-dimensionalised particle speed, u^* , from Eq. 4.3. (B-F) Flow fields while operating at differing impeller speeds (reconstructed as an averaged axisymmetric slice).

Using the particle velocity fields in Figure 4.14, it is possible to capture the intra-particle shear rate, shown in Figure 4.15. This particle-particle shear rate aligned well with theoretical scaling estimates (Phipps [298], Figure 4.15c) for the actual shear rate in similar stirred batch reactors, as both the highest 90th percentile and the central 50th percentile (by axisymmetric area) produced a scaling with respect to impeller speed Ω of $\dot{\gamma} \sim \Omega^{1.5}$ [298]. Figure 4.15d presents isobars of particle-particle shear rate, with a green line to indicate the impeller speed at which few-layer graphene production was first observed

($\Omega = 3800$ rpm). Paton et al. [7] found the shear rate of production to be around $\dot{\gamma}_{\text{crit}} \approx 1 \times 10^4 \text{ s}^{-1}$ for graphene. For reasons outlined in Section 4.3.10, the particle-particle shear rate measurements in this work are only representative of the shear field distribution within the exfoliation system, and never exceed $\dot{\gamma} \sim 10^4 \text{ s}^{-1}$ across all speeds measured. Residence itself is given as a percentage of the total time spent in the dispersion. It is important to note that residency seemed to differ significantly between glass and graphite tracers, due largely to how the glass bead seemed to spend less time within the bulk fluid regions. For the speeds measured, a residency comparison between the two tracers is given in the Figure 4.5. Despite the necessary compromises with tracer particle selection, the trends in Figure 4.15 demonstrate that with increasing impeller speed, precursors will experience both an increase in shear rate and exposure time to these higher levels of shear. This facilitates the increased frequency and likelihood of particle breakup events, resulting in significant differences in the concentration of few-layer graphene (Figure 4.9) and production times forecast for different impeller speeds (Figure 4.13).

Interestingly, the glass particle flow fields (Figure 4.14) demonstrate shifts in the circulation patterns within the mixer. Initially separated into three distinct circulations, the central circulation eventually dominates as speed increases, and moves away from the path of the blades. As the immediate volume swept by the blades is associated with blade impacts and high shear, reduced residency in these areas should correspond to a reduced efficacy in production. To examine the change in the volume swept by the blades, the mixer was analysed as two separate compartments, in the style of Alves, Vasconcelos, and Barata [299]. The first compartment (1) contained the swept volume of the blades, which is a region associated with the production of few-layered material ($r < 34$; mm, $y < 40$; mm). The second (2) denoted the rest of the mixer excluding compartment (1). Residence time was then calculated as:

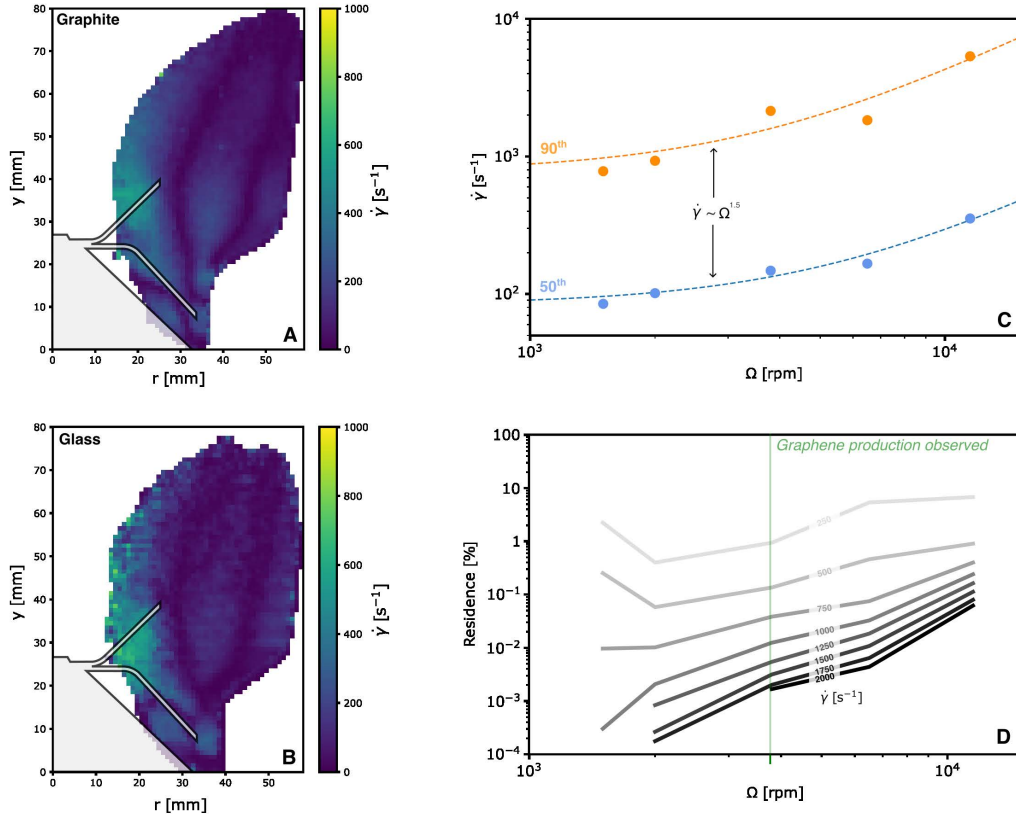


Figure 4.15: Graphite particle hydrodynamics within the liquid exfoliation system. Particle-particle shear rate fields at the lowest rotor speed (1500 rpm) for (A) graphite and (B) glass. (C) Scaling of the 90th and 50th percentile particle-particle shear rate with impeller speed. (D) The percentage of time a particle spends under the influence of different minimum shear rates. Dashed line represents the point at which nanomaterial production is first observed.

$$t_r = \frac{t_{r1}}{t_{r1} + t_{r2}}$$

Where t_{r1} and t_{r2} stand for the residence within compartments (1) and (2) respectively. This definition of residence time is then not a convolution of shear rate and residence time as opposed to the residence time in Figure 4.15d, and represents a close analog to ‘residence time’, t_r discussed in other works [2, 168]. This t_r is found to scale inversely with the impeller

speed, $t_r \sim \Omega^{-0.65}$. Using spinning disk and Taylor-Couette reactors, Stafford et al. [168] ascribes few-layer graphene concentration (C_g) to scale with $C_g \sim \dot{\gamma} t_r$. This was also found to agree with the characteristic timescale predicted for complete sliding of bi-layer sheets under shear flow [277]. Combining this with our measurements for shear rate scaling in this work ($\dot{\gamma} \sim \Omega^{1.5}$, also in agreement with theoretical scaling [298], Figure 4.15c), arrives at a few-layer graphene concentration scaling of $C_g \sim \Omega^{0.85}$. This solution correlates to the few-layer concentration measurements, which ascribe a scaling closer to linear ($C_g \sim \Omega$). Our work therefore confirms that the underlining mechanisms behind shear exfoliation processes have similarity, despite the wide diversity of production approaches that are available. Similarly, this supports the idea that the PBM approach presented can have general applicability for predicting nanosheet synthesis via liquid phase exfoliation.

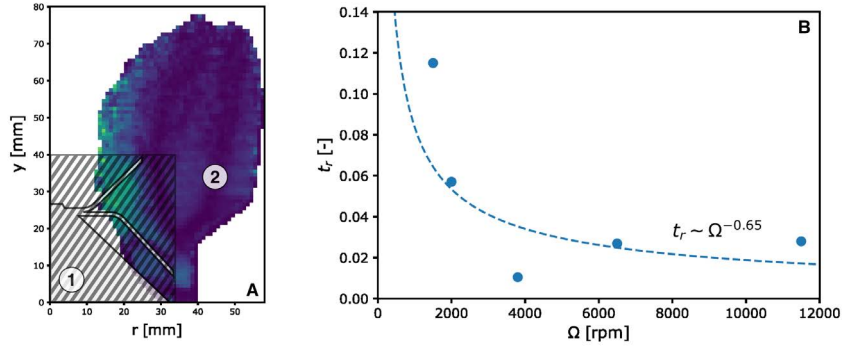


Figure 4.16: Compartmental analysis of the mixer system. Part (A) gives a visual description of the two compartments. Compartment 1 is defined as $r < 34$; mm, $y < 40$; mm, with compartment 2 adjoining the rest of the mixer. In (B), t_r is determined for all speeds for a glass tracer, and plotted against a scaling of $t_r \sim \Omega^{-0.65}$.

4.5 Conclusion

In this chapter, a method for modelling the production of few-layer graphene within liquid exfoliation processes was developed and validated following a population balance approach. For high-shear, turbulent, impeller-driven blending systems, the breakup process was found to obey simple breakage kernel and rate functions that were determined from observations of graphitic particle size distributions. A complete description of the exfoliation process was possible by implementing only three coefficients within this model, which were found to be sensitive to impeller rotational speed. The robustness was shown by the ability to correctly predict the evolution of graphitic particle size distributions that originated from different starting precursor sizes. By modelling the evolution of the full particle size distribution, the approach captures various carbon materials that have practical use in many applications, including few-layer graphene and Graphene Nano-Platelets (GNPs). Examination of the breakage model revealed physical insights on the breakage mechanisms. The high shear process used in this work produces a high probability for large particle breakup into small particles, indicative of an attritive process. This was confirmed with statistical Raman spectroscopy measurements which revealed a rapid conversion from graphitic to few-layer graphene materials in the first minutes of the process. We show that when coupled with nuclear magnetic resonance spectroscopy measurements performed on dispersions of graphitic materials, the model can also integrate particle surface area characteristics. Though these methods are expected to be repeatable in similar breakage conditions, changes to the setup could have an impact on the breakage mode, requiring the definition of new kernel and rate functions.

The dynamics within the graphene synthesis system were explored by performing PEPT to determine the graphite particle velocity, shear rate and residence distributions. This showed that increasing impeller speed leads to a combined positive effect, increasing

shear rate and the residence time of particles in areas of high shear in the system. This leads to the higher probability of breakup that was observed by the population balance models and graphene concentration data for increasing speeds. As the population balance requires empirical data to construct, an assessment on reduced sampling showed that the PSD data was important to use as an input, yet only a limited set of few-layer graphene concentration measurements were necessary to reconstruct the original model within 0.02%. Importantly, the population balance method is agnostic to the measurement technique used to determine the particle size distribution and graphene concentrations. This allows for the approach to be extended to other materials characterisation data available (e.g., statistical AFM, TEM) and other 2D materials that are produced using similar mechanochemical approaches (e.g., TMDs). Overall, this provides a promising avenue for creating physics-based predictive models of top-down synthesis, opening up opportunities to forecast long-duration product yields from shorter duration tests, and design synthesis approaches that improve process intensification, optimisation, and material sustainability.

5. Conclusions

This thesis has aimed to address key challenges surrounding the production of Two-Dimensional Material (2DM)-based photocatalysts for wastewater treatment. To explore synthesis, Liquid Phase Exfoliation (LPE) of layered materials was selected for its applicability to a wide range of materials, high quality output, being simple to explore in the lab and then scale to industrial processes. Moreover, all LPE demonstrated in this thesis was executed using sustainable dispersants to reduce the ecological impact of these methods. However, LPE synthesis of 2DMs suffers from low yield, slow production rate, unpredictable output and slow *ex situ* characterisation, which impact costs, process time and material quality control.

Chapter 2 presented *OpenLPE*, a repository for LPE hardware, validation and process knowledge. The equipment, modified from kitchen blenders, validated the production of different 2DMs useful for photocatalysis, including h-BN, graphene and MoS₂. The various construction steps are repeatable and customisable, ensuring that researchers interested in the scalable production of 2DMs can reliably create systems of their own at low cost, reducing the barrier to entry. Chapter 3 addressed concerns surrounding the characterisation of 2DM and monitoring of LPE processes, by analysing the system with an inline UV-vis-NIR spectroscopic fibre optic probe. This integration provided real-time insight of

material production, but was hampered by densely laden, bubbly flows inside the LPE system that rendered the solution opaque. These issues were overcome with short rest protocols and low material loading, allowing for very quick inline measurements taking around 5 min, which saved time over traditional *ex situ* measurements that take 1 hr to sample, separate and measure.

Finally, Chapter 4 demonstrated the use of Population Balance Models (PBMs) to simulate the yield of all material fractions within the mixer. This system was validated with Laser Diffraction (LD) particle size distribution measurements to understand the large scale material movements within the system, and UV-vis-NIR measurements to fit the smallest scales. This technique requires few measurements, yet offers a robust method for optimising LPE systems and forecasting yields, essential for the continued advancement of these manufacturing processes. In addition, Chapter 4 unveils the first direct measurements of conditions inside an active LPE process using Positron Emission Particle Tracking (PEPT), providing valuable information on the fluid dynamics in the system that drive the mechanical synthesis of these materials. Together, these chapters help to mitigate several challenges associated with LPE, broadening our understanding of these these complex mechanochemical processes.

Future Work

Following from this thesis, there have been a few promising areas of research highlighted, which due to time constraints or research failings have only been partially explored. These are:

Constructing Graphene-g-C₃N₄ photocatalytic composites. This thesis focuses exclusively on synthesizing graphene (and other 2DMs) that could be subsequently used for forming heterostructures. A potential study including this technique was explored, performing a one-

pot mechanochemical synthesis of photocatalytic composites. He et al. [247] demonstrates a simple method of synthesising a Graphene-g-C₃N₄ photocatalytic composite via LPE of graphite in a urea-water mixture, and polymerising the urea to form the sandwich composites (similar composites have been produced via different techniques [300]). After testing, it was found that the few layer material synthesized using the mixer system (Chapter 2), were destabilised by the urea mixture and very little few-layered graphene was produced. He et al. [247] provides great detail on the process used, and in the supplementary information of their paper they provide information suggesting that the use of a cooling jacket and low starting concentrations of graphite seemed to increase the material yield substantially, and when allowed to heat up under shear (above 5°C), material production drastically tailed off. Further testing by adding NaC surfactant to stabilise any few layer material demonstrated interesting behaviour:

- Adding NaC after a urea-assisted exfoliation run did not increase the amount of few-layered material in the system. Neither did it increase the amount after a light mixing cycle.
- Adding NaC to the urea-water and exfoliating the mixture produced few layer material.

These tests showed that the sheets were not being produced in the first place, as opposed to an agglomeration mechanism where the sheets were broken apart, but then loosely agglomerated soon after. Due to time constraints and the delicate nature of this process, further work in this area was halted, but it may be an interesting avenue to create a simple, functional composite material useful for photocatalytic processes.

Computational Fluid Dynamics (CFD) coupled with PBMs. CFD provides a way of approximating fluid motion through complex differential equations, coupling this system to PBMs has been explored recently [301] utilising particle-in-cell methods, tracking the motion of

so-called particle ‘parcels’ which led to crystallisation of the product. This approach would likely provide a way of linking the fluid conditions directly to material production at every size fraction. After exploring a simple multi-phase mixer simulation, the extreme speed and heavily aerated nature of the flow proved a difficult problem to simulate, and time constraints led to the research being paused in favour of direct measurements allowed by PEPT. Recreating the conditions using computational techniques would allow for deeper exploration and comparison between different LPE systems, and discovery of the driving forces that lead to few-layer material yield. A short section analysing the dimensions of these systems is presented in Appendix B, and would have served as a point of comparison for any model created.

Extending PEPT to monitor graphite breakups. Much of the work presented in this thesis surrounding PEPT involved a few firsts; first graphite trace activated by the universities’ cyclotron system, first actively breaking tracer within a liquid system, first time the universities’ PEPT equipment attempted to track such small particles at such speeds. These firsts, though exciting, brought with them a number of issues which had to be addressed. One of the most pertinent is due to the actively breaking graphite particle. Initially, it was hoped that this actively breaking particle would be a benefit, as it was theorised and proved with monte-carlo nuclear physics simulations that using the Birmingham method [280], it was possible to track a gradually decreasing tracer particle by comparing the number of LoRs originating from the largest particle to the number of LoRs originating from the fluid as a whole. Unfortunately, when applied to the data collected from the graphite tracer, the particle breaks too quickly to recover a trace. The remaining data is incredibly disperse, but when analysed using the Birmingham method, shows general, averaged motion¹ suggesting that the trace is still actively tracking many smaller particles at once. Again, time constraints

¹That is, general motion up and down as the mixer turns on and off, and the particles settle to the bottom of the mixer, or the particles are kicked up into the system.

and in this case, the difficulty of the problem, lead to this approach being abandoned in favour of the glass tracer which would remain intact under exfoliation². Nevertheless, this avenue of research presents a unique and direct way to measure LPE systems, so perhaps simply a change in technique (such as switching between tomographic or particle tracking depending on dispersion of LoRs) could provide useful insights. It is also important to note that particulate breakage processes are essential to numerous industries, including pharmaceuticals and construction aggregates [295]; hence, a method that is able to directly yield measurements of the internal machinations of such systems would be highly desirable.

Enhancing the modified blender. The blender modifications in Chapter 2 demonstrate a complete overhaul to the blender system, but more precise control over the rotor speed could be achievable with the correct control scheme. The greatest change here would be to switch the calculation of rotational speed depending on blade passes, as this would allow for greater control at the lowest speeds. Furthermore, the photointerrupter used to read the blender speed would reach its maximum working interval between crossings³, and any blender working at speeds above 20000 rpm would require a different system to measure rotational speed (such as Hall effect sensors).

Creating an inline monitoring system for few-layer material production. One of the largest issues in the inline probe system in Chapter 3 was the inability for the inline UV-vis-NIR probe to measure either high concentrations of nanomaterial or heavily aerated flows. To achieve truly inline measurements, it was clear what is required for this purpose is a self contained unit that can:

1. Sample continuously or in batches

²Though not always, the tracer did show signs of damage and lost appreciable mass during testing.

³That is, the infra-red encoder in the photointerrupter would not have enough time between signals to reach its ground state.

2. Be unaffected by aerated flows
3. Be unaffected by large particles

UV-vis-NIR spectroscopy could also be replaced by an inline NMR probe, or they could be used in tandem at different operating concentrations as complementary measurements, as UV-vis-NIR works well at low concentrations, while NMR proton relaxation measures all area in solution and is more accurate at high concentrations. Other complementary systems, such as LD-based PSD measurements (which are possible to run *in operando*) could be synthesised with a PBM to extrapolate future production in real time. Designing such a flow through system was deemed out of scope for this work, but there is potential in such systems, and their application could reach further than LPE processes.

A. Appendix: Derivation of the Population Balance Model

The simplest form of breakage modelling derives from the use of well known PBEs which provide a system of equations that track the change of a distribution relative to a set of input conditions. The standard PBE assuming no spatial variation and one internal dimension (v) is:

$$\frac{\partial n(v, t)}{\partial t} = \text{Birth} - \text{Death} \quad (\text{A.1})$$

Where n is the number of particles of size v at time t . The form of the birth and death terms then determine the dynamics of the breakage. For any breakage system, the Death term is simply the breakage frequency (k , units s^{-1}) at size v multiplied by the total number of particles at size v .

$$\text{Death} = k(v, t) n(v, t)$$

The birth term for a breakage system is more complex.

$$\text{Birth} = \int_v^\infty p(v', t) k(v', t) P(v|v', t) n(v', t).dv'$$

Assuming no particles aggregate and hence jump from a lower size state to a higher size state, the number of particles birthed into size v is the integral of all possible parent particle sizes v' to ∞ . p is the average number of particles formed from the breakage event (for a binary breakage system, $p = 2$), P is the probability density function for a parent particle v' to break into state v ; the function is also known as the stoichiometric kernel, or the aptly named daughter distribution, as this determines how the daughter particles are distributed. Combining the birth and death terms above with Equation A.1, assuming these kernels are static and are time invariant (as the conditions inside the vessel are kept constant):

$$\frac{\partial n(v, t)}{\partial t} = \int_v^\infty p(v') k(v') P(v|v') n(v', t).dv' - k(v)n(v, t) \quad (\text{A.2})$$

Note that by conservation of mass, the volume must remain constant:

$$V = \int_0^\infty v n(v, t).dv \quad \& \quad \frac{\partial}{\partial t} V = 0$$

A common issue in Equation A.2 is that it does not conserve mass. Refactoring to this end is possible; letting f be the volume fraction, such that $f(v, t) = vn(v, t)$, with P being refactored to represent a new overall kernel $\Phi = l_1(vpP)$ with l_1 indicating that Φ is normalised to 1 (l_1 norm), guaranteeing conservation of mass.

$$\frac{\partial f(v, t)}{\partial t} = \int_f^\infty k(v') \Phi(v|v') .df' - k(v) f(v, t) \quad (\text{A.3})$$

Using equations A.2 & A.3, a one-dimensional numerical solver [295] was set up and first validated against analytical results created by Ziff and McGrady [5]. For example, for the scenario of random, binary breakup with size-dependent rate, the analytical solution of which is:

$$\begin{aligned} \text{Number:} & \quad \left\{ k(x) = x^2, \quad p = 2, \quad P(x|x') = \frac{1}{x'} \right\} \\ \text{Fraction:} & \quad \left\{ k(x) = x^2, \quad \Phi(x|x') = l_1 \left(\frac{x}{x'} \right) \right\} \end{aligned}$$

$$n(x, t) = (1 + 2t(1 + x)) e^{-tx^2 - x}$$

Applying these relationships, the error between approaches can be evaluated against the analytical truth (Figure A.1).

The comparison is favourable in both cases, however it is evident from the error plots in Figure A.1 that the fractional solution exhibits less error predicting the dynamics of the smallest particles in the system, a favourable characteristic for applying to micro and nanoscale materials. The maximum error in the numerical solution for particles of size 1 mm and less is 0.05%. The final kernel function is defined as:

$$\Phi(v|v') = l_1 \left(\left(\frac{v}{v'} \right)^A \right) \quad (\text{A.4})$$

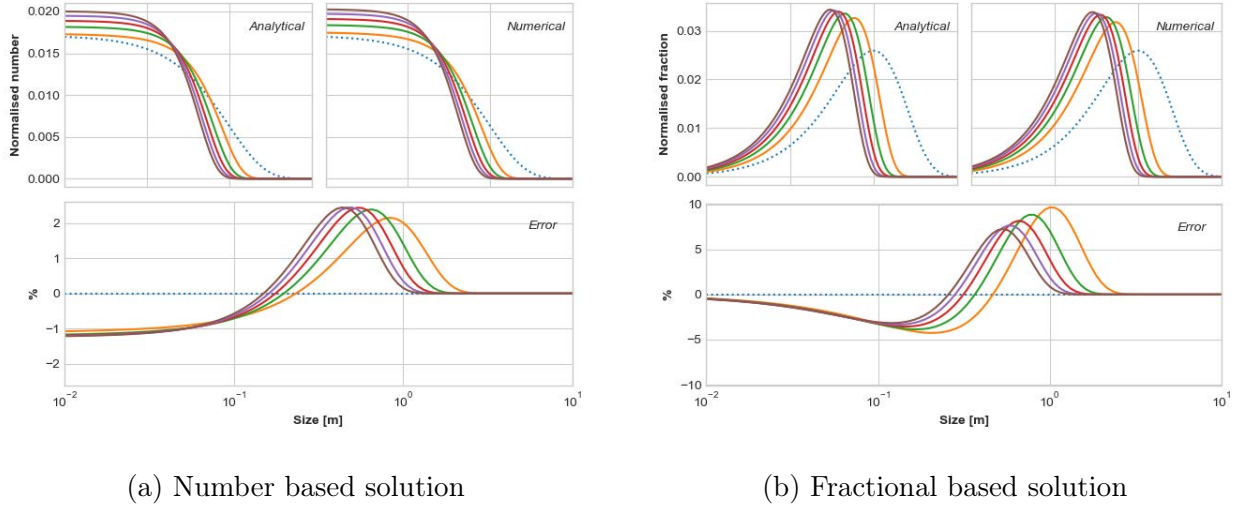


Figure A.1: Numerical methods compared to the base analytical truth according to Ziff and McGrady [5]. Zero time is indicated in the dotted blue line, with subsequent times in different colours. Though the maximum error is less when using a number-based solution (2%), a fractional solution is more accurate at the lowest sizes.

Converting to number basis yields:

$$P(v|v') = \frac{A}{v'} \left(\frac{v'}{v} \right)^{1-A} \Big|_{p=2} \quad (\text{A.5})$$

The rate is identical in both cases:

$$k(v) = \left(\frac{x_v}{B} \right)^E \quad (\text{A.6})$$

P , k and Φ all follow a power law relationship. Applying the model to the present case of shear exfoliation, the error in the number-based formulation can be clearly observed in Figure A.2 for few-layer graphene dispersions. Here, UV-vis-NIR spectroscopic measurements were

used to determine concentration as described in Chapter 4.

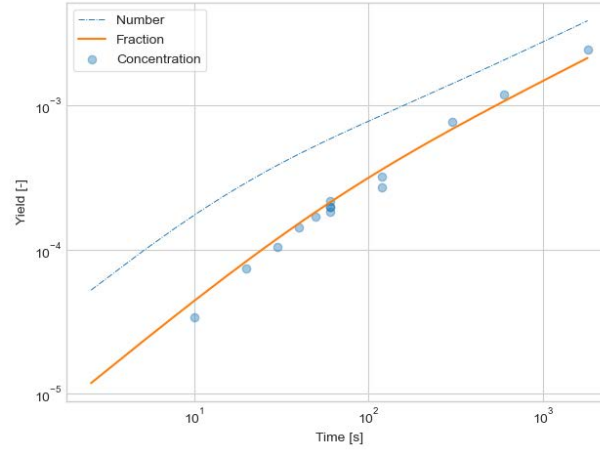


Figure A.2: Direct comparison between models tracking number and fraction at a cutoff value of $S = 1.6 \mu\text{m}$, against few-layer graphene yield measurements. All data fitted to 11500 rpm speed.

B. Appendix: Dimensional Analysis

Nomenclature

Symbol	Dimensions	Description
Y	-	Yield
C	M^1L^{-3}	Concentration of nanomaterial
C_i	M^1L^{-3}	Concentration of bulk precursor
C_s	M^1L^{-3}	Concentration of surfactant
ρ	M^1L^{-3}	Density
μ	$M^1L^{-1}T^{-1}$	Dynamic viscosity
d_i	L^1	Impeller diameter
d	L^1	Diameter

R	L^1	Radial distance
V	L^3	Volume
Q	L^3T^{-1}	Flow rate
f	T^{-1}	Process specific frequency
N	T^{-1}	Impeller speed
$\dot{\gamma}$	T^{-1}	Shear rate
t	T^1	Time
t_r	T^1	Total residence time
T	T^1	Total processing time

B.1 Introduction

Though many attempts have been made to define Liquid Phase Exfoliation (LPE) locally, or at the nano-scale at which it occurs, a holistic model of the phenomenon has not yet been introduced. In Chapter 4, a statistical model of shear exfoliation processes is presented. Although this Population Balance Model (PBM) describes production well, as a product of probable interactions between the bulk liquid carrier and a bulk precursor material (e.g. bulk graphite). By definition, this model conserves mass; however, it lacks any definition of energy. Energy has a significant impact, as it limits the number of interactions that can take place in the system and how much material is produced. Therefore, without prior knowledge of the expected nanomaterial concentration or a close estimate of the value of the coefficients of the PBM, it is difficult or impossible to predict nanomaterial production.

The properties of the liquid carrier with respect to the nanomaterial being created determine its suitability for LPE, and thus the bulk material itself has little impact on the system as a whole, save for the general point that the in, the more out. This result is well known and has been demonstrated in many different systems such as ultrasonication probes and baths, microfluidisation, and stirred batch reactors, thus it makes conceptual sense to think of LPE in terms of yield. Varrla et al. [6] examines effect of initial concentration, up to a limiting loading of $C_i \simeq 100$ mg/mL for graphene (though Varrla et al. vary surfactant concentration with material loading). Taking this as an indication of where four-way particle interactions begin under these conditions, the phase map presented in Figure 4.2 shows a slight overestimation of the conditions favouring four-way coupling¹. An increasing C_i would eventually lead to fully granular flow, changing the dynamics of the system substantially.

¹Though loading of bubbles would outweigh any loading of material, due to the heavily foamy nature of the flow.

When operating on the limit or under unfavourable conditions, proportionality breaks and $C \propto g(C_i)$, where usually $C \propto C_i^\chi$. An example of non-linearity between the initial bulk concentration and nanomaterial production is the case of MoS_2 , which has been observed behaving both superlinearly and sublinearly in different solutions [7, 8]. The difference in these results suggests that the solution in each case cannot stabilise nanomaterial adequately as it is being created. This reasoning suggests production should saturate at some total surface area of material in solution, specific to the solvent chosen and its solubility.

Dimensional analysis is a proven, powerful tool for reducing the space of complex engineering problems. Assuming the fluidic system is isotropic, it is possible to derive a general method to evaluate the effectiveness of disparate LPE systems. Applying dimensional analysis to a LPE gives insights into the effects of key system parameters, such as volume, time and power input. Often, a single composite dimensionless quantity with a power-law fit is enough to predict how systems will scale under disparate conditions [7]. Dimensional analysis is presented here as a supplement to the PBM demonstrated in Chapter 4. Together, they represent an analysis geared towards mass balance (PBM) and energy balance (Dimensional Analysis).

B.2 Analysis

Paton et al. [7] first showed that LPE occurs regardless of whether the conditions in the system are turbulent or laminar, but that it only occurs above a critical shear rate. For the purposes of defining LPE in the simplest terms, suppose it is purely an interaction between the average shear rate $\dot{\gamma}$ and the time the parent particles in suspension are exposed to this the shear rate t_r , as stated by Stafford et al. [168] under similar surfactant conditions. Applying Buckingham's theorem, the simplest possible equation to relate Yield Y to shear rate is with only one Π term:

$$0 = g(Y, \dot{\gamma}, t_r) \implies Y = \Phi(\dot{\gamma} \cdot t_r), \text{ where } Y = \frac{C}{C_i}$$

$$Y = \Phi(\dot{\gamma} \cdot t_r) \tag{B.1}$$

The equation above boils down to a balance of probabilities, with t_r typically requiring a *process specific* definition. For a homogeneous dispersion with stokes-like flow, the residence time is equivalent to the mixing time $t_r = t_m$. As it is difficult to measure t_r directly, it is possible to derive a Π -term by including a characteristic frequency f :

$$0 = g(Y, \dot{\gamma}, f, t) \implies Y = \Phi\left(\frac{\dot{\gamma}}{f}, ft\right)$$

With the simplest combination of these terms being:

$$Y = \Phi \left(\frac{\dot{\gamma}^2 t}{f} \right) \quad (\text{B.2})$$

This is equivalent to setting $t_r \propto \sqrt{\frac{t}{f}}$.

B.2.1 Shear mixers

Paton et al. [7] notes that the square root of energy dissipated per unit volume seems to collapse their data, and applying the power number relation for $\dot{\gamma}$ in shear mixers [248], arrive at:

$$\text{N.B.} \quad P/V = \mu \dot{\gamma}^2, \quad \dot{\gamma} = \sqrt{\frac{N_p \rho N^3 d_i^5}{\mu V}}$$

$$Y \sim \sqrt{\frac{E}{V}} = \sqrt{\frac{Pt}{V}} = \sqrt{\frac{N_p \rho N^3 d_i^5 t}{V}} \implies C \propto C_i t^{0.5} N^{1.5} d_i^{2.5} V^{-0.5}$$

The latter having SI units of $\text{kg}^{0.5} \text{m}^{0.5} \text{s}^{-1}$. Seeking instead to find a non-dimensional relation between P and Y (which is a non-dimensional quantity) using Equation B.2, one can arrive at a similar expression:

$$Y \sim \sqrt{\frac{\dot{\gamma}^2 t}{N}} = \sqrt{\frac{Pt}{\mu N V}} = \sqrt{\frac{N_p \rho N^2 d_i^5 t}{\mu V}} \implies C \propto C_i t^{0.5} N^1 d_i^{2.5} V^{-0.5}$$

A more complete view is to look at a system as a whole, with a relationship derived according

to all the parameters of the system. As an example, isolating the key fluidic parameters of shear mixers and applying the Buckingham Pi theorem yields:

$$0 = f(Y, \rho, t, N, d_i, \mu, V) \implies Y = \Phi\left(\frac{\rho N d_i^2}{\mu}, \frac{d_i^3}{V}, tN\right)$$

Note that the relations derived from Paton et al. [7] can be viewed as a subset of this general function. In experiments, note that shear mixers exhibit power law scaling in all cases, thus:

$$Y \sim \left(\frac{\rho N d_i^2}{\mu}\right)^r \left(\frac{d_i^3}{V}\right)^v (tN)^\tau \implies C \propto C_i t^\tau N^{\tau+r} d_i^{2r+3v} V^{-v} \quad (\text{B.3})$$

Where τ , r and v are fitted parameters, dependent on the conditions inside the blender. Note that Equation B.3 is a composite of three dimensionless terms; Reynolds, shape and time, the simplest combination of which is letting $\tau \equiv r \equiv v$:

$$Y \sim \left(\frac{\rho N^2 d_i^5 t}{\mu V}\right)^\tau \implies C \propto C_i t^\tau N^{2\tau} d_i^{5\tau} V^{-\tau} \quad (\text{B.4})$$

Equation B.4 is used here to fit all data involving shear mixer systems. This is for simplicity, as adding further fitting parameters (r & v) collapses the data negligibly close to their best fits. Note that a large amount of data for shear mixers is provided by Paton et al. [7] with the system being a rotor-stator mixer of differing design to other shear mixers (often kitchen blenders [3, 6, 8]), as it forces fluid through small channels to increase the shear rate, before dissipating into the vessel at large. All of these are operated in batch mode as opposed to a continuous mode. This final equation suggests the following relationship to yield:

$$Y \sim \Phi \left(\frac{\text{total inertial action}}{\text{total viscous action}} \right)$$

As an aside, if one instead looks solely to derive a non-dimensional representation for shear rate:

$$\dot{\gamma} \propto f(\rho, N, d_i, \mu, V) \implies \frac{\dot{\gamma}}{N} = \Phi \left(\frac{\rho N d_i^2}{\mu}, \frac{d_i^3}{V} \right)$$

And by setting $\Phi = k\sqrt{\Pi_1 \cdot \Pi_2}$:

$$\dot{\gamma} = k \sqrt{\frac{\rho N^3 d_i^5}{\mu V}}$$

This being equivalent to the theoretical definition of shear rate within stirred batch reactors, as $k = N_p^2$, where N_p is constant for baffled vessels, and has a slight negative slope for unbaffled vessels [248] (see Chapter 3).

Empirically derived exponents for dimensional relations from multiple sources are presented in Table B.1. Though a lot of information is marred through inconsistent surfactant conditions, it is still presented here because there is a lack of detailed research in this area. C_i for MoS₂, as mentioned previously was found to scale strangely, from 0.7 [7] in NMP and 1.25 [8] in a Sodium Cholate and Deionised water solution, indicating that MoS₂ is very sensitive to surfactant conditions. Varrla et al. [8], use $C_s = 10$ mg/mL, which is double the CMC for deionised water 4.3 mg/mL (and above the 10 mM limit specified by Griffin et al. [246], suggesting heavily adverse conditions), which would go some way to explaining the difference. **n** indicates the number of points with which these relations were established. d_i is only ever weakly varied between 10 mm to 32 mm by Paton et al. [7].

Table B.1: Table of empirically derived exponents for various shear mixer devices, from multiple sources. Orange text indicates that surfactant conditions were not constant across all fits. g is graphite/graphene, \downarrow indicates the data was replicated and fitted using Equation B.4. Highlighted rows indicate that not enough information is given to replicate the dataset.

Solution	t	N	d_i	V	\mathbf{n}	R^2	Ref
NMP							
g	0.66	1.13	2.28	-0.68	47	0.9161	[7]
\downarrow	0.49	0.98	2.46	-0.49	47	0.8859	
MoS ₂	0.56	1.26	1.83	-0.49	-	-	[7]
Fairy Liquid and Deionised Water							
g	1.00	0.53	-	-0.16	56	0.9654	[6]
\downarrow	0.98	1.95	-	-0.98	35	0.8981	
g	0.41	0.72	-	-0.28	19	0.8087	[2]
\downarrow	0.34	0.68	-	-0.34	19	0.8087	
Sodium Cholate Hydrate and Deionised Water							
g	1.08	2.54	3.34	-	-	-	[7]
g	0.77	1.46	-	-	41	0.9701	
\downarrow	0.76	1.52	-	-	41	0.9689	
MoS ₂	0.88	2.9	-	-0.41	26	0.9321	[8]
\downarrow	1.12	2.24	-	-1.12	26	0.9308	
WS ₂	0.55	7.15	-	-0.84	15	-	[233]
PVA and Deionised Water							
g	0.66	0.92	-	-	-	-	[7]

B.2.2 Sonicating probes

Though there are a large number of studies using sonicating probes for LPE, there are few which focus on process optimisation and key parameters. Utilising Equation B.1, one can predict the scaling to be:

$$Y = \Phi \left(\frac{Pt}{\mu f V} \right) \quad \text{or} \quad \Phi \left(\frac{\underline{e}t}{\mu V} \right)$$

Where \underline{e} is the energy delivered to the fluid per stroke. This ascribes the scaling:

$$C \propto C_i \underline{e}^\tau t^\tau V^{-\tau}$$

Table B.2: Table of empirical exponents for sonication, from multiple sources. g indicates graphite/graphene. Arao and Kubouchi [10] do exceptional work, varying volume from the tens of milliliters to the tens of litres.

Solution	C_i	t	V	Ref
NMP				
g	1	0.79	-0.68	[10]
g	1	0.5	-	[162]
g	1	0.5	-	[302]
NaC and deionised water				
g	1	0.77	-0.64	[10]

But without an in-depth parameter study, there is little opportunity to discover whether this relationship is correct. However, it does agree with the limited experimental data available for sonicating probes (See Table B.2). Here, the exponent for time follows the exponent for

volume [10], which much like in the shear mixer case, has a slightly lower-than expected value.

B.2.3 Microfluidisation

Microfluidisation has been shown to be incredibly effective for producing large quantities of pristine graphene [11, 165]. Unfortunately, these reports do not contain enough information to compare findings or to gain any useful insight on the hydrodynamics within the microfluidiser. Setting $f = \frac{Q}{V}$ in Equation B.1:

$$Y = \Phi \left(\frac{\Delta p t Q}{\mu f V} \right) \implies \Phi \left(\frac{\Delta p t}{\mu} \right)$$

$$C \propto C_i \Delta p^\tau t^\tau$$

This indicates that the yield for this process is volume independent, and that production will occur so long as there is some pressure drop Δp across the chamber. The continuous nature of the process suggests that it must be volume independent, as larger volumes at the same flow rate and pressure drop should have no impact on the yield of few-layer material produced (as yield scales with volume). This assumes that the shear rate is acting on the fluid continuously. Theory indicates that this pressure drop is however a function of flow rate Q and the geometry [298]:

$$\frac{\Delta p V}{\mu Q} = \Phi \left(\frac{\rho Q}{\mu d}, \frac{d}{R} \right)$$

Suggesting that their could be path to defining a hollistic expression, as in the shear mixer analysis. Arao et al. [9] modifies the applied pressure of a laminar-flow valve homogeniser at

a fixed flow rate $Q = 57 \text{ L min}^{-1}$, by modifying the width between the valve and its seat d to a mixture of NaC and deionised water. Through numerical simulations, they find shear rate to scale sublinearly with applied pressure, $\dot{\gamma} \propto p_a^{0.68}$ (though fit is only corroborated at one flow rate $Q = 22 \text{ L min}^{-1}$), which implies that the head loss due to shear rate alone is expected to scale superlinearly with applied pressure (as $\Delta p \sim \dot{\gamma}^2$, and $\dot{\gamma}^2 \propto p_a^{2 \times 0.68}$), hence:

$$C \propto C_i p_a^{1.36\tau} t^\tau$$

Experimentally, Arao et al. [9] finds exponents of $C \propto C_i^1 p_a^1 t^{0.72}$ at that fixed flow rate. This again fits the prediction driven from the numerical simulations and non-dimensional arguments (if $\tau = 0.72$ the numerical relation suggests $C \propto C_i p_a^{0.98} t^{0.72}$). Unfortunately, these two quantities (p_a, t) are evaluated under differing surfactant conditions C_s , so it is hard to draw causation from this notable similarity. For microfluidic channel mixers, estimating production should perceivably be much simpler, as one could easily check the pressure drop across the microchannels.

B.3 Results and Discussion

To examine the applicability of the dimensional relationships derived from Equation B.1, it was applied to the works of Varrla et al. [6, 8], Paton et al. [7], Arao et al. [9] and the results of Chapters 2-3 [2, 3]. However, several of these tests were unfortunately conducted at differing surfactant concentrations adding some uncertainty [2, 6, 9]. These articles alone provided enough information to replicate the dataset, presented in Figure B.1. After accruing the data, the best fit exponent according to the given parameters of the systems were calculated and plotted against the system yield in Figure B.2, as opposed to the non-dimensional fit presented in Figure B.1. As the best fit arguments represent the best fit for the given system, any global relation derived will stray from this perfect value.

In juxtaposition with Figure B.1 where all relations are 1 parameter (τ) in size, the ‘best fit’ relations are between 2 to 4 parameters in size. The refactoring according to Equation B.1 demonstrates little deviation from the best-fit exponents, in spite of varying conditions. Notably, Varrla et al. [6] vary surfactant conditions with C_i . In their later work [8] using MoS_2 , they kept to the CMC for the liquid. In the only example of its type, they also demonstrate a fitted exponent for N which is lower than the fitted exponent for t . Even with these uncertainties in the data, the non-dimensional rescaling still performed adequately. A more global inconsistency is that the exponent for volume is typically lower than the exponent for time when Equation B.4 suggests that they should be equal yet inverse of each other. In this case, isolating the shape term $\frac{d_i^3}{V}$ and treating the volume exponent v differently to τ reduces this discrepancy.

Dimensional analysis does correlate the information gathered herein on shear exfoliating methods, and presents a simple theoretical framework with which to analyse new shear exfoliating systems. The most basic interpretation involves shear rate and residency

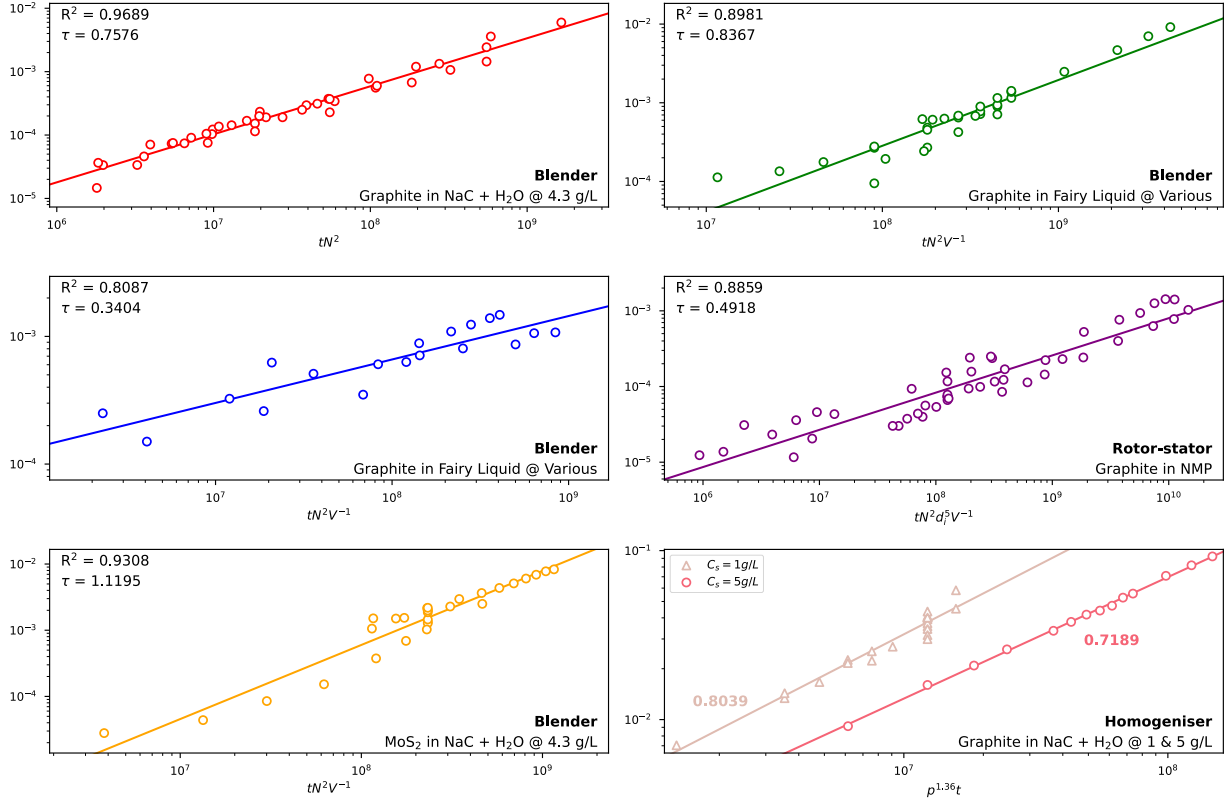


Figure B.1: Yield against a non-dimensional argument. From top left to bottom right, the works of Pérez-Álvarez, Brown, and Stafford [3], Varrla et al. [6], Pérez-Álvarez, Davies, and Stafford [2], Paton et al. [7], Varrla et al. [8] and Arao et al. [9] are digitised from their original sources. Surfactant concentration is indicated with @ where pertinent.

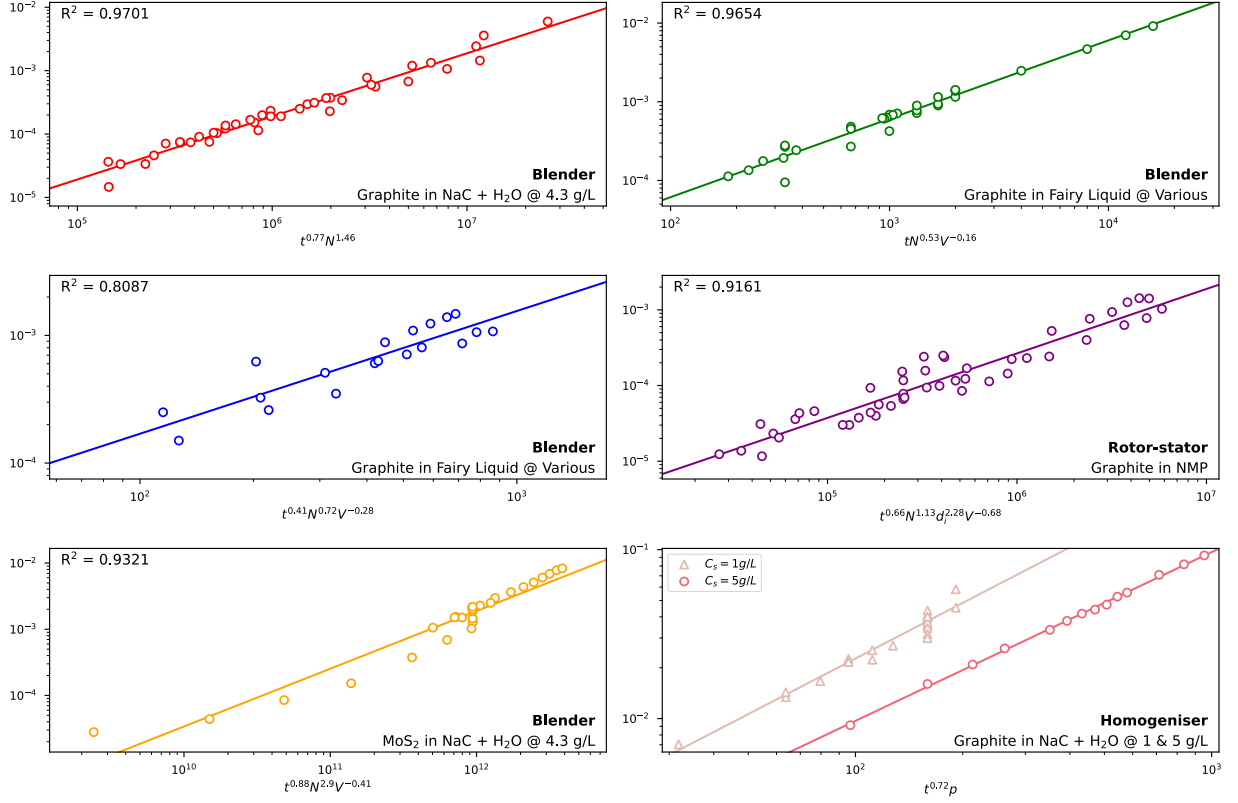


Figure B.2: Yield against the best fitting argument. From top left to bottom right, the works of Pérez-Álvarez, Brown, and Stafford [3], Varrla et al. [6], Pérez-Álvarez, Davies, and Stafford [2], Paton et al. [7], Varrla et al. [8] and Arao et al. [9] are digitised from their original sources, subject to information provided by their authors to recreate them here. Surfactant concentration is indicated with @ where pertinent.

time, which affords close correlation with empirical evidence (see Figure B.1). The largest discrepancy is due to volume, which shifts from $-1\times$ to $-0.5\times$ relative to the time exponent τ , though this can be mitigated by treating τ and v separately. One explanation for this behaviour is that many of these systems are not pressurised, and thereby exhibit heavily aerated and foamy flows when processing [2]. Thus by pressurising the system or under larger volumes where foam flows are less present, we would expect to find more of the energy dissipated within the fluid and the volume exponent to be closer to unity. The relationship in equation B.3 also suggests that if production is intensified and τ increases, the scalability of said process will reduce as volume scales with $-\tau$. Counter-intuitively, all systems analysed suggested that lowering the viscosity of the liquid would increase yield, though a method of testing this accurately without in turn impacting nanomaterial stability in solution seems difficult.

For shear mixers, the size of the blades has the largest impact on production with an exponent near 5τ , though blade speed is also a consistently high factor at 2τ . τ itself seems similar in the case of graphite in NaC solution, with most articles falling between $0.72 < \tau < 0.8$, while graphite in NMP behaves within $0.5 < \tau < 0.79$. Cases involving Fairy liquid had issues with changing surfactant conditions, which can go some way to explaining the large deviation in τ . What does seem interesting is that for similar dispersant conditions, τ remains relatively similar regardless of the process chosen. This is clearest in the cases of Graphite in NMP ($\tau \approx 0.66$ [7], see Figure B.3) and in NaC with deionised water ($\tau \approx 0.75$), as there is much data to correlate findings between researchers.

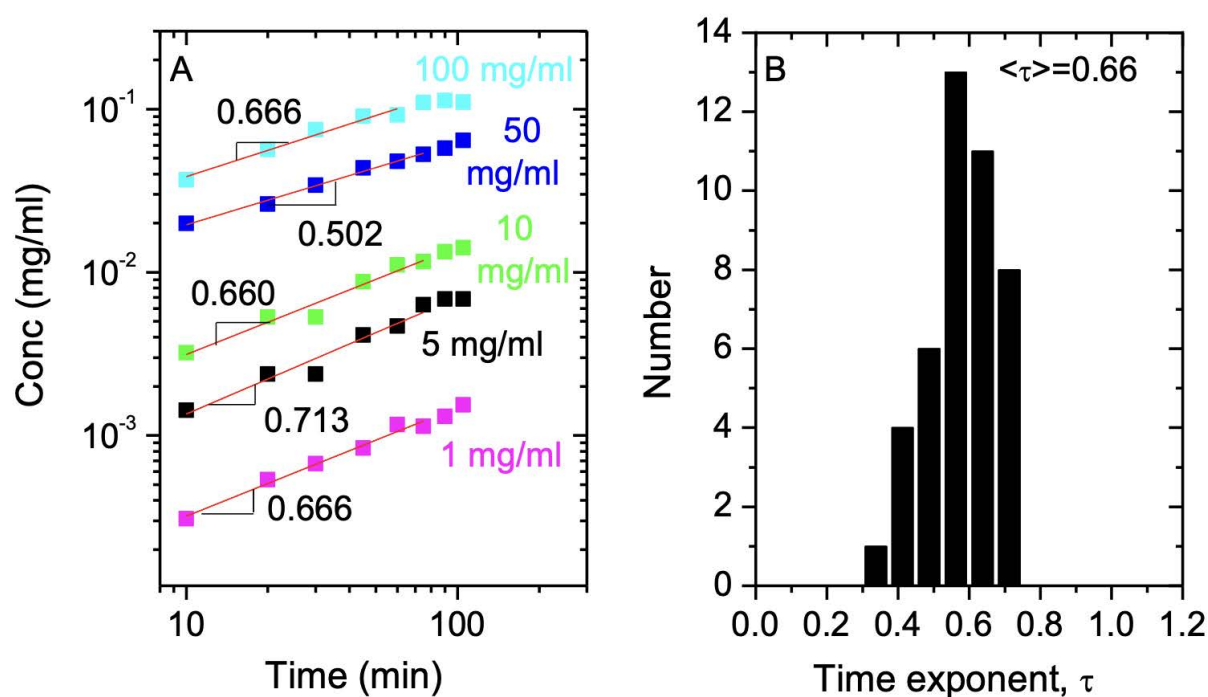


Figure B.3: Dispersed graphene concentration in NMP as a function of mixing time. These dispersions were prepared with $V=1500$ mL, $N=4500$ rpm and $D=32$ mm for a range of values of C_i . B) Histogram of all measured values of τ with the mean value of 0.66 shown. Reprint, with permission from Paton et al. [7].

B.4 Conclusion

Dimensional analysis provides a theoretical framework with which to analyse LPE in distinct scenarios, and suggests a simple intuition for LPE globally (Equation B.1). This assumption provides a remarkably accurate fit (see Figure B.1) to the data collated from multiple sources. The largest discrepancy between the non-dimensional relationships occurs in exponents relating to volume, though this discrepancy is negligible in most scenarios.

C. Appendix: Arduino Snippets

This section provides a place for snippets of Arduino code which would otherwise break up reading of the thesis.

C.1 Simple Triac Control

A simple triac module (detailed in Chapter 2) can be controlled using fairly simple code. Beginning by attaching the zero-cross pin of the module to an interrupt on a suitable microcontroller board (ZERO_PIN) and the gate pin to a PWM output (AC_LOAD):

```
1  void zeroCrossISR() {
2      digitalWrite(AC_LOAD, LOW); // Write the gate LOW
3      ZERO_FLAG = true; // Set a flag to indicate zero-cross
4      ZERO_TIME = micros(); // Set the time of the zero-cross
5  }
6
7  void setup() {
8      attachInterrupt( // Check whether signal is rising
9          digitalPinToInterrupt(ZERO_PIN),
```

```
10     zeroCrossISR, // ISR triggered
11     RISING // Trigger on a rising edge.
12 );
13 }
```

The above loop checks if the flag has been set by the Interrupt Service Routine (ISR) `zeroCrossISR`, which if true establishes the time since the last trigger; if this time is larger or equal to the phase angle (or dimming time), the loop then waits until a short propagation delay (10 μ s for most triacs) has been reached, at which point the flag is reverted and the gate pin is set back to `LOW`. Though this example could be handled in a single ISR, it leaves little scope for modifications to the code. Some board manufacturers have released [Arduino header files](#) to streamline the integration of triac boards into projects, but the simple implementation listed above worked well without this.

C.2 Measuring Rotational Speed

Rotational speed of the blender can be measured directly, and is implemented as an ISR in code:

```
1  void setup() {
2      attachInterrupt(
3          digitalPinToInterrupt(LIGHT_GATE),
4          updateCountISR, // Raises the count
5          RISING // Triggered when photointerrupt is RISING
6      );
7  }
8
9  void loop() {
10     READ_TIME = millis() - START_TIME; // Time between reads
```

```
11     READ_COUNT = ReadCount() - START_COUNT; // Counts between time
12     if (READ_TIME >= 1000) { // Update speed measurement every 1000 ms
13         OMEGA = ((60*1E3*READ_COUNT)/READ_TIME); // Calculate RPM
14         if (!OMEGA) { OMEGA = 0; } // Check for NaN values when count is low
15     }
16 }
```

The above stores and updates the blender speed every second as the variable OMEGA. This can be used by itself as a speed sensor without any further modification, though at this point it becomes trivial to implement closed loop control if one has already has the modifications in Section 2.4.2.

C.3 PID Control

By comparing a target speed to the actual speed every time OMEGA is calculated, one returns an error term, which can then feedback into the value for dim_time.

```
1     PID_ERROR[0] = OMEGA - SET_OMEGA; // Proportional
2     PID_ERROR[1] += PID_ERROR[0]; // Integral
3     PID_ERROR[2] = PID_ERROR[0] - PID_ERROR[3]; // Differential
4     PID_ERROR[3] = PID_ERROR[0]; // Previous error stored for next cycle
5     // Update DIM_TIME with PID output
6     control_signal = /*k_p*/PID_ERROR[0] + /*k_i*/PID_ERROR[1] + /*k_d*/PID_ERROR[2];
7     dim_time = SET_POINT + control_signal; // Update dim_time
```

This short section of code calculates the different PID terms and then goes on to modify the DIM_TIME accordingly. In Figure 2.4b, shows the rotational speed of the blender over the first 15 minutes *on* of a run (Manufacturer recommendation is to run for 1 minute *off* after every minute *on* to avoid overheating), and shows that the speed is maintained

very accurately except during the first second of the run when the rotor is still in the process of attaining its target speed. After the first cycle, the PID controller is set not to update after the first reading, so that this initial rise in velocity does not perturb the integral value discovered in previous cycles (it is also useful to limit this integral value `PID_ERROR[1]` as in the case of high speeds, it may drift)

References

- [1] Diego T. Pérez-Álvarez et al. “Challenges surrounding nanosheets and their application to solar-driven photocatalytic water treatment”. In: *Mater. Adv.* 3.10 (2022), pp. 4103–4131. DOI: [10.1039/D2MA00276K](https://doi.org/10.1039/D2MA00276K).
- [2] Diego T. Pérez-Álvarez, Philip Davies, and Jason Stafford. “Foam flows in turbulent liquid exfoliation of layered materials and implications for graphene production and inline characterisation”. In: *Chem. Eng. Res. Des.* 177 (Jan. 2022), pp. 245–254. ISSN: 0263-8762. DOI: [10.1016/j.cherd.2021.10.041](https://doi.org/10.1016/j.cherd.2021.10.041).
- [3] Diego T. Pérez-Álvarez, Jacob Brown, and Jason Stafford. “Modification of kitchen blenders into controllable laboratory mixers for mechanochemical synthesis of atomically thin materials”. In: *HardwareX* 16 (Dec. 2023), e00471. ISSN: 2468-0672. DOI: [10.1016/j.ohx.2023.e00471](https://doi.org/10.1016/j.ohx.2023.e00471).
- [4] Diego T. Perez-Alvarez et al. “Predicting graphene production with population balance modelling”. In: *Carbon* 231 (Jan. 2025), p. 119687. ISSN: 0008-6223. DOI: [10.1016/j.carbon.2024.119687](https://doi.org/10.1016/j.carbon.2024.119687).

-
- [5] R. M. Ziff and E. D. McGrady. “The kinetics of cluster fragmentation and depolymerisation”. In: *J. Phys. A: Math. Gen.* 18.15 (Oct. 1985), p. 3027. ISSN: 0305-4470. DOI: [10.1088/0305-4470/18/15/026](https://doi.org/10.1088/0305-4470/18/15/026).
- [6] Eswaraiiah Varrla et al. “Turbulence-assisted shear exfoliation of graphene using household detergent and a kitchen blender”. In: *Nanoscale* 6.20 (20 Oct. 2014), pp. 11810–11819. ISSN: 20403372. DOI: [10.1039/c4nr03560g](https://doi.org/10.1039/c4nr03560g).
- [7] Keith R. Paton et al. “Scalable production of large quantities of defect-free few-layer graphene by shear exfoliation in liquids”. In: *Nature Materials* 13 (6 June 2014), pp. 624–630. ISSN: 14764660. DOI: [10.1038/nmat3944](https://doi.org/10.1038/nmat3944).
- [8] Eswaraiiah Varrla et al. “Large-Scale Production of Size-Controlled MoS₂ Nanosheets by Shear Exfoliation”. In: *Chem. Mater.* 27.3 (Feb. 2015), pp. 1129–1139. ISSN: 0897-4756. DOI: [10.1021/cm5044864](https://doi.org/10.1021/cm5044864).
- [9] Yoshihiko Arao et al. “Mass production of high-aspect-ratio few-layer-graphene by high-speed laminar flow”. In: *Carbon* 102 (June 2016), pp. 330–338. ISSN: 0008-6223. DOI: [10.1016/j.carbon.2016.02.046](https://doi.org/10.1016/j.carbon.2016.02.046).
- [10] Yoshihiko Arao and Masatoshi Kubouchi. “High-rate production of few-layer graphene by high-power probe sonication”. In: *Carbon* 95 (Dec. 2015), pp. 802–808. ISSN: 0008-6223. DOI: [10.1016/j.carbon.2015.08.108](https://doi.org/10.1016/j.carbon.2015.08.108).
- [11] Panagiotis G. Karagiannidis et al. “Microfluidization of Graphite and Formulation of Graphene-Based Conductive Inks”. In: *ACS Nano* 11 (3 Mar. 2017), pp. 2742–2755. ISSN: 1936086X. DOI: [10.1021/acs.nano.6b07735](https://doi.org/10.1021/acs.nano.6b07735).
- [12] Hannah Ritchie. *Water Use and Stress*. <https://ourworldindata.org/water-use-stress>, (accessed November 2021). 2017.

-
- [13] Ahmed G Yehia et al. “Impact of extreme climate events on water supply sustainability in Egypt: case studies in Alexandria region and Upper Egypt”. In: *Journal of Water and Climate Change* 8.3 (2017), pp. 484–494.
- [14] Declan Conway. “From headwater tributaries to international river: Observing and adapting to climate variability and change in the Nile basin”. In: *Global Environmental Change* 15.2 (2005). Adaptation to Climate Change: Perspectives Across Scales, pp. 99–114. ISSN: 0959-3780. DOI: <https://doi.org/10.1016/j.gloenvcha.2005.01.003>. URL: <https://www.sciencedirect.com/science/article/pii/S0959378005000026>.
- [15] WHO, ed. *Progress on drinking water, sanitation and hygiene: 2017 update and SDG baselines*. World Health Organisation (WHO) and the United Nations Children’s Fund (UNICEF). 2017.
- [16] David L. Sedlak and Urs von Gunten. “The Chlorine Dilemma”. In: *Science* 331.6013 (2011), pp. 42–43. ISSN: 0036-8075. DOI: [10.1126/science.1196397](https://doi.org/10.1126/science.1196397). eprint: <https://science.sciencemag.org/content/331/6013/42.full.pdf>. URL: <https://science.sciencemag.org/content/331/6013/42>.
- [17] Vitaly Gitis and Nicholas Hankins. “Water treatment chemicals: Trends and challenges”. In: *Journal of Water Process Engineering* 25 (Oct. 2018), pp. 34–38. ISSN: 22147144. DOI: [10.1016/j.jwpe.2018.06.003](https://doi.org/10.1016/j.jwpe.2018.06.003).
- [18] Jia-Qian Jiang. “The role of coagulation in water treatment”. In: *Current Opinion in Chemical Engineering* 8 (2015). Nanotechnology • Separation engineering, pp. 36–44. ISSN: 2211-3398. DOI: <https://doi.org/10.1016/j.coche.2015.01.008>. URL: <https://www.sciencedirect.com/science/article/pii/S221133981500009X>.
- [19] Jaleh Mansouri, Simon Harrisson, and Vicki Chen. “Strategies for controlling bio-fouling in membrane filtration systems: challenges and opportunities”. In: *Journal of Materials Chemistry* 20.22 (2010), pp. 4567–4586.

- [20] Kevin G. McGuigan et al. “Solar water disinfection (SODIS): A review from bench-top to roof-top”. In: *Journal of Hazardous Materials* 235-236 (2012), pp. 29–46. ISSN: 0304-3894. DOI: <https://doi.org/10.1016/j.jhazmat.2012.07.053>. URL: <https://www.sciencedirect.com/science/article/pii/S0304389412007960>.
- [21] Bin Luo, Gang Liu, and Lianzhou Wang. “Recent advances in 2D materials for photocatalysis”. In: *Nanoscale* 8 (13 Apr. 2016), pp. 6904–6920. ISSN: 20403372. DOI: [10.1039/c6nr00546b](https://doi.org/10.1039/c6nr00546b).
- [22] K. Sunada et al. “Bactericidal and detoxification effects of TiO₂ thin film photocatalysts”. In: *Environmental Science and Technology* 32.5 (1998). cited By 743, pp. 726–728. DOI: [10.1021/es970860o](https://doi.org/10.1021/es970860o). URL: <https://www.scopus.com/inward/record.uri?eid=2-s2.0-0032033652%5C&doi=10.1021%5C%2fes970860o%5C&partnerID=40%5C&md5=a4869b5f80de7c08beef872d9c9c7e1>.
- [23] Guoqiang Zhang et al. “Nanostructured photocatalysts for nitrogen fixation”. In: *Nano Energy* 71 (2020), p. 104645. ISSN: 2211-2855. DOI: <https://doi.org/10.1016/j.nanoen.2020.104645>. URL: <https://www.sciencedirect.com/science/article/pii/S2211285520302020>.
- [24] Qiong Liu et al. “2D ZnIn₂S₄ Nanosheet/1D TiO₂ Nanorod heterostructure arrays for improved photoelectrochemical water splitting”. In: *ACS Applied Materials and Interfaces* 6 (19 Oct. 2014), pp. 17200–17207. ISSN: 19448252. DOI: [10.1021/am505015j](https://doi.org/10.1021/am505015j).
- [25] Wenguang Tu et al. “Hollow spheres consisting of Ti_{0.91}O₂/CdS nanohybrids for CO₂ photofixation”. In: *Chem. Commun.* 51 (69 2015), pp. 13354–13357. DOI: [10.1039/C5CC03905C](https://doi.org/10.1039/C5CC03905C). URL: <http://dx.doi.org/10.1039/C5CC03905C>.
- [26] Dong Liu et al. “Review of Z-Scheme Heterojunctions for Photocatalytic Energy Conversion”. In: *Acta Physico-Chimica Sinica* 37.6, 2010017 (2021), p. 2010017. DOI: [10.3866/PKU.WHXB202010017](https://doi.org/10.3866/PKU.WHXB202010017). URL: http://www.whxb.pku.edu.cn/EN/abstract/article%5C_36186.shtml.

- [27] Ricardo A.R. Monteiro et al. “Evaluation of a solar/UV annular pilot scale reactor for 24h continuous photocatalytic oxidation of n-decane”. In: *Chemical Engineering Journal* 280 (2015), pp. 409–416. ISSN: 1385-8947. DOI: <https://doi.org/10.1016/j.cej.2015.06.014>. URL: <https://www.sciencedirect.com/science/article/pii/S1385894715008530>.
- [28] B. L. Abrams and P. C. K. Vesborg. “Catalysts for Environmental Remediation—Examples in Photo- and Heterogeneous Catalysis”. In: *New and Future Developments in Catalysis*. Ed. by Steven L. Suib. Elsevier, 2013, pp. 63–85. DOI: [10.1016/b978-0-444-53870-3.00004-6](https://doi.org/10.1016/b978-0-444-53870-3.00004-6). URL: <https://dx.doi.org/10.1016/b978-0-444-53870-3.00004-6>.
- [29] Adriana Rioja-Cabanillas et al. “Hydrogen from wastewater by photocatalytic and photoelectrochemical treatment”. In: *Journal of Physics: Energy* 3.1 (Dec. 2020), p. 012006. DOI: [10.1088/2515-7655/abceab](https://doi.org/10.1088/2515-7655/abceab). URL: <https://doi.org/10.1088/2515-7655/abceab>.
- [30] Zhidong Wei et al. “Simultaneous visible-light-induced hydrogen production enhancement and antibiotic wastewater degradation using MoS₂Zn_xCd_{1-x}S: Solid-solution-assisted photocatalysis”. In: *Chinese Journal of Catalysis* 41.1 (2020), pp. 103–113. ISSN: 1872-2067. DOI: [https://doi.org/10.1016/S1872-2067\(19\)63479-0](https://doi.org/10.1016/S1872-2067(19)63479-0). URL: <https://www.sciencedirect.com/science/article/pii/S1872206719634790>.
- [31] Vicki L Colvin. “The potential environmental impact of engineered nanomaterials”. In: *Nature Biotechnology* 21 (10 2003), pp. 1166–1170. ISSN: 1546-1696. DOI: [10.1038/nbt875](https://doi.org/10.1038/nbt875). URL: <https://doi.org/10.1038/nbt875>.
- [32] Stephanie K. Loeb et al. “The Technology Horizon for Photocatalytic Water Treatment: Sunrise or Sunset?” In: *Environmental Science & Technology* 53.6 (2019), pp. 2937–2947. DOI: [10.1021/acs.est.8b05041](https://doi.org/10.1021/acs.est.8b05041).
- [33] *Global Photovoltaic Power By Country*. <https://solargis.com>, (accessed November 2021). 2020.

-
- [34] Jean-Marie Herrmann. “Photocatalysis fundamentals revisited to avoid several misconceptions”. In: *Applied Catalysis B: Environmental* 99.3 (2010). TiO₂ photocatalysis-25 years, pp. 461–468. ISSN: 0926-3373. DOI: <https://doi.org/10.1016/j.apcatb.2010.05.012>. URL: <https://www.sciencedirect.com/science/article/pii/S0926337310002110>.
- [35] Akira Fujishima and Kenichi Honda. “Electrochemical photolysis of water at a semiconductor electrode”. In: *Nature* 238 (5358 1972), pp. 37–38. ISSN: 00280836. DOI: [10.1038/238037a0](https://doi.org/10.1038/238037a0). URL: <https://www.nature.com/articles/238037a0>.
- [36] Jiarui Huang et al. “Flower-like and hollow sphere-like WO₃ porous nanostructures: Selective synthesis and their photocatalysis property”. In: *Materials Research Bulletin* 47.11 (2012), pp. 3224–3232. ISSN: 0025-5408. DOI: <https://doi.org/10.1016/j.materresbull.2012.08.009>. URL: <https://www.sciencedirect.com/science/article/pii/S0025540812005806>.
- [37] Gratian R Bamwenda and Hironori Arakawa. “The visible light induced photocatalytic activity of tungsten trioxide powders”. In: *Applied Catalysis A: General* 210.1 (2001), pp. 181–191. ISSN: 0926-860X. DOI: [https://doi.org/10.1016/S0926-860X\(00\)00796-1](https://doi.org/10.1016/S0926-860X(00)00796-1). URL: <https://www.sciencedirect.com/science/article/pii/S0926860X00007961>.
- [38] Lisha Zhang et al. “Sonochemical synthesis of nanocrystallite Bi₂O₃ as a visible-light-driven photocatalyst”. In: *Applied Catalysis A: General* 308 (July 2006), pp. 105–110. ISSN: 0926-860X. DOI: [10.1016/j.apcata.2006.04.016](https://doi.org/10.1016/j.apcata.2006.04.016).
- [39] Anthony Harriman et al. “A new family of photocatalysts based on Bi₂O₃”. In: *Journal of Solid State Chemistry* 72.1 (1988), pp. 126–130. ISSN: 0022-4596. DOI: [https://doi.org/10.1016/0022-4596\(88\)90015-1](https://doi.org/10.1016/0022-4596(88)90015-1). URL: <https://www.sciencedirect.com/science/article/pii/0022459688900151>.

-
- [40] Virendra K. Saharan et al. “Advanced Oxidation Technologies for Wastewater Treatment”. In: Elsevier, 2014, pp. 141–191. DOI: [10.1016/b978-0-08-099968-5.00003-9](https://doi.org/10.1016/b978-0-08-099968-5.00003-9). URL: <https://dx.doi.org/10.1016/b978-0-08-099968-5.00003-9>.
- [41] Davide Vione, Tatiana Picatonotto, and M. Carlotti. “Photodegradation of phenol and salicylic acid by coated rutile-based pigments: A new approach for the assessment of sunscreen treatment efficiency”. In: *Journal of cosmetic science* 54 (2003), pp. 513–24.
- [42] Lin Chen, Pei Xu, and Huiyao Wang. “Photocatalytic membrane reactors for produced water treatment and reuse: fundamentals, affecting factors, rational design, and evaluation metrics”. In: *Journal of Hazardous Materials* (2021), p. 127493. ISSN: 0304-3894. DOI: [10.1016/j.jhazmat.2021.127493](https://doi.org/10.1016/j.jhazmat.2021.127493). URL: <https://dx.doi.org/10.1016/j.jhazmat.2021.127493>.
- [43] Aditya Chauhan et al. “Janus nanostructures for heterogeneous photocatalysis”. In: *Applied Physics Reviews* 5.4 (2018), p. 041111. ISSN: 1931-9401. DOI: [10.1063/1.5039926](https://doi.org/10.1063/1.5039926). URL: <https://dx.doi.org/10.1063/1.5039926>.
- [44] Jieying Jing et al. “Photocatalytic degradation of nitrogen-containing organic compounds over TiO₂”. In: *Journal of Molecular Catalysis A: Chemical* 351 (2011), pp. 17–28. ISSN: 1381-1169. DOI: <https://doi.org/10.1016/j.molcata.2011.10.002>. URL: <https://www.sciencedirect.com/science/article/pii/S1381116911004006>.
- [45] Jenny Schneider et al. “Understanding TiO₂ Photocatalysis: Mechanisms and Materials”. In: *Chemical Reviews* 114.19 (2014). PMID: 25234429, pp. 9919–9986. DOI: [10.1021/cr5001892](https://doi.org/10.1021/cr5001892). eprint: <https://doi.org/10.1021/cr5001892>. URL: <https://doi.org/10.1021/cr5001892>.
- [46] W. Ho, J.C. Yu, and S. Lee. “Synthesis of hierarchical nanoporous F-doped TiO₂ spheres with visible light photocatalytic activity”. In: *Chemical Communications* 10 (2006). cited By 357, pp. 1115–1117. DOI: [10.1039/b515513d](https://doi.org/10.1039/b515513d). URL: <https://www.>

- scopus.com/inward/record.uri?eid=2-s2.0-33644763046%5C&doi=10.1039%5C%2fb515513d%5C&partnerID=40%5C&md5=2465c4f17055aa4317b5f03c17a4830e.
- [47] Y. Kondo et al. “Preparation, photocatalytic activities, and dye-sensitized solar-cell performance of submicron-scale TiO₂ hollow spheres”. In: *Langmuir* 24.2 (2008), pp. 547–550. DOI: [10.1021/la702157r](https://doi.org/10.1021/la702157r).
- [48] H. An et al. “Synthesis and characterization of thermally stable nanotubular TiO₂ and its photocatalytic activity”. In: *Journal of Physical Chemistry C* 112.48 (2008), cited By 37, pp. 18772–18775. DOI: [10.1021/jp8031258](https://doi.org/10.1021/jp8031258). URL: <https://www.scopus.com/inward/record.uri?eid=2-s2.0-57949096598%5C&doi=10.1021%5C%2fjp8031258%5C&partnerID=40%5C&md5=51647ef273d0d24b821f62b7241aee79>.
- [49] Lilac Amirav and A. Paul Alivisatos. “Photocatalytic Hydrogen Production with Tunable Nanorod Heterostructures”. In: *The Journal of Physical Chemistry Letters* 1.7 (2010), pp. 1051–1054. DOI: [10.1021/jz100075c](https://doi.org/10.1021/jz100075c).
- [50] Xinzhen Yue et al. “Well-controlled SrTiO₃Mo₂C core-shell nanofiber photocatalyst: Boosted photo-generated charge carriers transportation and enhanced catalytic performance for water reduction”. In: *Nano Energy* 47 (2018), pp. 463–473. ISSN: 2211-2855. DOI: <https://doi.org/10.1016/j.nanoen.2018.03.014>. URL: <https://www.sciencedirect.com/science/article/pii/S2211285518301435>.
- [51] He Rongan et al. “S-scheme photocatalyst Bi₂O₃/TiO₂ nanofiber with improved photocatalytic performance”. In: *Journal of Materials Science & Technology* 52 (2020), pp. 145–151. ISSN: 1005-0302. DOI: <https://doi.org/10.1016/j.jmst.2020.03.027>. URL: <https://www.sciencedirect.com/science/article/pii/S1005030220302929>.
- [52] J.-H. Choy et al. “Exfoliation and restacking route to anatase-layered titanate nanohybrid with enhanced photocatalytic activity”. In: *Chemistry of Materials* 14.6 (2002), pp. 2486–2491. DOI: [10.1021/cm010815m](https://doi.org/10.1021/cm010815m).

-
- [53] Qipeng Lu et al. “2D transition-metal-dichalcogenide-nanosheet-based composites for photocatalytic and electrocatalytic hydrogen evolution reactions”. In: *Advanced Materials* 28.10 (2016), pp. 1917–1933.
- [54] Qing Han et al. “Atomically thin mesoporous nanomesh of graphitic C₃N₄ for high-efficiency photocatalytic hydrogen evolution”. In: *ACS nano* 10.2 (2016), pp. 2745–2751.
- [55] Junwei Fu et al. “Ultrathin 2D/2D WO₃/g-C₃N₄ step-scheme H₂-production photocatalyst”. In: *Applied Catalysis B: Environmental* 243 (2019), pp. 556–565.
- [56] Sookwan Leong et al. “TiO₂ based photocatalytic membranes: A review”. In: *Journal of Membrane Science* 472 (2014), pp. 167–184. ISSN: 0376-7388. DOI: [10.1016/j.memsci.2014.08.016](https://doi.org/10.1016/j.memsci.2014.08.016). URL: <https://dx.doi.org/10.1016/j.memsci.2014.08.016>.
- [57] Y. Li et al. “Photocatalyst design based on two-dimensional materials”. In: *Materials Today Chemistry* 11 (2019), pp. 197–216. ISSN: 2468-5194. DOI: <https://doi.org/10.1016/j.mtchem.2018.11.002>.
- [58] Lu Wang, Zdenek Sofer, and Martin Pumera. “Will Any Crap We Put into Graphene Increase Its Electrocatalytic Effect?” In: *ACS Nano* 14 (1 Jan. 2020), pp. 21–25. ISSN: 1936086X. DOI: [10.1021/acsnano.9b00184](https://doi.org/10.1021/acsnano.9b00184).
- [59] Saoirse Dervin, Dionysios D. Dionysiou, and Suresh C. Pillai. “2D nanostructures for water purification: graphene and beyond”. In: *Nanoscale* 8.33 (2016), pp. 15115–15131. ISSN: 2040-3364. DOI: [10.1039/c6nr04508a](https://doi.org/10.1039/c6nr04508a).
- [60] Alan P. Kauling et al. “The Worldwide Graphene Flake Production”. In: *Advanced Materials* 30.44 (2018), p. 1803784. DOI: <https://doi.org/10.1002/adma.201803784>. eprint: <https://onlinelibrary.wiley.com/doi/pdf/10.1002/adma.201803784>. URL: <https://onlinelibrary.wiley.com/doi/abs/10.1002/adma.201803784>.

-
- [61] ISO/TS 21356-1:2021(E). *Nanotechnologies – Structural characterization of graphene – Part 1: Graphene from powders and dispersions*. Standard. Geneva, CH: International Organization for Standardization, Mar. 2021.
- [62] Xin Li et al. “Graphene in Photocatalysis: A Review”. In: *Small* 12 (48 Dec. 2016), pp. 6640–6696. ISSN: 16136829. DOI: [10.1002/sml.201600382](https://doi.org/10.1002/sml.201600382).
- [63] A Vidal et al. “Solar photocatalysis for detoxification and disinfection of contaminated water: pilot plant studies”. In: *Catalysis Today* 54 (1999), pp. 283–290.
- [64] Diego H. Quiñones et al. “Removal of emerging contaminants from municipal WWTP secondary effluents by solar photocatalytic ozonation. A pilot-scale study”. In: *Separation and Purification Technology* 149 (2015), pp. 132–139. ISSN: 1383-5866. DOI: <https://doi.org/10.1016/j.seppur.2015.05.033>. URL: <https://www.sciencedirect.com/science/article/pii/S1383586615300186>.
- [65] A. Durán et al. “Photocatalytic degradation of aniline using an autonomous rotating drum reactor with both solar and UV-C artificial radiation”. In: *Journal of Environmental Management* 210 (2018), pp. 122–130. ISSN: 0301-4797. DOI: <https://doi.org/10.1016/j.jenvman.2018.01.012>. URL: <https://www.sciencedirect.com/science/article/pii/S0301479718300124>.
- [66] Encarnación Moral Pajares, Leticia Gallego Valero, and Isabel María Román Sánchez. “Cost of urban wastewater treatment and ecotaxes: Evidence from municipalities in southern Europe”. In: *Water* 11.3 (2019), p. 423.
- [67] B. Ohtani et al. “What is Degussa (Evonik) P25? Crystalline composition analysis, reconstruction from isolated pure particles and photocatalytic activity test”. In: *Journal of Photochemistry and Photobiology A: Chemistry* 216.2 (2010). 3rd International Conference on Semiconductor Photochemistry, SP-3, April, 2010, Glasgow UK, pp. 179–182. ISSN: 1010-6030. DOI: <https://doi.org/10.1016/j.jphotochem.2010.07.024>. URL: <https://www.sciencedirect.com/science/article/pii/S1010603010002959>.

-
- [68] Joon Seok Lee, Kyeong Hwan You, and Chan Beum Park. “Highly Photoactive, Low Bandgap TiO₂ Nanoparticles Wrapped by Graphene”. In: *Advanced Materials* 24.8 (2012), pp. 1084–1088. DOI: <https://doi.org/10.1002/adma.201104110>. eprint: <https://onlinelibrary.wiley.com/doi/pdf/10.1002/adma.201104110>. URL: <https://onlinelibrary.wiley.com/doi/abs/10.1002/adma.201104110>.
- [69] Sixto Malato et al. “Photocatalysis with solar energy at a pilot-plant scale: an overview”. In: *Applied Catalysis B: Environmental* 37.1 (2002), pp. 1–15. ISSN: 0926-3373. DOI: [https://doi.org/10.1016/S0926-3373\(01\)00315-0](https://doi.org/10.1016/S0926-3373(01)00315-0). URL: <https://www.sciencedirect.com/science/article/pii/S0926337301003150>.
- [70] J.I. Ajona and A. Vidal. “The use of CPC collectors for detoxification of contaminated water: Design, construction and preliminary results”. In: *Solar Energy* 68.1 (2000), pp. 109–120. ISSN: 0038-092X. DOI: [https://doi.org/10.1016/S0038-092X\(99\)00047-X](https://doi.org/10.1016/S0038-092X(99)00047-X). URL: <https://www.sciencedirect.com/science/article/pii/S0038092X9900047X>.
- [71] Sixto Malato et al. “Photocatalytic decontamination and disinfection of water with solar collectors”. In: *Catalysis Today* 122.1 (2007). Materials, Applications and Processes in Photocatalysis, pp. 137–149. ISSN: 0920-5861. DOI: <https://doi.org/10.1016/j.cattod.2007.01.034>. URL: <https://www.sciencedirect.com/science/article/pii/S0920586107000478>.
- [72] Jingrun Ran et al. “Metal-Free 2D/2D Phosphorene/g-C₃N₄ Van der Waals Heterojunction for Highly Enhanced Visible-Light Photocatalytic H₂ Production”. In: *Advanced Materials* 30 (25 June 2018), p. 1800128. ISSN: 15214095. DOI: [10.1002/adma.201800128](https://doi.org/10.1002/adma.201800128).
- [73] Erik Casbeer, Virender K Sharma, and Xiang-Zhong Li. “Synthesis and photocatalytic activity of ferrites under visible light: a review”. In: *Separation and Purification Technology* 87 (2012), pp. 1–14.

-
- [74] B. Van der Bruggen, M. Mänttari, and M. Nyström. “Drawbacks of applying nanofiltration and how to avoid them: A review”. In: *Separation and Purification Technology* 63.2 (2008), pp. 251–263. ISSN: 1383-5866. DOI: <https://doi.org/10.1016/j.seppur.2008.05.010>. URL: <https://www.sciencedirect.com/science/article/pii/S1383586608002104>.
- [75] Himadri Rajput et al. “Photoelectrocatalysis as a high-efficiency platform for pulping wastewater treatment and energy production”. In: *Chemical Engineering Journal* 412 (2021), p. 128612. ISSN: 1385-8947. DOI: <https://doi.org/10.1016/j.cej.2021.128612>. URL: <https://www.sciencedirect.com/science/article/pii/S1385894721002102>.
- [76] Hao Wu et al. “Photocatalytic and Photoelectrochemical Systems: Similarities and Differences”. In: *Advanced Materials* 32.18 (2020), p. 1904717. DOI: <https://doi.org/10.1002/adma.201904717>. eprint: <https://onlinelibrary.wiley.com/doi/pdf/10.1002/adma.201904717>. URL: <https://onlinelibrary.wiley.com/doi/abs/10.1002/adma.201904717>.
- [77] Min-Quan Yang et al. “Artificial photosynthesis over graphene–semiconductor composites. Are we getting better?” In: *Chemical Society Reviews* 43.24 (2014), pp. 8240–8254.
- [78] Max Lu and Pierre Pichat. *Photocatalysis and Water Purification: From Fundamentals to Recent Applications*. Weinheim, Germany: John Wiley & Sons, Incorporated, 2013. ISBN: 978-3-527-64541-1. URL: <http://ebookcentral.proquest.com/lib/bham/detail.action?docID=1161963>.
- [79] A. H. Castro Neto et al. “The electronic properties of graphene”. In: *Rev. Mod. Phys.* 81 (1 Jan. 2009), pp. 109–162. DOI: [10.1103/RevModPhys.81.109](https://doi.org/10.1103/RevModPhys.81.109). URL: <https://link.aps.org/doi/10.1103/RevModPhys.81.109>.

-
- [80] A. K. Geim and K. S. Novoselov. “The rise of graphene”. In: *Nature Materials* 6 (3 Mar. 2007), pp. 183–191. ISSN: 14761122. DOI: [10.1038/nmat1849](https://doi.org/10.1038/nmat1849). URL: <https://www.nature.com/articles/nmat1849>.
- [81] Yasuo Ebina et al. “Restacked perovskite nanosheets and their Pt-loaded materials as photocatalysts”. In: *Chemistry of materials* 14.10 (2002), pp. 4390–4395.
- [82] Masaru Harada et al. “Preparation and characterizations of Fe- or Ni-substituted titania nanosheets as photocatalysts”. In: *Journal of Photochemistry and Photobiology A: Chemistry* 148.1 (2002). SEMICONDUCTOR PHOTOCHEMISTRY 1 FIRST INTERNATIONAL CONFERENCE ON SEMICONDUCTOR PHOTOCHEMISTRY, UNIVERSITY OF STRATHCLYDE, GLASGOW, JULY 2001., pp. 273–276. ISSN: 1010-6030. DOI: [https://doi.org/10.1016/S1010-6030\(02\)00053-9](https://doi.org/10.1016/S1010-6030(02)00053-9). URL: <https://www.sciencedirect.com/science/article/pii/S1010603002000539>.
- [83] Kazuya Nakata and Akira Fujishima. “TiO₂ photocatalysis: Design and applications”. In: *Journal of Photochemistry and Photobiology C: Photochemistry Reviews* 13.3 (2012), pp. 169–189. ISSN: 1389-5567. DOI: <https://doi.org/10.1016/j.jphotochemrev.2012.06.001>. URL: <https://www.sciencedirect.com/science/article/pii/S1389556712000421>.
- [84] Yunguo Li et al. “Review of two-dimensional materials for photocatalytic water splitting from a theoretical perspective”. In: *Catal. Sci. Technol.* 7 (3 2017), pp. 545–559. DOI: [10.1039/C6CY02178F](https://doi.org/10.1039/C6CY02178F). URL: <http://dx.doi.org/10.1039/C6CY02178F>.
- [85] Chingis Daulbayev et al. “0D, 1D and 2D nanomaterials for visible photoelectrochemical water splitting. A Review”. In: *International Journal of Hydrogen Energy* 45.58 (2020), pp. 33325–33342. ISSN: 0360-3199. DOI: <https://doi.org/10.1016/j.ijhydene.2020.09.101>. URL: <https://www.sciencedirect.com/science/article/pii/S0360319920335217>.
- [86] Claudia Backes et al. “Guidelines for Exfoliation, Characterization and Processing of Layered Materials Produced by Liquid Exfoliation”. In: *Chemistry of Materials* 29.1

- (2017), pp. 243–255. DOI: [10.1021/acs.chemmater.6b03335](https://doi.org/10.1021/acs.chemmater.6b03335). eprint: <https://doi.org/10.1021/acs.chemmater.6b03335>. URL: <https://doi.org/10.1021/acs.chemmater.6b03335>.
- [87] Riccardo Frisenda et al. “Naturally occurring van der Waals materials”. In: *npj 2D Materials and Applications* 4 (1 Dec. 2020), p. 38. ISSN: 23977132. DOI: [10.1038/s41699-020-00172-2](https://doi.org/10.1038/s41699-020-00172-2).
- [88] Jonathan N. Coleman et al. “Two-dimensional nanosheets produced by liquid exfoliation of layered materials”. In: *Science* 331.6017 (6017 Feb. 2011), pp. 568–571. ISSN: 00368075. DOI: [10.1126/science.1194975](https://doi.org/10.1126/science.1194975).
- [89] Valeria Nicolosi et al. “Liquid exfoliation of layered materials”. In: *Science* 340.6139 (2013), p. 1226419.
- [90] Arunima K. Singh et al. “Computational screening of 2D materials for photocatalysis”. In: *Journal of Physical Chemistry Letters* 6 (6 2015), pp. 1087–1098. ISSN: 19487185. DOI: [10.1021/jz502646d](https://doi.org/10.1021/jz502646d).
- [91] Yunxuan Zhao et al. “Two-dimensional photocatalyst design: A critical review of recent experimental and computational advances”. In: *Materials Today* 34 (Apr. 2020), pp. 78–91. ISSN: 18734103. DOI: [10.1016/j.mattod.2019.10.022](https://doi.org/10.1016/j.mattod.2019.10.022).
- [92] Savio JA Moniz et al. “Visible-light driven heterojunction photocatalysts for water splitting—a critical review”. In: *Energy & Environmental Science* 8.3 (2015), pp. 731–759.
- [93] Kai Ren et al. “Two-dimensional heterostructures for photocatalytic water splitting: a review of recent progress”. In: *Nano Futures* 4.3 (2020), p. 032006.
- [94] Zubia Saleem et al. “Two-Dimensional Materials and Composites as Potential Water Splitting Photocatalysts: A Review”. In: *Catalysts* 10 (4 2020), pp. 464–499. DOI: [10.3390/catal10050464](https://doi.org/10.3390/catal10050464). URL: www.mdpi.com/journal/catalysts.

-
- [95] Wee-Jun Ong and Katrina Pui Yee Shak. “2D/2D heterostructured photocatalysts: an emerging platform for artificial photosynthesis”. In: *Solar RRL* 4.8 (2020), p. 2000132.
- [96] Tongming Su et al. “An overview of photocatalysis facilitated by 2D heterojunctions”. In: *Nanotechnology* 30.50 (2019), p. 502002.
- [97] G Shiva Shanker, Abhijit Biswas, and Satishchandra Ogale. “2D materials and their heterostructures for photocatalytic water splitting and conversion of CO₂ to value chemicals and fuels”. In: *Journal of Physics: Energy* 3.2 (Mar. 2021), p. 022003. DOI: [10.1088/2515-7655/abdcab](https://doi.org/10.1088/2515-7655/abdcab). URL: <https://doi.org/10.1088/2515-7655/abdcab>.
- [98] Yanhui Zhang et al. “Engineering the Unique 2D Mat of Graphene to Achieve Graphene-TiO₂ Nanocomposite for Photocatalytic Selective Transformation: What Advantage does Graphene Have over Its Forebear Carbon Nanotube?” eng. In: *ACS nano* 5.9 (2011), pp. 7426–7435. ISSN: 1936-0851.
- [99] Kai Ren, Jin Yu, and Wencheng Tang. “Two-dimensional ZnO/BSe van der waals heterostructure used as a promising photocatalyst for water splitting: A DFT study”. In: *Journal of Alloys and Compounds* 812 (2020), p. 152049. ISSN: 0925-8388. DOI: <https://doi.org/10.1016/j.jallcom.2019.152049>. URL: <https://www.sciencedirect.com/science/article/pii/S0925838819332955>.
- [100] Haodong Ji et al. “2D/1D graphitic carbon nitride/titanate nanotubes heterostructure for efficient photocatalysis of sulfamethazine under solar light: Catalytic “hot spots” at the rutile–anatase–titanate interfaces”. In: *Applied Catalysis B: Environmental* 263 (2020), p. 118357.
- [101] Hossam A. El Nazer and Yasser Mahmoud A. Mohamed. “7 - Chalcogenide-based nanomaterials as photocatalysts for water splitting and hydrogen production”. In: *Chalcogenide-Based Nanomaterials as Photocatalysts*. Ed. by Mohammad Mansoob Khan. Micro and Nano Technologies. Elsevier, 2021, pp. 173–183. ISBN: 978-0-12-

- 820498-6. DOI: <https://doi.org/10.1016/B978-0-12-820498-6.00007-X>. URL: <https://www.sciencedirect.com/science/article/pii/B978012820498600007X>.
- [102] Hee Sung Lee et al. “MoS₂ Nanosheet Phototransistors with Thickness-Modulated Optical Energy Gap”. In: *Nano Letters* 12.7 (2012), pp. 3695–3700. DOI: [10.1021/nl301485q](https://doi.org/10.1021/nl301485q).
- [103] Zhongying Wang and Baoxia Mi. “Environmental applications of 2D molybdenum disulfide (MoS₂) nanosheets”. In: *Environmental science & technology* 51.15 (2017), pp. 8229–8244.
- [104] Te-Fu Yeh et al. “Nitrogen-doped graphene oxide quantum dots as photocatalysts for overall water-splitting under visible light illumination”. In: *Advanced materials* 26.20 (2014), pp. 3297–3303.
- [105] Yang Xia et al. “Near-infrared absorbing 2D/3D ZnIn₂S₄/N-doped graphene photocatalyst for highly efficient CO₂ capture and photocatalytic reduction”. In: *Science China Materials* (2020), pp. 1–14.
- [106] Zaiwang Zhao, Yanjuan Sun, and Fan Dong. “Graphitic carbon nitride based nanocomposites: a review”. In: *Nanoscale* 7.1 (Dec. 2014), pp. 15–37. ISSN: 2040-3364. DOI: [10.1039/C4NR03008G](https://doi.org/10.1039/C4NR03008G).
- [107] Cui Lai et al. “Future roadmap on nonmetal-based 2D ultrathin nanomaterials for photocatalysis”. In: *Chemical Engineering Journal* (2020), p. 126780.
- [108] Xu Zhang et al. “Computational screening of 2D materials and rational design of heterojunctions for water splitting photocatalysts”. In: *Small Methods* 2.5 (2018), p. 1700359.
- [109] Houlong L Zhuang and Richard G Hennig. “Computational search for single-layer transition-metal dichalcogenide photocatalysts”. In: *The Journal of Physical Chemistry C* 117.40 (2013), pp. 20440–20445.

-
- [110] Jinfeng Zhang et al. “New understanding of the difference of photocatalytic activity among anatase, rutile and brookite TiO₂”. In: *Phys. Chem. Chem. Phys.* 16 (38 2014), pp. 20382–20386. DOI: [10.1039/C4CP02201G](https://doi.org/10.1039/C4CP02201G). URL: <http://dx.doi.org/10.1039/C4CP02201G>.
- [111] Lianjun Liu et al. “Photocatalytic CO₂ reduction with H₂O on TiO₂ nanocrystals: Comparison of anatase, rutile, and brookite polymorphs and exploration of surface chemistry”. In: *ACS Catalysis* 2.6 (8 Aug. 2012), pp. 1817–1828. ISSN: 21555435. DOI: [10.1021/cs300273q](https://doi.org/10.1021/cs300273q).
- [112] Songfeng Pei and Hui-Ming Cheng. “The reduction of graphene oxide”. In: *Carbon* 50.9 (2012), pp. 3210–3228.
- [113] Yanwu Zhu et al. “Graphene and graphene oxide: synthesis, properties, and applications”. In: *Advanced materials* 22.35 (2010), pp. 3906–3924.
- [114] TS Sreeprasad and Vikas Berry. “How do the electrical properties of graphene change with its functionalization?” In: *Small* 9.3 (2013), pp. 341–350.
- [115] Leonardo Vicarelli et al. “Controlling defects in graphene for optimizing the electrical properties of graphene nanodevices”. In: *ACS nano* 9.4 (2015), pp. 3428–3435.
- [116] Nicholas Rono et al. “A comparative study between thermal etching and liquid exfoliation of bulk graphitic carbon nitride to nanosheets for the photocatalytic degradation of a model environmental pollutant, Rhodamine B”. In: *Journal of Materials Science: Materials in Electronics* 32 (1 Jan. 2021), pp. 687–706. ISSN: 1573482X. DOI: [10.1007/s10854-020-04849-8](https://doi.org/10.1007/s10854-020-04849-8).
- [117] Maryam Najafi et al. “Effect of TiO₂ morphology on structure of TiO₂-graphene oxide nanocomposite synthesized via a one-step hydrothermal method”. In: *Journal of Alloys and Compounds* 722 (2017), pp. 272–277. ISSN: 0925-8388. DOI: [https://](https://doi.org/10.1016/j.jallcom.2017.05.100)

- doi.org/10.1016/j.jallcom.2017.06.001. URL: <https://www.sciencedirect.com/science/article/pii/S0925838817319758>.
- [118] Hamed Safajou et al. “Enhanced photocatalytic degradation of dyes over graphene/Pd-TiO₂ nanocomposites: TiO₂ nanowires versus TiO₂ nanoparticles”. In: *Journal of Colloid and Interface Science* 498 (2017), pp. 423–432. ISSN: 0021-9797. DOI: [10.1016/j.jcis.2017.03.078](https://doi.org/10.1016/j.jcis.2017.03.078). URL: <https://dx.doi.org/10.1016/j.jcis.2017.03.078>.
- [119] Xiaoxiao Hu et al. “Synthesis and Characterization of WO₃/Graphene Nanocomposites for Enhanced Photocatalytic Activities by One-Step In-Situ Hydrothermal Reaction”. In: *Materials* 11.1 (2018), p. 147. ISSN: 1996-1944. DOI: [10.3390/ma11010147](https://doi.org/10.3390/ma11010147). URL: <https://dx.doi.org/10.3390/ma11010147>.
- [120] Ilknur Altin et al. “Hydrothermal preparation of B-TiO₂-graphene oxide ternary nanocomposite, characterization and photocatalytic degradation of bisphenol A under simulated solar irradiation”. In: *Materials Science in Semiconductor Processing* 123 (2021), p. 105591. ISSN: 1369-8001. DOI: <https://doi.org/10.1016/j.mssp.2020.105591>. URL: <https://www.sciencedirect.com/science/article/pii/S1369800120315237>.
- [121] Huynh Van Bao et al. “Behavior of ZnO-doped TiO₂/rGO nanocomposite for water treatment enhancement”. In: *Surfaces and Interfaces* 23 (2021), p. 100950. ISSN: 2468-0230. DOI: <https://doi.org/10.1016/j.surfin.2021.100950>. URL: <https://www.sciencedirect.com/science/article/pii/S2468023021000274>.
- [122] T. Govindaraj et al. “Fabrication of WO₃ nanorods/RGO hybrid nanostructures for enhanced visible-light-driven photocatalytic degradation of Ciprofloxacin and Rhodamine B in an ecosystem”. In: *Journal of Alloys and Compounds* 868 (2021), p. 159091. ISSN: 0925-8388. DOI: <https://doi.org/10.1016/j.jallcom.2021.159091>. URL: <https://www.sciencedirect.com/science/article/pii/S0925838821004989>.
- [123] Hossein Fattahimoghaddam, Tahereh Mahvelati-Shamsabadi, and Byeong-Kyu Lee. “Efficient Photodegradation of Rhodamine B and Tetracycline over Robust and Green

- g-C₃N₄ Nanostructures: Supramolecular Design”. In: *Journal of Hazardous Materials* 403 (2021), p. 123703. ISSN: 0304-3894. DOI: <https://doi.org/10.1016/j.jhazmat.2020.123703>. URL: <https://www.sciencedirect.com/science/article/pii/S0304389420316897>.
- [124] Amir Homayoun Keihan et al. “Solvothelmal preparation of Ag nanoparticle and graphene co-loaded TiO₂ for the photocatalytic degradation of paraoxon pesticide under visible light irradiation”. In: *RSC Advances* 6.87 (2016), pp. 83673–83687. ISSN: 2046-2069. DOI: [10.1039/c6ra19478h](https://doi.org/10.1039/c6ra19478h). URL: <https://dx.doi.org/10.1039/c6ra19478h>.
- [125] Wei Lin et al. “Defects remodeling of g-C₃N₄ nanosheets by fluorine-containing solvothelmal treatment to enhance their photocatalytic activities”. In: *Applied Surface Science* 474 (2019), pp. 194–202. ISSN: 0169-4332. DOI: <https://doi.org/10.1016/j.apsusc.2018.03.140>. URL: <https://www.sciencedirect.com/science/article/pii/S0169433218308250>.
- [126] Muneerah Alomar et al. “Controlling the growth of ultrathin MoS₂ nanosheets/CdS nanoparticles by two-step solvothelmal synthesis for enhancing photocatalytic activities under visible light”. In: *Applied Surface Science* 480 (2019), pp. 1078–1088. ISSN: 0169-4332. DOI: <https://doi.org/10.1016/j.apsusc.2019.03.014>. URL: <https://www.sciencedirect.com/science/article/pii/S0169433219306269>.
- [127] Andressa Jenifer Rubio Luciano et al. “Manganese ferrite dispersed over graphene sand composite for methylene blue photocatalytic degradation”. In: *Journal of Environmental Chemical Engineering* 8.5 (2020), p. 104191. ISSN: 2213-3437. DOI: <https://doi.org/10.1016/j.jece.2020.104191>. URL: <https://www.sciencedirect.com/science/article/pii/S2213343720305406>.
- [128] Raji Atchudan et al. “Direct solvothelmal synthesis of zinc oxide nanoparticle decorated graphene oxide nanocomposite for efficient photodegradation of azo-dyes”. In: *Journal of Photochemistry and Photobiology A: Chemistry* 337 (2017), pp. 100–111.

- ISSN: 1010-6030. DOI: <https://doi.org/10.1016/j.jphotochem.2017.01.021>. URL: <https://www.sciencedirect.com/science/article/pii/S101060301631190X>.
- [129] Asim Ali Yaqoob et al. “Advances and Challenges in Developing Efficient Graphene Oxide-Based ZnO Photocatalysts for Dye Photo-Oxidation”. In: *Nanomaterials* 10.5 (2020), p. 932. ISSN: 2079-4991. DOI: [10.3390/nano10050932](https://doi.org/10.3390/nano10050932). URL: <https://dx.doi.org/10.3390/nano10050932>.
- [130] Peng Gao et al. “Graphene oxide–CdS composite with high photocatalytic degradation and disinfection activities under visible light irradiation”. In: *Journal of Hazardous Materials* 250-251 (2013), pp. 412–420. ISSN: 0304-3894. DOI: <https://doi.org/10.1016/j.jhazmat.2013.02.003>. URL: <https://www.sciencedirect.com/science/article/pii/S030438941300109X>.
- [131] Feifei Wang et al. “Facile self-assembly synthesis of γ -Fe₂O₃ /graphene oxide for enhanced photo-Fenton reaction”. In: *Environmental Pollution* 248 (2019), pp. 229–237. ISSN: 0269-7491. DOI: <https://doi.org/10.1016/j.envpol.2019.01.018>. URL: <https://www.sciencedirect.com/science/article/pii/S026974911835084X>.
- [132] Percy J. Sephra et al. “Size controlled synthesis of SnO₂ and its electrostatic self-assembly over reduced graphene oxide for photocatalyst and supercapacitor application”. In: *Materials Research Bulletin* 106 (2018), pp. 103–112. ISSN: 0025-5408. DOI: <https://doi.org/10.1016/j.materresbull.2018.05.038>. URL: <https://www.sciencedirect.com/science/article/pii/S0025540818309073>.
- [133] Lin Wang et al. “Fabricating a novel ternary recyclable Fe₃O₄/graphene/sulfur-doped g-C₃N₄ composite catalyst for enhanced removal of ranitidine under visible-light irradiation and reducing of its N-nitrosodimethylamine formation potential”. In: *Journal of Hazardous Materials* 413 (2021), p. 125288. ISSN: 0304-3894. DOI: <https://doi.org/10.1016/j.jhazmat.2021.125288>. URL: <https://www.sciencedirect.com/science/article/pii/S030438942100251X>.

-
- [134] Abhilash Mavinakere Ramesh et al. "Synthesis of graphene nanosheets by emitted black carbon and its sustainable applications". In: *Journal of Environmental Chemical Engineering* 8.5 (2020), p. 104071. ISSN: 2213-3437. DOI: <https://doi.org/10.1016/j.jece.2020.104071>. URL: <https://www.sciencedirect.com/science/article/pii/S221334372030419X>.
- [135] Ying Zhang et al. "Universal substrate growth of Ag-modified ReS₂ as visible-light-driven photocatalyst for highly efficient water disinfection". In: *Chemical Engineering Journal* 430 (2022), p. 132918. ISSN: 1385-8947. DOI: <https://doi.org/10.1016/j.cej.2021.132918>. URL: <https://www.sciencedirect.com/science/article/pii/S1385894721044934>.
- [136] Huihui Liu et al. "Graphene Grown on Anatase–TiO₂ Nanosheets: Enhanced Photocatalytic Activity on Basis of a Well-Controlled Interface". In: *The Journal of Physical Chemistry C* 122.11 (2018), pp. 6388–6396. ISSN: 1932-7447. DOI: [10.1021/acs.jpcc.7b12305](https://doi.org/10.1021/acs.jpcc.7b12305). URL: <https://dx.doi.org/10.1021/acs.jpcc.7b12305>.
- [137] Yasser A. Attia, Yasser M. A. Mohamed, and Tariq A. Altalhi. "Photobiosynthesis of metal/graphene nanocomposites: new materials for water desalination and purification". In: *Desalination and Water Treatment* 57.54 (2016), pp. 26014–26021. ISSN: 1944-3994. DOI: [10.1080/19443994.2016.1159989](https://doi.org/10.1080/19443994.2016.1159989). URL: <https://doi.org/10.1080/19443994.2016.1159989>.
- [138] Yasser A. Attia and Yasser M. A. Mohamed. "Silicon-grafted Ag/AgX/rGO nanomaterials (X = Cl or Br) as dip-photocatalysts for highly efficient p-nitrophenol reduction and paracetamol production". In: *Applied Organometallic Chemistry* 33.3 (2019), e4757. ISSN: 0268-2605. DOI: [10.1002/aoc.4757](https://doi.org/10.1002/aoc.4757). URL: <https://dx.doi.org/10.1002/aoc.4757>.
- [139] Amna Irshad et al. "Ag-doped FeCo₂O₄ nanoparticles and their composite with flat 2D reduced graphene oxide sheets for photocatalytic degradation of colored and col-

- orless compounds”. In: *FlatChem* 31 (2022), p. 100325. ISSN: 2452-2627. DOI: <https://doi.org/10.1016/j.flatc.2021.100325>. URL: <https://www.sciencedirect.com/science/article/pii/S2452262721001045>.
- [140] V. Thirumal et al. “Efficient photocatalytic degradation of hazardous pollutants by homemade kitchen blender novel technique via 2D-material of few-layer MXene nanosheets”. In: *Chemosphere* 281 (2021), p. 130984. ISSN: 0045-6535. DOI: <https://doi.org/10.1016/j.chemosphere.2021.130984>. URL: <https://www.sciencedirect.com/science/article/pii/S0045653521014569>.
- [141] Hangkun Jing et al. “Synthesis of TiO₂ nanosheet photocatalysts from exfoliation of TiS₂ and hydrothermal treatment”. In: *Journal of Materials Research* 33.21 (2018), pp. 3540–3548. ISSN: 2044-5326. DOI: [10.1557/jmr.2018.165](https://doi.org/10.1557/jmr.2018.165). URL: <https://doi.org/10.1557/jmr.2018.165>.
- [142] Nadia Barbero and Davide Vione. “Why Dyes Should Not Be Used to Test the Photocatalytic Activity of Semiconductor Oxides”. In: *Environmental Science & Technology* 50.5 (2016), pp. 2130–2131. ISSN: 0013-936X. DOI: [10.1021/acs.est.6b00213](https://doi.org/10.1021/acs.est.6b00213). URL: <https://dx.doi.org/10.1021/acs.est.6b00213>.
- [143] Michael Grätzel. “Recent Advances in Sensitized Mesoscopic Solar Cells”. In: *Accounts of Chemical Research* 42.11 (2009), pp. 1788–1798. ISSN: 0001-4842. DOI: [10.1021/ar900141y](https://doi.org/10.1021/ar900141y). URL: <https://dx.doi.org/10.1021/ar900141y>.
- [144] S. Malato et al. “Decontamination and disinfection of water by solar photocatalysis: Recent overview and trends”. In: *Catalysis Today* 147.1 (2009), pp. 1–59. ISSN: 0920-5861. DOI: [10.1016/j.cattod.2009.06.018](https://doi.org/10.1016/j.cattod.2009.06.018). URL: <https://dx.doi.org/10.1016/j.cattod.2009.06.018>.
- [145] Jun Xiong et al. “Surface Defect Engineering in 2D Nanomaterials for Photocatalysis”. In: *Advanced Functional Materials* 28 (39 Sept. 2018), p. 16163028. DOI: [10.1002/adfm.201801983](https://doi.org/10.1002/adfm.201801983).

-
- [146] Haiping Liu et al. “Defective engineering in graphitic carbon nitride nanosheet for efficient photocatalytic pathogenic bacteria disinfection”. In: *Applied Catalysis B: Environmental* 261 (2020), p. 118201. ISSN: 0926-3373. DOI: <https://doi.org/10.1016/j.apcatb.2019.118201>. URL: <https://www.sciencedirect.com/science/article/pii/S0926337319309488>.
- [147] Yongjin Li et al. “Facile synthesis of high crystallinity and oxygen vacancies rich bismuth oxybromide upconversion nanosheets by air-annealing for UV–Vis–NIR broad spectrum driven Bisphenol A degradation”. In: *Chemical Engineering Journal* (2020), p. 127868. ISSN: 1385-8947. DOI: <https://doi.org/10.1016/j.cej.2020.127868>. URL: <https://www.sciencedirect.com/science/article/pii/S1385894720339875>.
- [148] Chengyang Feng et al. “A novel sulfur-assisted annealing method of g-C₃N₄ nanosheet compensates for the loss of light absorption with further promoted charge transfer for photocatalytic production of H₂ and H₂O₂”. In: *Applied Catalysis B: Environmental* 281 (2021), p. 119539. ISSN: 0926-3373. DOI: <https://doi.org/10.1016/j.apcatb.2020.119539>. URL: <https://www.sciencedirect.com/science/article/pii/S0926337320309541>.
- [149] Run Shi et al. “Defect Engineering in Photocatalytic Nitrogen Fixation”. In: *ACS Catalysis* 9.11 (2019), pp. 9739–9750. DOI: [10.1021/acscatal.9b03246](https://doi.org/10.1021/acscatal.9b03246).
- [150] Arne Thomas et al. “Graphitic carbon nitride materials: Variation of structure and morphology and their use as metal-free catalysts”. In: *Journal of Materials Chemistry* 18 (41 2008), pp. 4893–4908. ISSN: 09599428. DOI: [10.1039/b800274f](https://doi.org/10.1039/b800274f).
- [151] Junwei Fu et al. “g-C₃N₄-Based heterostructured photocatalysts”. In: *Advanced Energy Materials* 8.3 (2018), p. 1701503.
- [152] Jason Stafford et al. “Towards scale-up of graphene production via nonoxidizing liquid exfoliation methods”. In: *AIChE Journal* 64 (9 Sept. 2018), pp. 3246–3276. ISSN: 15475905. DOI: [10.1002/aic.16174](https://doi.org/10.1002/aic.16174).

-
- [153] Rinaldo Raccichini et al. “The role of graphene for electrochemical energy storage”. In: *Nature Materials* 14 (3 2015), pp. 271–279. ISSN: 1476-4660. DOI: [10.1038/nmat4170](https://doi.org/10.1038/nmat4170). URL: <https://doi.org/10.1038/nmat4170>.
- [154] Christos Tsakonas et al. “Growth and in situ characterization of 2D materials by chemical vapour deposition on liquid metal catalysts: A review”. In: *Nanoscale* 13 (6 Feb. 2021), pp. 3346–3373. ISSN: 20403372. DOI: [10.1039/d0nr07330j](https://doi.org/10.1039/d0nr07330j).
- [155] Yenny Hernandez et al. “High-yield production of graphene by liquid-phase exfoliation of graphite”. In: *Nature nanotechnology* 3.9 (2008), pp. 563–568.
- [156] Kevin D Ausman et al. “Organic solvent dispersions of single-walled carbon nanotubes: toward solutions of pristine nanotubes”. In: *The Journal of Physical Chemistry B* 104.38 (2000), pp. 8911–8915.
- [157] Graeme Cunningham et al. “Solvent exfoliation of transition metal dichalcogenides: Dispersibility of exfoliated nanosheets varies only weakly between compounds”. In: *ACS Nano* 6 (4 Apr. 2012), pp. 3468–3480. ISSN: 19360851. DOI: [10.1021/nm300503e](https://doi.org/10.1021/nm300503e).
- [158] H. J. Salavagione et al. “Identification of high performance solvents for the sustainable processing of graphene”. In: *Green Chemistry* 19 (11 2017), pp. 2550–2560. ISSN: 14639270. DOI: [10.1039/c7gc00112f](https://doi.org/10.1039/c7gc00112f).
- [159] Mohammad Choucair, Pall Thordarson, and John A Stride. “Gram-scale production of graphene based on solvothermal synthesis and sonication”. In: *Nature nanotechnology* 4.1 (2009), p. 30.
- [160] Zheling Li et al. “Mechanisms of Liquid-Phase Exfoliation for the Production of Graphene”. In: *ACS Nano* 14 (9 Sept. 2020), pp. 10976–10985. ISSN: 1936086X. DOI: [10.1021/acsnano.0c03916](https://doi.org/10.1021/acsnano.0c03916).
- [161] Jonathan N. Coleman. “Liquid-Phase Exfoliation of Nanotubes and Graphene”. In: *Advanced Functional Materials* 19.23 (2009), pp. 3680–3695. DOI: [https://doi.org/](https://doi.org/10.1002/adfm.200900368)

- 10.1002/adfm.200901640. eprint: <https://onlinelibrary.wiley.com/doi/pdf/10.1002/adfm.200901640>. URL: <https://onlinelibrary.wiley.com/doi/abs/10.1002/adfm.200901640>.
- [162] Jonathan N. Coleman. “Liquid exfoliation of defect-free graphene”. In: *Accounts of chemical research* 46.1 (2013), pp. 14–22.
- [163] Artur Ciesielski and Paolo Samori. “Graphene via sonication assisted liquid-phase exfoliation”. In: *Chemical Society Reviews* 43.1 (2014), pp. 381–398.
- [164] M. V. Bracamonte et al. “On the Nature of Defects in Liquid-Phase Exfoliated Graphene”. In: *The Journal of Physical Chemistry C* 118.28 (2014), pp. 15455–15459. DOI: [10.1021/jp501930a](https://doi.org/10.1021/jp501930a). eprint: <https://doi.org/10.1021/jp501930a>. URL: <https://doi.org/10.1021/jp501930a>.
- [165] Keith R. Paton et al. “Production of few-layer graphene by microfluidization”. In: *Materials Research Express* 4.2 (2 Feb. 2017), p. 20531591. ISSN: 2053-1591. DOI: [10.1088/2053-1591/aa5b24](https://doi.org/10.1088/2053-1591/aa5b24).
- [166] Nicholas Jeffers et al. “The influence of the stagnation zone on the fluid dynamics at the nozzle exit of a confined and submerged impinging jet”. In: *Experiments in Fluids* 57 (2016), p. 17. DOI: [10.1007/s00348-015-2092-6](https://doi.org/10.1007/s00348-015-2092-6).
- [167] Sonia Biccai et al. “Exfoliation of 2D materials by high shear mixing”. In: *2D Materials* 6 (2019), 015008(1–8).
- [168] Jason Stafford et al. “Real-time monitoring and hydrodynamic scaling of shear exfoliated graphene”. In: *2D Materials* 8.2 (Feb. 2021), p. 025029. ISSN: 2053-1583. DOI: [10.1088/2053-1583/abdf2f](https://doi.org/10.1088/2053-1583/abdf2f). URL: <https://doi.org/10.1088/2053-1583/abdf2f>.
- [169] Xiaoya Yuan et al. “Facile synthesis of 3D porous thermally exfoliated g-C₃N₄ nanosheet with enhanced photocatalytic degradation of organic dye”. In: *Journal of Colloid and*

- Interface Science* 468.86 (2016), pp. 211–219. ISSN: 0021-9797. DOI: <https://doi.org/10.1016/j.jcis.2016.01.048>.
- [170] Fan Dong et al. “Enhanced visible light photocatalytic activity and oxidation ability of porous graphene-like g-C₃N₄ nanosheets via thermal exfoliation”. In: *Applied Surface Science* 358 (2015). Graphene and C₃N₄-based Photocatalysts, pp. 393–403. ISSN: 0169-4332. DOI: <https://doi.org/10.1016/j.apsusc.2015.04.034>. URL: <https://www.sciencedirect.com/science/article/pii/S0169433215008740>.
- [171] Jingrun Ran et al. “Porous P-doped graphitic carbon nitride nanosheets for synergistically enhanced visible-light photocatalytic H₂ production”. In: *Energy & Environmental Science* 8.12 (2015), pp. 3708–3717.
- [172] Ping Niu et al. “Graphene-like carbon nitride nanosheets for improved photocatalytic activities”. In: *Advanced Functional Materials* 22.22 (2012), pp. 4763–4770.
- [173] Ching-Yuan Su et al. “High-Quality Thin Graphene Films from Fast Electrochemical Exfoliation”. In: *ACS Nano* 5 (3 Mar. 2011). doi: 10.1021/nn200025p, pp. 2332–2339. ISSN: 1936-0851. DOI: [10.1021/nn200025p](https://doi.org/10.1021/nn200025p). URL: <https://doi.org/10.1021/nn200025p>.
- [174] Yingchang Yang et al. “Electrochemical exfoliation of graphene-like two-dimensional nanomaterials”. In: *Nanoscale* 11 (1 Jan. 2019), pp. 16–33. ISSN: 20403372. DOI: [10.1039/c8nr08227h](https://doi.org/10.1039/c8nr08227h).
- [175] Na Liu et al. “Large-Area Atomically Thin MoS₂ Nanosheets Prepared Using Electrochemical Exfoliation”. In: *ACS Nano* 8 (7 July 2014). doi: 10.1021/nn5016242, pp. 6902–6910. ISSN: 1936-0851. DOI: [10.1021/nn5016242](https://doi.org/10.1021/nn5016242). URL: <https://doi.org/10.1021/nn5016242>.
- [176] Jing Xu et al. “Chemical exfoliation of graphitic carbon nitride for efficient heterogeneous photocatalysis”. In: *J. Mater. Chem. A* 1 (46 2013), pp. 14766–14772. DOI: [10.1039/C3TA13188B](https://doi.org/10.1039/C3TA13188B). URL: <http://dx.doi.org/10.1039/C3TA13188B>.

-
- [177] Ilias Papailias et al. “Chemical vs thermal exfoliation of g-C₃N₄ for NO_x removal under visible light irradiation”. In: *Applied Catalysis B: Environmental* 239 (2018), pp. 16–26. ISSN: 0926-3373. DOI: <https://doi.org/10.1016/j.apcatb.2018.07.078>. URL: <https://www.sciencedirect.com/science/article/pii/S0926337318307215>.
- [178] Ayrat M. Dimiev and James M. Tour. “Mechanism of Graphene Oxide Formation”. In: *ACS Nano* 8.3 (2014), pp. 3060–3068. DOI: [10.1021/nn500606a](https://doi.org/10.1021/nn500606a).
- [179] Changyuan Hu et al. “A brief review of graphene–metal oxide composites synthesis and applications in photocatalysis”. In: *Journal of the Chinese Advanced Materials Society* 1.1 (2013), pp. 21–39. DOI: [10.1080/22243682.2013.771917](https://doi.org/10.1080/22243682.2013.771917). eprint: <https://doi.org/10.1080/22243682.2013.771917>. URL: <https://doi.org/10.1080/22243682.2013.771917>.
- [180] Xiao Huang et al. “25th anniversary article: Hybrid nanostructures based on two-dimensional nanomaterials”. In: *Advanced Materials* 26 (14 Apr. 2014), pp. 2185–2204. ISSN: 15214095. DOI: [10.1002/adma.201304964](https://doi.org/10.1002/adma.201304964).
- [181] Chaoliang Tan et al. “Epitaxial growth of hybrid nanostructures”. In: *Nature Reviews Materials* 3 (Jan. 2018), p. 20588437. DOI: [10.1038/natrevmats.2017.89](https://doi.org/10.1038/natrevmats.2017.89).
- [182] Alfonso Reina et al. “Large Area, Few-Layer Graphene Films on Arbitrary Substrates by Chemical Vapor Deposition”. In: *Nano Letters* 9 (1 Jan. 2009). doi: [10.1021/nl801827v](https://doi.org/10.1021/nl801827v), pp. 30–35. ISSN: 1530-6984. DOI: [10.1021/nl801827v](https://doi.org/10.1021/nl801827v). URL: <https://doi.org/10.1021/nl801827v>.
- [183] Xiaolei Qu et al. “Nanotechnology for a Safe and Sustainable Water Supply: Enabling Integrated Water Treatment and Reuse”. In: *Accounts of Chemical Research* 46.3 (2013). PMID: 22738389, pp. 834–843. DOI: [10.1021/ar300029v](https://doi.org/10.1021/ar300029v).
- [184] M.F.J Dijkstra et al. “Comparison of the efficiency of immobilized and suspended systems in photocatalytic degradation”. In: *Catalysis Today* 66.2 (2001). Catalysis in

- multiphase reactors, pp. 487–494. ISSN: 0920-5861. DOI: [https://doi.org/10.1016/S0920-5861\(01\)00257-7](https://doi.org/10.1016/S0920-5861(01)00257-7). URL: <https://www.sciencedirect.com/science/article/pii/S0920586101002577>.
- [185] B. Srikanth et al. “Recent advancements in supporting materials for immobilised photocatalytic applications in waste water treatment”. In: *Journal of Environmental Management* 200 (2017), pp. 60–78. ISSN: 0301-4797. DOI: <https://doi.org/10.1016/j.jenvman.2017.05.063>. URL: <https://www.sciencedirect.com/science/article/pii/S0301479717305364>.
- [186] Hugo Savill Russell et al. “A review of photocatalytic materials for urban nox remediation”. In: *Catalysts* 11 (6 June 2021), p. 20734344. DOI: [10.3390/catal11060675](https://doi.org/10.3390/catal11060675).
- [187] Yongjun Chen and Dionysios Dionysiou. “Correlation of Structural Properties and Film Thickness to Photocatalytic Activity of Thick TiO₂ Films Coated on Stainless Steel”. In: *Applied Catalysis B: Environmental* 69 (Dec. 2006), pp. 24–33. DOI: [10.1016/j.apcatb.2006.05.002](https://doi.org/10.1016/j.apcatb.2006.05.002).
- [188] Jian Zeng et al. “TiO₂ Immobilized in Cellulose Matrix for Photocatalytic Degradation of Phenol under Weak UV Light Irradiation”. In: *The Journal of Physical Chemistry C* 114.17 (2010), pp. 7806–7811. DOI: [10.1021/jp1005617](https://doi.org/10.1021/jp1005617).
- [189] Doni SUGIYANA et al. “Photocatalytic degradation of textile wastewater containing reactive black 5 azo dye by using immobilized TiO₂ nanofiber-nanoparticle composite catalyst on glass plates”. In: *Journal of JSCE* 2.1 (2014), pp. 69–76.
- [190] J. Esteban Duran, Madjid Mohseni, and Fariborz Taghipour. “Computational fluid dynamics modeling of immobilized photocatalytic reactors for water treatment”. In: *AIChE Journal* 57.7 (2011), pp. 1860–1872. DOI: <https://doi.org/10.1002/aic.12399>. eprint: <https://aiche.onlinelibrary.wiley.com/doi/pdf/10.1002/aic.12399>. URL: <https://aiche.onlinelibrary.wiley.com/doi/abs/10.1002/aic.12399>.

-
- [191] R. Portela et al. “Solar/lamp-irradiated tubular photoreactor for air treatment with transparent supported photocatalysts”. In: *Applied Catalysis B: Environmental* 105.1 (2011), pp. 95–102. ISSN: 0926-3373. DOI: <https://doi.org/10.1016/j.apcatb.2011.03.039>. URL: <https://www.sciencedirect.com/science/article/pii/S0926337311001615>.
- [192] Craig S Turchi and David F Ollis. “Comment. Photocatalytic reactor design: an example of mass-transfer limitations with an immobilized catalyst”. In: *The Journal of Physical Chemistry* 92.23 (1988), pp. 6852–6853.
- [193] Norman S. Allen et al. “Photocatalytic Coatings for Environmental Applications”. In: *Photochemistry and Photobiology* 81.2 (2005), pp. 279–290. DOI: <https://doi.org/10.1111/j.1751-1097.2005.tb00185.x>. eprint: <https://onlinelibrary.wiley.com/doi/pdf/10.1111/j.1751-1097.2005.tb00185.x>. URL: <https://onlinelibrary.wiley.com/doi/abs/10.1111/j.1751-1097.2005.tb00185.x>.
- [194] Md. T. Islam et al. “Development of photocatalytic paint based on TiO₂ and photopolymer resin for the degradation of organic pollutants in water”. In: *Science of The Total Environment* 704 (2020), p. 135406. ISSN: 0048-9697. DOI: <https://doi.org/10.1016/j.scitotenv.2019.135406>. URL: <https://www.sciencedirect.com/science/article/pii/S0048969719353999>.
- [195] Manviri Rani et al. “Environmental, legal, health, and safety issues of green nanomaterials”. In: Elsevier, 2022, pp. 567–594. DOI: [10.1016/b978-0-12-823137-1.00020-8](https://doi.org/10.1016/b978-0-12-823137-1.00020-8). URL: <https://dx.doi.org/10.1016/b978-0-12-823137-1.00020-8>.
- [196] Amir Bayat, Mohammad Zirak, and Esmail Saievar-Iranizad. “Vertically Aligned MoS₂ Quantum Dots/Nanoflakes Heterostructure: Facile Deposition with Excellent Performance toward Hydrogen Evolution Reaction”. In: *ACS Sustainable Chemistry & Engineering* 6.7 (2018), pp. 8374–8382. ISSN: 2168-0485. DOI: [10.1021/acssuschemeng.8b00441](https://doi.org/10.1021/acssuschemeng.8b00441). URL: <https://dx.doi.org/10.1021/acssuschemeng.8b00441>.

-
- [197] I. R. Bellobono, B. Barni, and F. Gianturco. “Preindustrial Experience in Advanced Oxidation and Integral Photodegradation of Organics in Potable Waters and Wastewaters by Photoperm(tm) Membranes Immobilizing Titanium-Dioxide and Promoting Photocatalysis”. In: *Journal of Membrane Science* 102 (June 1995). Engineering of Membrane Processes II Conference - Environmental Applications, IL CIOCCO, ITALY, APR 26-28, 1994, pp. 139–147. ISSN: 0376-7388. DOI: [10.1016/0376-7388\(94\)00273-2](https://doi.org/10.1016/0376-7388(94)00273-2).
- [198] Xiang Zheng et al. “Photocatalytic membrane reactors (PMRs) in water treatment: Configurations and influencing factors”. In: *Catalysts* 7 (8 Aug. 2017), p. 20734344. DOI: [10.3390/catal7080224](https://doi.org/10.3390/catal7080224).
- [199] Wenxiang Zhang et al. “Membrane fouling in photocatalytic membrane reactors (PMRs) for water and wastewater treatment: A critical review”. In: *Chemical Engineering Journal* 302 (Oct. 2016), pp. 446–458. ISSN: 1385-8947. DOI: [10.1016/J.CEJ.2016.05.071](https://doi.org/10.1016/J.CEJ.2016.05.071).
- [200] Chhabilal Regmi et al. “Comparison of Photocatalytic Membrane Reactor Types for the Degradation of an Organic Molecule by TiO₂-Coated PES Membrane”. In: *Catalysts* 10.7 (2020), pp. 2073–4344. DOI: [10.3390/catal10070725](https://doi.org/10.3390/catal10070725). URL: <https://www.mdpi.com/2073-4344/10/7/725>.
- [201] Yun Seup Chung, Seung Bin Park, and Duk-Won Kang. “Magnetically separable titania-coated nickel ferrite photocatalyst”. In: *Materials Chemistry and Physics* 86.2 (2004), pp. 375–381. ISSN: 0254-0584. DOI: <https://doi.org/10.1016/j.matchemphys.2004.03.027>. URL: <https://www.sciencedirect.com/science/article/pii/S0254058404001798>.
- [202] Seyed Ali Heidari-Asil et al. “Amino acid assisted-synthesis and characterization of magnetically retrievable ZnCo₂O₄–Co₃O₄ nanostructures as high activity visible-light-driven photocatalyst”. In: *International Journal of Hydrogen Energy* 45.43 (2020),

- pp. 22761–22774. ISSN: 0360-3199. DOI: <https://doi.org/10.1016/j.ijhydene.2020.06.122>. URL: <https://www.sciencedirect.com/science/article/pii/S0360319920322606>.
- [203] Bo Weng et al. “Photocorrosion Inhibition of Semiconductor-Based Photocatalysts: Basic Principle, Current Development, and Future Perspective”. In: *ACS Catalysis* 9.5 (2019), pp. 4642–4687. DOI: [10.1021/acscatal.9b00313](https://doi.org/10.1021/acscatal.9b00313). eprint: <https://doi.org/10.1021/acscatal.9b00313>. URL: <https://doi.org/10.1021/acscatal.9b00313>.
- [204] Wei Wu, Changzhong Jiang, and Vellaisamy A. L. Roy. “Recent progress in magnetic iron oxide–semiconductor composite nanomaterials as promising photocatalysts”. In: *Nanoscale* 7 (1 2015), pp. 38–58. DOI: [10.1039/C4NR04244A](https://doi.org/10.1039/C4NR04244A). URL: <http://dx.doi.org/10.1039/C4NR04244A>.
- [205] Iván Sciscenko et al. “Magnetic Photocatalyst for Wastewater Tertiary Treatment at Pilot Plant Scale: Disinfection and Enrofloxacin Abatement”. In: *Water* 13.3 (2021), pp. 2073–4441. DOI: [10.3390/w13030329](https://doi.org/10.3390/w13030329). URL: <https://www.mdpi.com/2073-4441/13/3/329>.
- [206] Jenifer Gómez-Pastora et al. “Review and perspectives on the use of magnetic nanophotocatalysts (MNPCs) in water treatment”. In: *Chemical Engineering Journal* 310 (2017). Intensification of Photocatalytic Processes for Niche Applications in the Area of Water, Wastewater and Air Treatment, pp. 407–427. ISSN: 1385-8947. DOI: <https://doi.org/10.1016/j.cej.2016.04.140>. URL: <https://www.sciencedirect.com/science/article/pii/S1385894716305903>.
- [207] Maryam Shekofteh-Gohari et al. “Magnetically separable nanocomposites based on ZnO and their applications in photocatalytic processes: A review”. In: *Critical Reviews in Environmental Science and Technology* 48.10-12 (2018), pp. 806–857. DOI: [10.1080/10643389.2018.1487227](https://doi.org/10.1080/10643389.2018.1487227).

-
- [208] Qi Wang et al. “Recent advances in MOF-based photocatalysis: environmental remediation under visible light”. In: *Inorg. Chem. Front.* 7 (2 2020), pp. 300–339. DOI: [10.1039/C9QI01120J](https://doi.org/10.1039/C9QI01120J). URL: <http://dx.doi.org/10.1039/C9QI01120J>.
- [209] Zelal Isik et al. “Entrapment of TiO₂ and ZnO powders in alginate beads: Photocatalytic and reuse efficiencies for dye solutions and toxicity effect for DNA damage”. In: *Environmental Technology & Innovation* 14 (2019), p. 100358. ISSN: 2352-1864. DOI: <https://doi.org/10.1016/j.eti.2019.100358>. URL: <https://www.sciencedirect.com/science/article/pii/S2352186418303924>.
- [210] N. Daneshvar et al. “Immobilization of TiO₂ Nanopowder on Glass Beads for the Photocatalytic Decolorization of an Azo Dye C.I. Direct Red 23”. In: *Journal of Environmental Science and Health, Part A* 40.8 (2005), pp. 1605–1617. ISSN: 1093-4529. DOI: [10.1081/ese-200060664](https://doi.org/10.1081/ese-200060664). URL: <https://dx.doi.org/10.1081/ese-200060664>.
- [211] Dezhi Xiong et al. “Highly efficient and reusable BiOCl photocatalyst modulating by hydrogel immobilization and oxygen vacancies engineering”. In: *Separation and Purification Technology* 277 (2021), p. 119628. ISSN: 1383-5866. DOI: [10.1016/j.seppur.2021.119628](https://doi.org/10.1016/j.seppur.2021.119628). URL: <https://dx.doi.org/10.1016/j.seppur.2021.119628>.
- [212] Weng-Hoong Lam et al. “Physicochemical stability of calcium alginate beads immobilizing TiO₂ nanoparticles for removal of cationic dye under UV irradiation”. In: *Journal of Applied Polymer Science* 134 (2017), p. 26. ISSN: 0021-8995. DOI: [10.1002/app.45002](https://doi.org/10.1002/app.45002). URL: <https://dx.doi.org/10.1002/app.45002>.
- [213] Jiejie Feng et al. “Preparation of black-pearl reduced graphene oxide–sodium alginate hydrogel microspheres for adsorbing organic pollutants”. In: *Journal of Colloid and Interface Science* 508 (2017), pp. 387–395. ISSN: 0021-9797. DOI: [10.1016/j.jcis.2017.07.113](https://doi.org/10.1016/j.jcis.2017.07.113). URL: <https://dx.doi.org/10.1016/j.jcis.2017.07.113>.

-
- [214] Dunpu Zhang et al. “A bio-inspired inner-motile photocatalyst film: a magnetically actuated artificial cilia photocatalyst”. In: *Nanoscale* 6 (10 2014), pp. 5516–5525. DOI: [10.1039/C4NR00644E](https://doi.org/10.1039/C4NR00644E). URL: <http://dx.doi.org/10.1039/C4NR00644E>.
- [215] Menglong Sun et al. “Construction of a Facile Recyclable Graphene-Like C₃N₄ Cilia Array for Effective Visible-Light-Responsive Photocatalytic Hydrogen Production”. In: *Energy & Fuels* 34.8 (2020), pp. 10290–10298. DOI: [10.1021/acs.energyfuels.0c01971](https://doi.org/10.1021/acs.energyfuels.0c01971).
- [216] Guang Hu et al. “Recent developments and challenges in zeolite-based composite photocatalysts for environmental applications”. In: *Chemical Engineering Journal* 417.2 (2021), p. 129209. ISSN: 1385-8947. DOI: <https://doi.org/10.1016/j.cej.2021.129209>. URL: <https://www.sciencedirect.com/science/article/pii/S1385894721008007>.
- [217] Meng Nan Chong et al. “Recent developments in photocatalytic water treatment technology: a review”. In: *Water research* 44.10 (2010), pp. 2997–3027.
- [218] Agustina Manassero, María Lucila Satuf, and Orlando Mario Alfano. “Photocatalytic reactors with suspended and immobilized TiO₂: Comparative efficiency evaluation”. In: *Chemical Engineering Journal* 326 (2017), pp. 29–36. ISSN: 1385-8947. DOI: <https://doi.org/10.1016/j.cej.2017.05.087>. URL: <https://www.sciencedirect.com/science/article/pii/S1385894717308379>.
- [219] A. Rachel, M. Subrahmanyam, and P. Boule. “Comparison of photocatalytic efficiencies of TiO₂ in suspended and immobilised form for the photocatalytic degradation of nitrobenzenesulfonic acids”. In: *Applied Catalysis B: Environmental* 37.4 (2002). cited By 221, pp. 301–308. DOI: [10.1016/S0926-3373\(02\)00007-3](https://doi.org/10.1016/S0926-3373(02)00007-3). URL: <https://www.scopus.com/inward/record.uri?eid=2-s2.0-0037043133%5C&doi=10.1016%5C%2fS0926-3373%5C%2802%5C%2900007-3%5C&partnerID=40%5C&md5=f2ac7158d5bee7d2eb8e7252e7ff3ef3>.

-
- [220] Yash Boyjoo, Ming Ang, and Vishnu Pareek. “Some aspects of photocatalytic reactor modeling using computational fluid dynamics”. In: *Chemical Engineering Science* 101 (2013), pp. 764–784. ISSN: 0009-2509. DOI: <https://doi.org/10.1016/j.ces.2013.06.035>. URL: <https://www.sciencedirect.com/science/article/pii/S0009250913004429>.
- [221] Jia Wang et al. “Numerical simulation of radiation distribution in a slurry reactor: The effect of distribution of catalyst particles”. In: *Chemical Engineering Journal* 357 (Feb. 2019), pp. 169–179. ISSN: 1385-8947. DOI: [10.1016/j.cej.2018.09.126](https://doi.org/10.1016/j.cej.2018.09.126).
- [222] Yasmine Abdel-Maksoud, Emad Imam, and Adham Ramadan. “TiO₂ Solar Photocatalytic Reactor Systems: Selection of Reactor Design for Scale-up and Commercialization—Analytical Review”. In: *Catalysts* 6.9 (2016), pp. 2073–4344. DOI: [10.3390/catal6090138](https://doi.org/10.3390/catal6090138). URL: <https://www.mdpi.com/2073-4344/6/9/138>.
- [223] Gianluca Li Puma and Po Lock Yue. “Modelling and design of thin-film slurry photocatalytic reactors for water purification”. In: *Chemical Engineering Science* 58.11 (2003), pp. 2269–2281. ISSN: 0009-2509. DOI: [https://doi.org/10.1016/S0009-2509\(03\)00086-1](https://doi.org/10.1016/S0009-2509(03)00086-1). URL: <https://www.sciencedirect.com/science/article/pii/S0009250903000861>.
- [224] G. Li puma. “Dimensionless Analysis of Photocatalytic Reactors Using Suspended Solid Photocatalysts”. In: *Chemical Engineering Research and Design* 83.7 (2005). 7th World Congress of Chemical Engineering, pp. 820–826. ISSN: 0263-8762. DOI: <https://doi.org/10.1205/cherd.04336>. URL: <https://www.sciencedirect.com/science/article/pii/S0263876205727696>.
- [225] Chi “Chip” Le et al. “A General Small-Scale Reactor To Enable Standardization and Acceleration of Photocatalytic Reactions”. In: *ACS Central Science* 3.6 (2017). PMID: 28691077, pp. 647–653. DOI: [10.1021/acscentsci.7b00159](https://doi.org/10.1021/acscentsci.7b00159).
- [226] Naresh N. Mahamuni and Yusuf G. Adewuyi. “Advanced oxidation processes (AOPs) involving ultrasound for waste water treatment: A review with emphasis on cost

- estimation”. In: *Ultrasonics Sonochemistry* 17.6 (2010). Sonochemistry: Scale up and industrial development, pp. 990–1003. ISSN: 1350-4177. DOI: <https://doi.org/10.1016/j.ultsonch.2009.09.005>. URL: <https://www.sciencedirect.com/science/article/pii/S1350417709001576>.
- [227] Danilo Spasiano et al. “Solar photocatalysis: Materials, reactors, some commercial, and pre-industrialized applications. A comprehensive approach”. In: *Applied Catalysis B: Environmental* 170-171 (2015), pp. 90–123. ISSN: 0926-3373. DOI: <https://doi.org/10.1016/j.apcatb.2014.12.050>. URL: <https://www.sciencedirect.com/science/article/pii/S0926337315000028>.
- [228] Juan José Rueda-Marquez et al. “A critical review on application of photocatalysis for toxicity reduction of real wastewaters”. In: *Journal of Cleaner Production* 258 (2020), p. 120694. ISSN: 0959-6526. DOI: <https://doi.org/10.1016/j.jclepro.2020.120694>. URL: <https://www.sciencedirect.com/science/article/pii/S0959652620307411>.
- [229] Changgu Lee et al. “Measurement of the Elastic Properties and Intrinsic Strength of Monolayer Graphene”. In: *Science* 321.5887 (July 2008), pp. 385–388. ISSN: 0036-8075. DOI: [10.1126/science.1157996](https://doi.org/10.1126/science.1157996).
- [230] Andrea C. Ferrari et al. “Science and technology roadmap for graphene, related two-dimensional crystals, and hybrid systems”. In: *Nanoscale* 7.11 (Mar. 2015), pp. 4598–4810. ISSN: 2040-3364. DOI: [10.1039/C4NR01600A](https://doi.org/10.1039/C4NR01600A).
- [231] Reza Rizvi et al. “High-Throughput Continuous Production of Shear-Exfoliated 2D Layered Materials using Compressible Flows”. In: *Adv. Mater.* 30.30 (July 2018), p. 1800200. ISSN: 0935-9648. DOI: [10.1002/adma.201800200](https://doi.org/10.1002/adma.201800200).
- [232] Min Yi and Zhigang Shen. “Kitchen blender for producing high-quality few-layer graphene”. In: *Carbon* 78 (Nov. 2014), pp. 622–626. ISSN: 0008-6223. DOI: [10.1016/j.carbon.2014.07.035](https://doi.org/10.1016/j.carbon.2014.07.035).

-
- [233] Sonia Biccai et al. “Exfoliation of 2D materials by high shear mixing”. In: *2D Mater.* 6.1 (Oct. 2018), p. 015008. ISSN: 2053-1583. DOI: [10.1088/2053-1583/aae7e3](https://doi.org/10.1088/2053-1583/aae7e3).
- [234] David J. Finn et al. “Inkjet deposition of liquid-exfoliated graphene and MoS2 nanosheets for printed device applications”. In: *J. Mater. Chem. C* 2.5 (Jan. 2014), pp. 925–932. ISSN: 2050-7526. DOI: [10.1039/C3TC31993H](https://doi.org/10.1039/C3TC31993H).
- [235] Rafiq Mulla and Charles W. Dunnill. “Sensors-on-paper: Fabrication of graphite thermal sensor arrays on cellulose paper for large area temperature mapping”. In: *HardwareX* 11 (Apr. 2022). ISSN: 2468-0672. DOI: [10.1016/j.ohx.2021.e00252](https://doi.org/10.1016/j.ohx.2021.e00252).
- [236] A. K. Niketa et al. “An automated chemical vapor deposition setup for 2D materials”. In: *HardwareX* 9 (Apr. 2021), e00165. ISSN: 2468-0672. DOI: [10.1016/j.ohx.2020.e00165](https://doi.org/10.1016/j.ohx.2020.e00165).
- [237] Sebastiano Bellani et al. “Scalable Production of Graphene Inks via Wet-Jet Milling Exfoliation for Screen-Printed Micro-Supercapacitors”. In: *Adv. Funct. Mater.* 29.14 (Apr. 2019), p. 1807659. ISSN: 1616-301X. DOI: [10.1002/adfm.201807659](https://doi.org/10.1002/adfm.201807659).
- [238] K. S. Novoselov et al. “Electric Field Effect in Atomically Thin Carbon Films”. In: *Science* 306.5696 (Oct. 2004), pp. 666–669. ISSN: 0036-8075. DOI: [10.1126/science.1102896](https://doi.org/10.1126/science.1102896).
- [239] William S. Hummers Jr. and Richard E. Offeman. “Preparation of Graphitic Oxide”. In: *J. Am. Chem. Soc.* 80.6 (Mar. 1958), p. 1339. ISSN: 0002-7863. DOI: [10.1021/ja01539a017](https://doi.org/10.1021/ja01539a017).
- [240] Claudia Backes et al. “Spectroscopic metrics allow in situ measurement of mean size and thickness of liquid-exfoliated few-layer graphene nanosheets”. In: *Nanoscale* 8.7 (Feb. 2016), pp. 4311–4323. ISSN: 2040-3364. DOI: [10.1039/C5NR08047A](https://doi.org/10.1039/C5NR08047A).

-
- [241] Yenny Hernandez et al. “Measurement of Multicomponent Solubility Parameters for Graphene Facilitates Solvent Discovery”. In: *Langmuir* 26.5 (Mar. 2010), pp. 3208–3213. ISSN: 0743-7463. DOI: [10.1021/la903188a](https://doi.org/10.1021/la903188a).
- [242] P Rama Koteswararao, SL Tulasi, and Y Pavani. “Impact of solvents on environmental pollution”. In: *Journal of Chemical and Pharmaceutical Sciences* 3 (2014), pp. 132–135. ISSN: 0974-2115.
- [243] Adam G. Kelly et al. “Whiskey-phase exfoliation: exfoliation and printing of nanosheets using Irish whiskey”. In: *2D Mater.* 6.4 (Sept. 2019), p. 045036. ISSN: 2053-1583. DOI: [10.1088/2053-1583/ab3892](https://doi.org/10.1088/2053-1583/ab3892).
- [244] Zulhelmi Ismail et al. “Black tea assisted exfoliation using a kitchen mixer allowing one-step production of graphene”. In: *Mater. Res. Express* 4.7 (July 2017), p. 075607. ISSN: 2053-1591. DOI: [10.1088/2053-1591/aa7ae2](https://doi.org/10.1088/2053-1591/aa7ae2).
- [245] Jason Stafford and Emma Kendrick. “Sustainable Upcycling of Spent Electric Vehicle Anodes into Solution-Processable Graphene Nanomaterials”. In: *Ind. Eng. Chem. Res.* 61.44 (Nov. 2022), pp. 16529–16538. ISSN: 0888-5885. DOI: [10.1021/acs.iecr.2c02634](https://doi.org/10.1021/acs.iecr.2c02634).
- [246] Aideen Griffin et al. “Effect of Surfactant Choice and Concentration on the Dimensions and Yield of Liquid-Phase-Exfoliated Nanosheets”. In: *Chemistry of Materials* 32.7 (2020), pp. 2852–2862. ISSN: 0897-4756. DOI: [10.1021/acs.chemmater.9b04684](https://doi.org/10.1021/acs.chemmater.9b04684). URL: <https://dx.doi.org/10.1021/acs.chemmater.9b04684>.
- [247] Peng He et al. “Urea-assisted aqueous exfoliation of graphite for obtaining high-quality graphene”. In: *Chem. Commun.* 51.22 (Mar. 2015), pp. 4651–4654. ISSN: 1359-7345. DOI: [10.1039/C5CC00059A](https://doi.org/10.1039/C5CC00059A).
- [248] F. A. Holland and F. S. Chapman. *Liquid Mixing and Processing in Stirred Tanks*. New York: Reinhold Publishing Corporation, 1966.

-
- [249] Claudia Backes et al. “Production of Highly Monolayer Enriched Dispersions of Liquid-Exfoliated Nanosheets by Liquid Cascade Centrifugation”. In: *ACS Nano* 10 (2016), pp. 1589–1601. DOI: [10.1021/acs.nano.5b07228](https://doi.org/10.1021/acs.nano.5b07228).
- [250] Claudia Backes et al. “Edge and confinement effects allow in situ measurement of size and thickness of liquid-exfoliated nanosheets”. In: *Nature Communications* 5 (2014). DOI: [10.1038/ncomms5576](https://doi.org/10.1038/ncomms5576).
- [251] Aideen Griffin et al. “Spectroscopic Size and Thickness Metrics for Liquid-Exfoliated h-BN”. In: *Chem. Mater.* 30.6 (Mar. 2018), pp. 1998–2005. ISSN: 0897-4756. DOI: [10.1021/acs.chemmater.7b05188](https://doi.org/10.1021/acs.chemmater.7b05188).
- [252] Claudia Backes et al. “Production and processing of graphene and related materials”. In: *2D Mater.* 7.2 (Jan. 2020), p. 022001. ISSN: 2053-1583. DOI: [10.1088/2053-1583/ab1e0a](https://doi.org/10.1088/2053-1583/ab1e0a).
- [253] A. K. Geim and I. V. Grigorieva. “Van der Waals heterostructures”. In: *Nature* 499.7459 (2013), pp. 419–425. DOI: [10.1038/nature12385](https://doi.org/10.1038/nature12385).
- [254] Xianjue Chen et al. “Controlling nanomaterial synthesis, chemical reactions and self assembly in dynamic thin films”. In: *Chem. Soc. Rev.* 43 (5 2014), pp. 1387–1399. DOI: [10.1039/C3CS60247H](https://doi.org/10.1039/C3CS60247H).
- [255] Sanliang Zhang, Yueming Li, and Ning Pan. “Graphene based supercapacitor fabricated by vacuum filtration deposition”. In: *Journal of Power Sources* 206 (2012), pp. 476–482. ISSN: 0378-7753. DOI: [10.1016/j.jpowsour.2012.01.124](https://doi.org/10.1016/j.jpowsour.2012.01.124). URL: <https://dx.doi.org/10.1016/j.jpowsour.2012.01.124>.
- [256] A. Bakker and L.M. Oshinowo. “Modelling of Turbulence in Stirred Vessels Using Large Eddy Simulation”. In: *Chemical Engineering Research and Design* 82.9 (2004), pp. 1169–1178. DOI: [10.1205/cerd.82.9.1169.44153](https://doi.org/10.1205/cerd.82.9.1169.44153).

-
- [257] Gábor Janiga. “Large-eddy simulation and 3D proper orthogonal decomposition of the hydrodynamics in a stirred tank”. In: *Chemical Engineering Science* 201 (2019), pp. 132–144. ISSN: 0009-2509. DOI: [10.1016/j.ces.2019.01.058](https://doi.org/10.1016/j.ces.2019.01.058).
- [258] Vikash and Vimal Kumar. “Turbulent statistics of flow fields using large eddy simulations in batch high shear mixers”. In: *Chemical Engineering Research and Design* 147 (2019), pp. 561–569. ISSN: 0263-8762. DOI: [10.1016/j.cherd.2019.05.045](https://doi.org/10.1016/j.cherd.2019.05.045).
- [259] A.W. Nienow. “On impeller circulation and mixing effectiveness in the turbulent flow regime”. In: *Chemical Engineering Science* 52.15 (1997), pp. 2557–2565. DOI: [10.1016/S0009-2509\(97\)00072-9](https://doi.org/10.1016/S0009-2509(97)00072-9).
- [260] Robert C. Sinclair, James L. Suter, and Peter V. Coveney. “Graphene–Graphene Interactions: Friction, Superlubricity, and Exfoliation”. In: *Advanced Materials* 30.13 (2018), p. 1705791. DOI: [10.1002/adma.201705791](https://doi.org/10.1002/adma.201705791).
- [261] Nicola Maria Pugno Giulia Salussolia Ettore Barbieri and Lorenzo Botto. “Micromechanics of liquid-phase exfoliation of a layered 2D material: A hydrodynamic peeling model”. In: *Journal of the Mechanics and Physics of Solids* 134 (2020), p. 103764. ISSN: 0022-5096. DOI: [10.1016/j.jmps.2019.103764](https://doi.org/10.1016/j.jmps.2019.103764).
- [262] Zheling Li et al. “Mechanisms of Liquid-Phase Exfoliation for the Production of Graphene”. In: *ACS Nano* 14.9 (2020), pp. 10976–10985. DOI: [10.1021/acsnano.0c03916](https://doi.org/10.1021/acsnano.0c03916).
- [263] Mustafa Lotya et al. “Liquid Phase Production of Graphene by Exfoliation of Graphite in Surfactant/Water Solutions”. In: *Journal of the American Chemical Society* 131.10 (2009), pp. 3611–3620. DOI: [10.1021/ja807449u](https://doi.org/10.1021/ja807449u).
- [264] Mustafa Lotya et al. “High-Concentration, Surfactant-Stabilized Graphene Dispersions”. In: *ACS Nano* 4.6 (2010), pp. 3155–3162. DOI: [10.1021/nn1005304](https://doi.org/10.1021/nn1005304).

-
- [265] N. Harnby, M. F. Edwards, and A. W. Nienow. *Mixing in the Process Industries*. 2nd. Oxford: Butterworth-Heinemann, 1992.
- [266] A M Kraynik. “Foam Flows”. In: *Annual Review of Fluid Mechanics* 20.1 (1988), pp. 325–357. DOI: [10.1146/annurev.fl.20.010188.001545](https://doi.org/10.1146/annurev.fl.20.010188.001545).
- [267] W. Thielicke and E.J. Stamhuis. “PIVlab – Towards User-friendly, Affordable and Accurate Digital Particle Image Velocimetry in MATLAB”. In: *Journal of Open Research Software* 2.1 (2014), p.e30. DOI: [10.5334/jors.bl](https://doi.org/10.5334/jors.bl).
- [268] Jason Stafford, Ed Walsh, and Vanessa Egan. “A statistical analysis for time-averaged turbulent and fluctuating flow fields using Particle Image Velocimetry”. In: *Flow Measurement and Instrumentation* 26 (2012), pp. 1–9. DOI: doi.org/10.1016/j.flowmeasinst.2012.04.013.
- [269] J.A. Sánchez Pérez et al. “Shear rate in stirred tank and bubble column bioreactors”. In: *Chemical Engineering Journal* 124.1 (2006), pp. 1–5. DOI: <https://doi.org/10.1016/j.cej.2006.07.002>.
- [270] Shinji Nagata. *Mixing : Principles and applications*. Tokyo ; New York: Kodansha : Wiley, 1975.
- [271] *Standard Test Method for Foam in Aqueous Media (Blender Test)*. Standard. PA, USA: ASTM International, 2007.
- [272] Ezzatollah Shamsaei et al. “Graphene-based nanosheets for stronger and more durable concrete: A review”. In: *Constr. Build. Mater.* 183 (Sept. 2018), pp. 642–660. ISSN: 0950-0618. DOI: [10.1016/j.conbuildmat.2018.06.201](https://doi.org/10.1016/j.conbuildmat.2018.06.201).
- [273] Diego T. Pérez-Álvarez et al. “Challenges surrounding nanosheets and their application to solar-driven photocatalytic water treatment”. In: *Mater. Adv.* 3.10 (May 2022), pp. 4103–4131. ISSN: 2633-5409. DOI: [10.1039/D2MA00276K](https://doi.org/10.1039/D2MA00276K).

-
- [274] Muhammad Tawalbeh, Hafsa A. Khan, and Amani Al-Othman. “Insights on the applications of metal oxide nanosheets in energy storage systems”. In: *J. Energy Storage* 60 (Apr. 2023), p. 106656. ISSN: 2352-152X. DOI: [10.1016/j.est.2023.106656](https://doi.org/10.1016/j.est.2023.106656).
- [275] Syed Nasimul Alam, Nidhi Sharma, and Lailesh Kumar. “Synthesis of graphene oxide (GO) by modified hummers method and its thermal reduction to obtain reduced graphene oxide (rGO)”. In: *Graphene* 6.1 (2017), pp. 1–18.
- [276] Thomas C. Achee et al. “High-yield scalable graphene nanosheet production from compressed graphite using electrochemical exfoliation”. In: *Sci. Rep.* 8.14525 (Sept. 2018), pp. 1–8. ISSN: 2045-2322. DOI: [10.1038/s41598-018-32741-3](https://doi.org/10.1038/s41598-018-32741-3).
- [277] G. Salussolia et al. “Simulation of interacting elastic sheets in shear flow: Insights into buckling, sliding, and reassembly of graphene nanosheets in sheared liquids”. In: *Physics of Fluids* 34.5 (May 2022), p. 053311. DOI: [10.1063/5.0087192](https://doi.org/10.1063/5.0087192).
- [278] Lorenzo Botto. “Toward Nanomechanical Models of Liquid-Phase Exfoliation of Layered 2D Nanomaterials: Analysis of a π - peel Model”. In: *Front. Mater.* 6 (Nov. 2019), p. 448137. ISSN: 2296-8016. DOI: [10.3389/fmats.2019.00302](https://doi.org/10.3389/fmats.2019.00302).
- [279] Andrea Liscio et al. “Evolution of the size and shape of 2D nanosheets during ultrasonic fragmentation”. In: *2D Materials* 4.2 (Feb. 2017), p. 025017. DOI: [10.1088/2053-1583/aa57ff](https://doi.org/10.1088/2053-1583/aa57ff). URL: <https://dx.doi.org/10.1088/2053-1583/aa57ff>.
- [280] D. J. Parker et al. “Positron emission particle tracking - a technique for studying flow within engineering equipment”. en. In: *Nuclear Instruments and Methods in Physics Research Section A: Accelerators, Spectrometers, Detectors and Associated Equipment* 326.3 (Mar. 1993), pp. 592–607. ISSN: 01689002. DOI: [10.1016/0168-9002\(93\)90864-E](https://doi.org/10.1016/0168-9002(93)90864-E). URL: <https://linkinghub.elsevier.com/retrieve/pii/016890029390864E>.
- [281] Isaac Chen and Sebastiano Cassaro. *Physiology, Bile Acids*. May 2023. URL: <https://www.ncbi.nlm.nih.gov/books/NBK549765>.

-
- [282] Tomislav Ivanković and Jasna Hrenović. “Surfactants in the Environment”. In: *Archives of Industrial Hygiene and Toxicology* 61.1 (2010), pp. 95–110. DOI: <https://doi.org/10.2478/10004-1254-61-2010-1943>.
- [283] S. Elghobashi. “On predicting particle-laden turbulent flows”. In: *Appl. Sci. Res.* 52.4 (June 1994), pp. 309–329. ISSN: 1573-1987. DOI: [10.1007/BF00936835](https://doi.org/10.1007/BF00936835).
- [284] Juan Amaro-Gahete et al. “A Comparative Study of Particle Size Distribution of Graphene Nanosheets Synthesized by an Ultrasound-Assisted Method”. In: *Nanomaterials* 9.2 (Feb. 2019). DOI: [10.3390/nano9020152](https://doi.org/10.3390/nano9020152).
- [285] M. K. Rabchinskii et al. “Establishing the applicability of the laser diffraction technique for the graphene oxide platelets lateral size measurements”. In: *J. Phys. Conf. Ser.* 1695.1 (Dec. 2020), p. 012070. ISSN: 1742-6596. DOI: [10.1088/1742-6596/1695/1/012070](https://doi.org/10.1088/1742-6596/1695/1/012070).
- [286] Vasco Filipe, Andrea Hawe, and Wim Jiskoot. “Critical Evaluation of Nanoparticle Tracking Analysis (NTA) by NanoSight for the Measurement of Nanoparticles and Protein Aggregates”. In: *Pharm. Res.* 27.5 (May 2010), pp. 796–810. ISSN: 1573-904X. DOI: [10.1007/s11095-010-0073-2](https://doi.org/10.1007/s11095-010-0073-2).
- [287] Sofia Marchesini et al. “Rapid monitoring of graphene exfoliation using NMR proton relaxation”. In: *Nanoscale* 13.34 (2021), pp. 14518–14524. DOI: [10.1039/D1NR03361A](https://doi.org/10.1039/D1NR03361A).
- [288] P. J. Davis, D. P. Gallegos, and D. M. Smith. “Rapid surface area determination via NMR spin-lattice relaxation measurements”. In: *Powder Technol.* 53.1 (Nov. 1987), pp. 39–47. ISSN: 0032-5910. DOI: [10.1016/0032-5910\(87\)80123-7](https://doi.org/10.1016/0032-5910(87)80123-7).
- [289] C. R. K. Windows-Yule et al. “Positron Emission Particle Tracking of Granular Flows”. In: *Annu. Rev. Chem. Biomol. Eng.* 11.1 (June 2020), pp. 367–396. ISSN: 1947-5438. DOI: [10.1146/annurev-chembioeng-011620-120633](https://doi.org/10.1146/annurev-chembioeng-011620-120633).

-
- [290] Kit Windows-Yule et al. *Positron Emission Particle Tracking – A comprehensive guide*. Bristol, England, UK: IOP Publishing, June 2022. ISBN: 978-0-7503-3071-8. DOI: [10.1088/978-0-7503-3071-8](https://doi.org/10.1088/978-0-7503-3071-8).
- [291] A. L. Nicuşan and C. R. K. Windows-Yule. “Positron emission particle tracking using machine learning”. In: *Rev. Sci. Instrum.* 91.1 (Jan. 2020). ISSN: 0034-6748. DOI: [10.1063/1.5129251](https://doi.org/10.1063/1.5129251).
- [292] Matthew Herald, Tzany Wheldon, and Christopher Windows-Yule. “Monte Carlo model validation of a detector system used for Positron Emission Particle Tracking”. In: *Nucl. Instrum. Methods Phys. Res., Sect. A* 993 (Mar. 2021), p. 165073. ISSN: 0168-9002. DOI: [10.1016/j.nima.2021.165073](https://doi.org/10.1016/j.nima.2021.165073).
- [293] D.M. Hampel et al. “SuperPEPT: A new tool for positron emission particle tracking; first results”. In: *Nuclear Instruments and Methods in Physics Research Section A: Accelerators, Spectrometers, Detectors and Associated Equipment* 1028 (2022), p. 166254. ISSN: 0168-9002. DOI: <https://doi.org/10.1016/j.nima.2021.166254>.
- [294] Davide Dapelo, Federico Alberini, and John Bridgeman. “Euler-Lagrange CFD modelling of unconfined gas mixing in anaerobic digestion”. In: *Water Research* 85 (2015), pp. 497–511. ISSN: 0043-1354. DOI: <https://doi.org/10.1016/j.watres.2015.08.042>. URL: <https://www.sciencedirect.com/science/article/pii/S0043135415301937>.
- [295] Jim Litster. *Design and Processing of Particulate Products*. 2016.
- [296] A. C. Ferrari et al. “Raman Spectrum of Graphene and Graphene Layers”. In: *Phys. Rev. Lett.* 97.18 (Oct. 2006), p. 187401. ISSN: 1079-7114. DOI: [10.1103/PhysRevLett.97.187401](https://doi.org/10.1103/PhysRevLett.97.187401).
- [297] B. N. J. Persson. “On the Fractal Dimension of Rough Surfaces”. In: *Tribol. Lett.* 54.1 (Apr. 2014), pp. 99–106. ISSN: 1573-2711. DOI: [10.1007/s11249-014-0313-4](https://doi.org/10.1007/s11249-014-0313-4).

-
- [298] L. W. Phipps. “The fragmentation of oil drops in emulsions by a high-pressure homogenizer”. In: *J. Phys. D: Appl. Phys.* 8.4 (Mar. 1975), p. 448. ISSN: 0022-3727. DOI: [10.1088/0022-3727/8/4/018](https://doi.org/10.1088/0022-3727/8/4/018).
- [299] S. S. Alves, J. M. T. Vasconcelos, and J. Barata. “Alternative Compartment Models of Mixing in Tall Tanks Agitated by Multi-Rushton Turbines”. In: *Chem. Eng. Res. Des.* 75.3 (Mar. 1997), pp. 334–338. ISSN: 0263-8762. DOI: [10.1205/026387697523642](https://doi.org/10.1205/026387697523642).
- [300] Wee-Jun Ong et al. “Graphene oxide as a structure-directing agent for the two-dimensional interface engineering of sandwich-like graphene-g-C₃N₄ hybrid nanostructures with enhanced visible-light photoreduction of CO₂ to methane”. In: *Chem. Commun.* 51.5 (Dec. 2014), pp. 858–861. ISSN: 1359-7345. DOI: [10.1039/C4CC08996K](https://doi.org/10.1039/C4CC08996K).
- [301] Shin Hyuk Kim, Jay H. Lee, and Richard D. Braatz. “Multi-phase particle-in-cell coupled with population balance equation (MP-PIC-PBE) method for multiscale computational fluid dynamics simulation”. In: *Comput. Chem. Eng.* 134 (Mar. 2020), p. 106686. ISSN: 0098-1354. DOI: [10.1016/j.compchemeng.2019.106686](https://doi.org/10.1016/j.compchemeng.2019.106686).
- [302] Umar Khan et al. “High-Concentration Solvent Exfoliation of Graphene”. In: *Small* 6.7 (Apr. 2010), pp. 864–871. ISSN: 1613-6810. DOI: [10.1002/sml.200902066](https://doi.org/10.1002/sml.200902066).
- [303] Bentuo Xu et al. “Graphitic carbon nitride based nanocomposites for the photocatalysis of organic contaminants under visible irradiation: Progress, limitations and future directions”. In: *Science of The Total Environment* 633 (2018), pp. 546–559. ISSN: 0048-9697. DOI: [10.1016/j.scitotenv.2018.03.206](https://doi.org/10.1016/j.scitotenv.2018.03.206). URL: <https://dx.doi.org/10.1016/j.scitotenv.2018.03.206>.